IUTAM Bookseries

Ivana Kovacic
Stefano Lenci *Editors*

IUTAM Symposium on Exploiting Nonlinear Dynamics for Engineering Systems

Springer

IUTAM Bookseries

Volume 37

The IUTAM Bookseries publishes the refereed proceedings of symposia organised by the International Union of Theoretical and Applied Mechanics (IUTAM).

Every two years the IUTAM General Assembly decides on the list of IUTAM Symposia. The Assembly calls upon the advice of the Symposia panels. Proposals for Symposia are made through the Assembly members, the Adhering Organizations, and the Affiliated Organizations, and are submitted online when a call is launched on the IUTAM website.

The IUTAM Symposia are reserved to invited participants. Those wishing to participate in an IUTAM Symposium are therefore advised to contact the Chairman of the Scientific Committee in due time in advance of the meeting. From 1996 to 2010, Kluwer Academic Publishers, now Springer, was the preferred publisher of the refereed proceedings of the IUTAM Symposia. Proceedings have also been published as special issues of appropriate journals. From 2018, this bookseries is again recommended by IUTAM for publication of Symposia proceedings.

Indexed in Ei Compendex and Scopus.

More information about this series at http://www.springer.com/series/7695

Ivana Kovacic · Stefano Lenci
Editors

IUTAM Symposium on Exploiting Nonlinear Dynamics for Engineering Systems

Springer

Editors
Ivana Kovacic
Centre for Vibro-Acoustic Systems
and Signal Processing
Faculty of Technical Sciences
University of Novi Sad
Novi Sad, Serbia

Stefano Lenci
Department of Civil and Building
Engineering, and Architecture
Polytechnic University of Marche
Ancona, Italy

ISSN 1875-3507 ISSN 1875-3493 (electronic)
IUTAM Bookseries
ISBN 978-3-030-23691-5 ISBN 978-3-030-23692-2 (eBook)
https://doi.org/10.1007/978-3-030-23692-2

This Springer imprint is published by the registered company Springer Nature Switzerland AG
The registered company address is: Gewerbestrasse 11, 6330 Cham, Switzerland

Preface

ENOLIDES 2018 is the IUTAM (International Union of Theoretical and Applied Mechanics) Symposium entitled 'Exploiting Nonlinear Dynamics for Engineering Systems', which was held in Novi Sad, Serbia, 15–19 July 2018.

The Symposium brought together academics, researchers and practitioners dealing with dynamical systems and associated applications in science and engineering with a common goal: to review recent achievements and improved knowledge in areas where the performance of dynamical systems can be potentially enhanced due to the effects of nonlinearity or optimized through certain nonlinear interaction/behaviour.

The motivation was related to the fact that the Nonlinear Dynamics of today is experiencing a profound shift of paradigm since recent investigations rely on a different strategy, which brings good effects of nonlinear phenomena to the forefront. This strategy has a positive impact on different fields in science and engineering such as vibration isolation, energy harvesting, micro/nano-electromechanical systems, etc. The ENOLIDES Symposium was, therefore, devoted to demonstrating the benefits and unlocking the potential of exploiting nonlinear dynamical behaviour in these, but also in other fields of science and engineering.

The collection of papers included in this publication are associated with some of Tribute lectures or regular/shorter presentations given at ENOLIDES 2018. We do hope that they will be of interest for specialists in the field but also for a wider spectrum of researchers and practitioners. We would like to thank members of the Scientific Committee for their help over the past year or so in helping to shape the Symposium and their invaluable assistance in the paper review process, together with a number of other reviewers. Lastly, we would like to thank all authors for supporting the Symposium and contributing to this publication—we do hope that their papers will draw the attention of a great number of readers.

Novi Sad, Serbia
Ancona, Italy

Ivana Kovacic
Stefano Lenci
Co-Chairs of ENOLIDES 2018

Contents

Chapter 1
Tribute to Ali H. Nayfeh (1933–2017)

Giuseppe Rega

Abstract Ali H. Nayfeh has been the most influential scholar and scientist of the contemporary era of nonlinear dynamics in mechanics and engineering. Upon summarizing his publications and achievements, due to space restriction attention is only paid to his successful activity as a books' author, discussing specific/novel aspects and highlighting some common underlying methodological features.

Keywords Ali Nayfeh · Perturbation methods · Nonlinear oscillations · Structural mechanics

1.1 Introduction

In the last 40 years, Ali H. Nayfeh has been the most influential, worldwide recognized, scholar and scientist in the area of nonlinear dynamics applied to mechanics and engineering. He embodied a rare mixture of scientific training and expertise/interests. Indeed, upon starting as a fluid dynamicist and an applied mathematician (60s and early 70s), he turned into a combined applied mathematician, dynamicist and physicist (70s and 80s) and then a comprehensive dynamicist, with resumed and enhanced attention to structural mechanics (90s and the new millennium). He worked in many scientific areas, dealing with perturbation techniques, nonlinear oscillations, aerodynamics, flight mechanics, acoustics, ship motion, hydrodynamic stability, nonlinear waves, structural dynamics, experimental dynamics, linear and nonlinear control, micromechanics, and providing outstanding contributions. During four decades he was also a brilliant educator for thousands of student, and wrote a meaningful number of important books.

Due to lack of space, it is impossible to dwell here on all aspects of Nayfeh's scientific activity, thus choosing to solely focus on his contributions as a scholar and

G. Rega (✉)
Department of Structural and Geotechnical Engineering, Sapienza University of Rome, Via A. Gramsci 53, 00197 Rome, Italy
e-mail: giuseppe.rega@uniroma1.it

I. Kovacic and S. Lenci (eds.), *IUTAM Symposium on Exploiting Nonlinear Dynamics for Engineering Systems*, IUTAM Bookseries 37,
https://doi.org/10.1007/978-3-030-23692-2_1

a successful books' author, while leaving to a more extended paper [16] a general discussion on his many original contributions as a scientist.

Upon summarizing his life, publications and achievements [2, 4, 18] in Sect. 1.2, Nayfeh's books are comprehensively discussed in Sect. 1.3, by analyzing specific features and novel aspects of a number of them, and by highlighting some underlying common methodological features. Section 1.4 provides a summary portrait of Ali Nayfeh as an outstanding scholar and scientist in nonlinear dynamics, at the crossroad between applied mathematics and engineering.

1.2 Life, Publications, Achievements: A Short Summary

Ali H. Nayfeh was born on December 21, 1933 in Shuwaikah, Palestine, to an illiterate and poor family which, nonetheless, highly encouraged him to acquire education and maximum possible knowledge. Owed to the harsh conditions in his country and lack of higher-education institutes, Ali worked as a teacher of mathematics in small villages and towns for ten years. At the age of 26 he won a scholarship to study in the USA, and in only 5 years moved from a 1 year junior college up to getting Bachelor's Degree in engineering science (1962), Master of Science (1963), and Ph.D. in Aeronautics and Astronautics (1964) at Stanford University.

For six years (1964–1970) he worked in the aerospace industry, upon which he was appointed at Virginia Tech as a Professor (1971) and then as a University Distinguished Professor (1976). Nayfeh:

- Wrote: (i) 10 books in perturbation methods and nonlinear dynamics, several of them with thousands of citations, considered as the most valuable and fundamental references in their fields, translated into Russian, Chinese, and German, and used as textbooks in top schools; (ii) nearly 480 papers in refereed journals.
- Was the Founder and Editor of two fundamental journals, *Nonlinear Dynamics* and *Journal of Vibration and Control*.
- Advised 69 Ph.D. students: many of them became prominent scholars, department chairs and deans in top ranked institutes all over the world.
- Established the highly successful series of 13 Conferences on *Nonlinear Vibrations, Stability, and Dynamics of Structures* at Virginia Tech (1986–2010).
- Received honorary doctorates from Politechnika Szczecinska, Poland, Technical University of Munich, Germany, and Marine Technical University of St. Petersburg, Russia, along with an incredible number of Awards, including:

1995 AIAA Pendray Aerospace Literature, "for seminal contributions to perturbation methods, nonlinear dynamics, acoustics, and boundary-layer transition."
1996 ASME Den Hartog, "for lifetime contributions to the teaching and practice of vibration engineering."
2005 ASME Lyapunov (first recipient), "for lifelong contributions to the field of nonlinear dynamics."

2008 ASME Thomas Caughey (first recipient), "for significant contributions to the field of nonlinear dynamics through practice, research, teaching, and outstanding leadership."
2014 Benjamin Franklin Medal in Mechanical Engineering, "for developing novel methods to model complex engineering systems in structural dynamics, acoustics, fluid mechanics, and electromechanical systems."

Ali always aimed at contributing to the development of science in the Arab World. He established the college of engineering at King Abdel Aziz University in Jeddah, Saudi Arabia (1976), and an engineering college in Jordan where he served as Dean and Vice-president for engineering affairs for four years (1980). He also helped establishing a new graduate and internationally reputable program in mechanics in Tunisia (2002).

Upon retiring from Virginia Tech, he volunteered at the University of Jordan, under the condition of working without pay, helping scientists and researchers, and providing advice and consultations; he even established and funded a modern school in his birth village of Palestine, to offer the best education and produce a new generation of brilliant scientists.

Quoting from [18]: "Anyone who has met Dr. Nayfeh knows well his inexhaustible energy and deep desire for knowledge; and more importantly, his passion to share and spread his knowledge with others. … He was a brilliant scientist, a distinguished teacher, an inspiring motivator, a great community leader, and an amazing and lovely human. He will be truly and deeply missed."

1.3 Nayfeh's Books

Nayfeh wrote several books, generally clearly distinct from each other and of high impact. They are summarized in Fig. 1.1, by grouping them in three main areas, with well-identified and coherent features.

The first group is concerned with analytical methods, and includes all books on asymptotic techniques, with special emphasis on the method of multiple time scales (MMS) which was Nayfeh's most originally addressed theme within the realm of applied mathematics. Within this overall context, the transition can be recognized from a theoretically-oriented approach [6] to a more introductory treatment of mathematical aspects [7], with also clear educational purposes [8], up to a modern popularization of the MMS [12] taking advantage of symbolic algebra, as well as the independent treatment of a method [9] playing an important role in nonlinear dynamics.

Books in the second group are more physically-oriented, and also more varied. Indeed, they range from the effective use of asymptotic techniques for the analysis of weakly nonlinear archetypal oscillators [13], to the presentation of computational and geometrical concepts, techniques and tools of the modern theory of dynamical systems also allowing to deal with strongly nonlinear and complex phenomena [11], up to the analysis of the involved interaction phenomena, regular or non-regular, which

	ANALYTICAL METHODS	NONLINEAR PHYSICAL ASPECTS	STRUCTURAL MECHANICS
1970-79	*Perturbation Methods* (1973) 	*Nonlinear Oscillations* (1979) with D.T. Mook	
1980-89	*Introduction to Perturbation Techniques* (1980) *Problems in Perturbations* (1985)		
1990-99	*Method of Normal Forms* (1993) *Perturbation Methods with Mathematica, Maple* (1999) with C.M. Chin	*Applied Nonlinear Dynamics* *Analytical, Computational and Experimental Methods* (1995) with B. Balachandran	
2000-09		*Nonlinear Interactions* *Analytical, Computational and Experimental Methods* (2000)	*Linear and Nonlinear Structural Mechanics* (2004) with P.F. Pai

Fig. 1.1 Ali Nayfeh's books

characterize the nonlinear dynamics of multi-mode models reliably representative of actual engineering systems [10].

The third group consists of a book [14] which, pushing forward the interest towards distributed parameter systems already apparent in [10], deals more generally with structural mechanics issues in terms of modelling, dynamic analyses, and exemplary phenomenological aspects.

In the following, the main features and novel aspects of some of these books with respect to their publication time are discussed, by citing a few author's sentences from the corresponding prefaces (as per the writer's choice) and by summarizing a few characterizing aspects.

1.3.1 Specific and Novel Features

Although being certainly linked with each other, Nayfeh's two fundamental books on perturbation methods were driven by a different perspective.

- *Perturbation Methods* (1973). "The different *techniques are described using examples* which start with model simple ordinary equations that can be solved exactly and *progress toward complex* partial differential equations", with "examples drawn

from *different branches of physics and engineering*", and "the different techniques described as formal procedures *without any attempt at justifying them rigorously*."

- *Introduction to Perturbation Techniques* (1980). In contrast with the former book, where "*coincise* and *advanced* material" is dealt with, this second one presents the same material "in *elementary* way." Indeed, "a*s a result of teaching perturbation methods for eight years* to first-year and advanced graduate students at Virginia Polytechnic Institute and State University, I have *selected a limited number of techniques and amplified their description* considerably. Also I have attempted to answer the questions most frequently raised by my students. … A new chapter is devoted to the determination of the adjoints of homogeneous linear equations and the *solvability conditions* of linear inhomogeneous problems."

However, Nayfeh's research activity on mathematical aspects of ordinary differential equations was always paralleled by a deep interest towards physical aspects of the nonlinear oscillations described by those equations.

Nonlinear Oscillations (1979) was the comprehensive outcome of intense and extended applications of the multiple scale technique to obtain the solution of both archetypal oscillators (representing discrete systems, or simplified reduced models of continuous systems) and some multidegree-of-freedom models.

In the preface, referring to a comprehensive list of books on the same topic and generally with a similar title, it is stated that "the *previously published books emphasized*, and some exclusively treated, systems having a *single degree of freedom*", whereas "the *primary purpose* of this book *is to fill this void.*" Specifically, Chap. 1 (Introduction) "attempts to *abstract the entire book*" and provides an useful and *comprehensive overview* of the addressed topics (according to a criterion later on adopted successfully in the introduction of other books), describing "*only the physical phenomena, leaving all the algebra to the subsequent chapters.*"

Seven chapters are devoted to Single-Degree-of-Freedom Systems (conservative, nonconservative, forced); Parametrically excited systems; Systems having finite degrees of freedom, with the treatment of internal resonance; Continuous systems (beams, string, plates); and Traveling waves. In particular, Chap. 7 "concentrates on the *physical mechanisms* and *effects*, restricting the attention to uniform systems with simple boundary conditions whose linear natural modes can be obtained analytically; then using the method of multiple scales to solve the equations describing the temporal functions"; Chap. 8 refers to "simple *physical examples* to explain nonlinear dispersive and nondispersive waves."

Nonlinear Oscillations (1979) was translated in many languages, and became a fundamental classroom textbook in many academic institutions, summing up to 9402 citations (as of April 28, 2019, according to Google Scholar).

Between the 80s and the 90s, a substantial enlargement of research perspectives in nonlinear dynamics occurred within the community of applied mechanicians, with the attention being increasingly paid to strongly nonlinear dynamic phenomena. Nearly in parallel with such developments, the role played by experimental (physical) techniques for a reliable and exhaustive characterization of the dynamics of (mostly) multi/infinite-dimensional systems became fully apparent.

Although not providing specific foundational contributions to the development of these novel topics, Nayfeh swiftly grasped the importance of properly complementing the treatment of nonlinear oscillations via classical perturbation methods with the intensive use of advanced *geometrical* and *computational* techniques from the dynamical system theory also allowing to deal with strongly nonlinear and complex dynamics, along with the need to validate theoretical/numerical outcomes through *experimental* approaches.

Applied Nonlinear Dynamics (1995) testifies to Nayfeh's great capability to grasp recent advancements and scientific trends, and *timely make them available to people involved with research,* and to practicing engineers working on challenging problems in applied mechanics.

Upon worthily summarizing the overall book contents in the introduction, seven chapters are dedicated to Equilibrium Solutions, Periodic Solutions, Quasiperiodic Solutions, Chaos, Numerical Methods, Tools to Analyze Motions, and Control. Specifically, quoting from ca.wiley.com website:

- "*Analytical* approaches based on perturbation methods and *dynamical systems theory* are presented and illustrated through *applications to a wide range of nonlinear systems*."
- "*Geometrical* concepts, such as Poincaré maps, are treated at length, with a thorough discussion of stability and *local and global bifurcation* analyses for systems of differential equations and algebraic equations conducted with the aid of *examples* and *illustrations*. *Continuation methods* for fixed points and periodic solutions, and *homotopy methods* for determining fixed points, are detailed. Bifurcations of fixed points, limit cycles, tori, and chaos are discussed."
- *Chaos* is explored, with many routes treated at length, by also describing methods for "*controlling bifurcations and chaos*."
- "*Numerical* methods and *tools* (Poincaré sections, Fourier spectra, autocorrelation functions, Lyapunov exponents, dimension calculations)" for the *analysis* and *characterization* of motion in both the analytical and experimental context are presented.

Consistent with the awareness of being substantially a (though smart) user of techniques developed by others and with the willingness to provide an understandable framework to effectively implement them in applications, "proofs are not provided but references that provide them are included, some chapters (2, 3) are not written within a mathematically rigorous framework" [11], and many examples are used to explain the different concepts.

The last two books mark a progressive shift (or, indeed, an extension) of Nayfeh's interests (already present in his earlier activity) towards applied dynamics problems in structural and mechanical engineering.

Nonlinear Interactions (2000) is built on the awareness that "an understanding of dynamic characteristics of a *structural system* is essential for its *design and control.*"

(a) A *variety of nonlinear interactions* based on (2:1, 1:1, 3:1) autoparametric and combination resonances are addressed.

(b) *Another type* of experimentally observed interaction between a *directly excited high-frequency* mode and a *low-frequency* mode, accompanied by a *slow modulation* of amplitude and phase of the former, is discussed. It is a mechanism of *great practical importance*, through which *energy from high-frequency low-amplitude sources* (such as rotating machineries, waves, propeller blades passing the rudder) can be *transferred* to *large-amplitude low-frequency modes* of supporting structures and foundations, resulting in their possible *harmful oscillations*, or may entail *decrease of vibration* of a *main system* and *increase of its fatigue life* to the expense of a *sacrificial subsystem*.

Upon the introduction, seven chapters include treatment of (5) Systems with widely spaced modes, (6) Multiple internal resonances, and (7) Nonlinear normal modes. Among meaningfully addressed topics, the following ones are mentioned.

- *Multidegree-of-freedom* systems, with a marked interest to *distributed parameter* (structural) systems besides discrete (mechanical) ones.
- Modulation equations: equilibrium solutions; stability and bifurcation analysis; dynamic solutions. This delineates a *number of issues to be sequentially faced* for a *comprehensive nonlinear dynamic analysis* of a generic system, according to a scheme later on *adopted in hundreds of papers by other authors*.
- Confronting *direct* versus *discretization* approach in asymptotics.
- *Control strategies* based on internal resonances and ensuing phenomena (e.g., saturation in 2:1 resonance).
- Importance of *higher-order approximations*.
- Comparing methods to obtain *nonlinear normal modes* for discrete and continuous systems (direct multiple scales, method of normal form, real- versus complex-valued invariant manifold approach).

Overall, the book is indeed a *mine of information* about the richness and variety of nonlinear phenomena, along with the theory behind them, and a valuable *blend* of *author's expertise* on *classical perturbation* methods and *nonlinear oscillations* theory—revisited through symbolic algebra—with knowledge and tools from *dynamical system theory* and *experimental nonlinear dynamics*.

Twenty years after the publication of [13], the book can be considered as its *continuation* and *update*, and turns out to be "more *in the genuine author's attitude of mind* than some other of his recent books" [15].

Linear and Nonlinear Structural Mechanics (2004) dwells on how the "nonlinear modeling and dynamic analysis of structures becomes a complex but important step in advancing the design and optimization of modern structural systems (with special attention to composites)" and aims "to close the gap between the practicing engineer and the applied mathematician in the modeling and analysis of geometrically nonlinear structures."

- "*Mathematically consistent* and *systematic* derivations of *comprehensive* and *refined structural theories*" of strings, cables, beams, plates and shells, both *exact* and *approximate*, are presented, also including laminates, integration with piezoelectric materials, thermoelasticity, and microbeams/plates.

- "*Physical meaning* of linear and nonlinear structural mechanics" is detailed.
- "*Ready-to-use governing equations* and *boundary conditions*" are provided, "ranging from simple linear to complex nonlinear."
- Exemplary *nonlinear structural analyses* of refined and/or reduced order models are summarized.
- Some main treatments and outcomes of *linear/nonlinear dynamics* for beams, plates and shells are obtained, referring to refined and/or reduced order models.

1.3.2 Some Characterizing Methodological Aspects

Some main *methodological aspects* common to all Nayfeh's books are highlighted and illustrated with examples in the following. His overall production exhibits four basic characteristics.

1. Topics are addressed and presented based on an *incremental/additive* (and overall *inductive*) perspective, via a *series of case histories*.
2. Specific outcomes (about *analytical techniques*, *different methods* and/or *systems*) are embedded into a *unified, comprehensive*, and *comparative* framework.
3. Concepts are illustrated with *numerous examples* and many *exercises* aimed to reinforce and assess *progress in understanding*.
4. *Extended* and *updated bibliographies* are provided.

The incremental/additive perspective can be recognized in the contents of anyone of Nayfeh's books. Figure 1.2 shows two examples [13] concerned with the forced oscillations of systems with a single or finite number of degrees of freedom. Considering "simple systems that exhibit the essential ideas, instead of treating general systems for which the algebra is involved" produces lists of case studies of progressively increased difficulty. Basic nonlinearities (cubic, or quadratic and cubic) and self-sustained oscillations are addressed in the first example, considering different resonant (primary, subharmonic, superharmonic, combination, simultaneous) or nonresonant excitations. In turn, the second example refers to diverse physical systems and deals with various cases of resonance between excitation and system natural frequencies for those having quadratic nonlinearities. The adopted scheme is certainly repetitive. Yet, while being somehow encyclopedic, the underlying comprehensive perspective allows to easily point out differences and peculiarities of distinct nonlinear aspects of both the analytical treatment and the considered systems/excitations. This results in a meaningful amount of information about the richness and variety of nonlinear phenomena, and the theory behind them.

A similar example (Fig. 1.3) is taken from [9], where the general idea of the method of normal forms to "use a 'local' (i.e., near-identity) coordinate transformation to 'simplify' the equations describing the dynamics of the system under consideration" is applied to parametrically excited systems.

Two more incremental/additive examples (Fig. 1.4) refer to topics addressed by Nayfeh later on in the more engineering oriented stage of his activity, and also high-

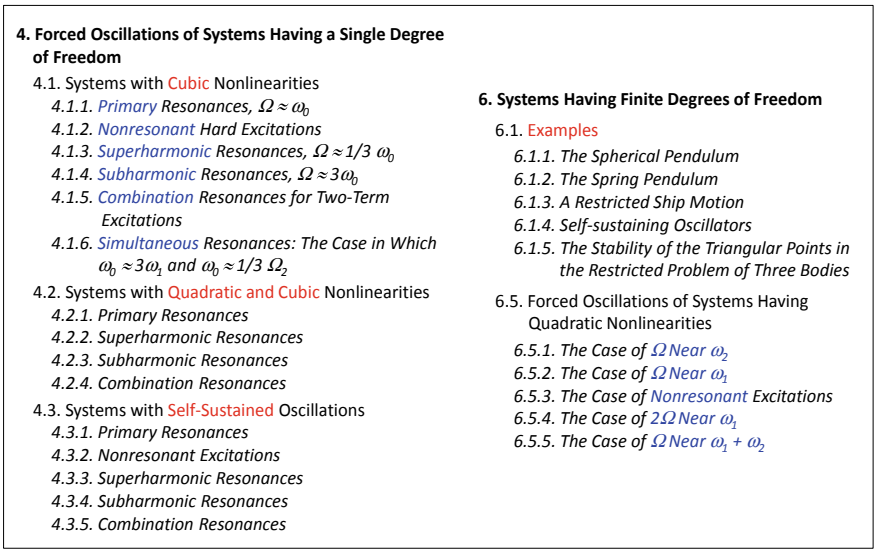

Fig. 1.2 Incremental/additive approach in the contents of [13]

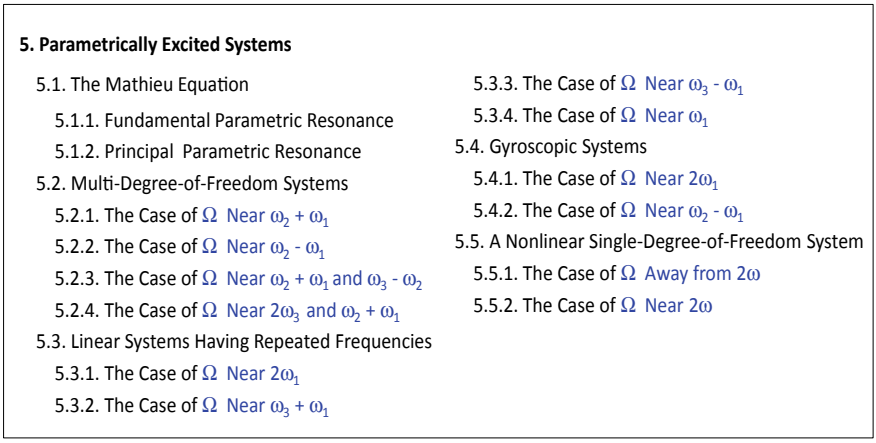

Fig. 1.3 Incremental/additive approach in the contents of [9]

light the *inductive* character of his approach: the same form of modulation equations is recognized for systems belonging to a certain group of symmetry [10], and methods of linear/nonlinear structural mechanics can be readily extended to different and/or more complex structures [14].

Overall, as explicitly declared in the prefaces of all Nayfeh's books (starting with the more theoretical one [6]), the material is not presented "within a mathematically rigorous framework." This originated criticisms from more dynamical system-oriented (and generally more rigorous) scientists. But this characterizing

***Nonlinear Interactions* (2000):**

- *2:1, 1:1, or 3:1 Internal Resonances*: primary resonance, principal parametric resonance (of first mode, of second mode), fundamental parametric resonance
  Combination Resonances: parametric, external, internal; of the additive or difference type
- *Nonlinear Normal Modes*: a symmetric 2-dof system; an asymmetric 2-dof system; cubic and quintic nonlinearities; quadratic and cubic nonlinearities; multi-dof systems; systems with internal resonances; continuous systems

Inductive: for systems with 1:1 internal resonance:

"the modulation equations have the same form for all systems with O_2 symmetry, irrespective of their physical origin and/or the source of the nonlinearity"

***Linear and Nonlinear Structural Mechanics* (2004):**

- *Plates*: linear classical; linear shear-deformable; nonlinear classical; general nonlinear classical; nonlinear shear-deformable; nonlinear layerwise shear-deformable

Incremental/Inductive:

"as a result, the reader can readily extend the methods to formulate and analyze different and/or more complex structures"

Fig. 1.4 Incremental/inductive approach in [10, 14]

feature of Nayfeh's scientific personality ensued from his being basically a scholar in engineering sciences capable of exploiting a strongly founded knowledge of fundamentals of applied mathematics to understand the nonlinear behavior of involved mechanical/structural systems; this being the actual main focus of his research interests. The inductive approach adopted by Nayfeh in his presentations of scientific material was likely brought to its extreme consequences. Yet, it was somehow in line with the perspective adopted by most of the earlier scientists active in nonlinear dynamics (including mathematicians), who "were not led to their discoveries by a process of deduction from general postulates or principles, but rather by a thorough examination of properly chosen particular cases", with the generalization coming later "because it is far easier to generalize an established result than to discover a new line of argument" [5]. In this sense, Nayfeh's approach was not too far from the purpose of studying *concrete nonlinear systems* with their "natural effects", which also inspired earlier theoretical research in nonlinear dynamics at Moscow [1] and Kiev [3] schools.

It is anyway important to notice that such a 'list-looking' aspect of his presentations was constantly paralleled in all books by the successful attempt to achieve a *unified, comprehensive,* and *comparative* framework into which presenting the various case-studies and highlighting the relevant differences and peculiarities. Sentences from the prefaces of some Nayfeh's books quoted in Fig. 1.5 witness the care he always paid to the matter.

Two more aspects of Nayfeh's fully effective educational and professional perspective as a book author are to be mentioned. Concepts were always illustrated through worked-out examples and exercises useful to reinforce understanding and

- *Perturbation Methods* (1973):
  "Presents in ***a unified*** way an account of most of the ***perturbation*** techniques, pointing out their ***similarities, differences, and advantages,*** as well as their ***limitations***"
- *Applied Nonlinear Dynamics* (1995):
  "Unlike most other texts, which emphasize either classical methods, experiments and physics, geometrical methods, computational methods, or applied mathematics, provides **a** ***coherent and unified*** treatment of ***analytical, computational, and experimental*** methods and concepts of ***nonlinear dynamics***"
- *Nonlinear Interactions* (2000):
  "Provides a ***coherent and unified*** treatment of ***analytical, computational, and experimental*** methods and concepts of ***modal interactions***"
  As an obvious extension of *Applied Nonlinear Dynamics* (1995), the relevant "methods are used to explore and unfold in a ***unified*** manner the ***fascinating complexities*** in nonlinear dynamical systems"
- *Linear and Nonlinear Structural Mechanics* (2004):
  "A ***unique unified*** approach, more general than those found in most structural mechanics books, is used to model ***geometric nonlinearities*** of structures"

Fig. 1.5 A unified framework

assess progress of students. Moreover, very rich and (for their time) updated bibliographies were provided at the end of each book. They are still invaluable sources of information/knowledge about 'classical' and more recent books and journal/conference papers, for scholars in nonlinear dynamics. This is even more important in the current time in which scientific problems are sometime 'rediscovered', in a context of overall minor care paid to the historical evolution and advancement of science by some young scientist mostly aimed at attaining specific, and also possibly limited, goals.

1.4 Complementing Mathematical and Engineering Approaches to Nonlinear Systems

A fundamental part of Ali Nayfeh's legacy consists of the conceptual, and mostly operational, contributions to the method of multiple time scales provided at the beginning of his scientific activity, and later on expanded in the direction of frequently needed higher-order expansions and in terms of popularization. As a matter of fact, multiple time scales are continuously being used by generations of scientists for solving nonlinear dynamics problems. This holds irrespective of mathematical warnings raised about pitfalls possibly occurring in the asymptotics of the MMS

owed mostly to the anticipated choice of timescales, a feature which does not occur in the averaging method where they emerge by nonsecularity conditions without any a priori assumption [17]. But Nayfeh was most likely aware of those pitfalls. This is witnessed both by the reference constantly made to the need to *properly select timescales* (including fractional ones) depending on the dynamic problem at hand, and by his many performed *comparisons of equivalent approximations* provided by multiple scales and averaging. It is however to be noticed that Nayfeh's *enormous skill and experience* about how *properly selecting* a priori the timescales necessary for a reliable asymptotic solution of a given problem ensue from exceptional *personal* features in terms of *intuition* and *overall understanding* which are not in the patrimony of all scientists.

As a matter of fact, looking at his outstanding scientific activity on a huge variety of themes [16], Nayfeh's main nature of a *scholar in engineering sciences* could be further highlighted. While being well-acquainted with applied mathematics, he was fundamentally interested in using his skill and expertise to catch *the nonlinear behavior* of *mechanical and structural systems*. Indeed, moving from his earlier achievements on the nonlinear oscillations of simple models, in the second part of Nayfeh's academic life further *distinguishing* and highly *influential features* in the realm of *applied mechanics* and *engineering* emerged clearly. Therein, with an unrivaled capability to *grasp novel advancements* and *research trends*, he succeeded in remarkably complementing a profound *expertise* on *asymptotic methods* and *nonlinear oscillations* theory, revisited through modern symbolic algebra, with the effective *interpretation* and *organization* of *experimental outcomes*, both in-house and from the literature, along with the *smart use* of *knowledge and tools* from *modern dynamical system* theory.

Acknowledgements The financial support of the Italian Research Project PRIN 2015 (No. 2015JW9NJT) is acknowledged.

References

1. Andronov, A.A., Witt, A.A., Khaïkin, S.E.: Theory of Oscillators. Pergamon, London (1966). (Russian edition, Moscow 1937)
2. Balachandran, B., Younis, M.I., Shen, I.Y.: In memoriam: Ali Hasan Nayfeh. J. Vib. Acoust. **139**, 040101–1 (2017)
3. Krylov, N.M., Bogoliubov, N.N.: Introduction to Nonlinear Mechanics. Princeton University Press, Princeton (1947). (Russian edition, Moscow, 1937)
4. Lacarbonara, W.: Obituary: Professor Ali H. Nayfeh 21 December 1933–27 March 2017. J. Sound Vib. **400**, 680–683 (2017)
5. Mira, C.: Some historical aspects of nonlinear dynamics: possible trends for the future. Int. J. Bifurc. Chaos **7**, 2145–2173 (1997)
6. Nayfeh, A.H.: Perturbation Methods. Wiley, New York (1973)
7. Nayfeh, A.H.: Introduction to Perturbation Techniques. Wiley, New York (1980)
8. Nayfeh, A.H.: Problems in Perturbations. Wiley, New York (1985)
9. Nayfeh, A.H.: Method of Normal Forms. Wiley, New York (1993)
10. Nayfeh, A.H.: Nonlinear Interactions. Wiley, New York (2000)

11. Nayfeh, A.H., Balachandran, B.: Applied Nonlinear Dynamics. Wiley, New York (1995)
12. Nayfeh, A.H., Chin, C.M.: Perturbation Methods with Mathematica/Maple. Dynamics Press, Virginia. http://www.esm.vt.edu/~anayfeh/ (1999)
13. Nayfeh, A.H., Mook, D.T.: Nonlinear Oscillations. Wiley, New York (1979)
14. Nayfeh, A.H., Pai, P.F.: Linear and Nonlinear Structural Mechanics. Wiley, Hoboken (2004)
15. Rega, G.: Nonlinear interactions: analytical, computational, and experimental methods (AH Nayfeh). Meccanica **35**, 583–585 (2000)
16. Rega, G.: Nonlinear dynamics in mechanics and engineering: forty years of developments and Ali H. Nayfeh's legacy. Nonlinear Dyn. (2019). https://doi.org/10.1007/s11071-019-04833-w
17. Verhulst, F.: Profits and pitfalls of timescales in asymptotics. SIAM Rev. **57**, 255–274 (2015)
18. Younis, M.I.: In memoriam: Ali Hasan Nayfeh 1933–2017. Nonlinear Dyn. **88**, 1535–1536 (2017)

Chapter 2
Henri Poincaré (1854–1912) Engineer, Mathematician, Physicist and Philosopher

Ferdinand Verhulst

Abstract We present a brief introduction to Poincaré's ideas and projects. After a global survey of his life and work we give an extensive evaluation of his famous Prize Essay and discuss his concepts of dynamical systems. A section is devoted to Poincaré's influence on theoretical engineering and one on his many results in mathematical physics.

Keywords Poincaré · Dynamical systems · Mathematical physics

2.1 Introduction, Poincaré's Life and Work

There exist a number of biographies of Henri Poincaré. A recent one is [4] which emphasizes the historical relation between Poincaré and earlier and contemporary scientists; [1] is unusual, it contains information of the reactions to Poincaré's ideas and papers in the newspapers and other public media. A similar interesting book was composed by Ginoux on Albert Einstein [2]; Poincaré and Einstein discussed relativity and the first ideas on quantum mechanics at the 1911 Solvay conference in Brussels. The present paper is based on [8] with a number of additions on the impact of Poincaré on engineering and mathematical physics, see also [3].

Other important aspects were discussed in [9] where the development of Poincaré's *analysis situs* (algebraic topology) was studied in relation to his various ideas and projects. In [10] two neglected ideas of Poincaré were revived and shown to be very useful.

In 1854 Henri Poincaré was born in Nancy, Eastern France. It was natural to have in his family lively discussions on scientific and social issues. It seems that at an early stage these discussions stimulated Henri's interest in scientific problems. His father was a medical specialist with research activities who later became professor

F. Verhulst (✉)
Mathematisch Instituut, University of Utrecht, PO Box 80.010,
3508 TA Utrecht, The Netherlands
e-mail: f.verhulst@uu.nl

I. Kovacic and S. Lenci (eds.), *IUTAM Symposium on Exploiting Nonlinear Dynamics for Engineering Systems*, IUTAM Bookseries 37,
https://doi.org/10.1007/978-3-030-23692-2_2

at the University of Nancy. The family lived in a building that also housed the pharmacy of his grandfather Poincaré; this grandfather wrote among other things a flora of nature around the river Mosel. The brother of his father, Antoni Poincaré, was an influential civil engineer in Northern France. Uncle Antoni had two sons, Raymond and Lucien. Raymond became an important politician, prime minister and later President of the French Republic. Lucien became general supervisor of secondary education in France.

When Henri was 5 years old, he contracted diphteria, a life-threatening illness. This caused temporary paralysis of his legs and made it impossible for him to talk. This illness lasted 9 months but, remarkable enough, there seemed to be few consequences of the illness later on. Another event that certainly made an impression on Henri was the war 1870–1871, between Prussia and France. The Prussians occupied Nancy; Henri who was 16 years old at that time, served as a medical assistant to his father, tending the wounded. The important dates of Poincaré's life are:

- Born in 1854, Nancy, Loraine.
- School years in Nancy, 1860–1873.
- École Polytechnique, 1873–1875, Paris (general science education).
- École des Mines, 1875–1878, Paris, to become a mining engineer.
- Submission Mathematics Thesis, Sorbonne, 1878 (University of Paris, supervisors Darboux, Laguerre and Bonnet).
- Mining engineer Vesoul/Ronchamps, 1879 (Eastern France).
- Mathematics lecturer in Caen, Normandy, 1879–1881.
- Marriage with Louise Poulain d'Andecy, 1881 (4 children).
- Appointment at Paris University (Sorbonne), 1881–1912. He taught many different subjects, for instance experimental physics, celestial mechanics, electricity and optics, elasticity, probability. There exist 14 lecture note books composed by his students.
- Died July 17, 1912, 58 years old.

The mathematical style of Poincaré is at present appreciated more by physicists than by pure mathematicians. He was in his youth influenced by M. Chasles who wrote in his inaugural lecture (1846):

> One can see the respective advantages of Analysis and Geometry: the first one leads by using the miraculous mechanism of its transformations quickly from the starting point to the point to be reached, but often without revealing the road that was travelled or the significance of the numerous formulas that one has used. Geometry on the other hand derives its inspiration from thoughtful consideration of things and from the ordered arrangement of ideas. She is obliged to discover in a natural way the statements that Analysis could neglect and ignore.

This is in contrast with the style of Lagrange, Laplace, Weierstrass and other mathematicians who promoted analytic and algorithmic approaches. In his book of essays 'La valeur de la science' Poincaré compares the style and perception of various mathematicians, geometric, intuitive and analytic. It is clear from his writing that he used both approaches, he felt rightly that both are necessary for the progress of science (Fig. 2.1).

Fig. 2.1 Henri Poincaré around the time of writing his famous Prize Essay

We present a global survey of Poincaré's work. First the theory:

- The qualitative theory of differential equations
- Automorphic functions, uniformisation
- Bifurcation theory
- Asymptotic expansions, normal forms
- Dynamical systems, integrability
- Mathematical physics, PDEs
- Topology (analysis situs)
- Philosophy

Among many applications, we mention:

- 1st order PDEs with singularities (his thesis)
- Self-excited oscillations in telegraphy
- The gravitational three-body problem
- Transport of heat
- Estimates for eigenvalues
- Cosmogonic hypotheses,
- Formulation of the principle of relativity (1905).

2.2 Thesis, Prize Essay and Dynamical Systems

From the beginning of Poincaré's career in science dynamical systems played an important part in his work. One of his thesis supervisors, Gaston Darboux, pointed out to him that recent work by Briot and Bouquet showed how to obtain series solutions of ODEs near regular points and near singularities. He should try to extend these results to first order partial differential equations.

2.2.1 The Doctorate Thesis

It seems that Henri Poincaré wrote his thesis almost casually during his second and third year at the École des Mines. Using the method of characteristics the problems for first order partial differential equations can be reduced to n-dimensional nonlinear ODEs with singularities. His supervisors were not very happy with the first version, there were many gaps in the reasoning. Poincaré filled in all the gaps rather reluctantly, he was already working on a different topic, automorphic functions.

The thesis contains new concepts, the notion of a so-called *algebroid function* and what is now called the *Poincaré domain* in complex parameter space. This domain tells us for which subset of parameters certain expansions are possible. Using these concepts we can in a number of cases determine whether holomorphic series expansions exist near a singularity and whether there are certain algebraic elements in the expansions; Poincaré gives examples, some of which are cases that are undecided. The thesis is still of interest as it covers also a discussion of expansion near irregular singular points.

2.2.2 The Prize Essay

In 1885, it was announced by Gösta Mittag-Leffler, professor of mathematics in Stockholm, that King Oscar II of Sweden and Norway sponsored a scientific competition for his 60th birthday in 1889. Essays had to be handed in by June 1, 1888. Problem 1 of the four topics was:

Dirichlet communicated to a friend that he could solve the equations describing Newtonian motion. This could be used to demonstrate the stability of the Solar System. Topic: reconstruct Dirichlet's reasoning.

Other topics were concerned with automorphic functions and special functions. The committee for the essays consisted of Mittag-Leffler (chairman, Stockholm), Weierstrass (Berlin) and Hermite (Paris), see Fig. 2.2. Poincaré won the prize, his life-long friend Paul Appell became second.

Nowadays there has been much discussion on an error by Poincaré in the first version of the prize essay. We will describe the contents of his essay and finish with an evaluation.

It is clear that the topic of the essay is dynamical systems with as example the gravitational three-body problem. The aim was to add to solving the question of stability of the solar system, a question still completely unsolved today. There are 4 main achievements in the essay:

1. The recurrence theorem for conservative systems on a bounded domain: "orbits will always return infinitely many times arbitrarily close to the original position". It is interesting that this idea was considered a useless tool in statistical mechanics. It is now coming up as a tool for lower-dimensional Hamiltonians, less than 50 dof instead of 10^{22} dof as in statistical mechanics; see [10].

Fig. 2.2 From left to right: Gösta Mittag-Leffler, Karl Weierstrass, Charles Hermite

2. Periodic solutions, existence and convergence or asymptotic character of series expansions. Until the time of the results obtained by Poincaré the series in celestial mechanics were formal; there was on this question a famous discussion between Laplace and Cauchy on the convergence of the series of Laplace. Poincaré considered differential equations involving a small parameter ε (he used μ). If $\varepsilon = 0$ the problem can be solved, some solutions are periodic. Can we continue the periodic solutions for $\varepsilon > 0$? Think as examples of perturbed harmonic motion or the perturbed gravitational two-body problem. Poincaré uses as an example the planar restricted three-body problem showing that most classical expansions do not satisfy the implicit function theorem and so cannot be expected to converge. This caused quite an uproar at the time as contemporary scientists published only formal expansions.

3. Bifurcations. It is typical for Poincaré's inquisitive mind that he studied then the cases where the implicit function theorem could not be applied. What happens when holomorphic expansions break down? His answer: new expansions and new phenomena which was the birth of bifurcation theory. He returned to these problems in his famous 3 books [7].

4. Integrability versus non-integrability. In the first version of his essay Poincaré wanted to demonstrate that the stable and unstable solutions of the planar restricted three-body problem would be surrounded by invariant tori that could be glued together globally. The implication was integrability of this problem. When editing the essay for publication in the *Acta Mathematica*, Lars Phragmén had many queries. This was not unusual for Poincaré, he was inclined to make big steps in his reasoning and was often too impatient to discuss all (tedious) details. He had to add nearly 100 pages to fill in gaps, but one gap could not be filled. To his chagrin he found that the reasoning on integrability was not sound. With an enormous tour de force he then showed that the planar restricted three-body problem is not integrable. The expansions he computed can not be used to obtain invariant tori.

It should be stressed that Poincaré recognized the error himself and repaired it. Credit goes to Phragmén for his many questions asking for clarifications and

improvements. In addition we conclude that the first three results of the prize essay were each of them enough to grant Poincaré the prize.

Generalization

In [7] he returns to the integrability question showing by different means that in general Hamiltonian systems are non-integrable. Consider for this strong generalization of the Prize Essay a time-independent Hamiltonian system $H(x, y)$ with $2n$ variables of the form:

$$\dot{x} = \frac{\partial H}{\partial y}, \dot{y} = -\frac{\partial H}{\partial x}. \tag{2.1}$$

$H(x, y)$ is a first integral, suppose that H depends on a small parameter μ with convergent series expansion

$$H = H_0(x, y) + \mu H_1(x, y) + \mu^2 H_2(x, y) + \cdots \tag{2.2}$$

Suppose that x, y are action-angle variables and that H_0 depends on x alone, the Jacobian $|\partial H_0/\partial x|$ is non-singular, $H(x, y)$ is periodic in y, analytic in its variables in a domain $D \subset \mathbb{R}^{2n}$. Suppose there exists an analytic independent second integral $\phi(x, y)$, periodic in y and with convergent expansion:

$$\phi(x, y) = \phi_0(x, y) + \mu\phi_1(x, y) + \mu^2\phi_2(x, y) + \cdots \tag{2.3}$$

Poincaré shows that $\phi(x, y)$ can only be an analytic independent second integral if we impose further conditions. The proof uses expansion with respect to μ of the Poisson bracket that establishes independence. The subsequent equations can be solved only when $\phi(x, y)$ at each order of μ is dependent on H. It took roughly 80 years for scientists to realise the implications of this result in the context of chaos theory.

2.2.3 Bifurcations

Early examples in the theory of rotating fluid masses (MacLaurin, Jacobi, Dirichlet, Dedekind, Riemann, 1750–1850) suggested bifurcation phenomena. The 2-axial and 3-axial ellipsoidal fluid shapes that were found to exist for self-gravitating fluid masses change with the rotation velocity. At a certain velocity the ellipsoidal fluid breaks up (bifurcates) into two parts (bifurcation = two-forking).

Poincaré (1892) considers bifurcations in a very general setting for systems of differential equations with parameters, dissipative and conservative. He considers any qualitative change of the solutions of a differential equation by a change of parameters a bifurcation; he develops the idea of a bifurcation set, the set of parameter values where such changes occur. In this context it is of interest to consider a periodic solution $\phi(t)$ of an n-dimensional ODE containing parameters. Perturb with a small parameter ε around such a periodic solution; for $\varepsilon = 0$ one finds periodic

solution $\phi(t)$. Apply the implicit function theorem and the periodicity condition to the perturbed n-dimensional equation with an n-dimensional perturbed initial value $\beta = (\beta_1, \ldots, \beta_n)$. This produces n periodicity equations for n unknowns β_n. If a certain Jacobi determinant J is nonzero, a new periodic solution has been found.

This is the famous Poincaré-Lindstedt method. The perturbation expansion was applied formally by Lindstedt to perturbed harmonic equations. Poincaré formulated the method in a general n-dimensional setting and gave a proof by continuation using the implicit function theorem.

Poincaré-Andronov-Hopf Bifurcation

The bifurcation set may contain points with purely imaginary eigenvalues or cases when the Jacobi determinant J vanishes, it is structurally unstable at these points. The case of purely imaginary eigenvalues includes the so-called Hopf-bifurcation, formulated in general form by Poincaré, reformulated later by Andronov and rediscovered by Hopf again much later. The classical example is the equation formulated by Balthasar van der Pol:

$$\ddot{x} + x = \varepsilon \dot{x}(1 - x^2). \tag{2.4}$$

Poincaré studies this bifurcation in the Méthodes Nouvelles [7] vol. 1 (1892).

His prominent publications in dynamical systems are the Mémoire of 1881–1882 [6] and Méthodes Nouvelles de la Mécanique Célèste (1892–1899) [7].

A common misunderstanding is that the 3 books Méthodes Nouvelles are books on celestial mechanics; instead they can be considered the first systematic books on dynamical systems. Problems of celestial mechanics are often discussed as examples in [7] but the treatment on bifurcations and on characteristic exponents is completely general, as are the results on conservative dynamics. A brief contents of the 3 volumes would include: Poincaré expansion with respect to a small parameter, the Poincaré-Lindstedt method, characteristic exponents including the important cases where first integrals exist, the famous proof of general non-integrability of time-independent Hamiltonian systems, the idea of asymptotic approximation, the Poincaré domain in normal form theory, asymptotic invariant manifolds, the recurrence theorem, Poincaré maps as a tool, homoclinic and heteroclinic solutions of dynamical systems. See [8] for more details and discussion.

2.3 Poincaré and Engineering

Already as a boy Henri Poincaré took a keen interest in engineering, see [8]. After becoming a mining engineer in 1878 he spent a year supervising the Vesoul mines in Eastern France. His responsibilities were the production capacity and safety. His last report as an inspector was to propose a new ventilation system for the Magny mine, see the plan of the mine in Fig. 2.3. He continued to hold a position in the Corps des Mines; in 1910 he became inspector-general of the French mines, a mainly honorary position.

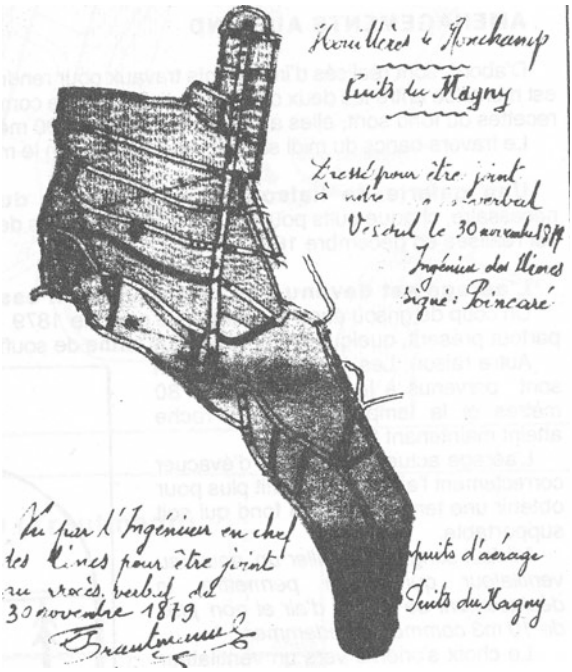

Fig. 2.3 Plan of the Vesoul mine from Poincaré's report on its safety

At the same time and later in Caen he continued his study of nonlinear oscillations described by ODEs. One of his achievements was his study of so-called sustained oscillations, self-excitation and limit cycles. Poincaré lectured at the *École supérieure des Postes et Télegraphs*. He published lecture notes on electrical oscillations and the theory of Maxwell. An application proposed by Poincaré in 1908 was to wireless telegraphy. In Fig. 2.4 an electrical circuit is shown that can produce sustained oscillations. The electrical circuit is described by:

$$Lx'' + \rho x' + \theta(x') + Hx = 0; \tag{2.5}$$

$\rho x'$ represents the resistance and other energy losses in the circuit, $\theta(x')$ is the radiation term produced by the electric arc, L the self-induction. Knowing a suitable function θ, one can construct isolated periodic solutions of this equation. He goes in detail about the various designs of the antenna. The emitted radiation takes the form of a plane wave described by a Fourier integral. The design of these self-excited oscillations predates Van der Pol's triode by many years.

Two revolutionary papers by Poincaré on periodic solutions, in particular limit cycles, were published already in 1881–1882 [6]. They contain the analysis of second order autonomous ODEs using projection on what is now called the Poincaré sphere; the papers introduce index theory and discuss the presence of periodic solutions in the phase-plane. It took a long time for this basic theory to reach the field of applications.

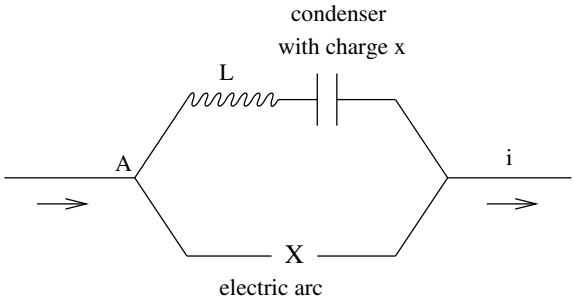

Fig. 2.4 Design of a circuit to use for wireless telegraphy, the singing arc

An extensive study of the development of nonlinear oscillation theory in France is [3]. It is a remarkable fact that during roughly 20 years, say 1910–1930, the name of Poincaré hardly appears in the French engineering literature. Ginoux [3] (see references there) attributes this to the absence of theoretical framework in French engineering in this period. For instance André Blondel analyses sustained oscillations without using and referring to Poincaré's basic results. Alfred Liénard obtained results for periodic solutions in a way that is clearly reminiscent of Poincaré's work, but it is not clear if he was aware of the relation. The French engineers were acquainted with Van der Pol's work but this inventive scientist does not cite Poincaré in the context of his own work on self-excitation. Later Philippe Le Corbeiller became a prominent scientist, he was an admirer of Van der Pol but failed also to discuss Poincaré.

Between 1920 and 1940 the engineering and nonlinear oscillation results of Poincaré were mainly continued and extended in the Soviet Union by Andronov, Krylov and Bogoliubov. One of the conclusions of this period in France may be that it is not good for engineering to neglect in teaching and research new theoretical developments.

2.4 Mathematical Physics

Poincaré's interest in physics extended beyond mathematics to explain and understand real-life phenomena. In our subsequent summary we cover many papers and books, for references see [8].

2.4.1 Partial Differential Equations

It is not well-known that Poincaré made fundamental contributions to the theory of PDEs (I owe much information to a paper by Jean Mawhin [5]). He noticed that the equation of Laplace, the heat equation, the Helmholtz equation arise in many fields of physics, so he paid special attention to these basic equations. We mention:

- Balayage or sweeping method (1890). "Balayage" is used to solve Poisson equations to determine the gravitational field of arbitrarily shaped bodies. Replace mass elements by spherical surfaces with mass, then construct a covering of the whole body by these surfaces. Nowadays one uses variational methods for existence questions in potential theory, balayage is still used in abstract potential theory.
- Minimax estimates of eigenvalues (1894). The minimax eigenvalue estimates are concerned with the Helmholtz equation on bounded domains. Poincaré uses the Dirichlet principle and a minimizing procedure to estimate subsequently the eigenfunctions and eigenvalues of the equation. The method still plays an important part in eigenvalue estimation theory.
- Introduction of generalized functions (1894). Boundary value problems involving continuous boundary conditions can be interpreted using Green's functions with integral expressions as "solution" instead of explicit twice differentiable functions. This work predates the analysis of later mathematicians of generalized solutions.
- Convergence in the mean of Fourier series (1890–1894, far before Hilbert) Discontinuities in the boundary conditions lead to convergence problems in Fourier series. Convergence in the mean is introduced inspired by variational calculus.

In all these cases actual physical problems suggested the development of mathematical tools.

2.4.2 Rotating Fluid Masses

The study of rotating self-gravitating fluids is preliminary for studying star and planet formation. When Poincaré considered these problems many prominent scientists had already obtained important results, for instance MacLaurin, Jacobi, Dirichlet, Dedekind, Riemann. In Poincaré's lecture notes attention is paid to suitable orthogonal special functions. Higher-order Lamé functions play a part in the expansions of MacLaurin's and Jacobi's triaxial ellipsoids. Poincaré discovered a new series of pear-shaped equilibrium configurations branching off the Jacobi ellipsoids. The stability analysis takes place by linearization. Interestingly, he describes the transcritical bifurcation (without using this modern term) that produces an exchange of stabilities between two equilibrium configurations when a bifurcation parameter passes a certain critical value.

2.4.3 Dynamics of the Electron, Special Relativity

In 1895 Poincaré wrote 4 articles on theory and experiments in optics and electricity. He stated that absolute motion can not be demonstrated, only relative motion of matter with respect to matter. In 1904 Hendrik A. Lorentz stated that time was not absolute, it depends on the location and motion in space. Also he gave his brilliant

formulation for the length contraction of bodies in relative motion with velocity v introducing the contraction factor:

$$k = \sqrt{\frac{1}{1 - v^2/c^2}}, \tag{2.6}$$

where c is the velocity of light. For motion in the x-direction the transformation according to Lorentz is:

$$x' = kl(x + \frac{v}{c}t),\ y' = ly,\ z' = lz,\ t' = kl(t + \frac{v}{c}x). \tag{2.7}$$

The factor k and parameter l arise in Lorentz' group of transformations describing motion of mass in x-direction in space and time. Poincaré derived this group of transformations rigorously in 1905 showing that rotational invariance required that $l = 1$; Eq. (2.7) is called the Lorentz-Poincaré transformation. The transformations admit dilation, boosts along the axes and rotations. He concludes that combination of transformations of this group conserves the quadratic form:

$$x^2 + y^2 + z^2 - t^2. \tag{2.8}$$

Another consequence of these transformations on which Lorentz and Poincaré agreed is that gravitational waves and interactions have to propagate with the velocity of light. The position and motion of a moving body determines the gravitational attraction and so the emitted gravitational wave. For details and references see again [8].

2.4.4 Cosmogony

Poincaré's book on cosmogony is still useful for his critical appraisal of the various hypotheses regarding the origin and stability of the solar system. He gives credit to the nebula hypothesis of Laplace, considers evolution by contraction and tidal effects, and the capture hypothesis. Noteworthy are Poincaré's reviews of (at the time) new hypotheses by H. Faye, R. du Ligondès and T. J. J. See; he presents a proof and applications of the virial theorem. Many cosmogonic hypotheses are a mixture of qualitative and quantitative arguments with most problems still unsolved.

2.5 Conclusions

We have discussed only a few of the many topics studied by Poincaré. We mention briefly some related aspects.

1. For Poincaré concrete problems were of great interest, but immediately while tackling them he developed new concepts and tools in mathematics. An example is the theory of automorphic functions which he developed as a young man in Caen and Paris. It started with obtaining insight in singularities of linear ODEs. Such equations defining special functions arise naturally in mathematical physics (Lamé functions, hypergeometric functions etc.). For Poincaré there was the beauty of these transformations and the insight in singularities of linear ODEs in the complex plane. His remarkable insight was that some of the transformations near singularities lead to behaviour on Riemann sheets that can only be understood in terms of non-Euclidean geometry. Poincaré clearly enjoyed this. The theory of automorphic functions amounts to about 10% of his publications.
2. There was a deep link between very different looking topics of his studies. For instance, at the same time when Poincaré developed his Méthodes Nouvelles [7] he created new concepts of algebraic topology (Analysis Situs). The first paper "Analysis Situs" appeared in 1895, followed by 5 supplements. Topology gave deeper understanding in both the tools of automorphic functions which he studied earlier in his career and manifolds in Hamiltonian dynamics; see [9].
3. As is shown in Henri Poincaré's work, in a fruitful development of science, concepts and tools are closely bound together. New calculational tools for examples produce intuition for underlying structures leading to new concepts and theory.

References

1. Ginoux, J.-M.: Henri Poincaré, A Biography Through the Daily Papers. World Scientific (2012)
2. Ginoux, J.-M.: In: Albert Einstein, A Biography Through the Time(s). Éditions Hermann (2016)
3. Ginoux, J.-M.: History of Nonlinear Oscillations Theory in France (1880–1940). Springer (2017)
4. Gray, J.: Henri Poincaré, A Scientific Biography. Princeton University Press (2012)
5. Mawhin, J.: Henri Poincaré and the partial differential equations of mathematical physics. In: Charpentier, E., Ghys, E., Lesne, A. (eds.) The Scientific Legacy of Poincaré. History of Mathematics, vol. 36, pp. 373–391. Providence, AMS (2010)
6. Poincaré, H.: Mémoire sur les courbes définies par une équation differentielle. J. de Mathématique 3e série **7**, 375–422 (1881); **8**, 251–296 (1882)
7. Poincaré, H.: Les Méthodes Nouvelles de la Mécanique Célèste, 3 vols. Gauthier-Villars, Paris (1892, 1893, 1899)
8. Verhulst, F.: Henri Poincaré, Impatient Genius. Springer (2012)
9. Verhulst, F.: Henri Poincare's inventions in dynamical systems and topology, Ch. 1. In: Skiadas, C. (ed.) The Foundations of Chaos Revisited: From Poincare to Recent Advancements, pp. 1–25. Springer (2016)
10. Verhulst, F.: Henri Poincaré's neglected ideas. In: Hagen, T., Johann, A., Kruse, H.-P., Rupp, F., Walcher, S. (eds.) Discrete & Continuous Dynamical Systems—Series S (DCDS-S) (to be published)

Chapter 3
Basins of Attraction for Higher-Dimensional Nonlinear Dynamical Systems: Preliminary Results on the Case Study of a Sympodial Tree

Nemanja Andonovski, Stefano Lenci and Ivana Kovacic

Abstract Analysis of global behaviour of low-dimensional, strongly nonlinear dynamical systems has been well explored in the past, and modern trends are directed toward the investigation of dynamics of systems whose dimension is large, i.e. higher or equal to six. To deal with the huge number of computations required for high-dimensional global analysis, we are developing a software which exploits High Performance Computing (HPC) frameworks on cluster computers (distributed memory systems). In this work, we present preliminary results obtained during the global analysis of a model of a sympodial tree with the first/level branches, which has three degrees of freedom, i.e. six state variables.

Keywords Basin of attraction · High performance computing · Sympodial tree · Nonlinear dynamics

3.1 Introduction

A lack of suitable analytical methods to investigate the global behaviour of strongly nonlinear, high-dimensional dynamical systems triggered intensive development of numerical methods for their global analysis. The global behaviour of such systems is determined once the attractors *and* corresponding basins of attraction are discovered and computed [1, 2]. In fact, often knowing the type of attractors is not enough in engineering applications where the compactness of the basin surrounding the attractors is also highly relevant [3]. Thus, the importance of global analysis lies in

N. Andonovski (✉) · S. Lenci
Polytechnic University of Marche, Ancona, Italy
e-mail: n.andonovski@pm.univpm.it

S. Lenci
e-mail: lenci@univpm.it

I. Kovacic
CEVAS, Faculty of Technical Sciences, University of Novi Sad, Novi Sad, Serbia
e-mail: ivanakov@uns.ac.rs

I. Kovacic and S. Lenci (eds.), *IUTAM Symposium on Exploiting Nonlinear Dynamics for Engineering Systems*, IUTAM Bookseries 37,
https://doi.org/10.1007/978-3-030-23692-2_3

the fact that the structure of the basins of attraction gives additional information on the robustness of an attractor, which is strongly related to the practical stability, and thus, to the reliable use of the considered attractor in applications.

Numerical methods widely used to compute basins can be divided into two categories by the technique used to discretize the continuous state-space. The first type of methods use points as discretization entities, and are often not suitable as the regions between points remain undefined. To avoid possible issues with undefined regions, the majority of methods (second category) divide the state-space into collection of small volumes, commonly called cells [4].

With the Grid-of-Starts (GoS) method [5] (pages 311, 313 and 323), attractors and basins are computed by time-integrating all initial conditions (in the discretized domain) up to the steady-state behaviour. It is accurate and easy to implement, often used to examine basins on arbitrary cross-sections. It can give full-dimensional basins, but it requires a large amount of CPU time to execute all computations.

In this work, we use algorithms based on cell mappings—a family of methods developed to reduce the computational time. Initially developed in [4] and improved by many others (e.g. [6–8]), cell mapping methods approximate continuous trajectories by defining a mapping function between the cells. A discrete map is obtained by the integration over only one excitation period (or, more generally, from one Poincaré section—not necessarily the stroboscopic one—to itself). The results are again given in form of full-dimensional basins of attraction.

Beside requirements for large computational power [9], full-dimensional basins (especially those computed with cell-mapping methods) also occupy large amounts of memory, which is not available on conventional computers.

To overcome limitations of high dimensionality, steps are made toward the usage of HPC in global analysis. Cluster computations with GoS method that produce full-dimensional basin have been developed in [10–12] and parallelization of cell mapping methods has been discussed in [7, 13–15].

The ultimate goal of our work is to explore structural stability of nonlinear dynamical systems in at least six dimensions. To do so, the first part is dedicated to developing a software tool that can be used by engineers and scientists that have access to *small clusters* (several dozen of cores) and need *full-dimensional* basins. The program numerically computes attractors and their basins with the Simple Cell Mapping (SCM) method and prepares the data for visualization in an external freeware software (i.e. ParaView© [16]).

In this work, our software is applied to the model of sympodial tree with first-level branches [17]. The interest in studying this subject comes from the fact that trees are able to endure variety of negative natural conditions, showing a resilient behaviour that needs to be understood, first, and then it might be appropriately exploited in engineering applications. This system is particularly worth of global analyses, since the preliminary investigations herein reported highlight the complex behaviour of basins of attraction, showing, in particular, that not all the attractors are equally robust.

3.2 Sympodial Tree Model

The sympodial tree model shown in Fig. 3.1a mimics trunk with two identical leafless branches. The trunk of mass m, length l and diameter D is attached to the ground by a viscous damper (its damping coefficient is labelled by b) and a spring (its stiffness is labelled by k) and is able to oscillate around its base. Two identical branches with the corresponding parameters m_1, l_1, D_1 are attached to the trunk. There are viscous dampers and springs between the branches and the trunk, and their respective coefficients are labelled by b_1 and k_1. The trunk is excited by a periodic torque of magnitude M and angular frequency Ω. The additional parameter used to model tree-like structures is the *branching angle* α. The generalized coordinates are defined in terms of the absolute angles, φ for trunk and ψ_1, ψ_2 for the branches, measured from the respective equilibrium positions, as shown on Fig. 3.1b.

To derive dimensionless differential equations of motion, the following parameters are used: the *diameter ratio* $D_1/D = \lambda^{1/2}$, the *length ratio* $l_1/l = \lambda^{1/2s}$, the *mass ratio* $m_1/m = \lambda^{4/3}$, the *stiffness ratio* $\kappa = k_1/k$, the dimensionless *damping coefficient* $\zeta = b/2l\sqrt{3/km}$ and the *damping ratio* $\beta = b_1/b$. The governing equations are then:

$$\begin{aligned} &-2\kappa(\psi_1+\psi_2) - 4\beta\zeta(\dot{\psi}_1+\dot{\psi}_2) \\ &-3\lambda^{5/3}\dot{\psi}_2^2\sin(\alpha-\varphi+\psi_2) + 2(1+\kappa)\varphi + 4(1+2\beta)\zeta\dot{\varphi} \\ &+3\lambda^{5/3}\dot{\psi}_1^2\sin(\alpha+\varphi-\psi_1) + 2(1+6\lambda^{4/3})\ddot{\varphi} \\ &+3\lambda^{5/3}\ddot{\psi}_1 cos(\alpha+\varphi-\psi_1) - 3\lambda^{5/3}\ddot{\psi}_2\cos(\alpha-\varphi+\psi_2) = 2M\cos(\Omega t), \end{aligned} \quad (3.1)$$

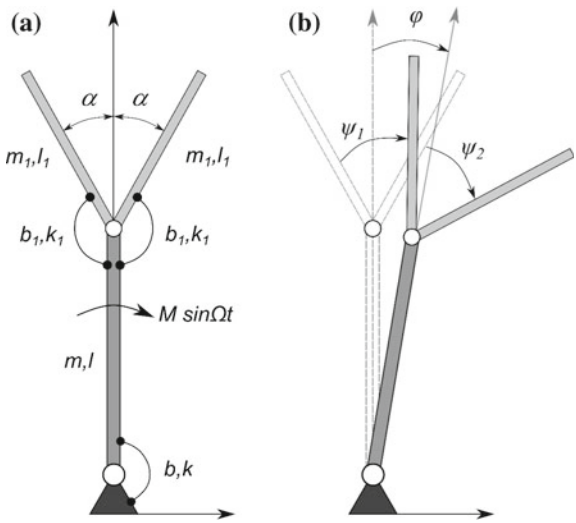

Fig. 3.1 Model of sympodial tree with first-level branches, **a** model properties, **b** generalized coordinates

$$2\kappa\varphi + 4\beta\zeta\dot{\varphi} + 3\lambda^{5/3}\dot{\varphi}^2\sin(\alpha+\varphi-\psi_1) - 2\kappa\psi_1 \\ -4\beta\zeta\dot{\psi}_1 - 3\lambda^{5/3}\ddot{\varphi}\cos(\alpha+\varphi-\psi_1) - 2\lambda^2\ddot{\psi}_1 = 0, \tag{3.2}$$

$$2\kappa\varphi + 4\beta\zeta\dot{\varphi} - 3\lambda^{5/3}\dot{\varphi}^2\sin(\alpha-\varphi+\psi_2) - 2\kappa\psi_1 \\ -4\beta\zeta\dot{\psi}_2 - 3\lambda^{5/3}\ddot{\varphi}\cos(\alpha-\varphi+\psi_2) + 2\lambda^2\ddot{\psi}_2 = 0. \tag{3.3}$$

In the following analysis we will use $\lambda = 1/2$ and $s = 3/2$. These parameters are taken from previous theoretical and experimental works [18, 19].

Equations (3.1–3.3) are coupled by second-order time-derivatives, and are not easy to be handled by classical numerical integrators. By introducing $y_0 = \varphi$, $y_1 = \dot{\varphi}$, $y_2 = \psi_1$, $y_3 = \dot{\psi}_1$, $y_4 = \psi_2$, $y_5 = \dot{\psi}_2$, the system (3.1–3.3) is transformed into a system of six first-order ordinary differential equations, which is more amenable for numerical simulations, although it is yet cumbersome due to the existing strong nonlinearities of the problem.

3.3 Computation Method

Since our main goal is to compute full-dimensional basins in six dimensions and this is challenging from a computational point of view, we need to choose the method which balances between the working efficiency on small clusters and result accuracy. Good methods are cell mappings since they have, with respect to GoS method, much shorter integration time (but larger memory requirements). In our case, the Simple Cell Mapping [4] is an adequate choice for basin computation as other, more advanced, cell mapping methods are focused on getting more accurate attractors and utilize more computing resources.

SCM integration stage—The first step in the computation of basins on a cluster is to collocate initial conditions among nodes. The process is analog to state-space partitioning in parallelized multi-degree-of-freedom cell mapping [13]. Then each node integrates the dedicated portion of initial conditions. Integration time is equal to one excitation period (because the excitation is periodic and we consider the stroboscopic Poincaré map) for systems where transient behaviour does not escape from the predefined state-space window. In cases where this happens, the integration time is prolonged until the trajectories return to the state-space window. This can significantly increase integration time, but for some systems it is necessary, and in the majority of cases trajectories return in less periods than it is required to settle on an attractor as in GoS method. If, after an integration over the fixed number of periods (120 in this example), the solution does not return to the considered window, we assign it to the unique "external attractor", which actually is the union of all attractors—including the one at infinity, if any—residing outside the considered region of the phase space.

The integration part of computations is highly parallelizable, as integrations are independent of each other. This gives opportunity for very high scalability of computations, which means that execution time can be reduced proportionally to the

increase of computing processor cores. As systems grow in complexity, some loss of scalability is expected due to various technical restrictions [20].

SCM post-processing and visualization—The result of the integration stage is a mapping function which is in fact a discrete approximation of trajectories. A post-processing algorithm [4] follows trajectories and discovers loops of the mapping function. A recursive point of the mapping corresponds to a (crude) approximation of a periodic solution in the original system. A set of points lying on a closed curve corresponds to a quasi-periodic motion, while stationary points having more complex structure represent chaotic attractors. Post-processing concludes when all cells (initial conditions) are assigned to the corresponding attractor.

A drawback is that the original post-processing algorithm is inherently sequential and is not suited for computation on cluster computers. Possibility to parallelize post-processing or to simultaneously integrate and process cells is investigated in [13–15]. Some of those methods are developed for computational GPUs that are efficient for computing when data can be accessed very quickly. As data between cluster nodes must be exchanged through designated communication channels (significantly slower than access to the dynamic memory of CPU/GPU), it automatically prevents us from using algorithms adapted for GPU computations. In cases of joint algorithms, where integration and basin processing are done simultaneously, a very large number of unpredictable accesses to storage arrays are required. There is no way to know *a priori* in what manner the storage arrays will be accessed, as it depends on the considered dynamical system. This is an effective approach for shared memory tools where any parallel process can access data directly from dynamic memory. On a cluster those arrays are distributed among nodes which lead to highly unpredictable and irregular number of communication operations per node. As nodes are doing drastically unequal amount of work, the computing efficiency of this approach is sometimes comparable to sequential and often worse. In any case, it does not provide efficiency benefits over sequential post-processing and requires much more additional programming effort to realise the algorithm itself and to manage load balancing or job scheduling of parallel processes.

Therefore, the original serial post-processing method has been proven to be most suitable approach so far. Also, as the dimension increases, the number of initial conditions that have to be integrated increases with geometrical progression and the integration time becomes significantly longer than (serial) post-processing. Therefore, it is justified to retain serial post-processing and an effort to parallelize it, at this moment, would not bring any particular improvement in efficiency.

In summary, the optimal approach for six-dimensional systems on small clusters is the SCM method with a highly parallelized integration stage and sequential post-processing. For larger clusters, it is an open possibility that parallelization of post-processing can bring benefits, which we have not investigated yet.

After post-processing, basins of attraction are stored in a file that can often be too large for stand-alone computers to handle. In such cases, ParaView© can exploit cluster to visualize large data sets. Another option is to use the additional program to extract $2D$ and $3D$ cross-sections so the visualization does not have to be constrained to a cluster.

3.4 Results

To compute basins, we use the model parameters $\beta = 1/2$, $\kappa = 0.3$, $\zeta = 0.03$ and $\alpha = 20°$ as in [17] and also the excitation amplitude $M = 0.5$. To identify regions of interest (excitation frequencies where multiple attractors exist), we plotted the frequency/response diagram in Fig. 3.2, and the brute force bifurcation diagram in Fig. 3.3.

A single Period-1 (P1) attractor exists for the frequencies up to the first bifurcation point at $\Omega = 1.5475$, where a quasi-period (QP) attractor is born by a saddle-node-like bifurcation. An example of this attractor is reported in Fig. 3.4. Increasing the frequency, the P1 branch continues to exist, but now it is paralleled by the QP one. In this range, P1 and QP co-exist and compete (see the forthcoming basins of attraction). At $\Omega = 1.5962$, P1 disappears through a saddle-node bifurcation. Above this threshold, only the QP exists. It survives up to $\Omega = 1.622$, where it disappears likely as a consequence of a reverse Hopf bifurcation.

At $\Omega = 1.618$, a new periodic attractor P1′ appears. In the interval between $\Omega = 1.618$ and $\Omega = 1.622$ again both periodic and quasi-periodic attractors coexist. After $\Omega = 1.622$, P1′ is the unique attractor of the system.

To examine the structure of the basins we consider, as an illustrative example, the frequency fixed at $\Omega = 1.57$, where P1 and QP co-exist (see Fig. 3.2). Here the P1 state-space coordinates, computed by direct integration, are

$$\boldsymbol{y} = (0.094, 0.089, -0.451, -0.248, -0.385, -0.278), \tag{3.4}$$

while QP is reported in Fig. 3.4. To capture all attractors we then used the state-space region delimited by $y_i = (-2, 1)$. The maximum resolution we are able to achieve is 38 cells per dimension (which means $38^6 = 3'010'936'384$ cells), as we are memory-constrained to cluster with total $32GB$ of RAM. For the system of Eqs.

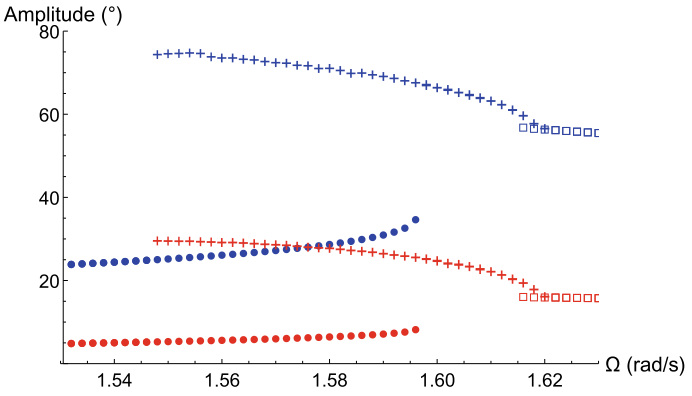

Fig. 3.2 Frequency-response diagram. Trunk φ (red) and branches ψ_1 and ψ_2 displacements (blue), "•" = P1, "+" = QP and "□" = P1′

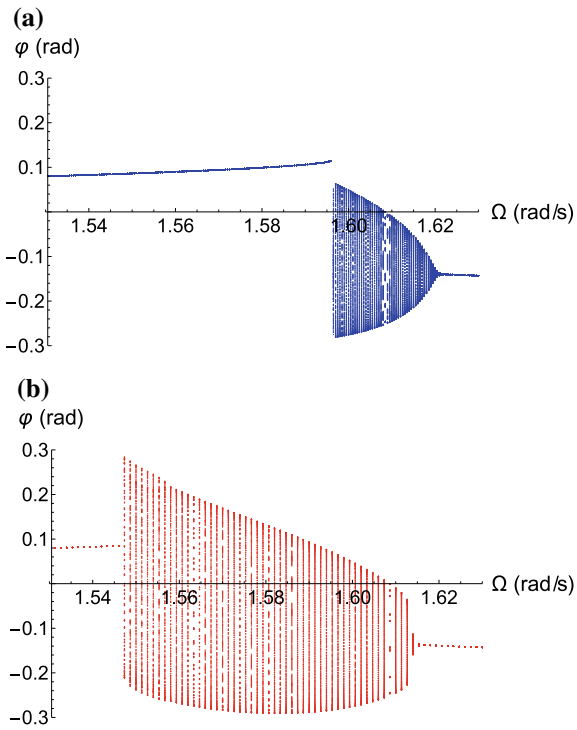

Fig. 3.3 Brute force bifurcation diagram of φ for **a** increasing, **b** decreasing frequencies

(3.1–3.3), a predicted integration time for this resolution is about 32 days with the cluster with 16 single-core nodes. Such long integration time was unacceptable to us at this moment, so we reduced the resolution to 25 cells per dimension, ending up with "only" $25^6 = 244'140'625$ cells. Even with such a low resolution, the computation lasted 50.3 h, while post-processing was finished within 18 minutes.

The resulting basins of attraction are stored in a file from which arbitrary $2D$ or $3D$ cross-sections can be extracted in the Visualization Tool Kit format (VTK). For demonstration purposes, we examine basins on $3D$ cross-sections containing the P1 attractor whose actual state-space coordinates are reported in the Eq. (3.4) and cell-space coordinates (computed with the SCM) are $y_0 = 17$, $y_1 = 18$, $y_2 = 14$, $y_3 = 15$, $y_4 = 14$, $y_5 = 15$ (it is given by the green cell in Fig. 3.5). Note that, due to low resolution of computations, the coordinates reported in Eq. 3.4 do not overlap exactly with those computed with the SCM. This is a well-known issue, already reported in [4]. In Fig. 3.5a, the y_0, y_2, y_4 cross-section with remaining cell-space coordinates fixed at $y_1 = 18$, $y_3 = 15$, $y_5 = 15$ is presented, while Fig. 3.5b shows the y_1, y_3, y_5 cross-section with $y_0 = 17$, $y_2 = 14$, $y_4 = 14$. It is evident from Fig. 3.5 that the basin of the P1 attractor (the transparent cells) dominates. In certain cross-sections, there are no basin traces of the QP attractor (labelled by the red cells) showing how it does not fill the entire window considered in this case.

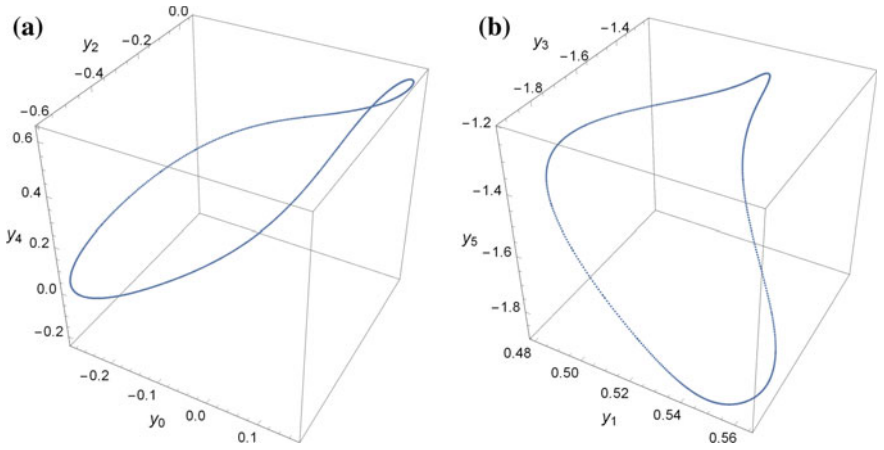

Fig. 3.4 QP attractor projections (Poincaré sections) in **a** y_0, y_2, y_3, **b** y_1, y_3, y_5 sub-space at $\Omega = 1.57$

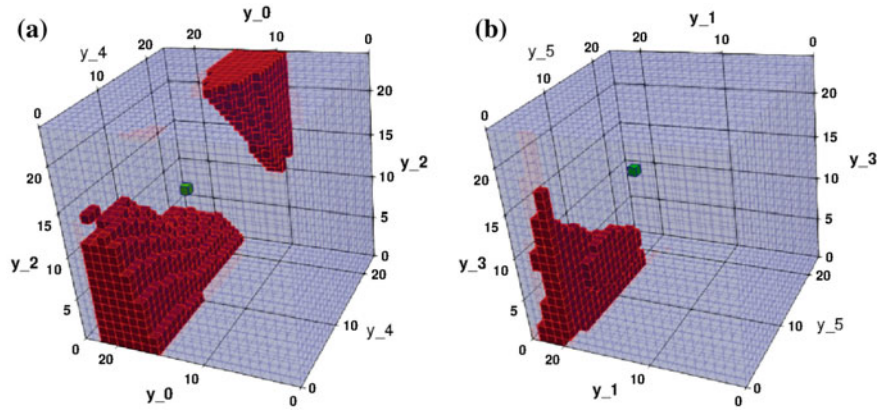

Fig. 3.5 Basins $3D$ cross-section with the period-1 attractor (green cell). **a** y_0, y_2, y_4 with $y_1 = 18$, $y_3 = 15$, $y_5 = 15$ and **b** y_1, y_3, y_5 with $y_0 = 17$, $y_2 = 14$, $y_4 = 14$

For other dynamical systems, or for other values of Ω in the system considered, it may happen that the basins around relevant attractors are *not* compact, so that it not so easy to understand its (likely fractal) structure. In this respect, different and involved views are needed, which we have obtained by using the post-processing software Paraview©. A non-exhaustive list of some basic manipulation features is shown in Fig. 3.6, for the cross-section y_2, y_3, y_4 with $y_0 = 18$, $y_1 = 18$, $y_5 = 18$, where again, the transparent cells refer to the basin of P1 and the red cells belong to the basin of QP. The basins are shown on the Fig. 3.6a, a $2D$ cross-section of the $3D$ view on Fig. 3.6b, an intersection with a cylinder on the Fig. 3.6c and the extraction of a $3D$ cylinder-like section on the Fig. 3.6d.

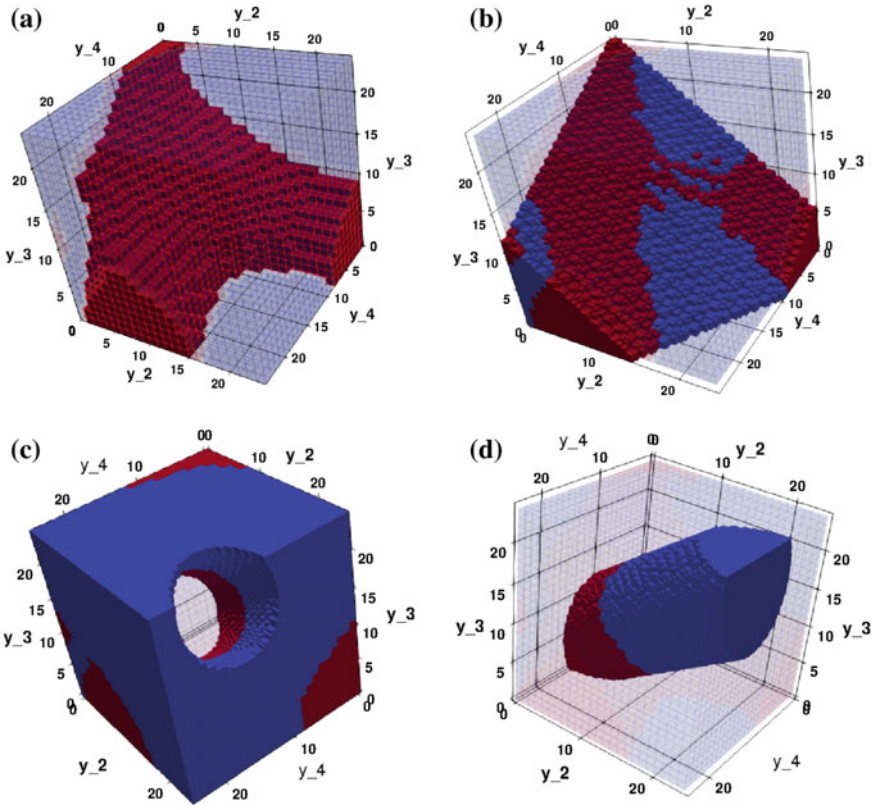

Fig. 3.6 $3D$ cross-section y_2, y_3, y_4 with $y_0 = 18, y_1 = 18, y_5 = 18$, **a** basins; cross-section manipulation by cutting with **b** plane, **c** cylinder, **d** inverted cylinder. Please note that the blue cells are the same as the transparent cells (P1 attractor) of the other figures, here reported in blue only for highlighting the cross-sections within the 3D region

3.5 Conclusions

In this work, we presented an ongoing development of a software tool, implemented with the MPI standard [21] for cluster computers, which numerically computes basins of attraction and prepares data for visualization in the external software. Full-dimensional basins can be visualized and manipulated by any software that is able to read a VTK file format, which offers a range of useful features that greatly help to examine the structure of basins.

For global analyses on small clusters, it has been found that the SCM is the most appropriate method since it uses minimal computing resources and it gives results in the form of full-dimensional basins of attraction. In cases where fractality is present (and important to examine), the SCM method is not accurate enough, and other methods that work on an isolated cross-section in much higher resolution must be used.

A case study of a sympodial tree model demonstrates the difficulties that can be encountered during numerical computations in terms of both its memory and CPU time.

References

1. Hilborn, R.C.: Chaos and Nonlinear Dynamics: An Introduction for Scientists and Engineers, 2nd edn. Oxford University Press, Oxford (2000)
2. Strogatz, S.H.: Nonlinear Dynamics and Chaos: With Applications in Physics, Biology, Chemistry, and Engineering. Addison-Wesley Publisher (1994)
3. Rega, G., Lenci, S.: Identifying, evaluating, and controlling dynamical integrity measures in non-linear mechanical oscillators. Nonlinear Anal. Theory Methods Appl. **63**(5), 902–914 (2005)
4. Hsu, C.S.: Cell-to-Cell Mapping: A Method of Global Analysis for Nonlinear Systems. Springer, New York (1987)
5. Szemplinska-Stupnicka, W., Troger, H.: Engineering Applications of Dynamics of Chaos. CISM International Centre for Mechanical Sciences. Springer, Vienna (2014)
6. van der Spek, J.A.W., van Campen, D.H., de Kraker, A.: Cell mapping for multi degrees of freedom systems. In: Nonlinear and Stochastic Dynamics, AMD, pp. 151–159. ASME (1994)
7. Sun, J.Q., Luo, A.C.J. (eds.): Global Analysis of Nonlinear Dynamics. Springer, New York (2012)
8. Tongue, B.H., Gu, K.: Interpolated cell mapping of dynamical systems. J. Appl. Mech. **55**(2), 461–466 (1988)
9. Nusse, H.E., Hunt, B.R., Kostelich, E.J., Yorke, J.A.: Dynamics: Numerical Explorations. Applied Mathematical Sciences, 2nd edn. Springer, New York (1998)
10. Belardinelli, P., Lenci, S.: A first parallel programming approach in basins of attraction computation. Int. J. Non-Linear Mech. **80**, 76–81 (2016)
11. Belardinelli, P., Lenci, S.: An efficient parallel implementation of cell mapping methods for MDOF systems. Nonlinear Dyn. **86**(4), 2279–2290 (2016)
12. Belardinelli, P., Lenci, S.: Improving the global analysis of mechanical systems via parallel computation of basins of attraction. Procedia IUTAM **22**, 192–199 (2017)
13. Eason, R.P., Dick, A.J.: A parallelized multi-degrees-of-freedom cell mapping method. Nonlinear Dyn. **77**(3), 467–479 (2014)
14. Fernández, J., Schütze, O., Hernández, C., Sun, J.Q., Xiong, F.R.: Parallel simple cell mapping for multi-objective optimization. Eng. Optim. **48**(11), 1845–1868 (2016)
15. Xiong, F., Qin, Z.C., Ding, Q., Hernández, C., Fernández, J., Schüetze, O., Sun, J.Q.: Parallel cell mapping method for global analysis of high-dimensional nonlinear dynamical systems. J. Appl. Mech. **82**, 111010–111010–12 (2015)
16. ParaView—scientific data analysis and visualization: https://www.paraview.org. Accessed 15 Sept 2018
17. Kovacic, I., Zukovic, M., Radomirovic, D.: Sympodial tree-like structures: from small to large-amplitude vibrations. Bioinspiration Biomim. **13**(2), 026002 (2018)
18. Rodriguez, M., Langre, E., Moulia, B.: A scaling law for the effects of architecture and allometry on tree vibration modes suggests a biological tuning to modal compartmentalization. Am. J. Bot. **95**(12), 1523–1537 (2008)
19. Sellier, D., Fourcaud, T.: Crown structure and wood properties: influence on tree sway and response to high winds. Am. J. Bot. **96**(5), 885–896 (2009)
20. Rauber, T., Rünger, G.: Parallel Programming for Multicore and Cluster Systems, 2nd edn. Springer, Berlin, Heidelberg (2013)
21. Message Passing Interface: https://www.mpi-forum.org. Accessed 15 Jan 2018

Chapter 4
Dynamic Morphing of Actuated Elastic Membranes

Andrea Arena, Flavio Massimi and Walter Lacarbonara

Abstract Parametric resonances of elastic membranes actuated by harmonic in-plane strains prescribed along given directions are exploited to drive dynamic morphing of lightweight, flexible panels employed in engineering applications which require active, shape-changing surfaces. An approximate nonlinear model of a pre-tensioned membrane together with its Galerkin discretization are adopted to describe the membrane out-of-plane motion. The method of multiple scales is used to explore the bifurcation scenarios and the instability regions (i.e., morphing regions) associated with the principal parametric resonances. Moreover, parameter continuation of the periodic solutions of the ordinary differential equations describing the membrane motion is performed via a path following procedure implemented in Matlab. The study shows that single- and multi-mode parametric responses can be achieved by suitable tuning of the excitation amplitude and frequency.

Keywords Parametric resonances · Dynamic morphing · Elastic membranes · Strutt diagrams

4.1 Introduction

Morphing technology is a new paradigm in many engineering fields aiming to realize self-actuating, active, smart structures such as skins, wings, architectural surfaces that undergo shape changes when subject to external stimuli (pressure, velocity,

A. Arena (✉) · W. Lacarbonara
Department of Structural and Geotechnical Engineering, Sapienza University of Rome, Via Eudossiana 18, 00184 Rome, Italy
e-mail: andrea.arena@uniroma1.it

W. Lacarbonara
e-mail: walter.lacarbonara@uniroma1.it

F. Massimi
Department of Mechanical and Aerospace Engineering, Sapienza University of Rome, Via Eudossiana 18, 00184 Rome, Italy
e-mail: flavio.emme93@gmail.com

I. Kovacic and S. Lenci (eds.), *IUTAM Symposium on Exploiting Nonlinear Dynamics for Engineering Systems*, IUTAM Bookseries 37,
https://doi.org/10.1007/978-3-030-23692-2_4

temperature change, light, etc.). In aerospace, for example, the concept of morphing wing is likely to enhance performance and efficiency over a wider range of flight conditions in future aerostructures [1].

In the present work, a new concept of dynamic morphing of flexible membranes is explored by exploiting the strain-induced parametric resonances of the membrane modes. In the context of classical linear theories, closed-form solutions for the transverse motion of elastic membranes were recently proposed in [2] where a Fourier-Bessel solution was found for a linear circular membrane subject to uniform radial tension at its boundary. In [3] a geometrically fully nonlinear model of prestressed micromembranes was employed to explore the nonlinear range in which the high sensitivity of the nonlinear frequency with respect to the applied pressure is proposed for pressure sensing purposes.

The geometric nonlinearities—due to the coupling between stretching and curvature—can affect very much the nonlinear dynamic response and can be suitably exploited for practical applications. In particular, the dynamic amplification of transverse motion caused by the principal parametric resonance of any of the membrane modes can be exploited for dynamic morphing to achieve drag reduction in lifting surfaces, hence, better aerodynamic efficiency.

In [4] the principal parametric instability regions of the radial motions of nonlinearly viscoelastic cylindrical/spherical shells under pulsating pressures were studied via the method of multiple scales (MMS). Studies employing the same perturbation method to analyze the free nonlinear planar extensional-flexural motions of unshearable nonlinearly elastic rings were presented in [5] showing that the presence of extensibility preserves the softening characteristics of extensional-flexural modes of linearly elastic rings. Together with perturbation approaches, to study the bifurcation behavior of nonlinear systems, numerical continuation techniques are commonly applied to low-dimensional systems of ordinary differential equations to extend the predictions of local analyses. In [6] this numerical approach was used to perform parameter continuation and to pursue concurrent bifurcation analysis of periodic solutions of directly excited structural nonlinear systems.

In the present study, the dynamic morphing response under parametric excitation effected by strain actuation is investigated first via the method of multiple scales applied to a reduced order model of elastic membranes. To investigate the nonlinear response of the parametrically excited lowest modes, the nonlinear partial differential equation (PDE) of motion describing the membrane out-of-plane motion is discretized according to the Faedo-Galerkin procedure, and a fifth-order asymptotic expansion of the solution of the resulting ordinary differential equation (ODE) for the mth mode is performed to study the bifurcation behavior. To prove the accuracy of the results obtained via the MMS, path following of the parametric response of the actuated membrane is performed by means of a continuation toolbox called COCO [7]. The Strutt diagrams with the instability regions, where the parametric resonance morphing can be achieved, are obtained for the lowest nine membrane modes. A study of the nonlinear response is further carried out via time integration of the nonlinear equation of motion to demonstrate that the membrane dynamic mor-

phing can be suitably driven and optimized for innovative design of active surfaces in engineering applications.

4.2 Problem Formulation

An approximate nonlinear model of pretensioned elastic membranes subject to parametric excitation is proposed. The model considers only the membrane transverse motion by condensing the nonlinear effect of the in-plane stresses in the governing equation of motion. The source of the parametric excitation is provided by prescribed dynamic strains acting along a selected number of active strings orthogonally collocated within the membrane.

As depicted in Fig. 4.1, the reference square membrane configuration is assumed to be planar and coinciding with the equilibrium under the effect of a uniform prestress N_0. The Cartesian frame $\{\mathbf{e}_1, \mathbf{e}_2, \mathbf{e}_3\}$, having its origin in one of the membrane corners, is such that $\mathbf{e}_3$ is normal to the reference configuration and the membrane midplane lies in the $\{\mathbf{e}_1, \mathbf{e}_2\}$-plane. The position of each material point of the membrane is thus described by the space coordinates x_1 and x_2 along $\mathbf{e}_1$ and $\mathbf{e}_2$, respectively, while $w(x_1, x_2, t)$ represents the transverse displacement, and t denotes time. In the case study here investigated, the thickness is $h = 2 \times 10^{-4}$ m and the edge length is $l = 2 \times 10^{-2}$ m. The Young modulus, Poisson ratio, and mass density are those of an engineering polymer (i.e., PEEK); namely, $E = 3.6$ GPa, $\nu = 0.4$, and $\rho = 1320$ kg/m^3, respectively.

The analytical model is cast in nondimensional form by adopting the membrane edge length l and the frequency $\omega_c = \sqrt{E/[(1-\nu^2)\,\rho\, l^2]}$ as characteristic length and frequency, respectively, for the nondimensionalization. Therefore, the space and time nondimensional coordinates become $\bar{x}_i = x_i/l$ $(i = 1, 2)$ and $\bar{t} = \omega_c\, t$, respectively, while $\bar{N}_0 = N_0/[\rho\, h\, \omega_c^2 l^2]$ and $\alpha = E/[(1-\nu^2)\,\rho\, \omega_c^2 l^2]$ are the nondimensional prestress and elastic stiffness, respectively.

The parametric excitation is provided by the membrane forces $N_1(x_2, t)$ and $N_2(x_1, t)$ acting along the directions $\mathbf{e}_1$ and $\mathbf{e}_2$, respectively, and whose position

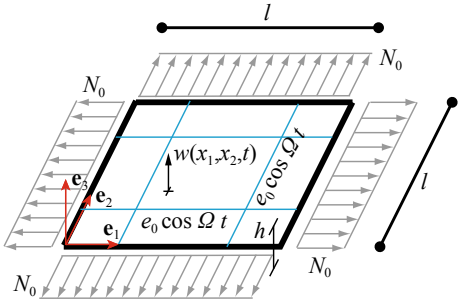

Fig. 4.1 Membrane reference, prestressed configuration

within the membrane midplane is given by Dirac-delta functions (see cyan lines in Fig. 4.1). These excitation forces, generated by a periodic strain e_0, have the following nondimensional expressions:

$$\bar{N}_1 = \alpha\, e_0 \cos \bar{\Omega} t \sum_{i=1}^{n_s} \delta\left(\bar{x}_2 - \bar{x}_{2,i}\right)\,,\quad \bar{N}_2 = \alpha\, e_0 \cos \bar{\Omega} t \sum_{j=1}^{n_s} \delta\left(\bar{x}_1 - \bar{x}_{1,j}\right), \tag{4.1}$$

where n_s is the number of active strings, $\bar{x}_{1,j}$ and $\bar{x}_{2,j}$ indicate the position of the string across the membrane, and e_0 is the amplitude of the prescribed strain. The number of strings and their position are chosen so as to provide optimal actuation for both symmetric and skew-symmetric membrane modes. In particular, here it is $n_s = 2$ and $\bar{x}_{1,1} = 1/4$, $\bar{x}_{1,2} = 3/4$, $\bar{x}_{2,1} = 1/4$, $\bar{x}_{2,2} = 3/4$, respectively.

By assuming the classical linear viscous force $f_d = \zeta\, \partial\bar{w}/\partial\bar{t}$, where ζ is the damping ratio, and by enforcing the balance of linear momentum, the nondimensional equation of motion for the square, prestressed membrane, obtained from the model proposed in [8], can be written as:

$$\frac{\partial^2 \bar{w}}{\partial \bar{t}^2} + \zeta \frac{\partial \bar{w}}{\partial \bar{t}} - \bar{N}_0 \nabla^2 \bar{w} - \frac{\alpha}{2}\left[\frac{\partial^2 \bar{w}}{\partial \bar{x}_1^2}\int_0^1 \left(\frac{\partial \bar{w}}{\partial \bar{x}_1}\right)^2 d\bar{x}_1 + \frac{\partial^2 \bar{w}}{\partial \bar{x}_2^2}\int_0^1 \left(\frac{\partial \bar{w}}{\partial \bar{x}_2}\right)^2 d\bar{x}_2\right] + \bar{N}_1 \frac{\partial^2 \bar{w}}{\partial \bar{x}_1^2} + \bar{N}_2 \frac{\partial^2 \bar{w}}{\partial \bar{x}_2^2} = 0\,, \tag{4.2}$$

together with the boundary conditions $\bar{w}(0, \bar{x}_2, \bar{t}) = \bar{w}(1, \bar{x}_2, \bar{t}) = 0$, $\bar{w}(\bar{x}_1, 0, \bar{t}) = \bar{w}(\bar{x}_1, 1, \bar{t}) = 0$, $\partial^2_{\bar{x}_1} \bar{w}(0, \bar{x}_2, \bar{t}) = 0 = \partial^2_{\bar{x}_1} \bar{w}(1, \bar{x}_2, \bar{t})$, $\partial^2_{\bar{x}_2} \bar{w}(\bar{x}_1, 0, \bar{t}) = 0 = \partial^2_{\bar{x}_2} \bar{w}(\bar{x}_1, 1, \bar{t})$, and the initial conditions. In Eq. (4.2), $\partial\bar{t}$ and $\partial\bar{x}_i$ $(i = 1, 2)$ indicate partial differentiation with respect to the nondimensional time and space coordinates, respectively, while ∇^2 is the Laplace operator.

4.3 Asymptotic Approach

The parametric resonances of the lowest nine membrane modes are investigated. To this end, the Faedo-Galerkin method is employed to reduce the partial differential equation of motion into the ODE governing the dynamics of each mode. According to the adopted discretization, the transverse displacement is expressed as $\bar{w}(\bar{x}_1, \bar{x}_2, \bar{t}) = 2q_{m,n}(\bar{t}) \sin m\,\pi\,\bar{x}_1 \sin n\,\pi\,\bar{x}_2$, where $q_{m,n}(\bar{t})$ is the (m, n)th generalized coordinate, thus, the single-mode projection of Eq. (4.2) can be written as

$$\ddot{q}_{m,n} + \zeta \dot{q}_{m,n} + \bar{\omega}_{m,n} q_{m,n} + \frac{3}{4}\alpha\pi^4 \left(m^4 + n^4\right) q_{m,n}^3 + \alpha\pi^2 \left[-2\left(m^2 + n^2\right) + m^2 \left(\cos\frac{n\pi}{2} + \cos\frac{3n\pi}{2} \right) + n^2 \left(\cos\frac{m\pi}{2} + \cos\frac{3m\pi}{2} \right) \right] e_0 \, q_{m,n} \cos\bar{\omega} t = 0, \tag{4.3}$$

where the overdot indicates differentiation with respect to the nondimensional time $\bar{t}$ and $\bar{\omega}_{m,n} = \pi\sqrt{\left(m^2 + n^2\right)\bar{N}_0}$ is the linear nondimensional circular frequency of the (m, n)th mode.

The method of multiple scales is employed to perform a perturbation analysis of Eq. (4.3); by letting ε denote a small nondimensional parameter, a fifth-order expansion of the solution of the discrete form of Eq. (4.2) is sought as $q_{m,n}(\bar{t}) = \sum_{i=1}^{5} \varepsilon^i q_i(t_0, t_2, t_4)$, where $t_0 = \bar{t}$ is the nondimensional fast time scale, and $t_2 = \varepsilon^2 \bar{t}$ and $t_4 = \varepsilon^4 \bar{t}$ are the nondimensional slow time scales. Since the nonlinearity of Eq. (4.3) is purely cubic and due to the fifth-order expansion adopted in the perturbation procedure, only even powers of ε are considered in the expansion [4]. The dissipative effects due to the damping force as well as the periodic strain e_0 which provides the membrane actuation are here supposed to be higher order effects with respect to the first order inertial and elastic restoring forces of the membrane; therefore, the corresponding mechanical parameters are rescaled as follows: $\zeta = \varepsilon^2 \zeta$ and $e_0 = \varepsilon^2 e_0$. By substituting the fifth-order expansion of the solution into the discrete form of the equation of motion, a hierarchy of problems of order ε, ε^3, and ε^5, respectively, is obtained by equating to zero coefficients of like powers of ε. Finally, the lowest three perturbation problems, specialized to the lowest membrane mode, i.e., $m = 1 = n$, are given by

$$\begin{aligned}
&\varepsilon: \quad D_0^2 q_1 + \bar{\omega}_{1,1}^2 q_1 = 0, \\
&\varepsilon^3: \quad D_0^2 q_3 + \bar{\omega}_{1,1}^2 q_3 = -\frac{3}{2}\pi^4 \alpha \, q_1^3 - \zeta D_0 q_1 - 2 D_0 D_2 q_1 + 4\alpha\pi^2 e_0 q_1 \cos\bar{\Omega}\bar{t}, \\
&\varepsilon^5: \quad D_0^2 q_5 + \bar{\omega}_{1,1}^2 q_5 = -\frac{9}{2}\pi^4 \alpha \, q_1^2 q_3 - \zeta \left(D_2 q_1 + D_0 q_3\right) - D_2^2 q_1 - 2 D_0 D_4 q_1 \\
&\qquad\qquad -2 D_0 D_2 q_3 + 4\alpha\pi^2 e_0 q_3 \cos\bar{\Omega}\bar{t},
\end{aligned} \tag{4.4}$$

where D_0, D_2 and D_4 are operators indicating differentiation with respect to t_0, t_2, and t_4, respectively. The general solution of the linear problem can be written as $q_1(t_0, t_2, t_4) = A(t_2, t_4) e^{i\,\bar{\omega}_{m,n} t_0} + \tilde{A}(t_2, t_4) e^{-i\,\bar{\omega}_{m,n} t_0}$, where $A(t_2, t_4)$ is the unknown complex-valued amplitude of the (m, n)th mode and $\tilde{A}(t_2, t_4)$ is its complex-conjugate. By substituting the solution of order ε into the second perturbation, letting $\cos\bar{\Omega}\bar{t} = 1/2\, e^{i\bar{\Omega}\bar{t}} + cc$ (where cc stands for the complex conjugate) and expressing the frequency of the external parametric excitation as $\bar{\Omega} = 2\bar{\omega}_{m,n} + \varepsilon^2\sigma$, being σ a detuning parameter, the modulation equation for the amplitude $A(t_2, t_4)$ can be

obtained by setting to zero the secular terms. In particular, for the case $(m, n) = (1, 1)$ one obtains:

$$2\,i\bar{\omega}_{1,1}D_2A + \; i\zeta\bar{\omega}_{1,1}A + \frac{9}{2}\pi^4\alpha\; A^2\tilde{A} - 2\alpha\pi^2 e_0\tilde{A}\,e^{it_2\sigma} = 0. \tag{4.5}$$

4.3.1 Nonlinearity of the Membrane Modes

Before moving towards the investigation of the principal parametric resonances, by setting $e_0 = 0$ in Eq. (4.5), it is possible to study the nonlinearity of the lowest membrane modes through the backbone curves which regulate variation of the nonlinear frequency $\bar{\omega}^{NL}_{m,n}$ of each mode with the modal amplitude. This can be done by introducing the polar form of the complex amplitudes as $A(t_2, t_4) = 1/2\,a(t_2, t_4)e^{i\theta(t_2,t_4)}$ and $\tilde{A}(t_2, t_4) = 1/2\,a(t_2, t_4)e^{-i\theta(t_2,t_4)}$, substituting it into the modulation equation, separating real and imaginary parts and obtaining the two differential equations governing the modulation of the real amplitude a and relative phase $\gamma = \sigma\, t_2 - \theta$, where σ represents the detuning between the linear and the nonlinear frequencies of the (m, n)th mode (i.e., $\bar{\omega}^{NL}_{1,1} = \bar{\omega}_{1,1} + \varepsilon^2\sigma$).

By seeking periodic solutions (i.e., by imposing $D_2a(t_2, t_4) = 0 = D_2\gamma(t_2, t_4)$), it is then possible to obtain the closed-form expression, up to the third order approximation, of the backbone curve for each investigated mode. In particular, for the mode $(m, n) = (1, 1)$, the latter has the expression $\bar{\omega}^{NL}_{1,1} = \bar{\omega}_{1,1} + \varepsilon^2\frac{9\pi^4\alpha a^2}{16\bar{\omega}_{1,1}}$. The backbone curves shown in Fig. 4.2 for the lowest six membrane modes highlight the hardening feature of the membrane nonlinear normal modes. Due to the symmetry of the membrane, modes (1, 2), (1, 3), and (2, 3) and their companion modes (2, 1), (3, 1), and (3, 2) share the same backbone curves.

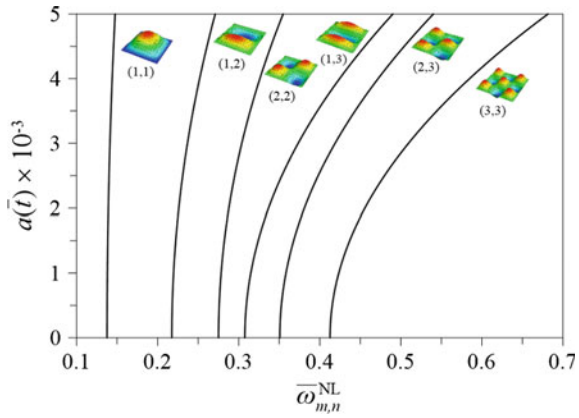

Fig. 4.2 Backbones of the lowest six membrane mode shapes

4.3.2 Principal Parametric Resonance

Before studying the parametric resonances, conditions for possible activation of internal resonances are sought. Two-to-one ratios occur for the lowest two modes while three-to-one ratios take place between the third and the first mode. However, these modes turn out to be uncoupled due to nonlinear orthogonality between them [9].

Next, parametric resonances of individual modes are studied via the method of multiple scales. Substituting into the second perturbation the expression of the t_2-rate-of-change of the complex-valued amplitude $A(t_2, t_4)$ obtained by solving the modulation equation Eq. (4.5), third order nonresonant terms can be found in the right-hand side of the second perturbation problem. Thus, the particular solution of the inhomogeneous problem of order ε^3 can be found in the form $q_3(t_0, t_2, t_4) = b_1 A^3(t_2, t_4)e^{3i\bar{\omega}_{m,n}t_0} + b_2 A(t_2, t_4)e^{i\bar{\Omega}t_0+i\bar{\omega}_{m,n}t_0} + b_3\tilde{A}^3(t_2, t_4)e^{-3i\bar{\omega}_{m,n}t_0} + b_4\tilde{A}(t_2, t_4)e^{-i\bar{\Omega}t_0-i\bar{\omega}_{m,n}t_0}$, where the real coefficients b_i $(i = 1, \ldots, 4)$ are obtained by equating coefficients of like terms (i.e., having the same frequency) in the inhomogeneous problem; those, for $(m, n) = (1, 1)$, have the following expressions: $b_1 = b_3 = \frac{3\pi^4\alpha}{16\bar{\omega}_{1,1}^2}$ and $b_2 = b_4 = -\frac{2\alpha\pi^2 e_0}{\bar{\Omega}(\bar{\Omega}+2\bar{\omega}_{1,1})}$.

At fifth order, the annihilation of secular terms leads to the following equation that modulates on the time scale t_4 the amplitude $A(t_2, t_4)$ for $(m, n) = (1, 1)$:

$$
\begin{aligned}
&2\,i\bar{\omega}_{1,1}D_4A - \frac{1}{4}\zeta^2 A - \frac{9\zeta\pi^4\alpha\, i A^2\tilde{A}}{4\bar{\omega}_{1,1}} - \frac{135\pi^8\alpha^2A^3\tilde{A}^2}{32\bar{\omega}_{1,1}^2} \\
&+e_0\left(\frac{9A\,\tilde{A}^2\pi^6\alpha^2}{4\bar{\omega}_{1,1}^2} + \frac{\tilde{A}\pi^2\alpha\sigma}{\bar{\omega}_{1,1}} - \frac{9A\,\tilde{A}^2\pi^6\alpha^2}{\sigma^2+6\sigma\bar{\omega}_{1,1}+8\bar{\omega}_{1,1}^2}\right)e^{i\sigma t_2} \\
&-\frac{21A^3\pi^6\alpha^2e_0}{8\bar{\omega}_{1,1}^2}\,e^{-i\sigma t_2} + e_0^2\left(\frac{A\pi^4\alpha^2}{\bar{\omega}_{1,1}^2} + \frac{4A\pi^4\alpha^2}{\sigma^2+6\sigma\bar{\omega}_{1,1}+8\bar{\omega}_{1,1}^2}\right) = 0.
\end{aligned}
\tag{4.6}
$$

By adopting the same procedure used to find the third order solution, the solution of order ε^5 can be then found in the form $q_5(t_0, t_2, t_4) = c_1(t_2, t_4)e^{3i\bar{\omega}_{1,1}t_0} + c_2(t_2, t_4)e^{5i\bar{\omega}_{1,1}t_0} + c_3(t_2, t_4)e^{i\bar{\Omega}t_0+i\bar{\omega}_{1,1}t_0} + c_4(t_2, t_4)e^{i\bar{\Omega}t_0+3i\bar{\omega}_{1,1}t_0} + c_5(t_2, t_4)e^{2i\bar{\Omega}t_0+i\bar{\omega}_{1,1}t_0} + c_6(t_2, t_4)e^{2i\bar{\Omega}t_0-i\bar{\omega}_{1,1}t_0} + cc$, where $c_i(t_2, t_4)$ $(i = 1, \ldots, 12)$ are complex-valued coefficients found by equating coefficients of like terms (i.e., having the same frequency) in the inhomogeneous fifth-order problem. For the sake of conciseness, the expressions of such coefficients are not reported here.

By using the method of reconstitution [10], the time rate of change of the modal amplitude can be expressed as $\dot{A}(\bar{t}) = \varepsilon^2 D_2 A(t_2, t_4) + \varepsilon^4 D_4 A(t_2, t_4)$ and, thus, it is possible to obtain the modulation equation up to fifth order. Finally, by introducing the polar form of the complex amplitudes as $A(\bar{t}) = 1/2\, a(\bar{t})e^{i\theta(\bar{t})}$ and $\tilde{A}(\bar{t}) = 1/2\, a(t)e^{-i\theta(\bar{t})}$, substituting it into the reconstituted modulation equation, and separating real and imaginary parts, the two differential equations governing the

modulation of the real modal amplitude $a(\bar{t})$ and relative phase $\gamma(\bar{t}) = \sigma\,\bar{t} - 2\theta(\bar{t})$ can be straightforwardly obtained.

The fixed points of the fifth-order modulation equation are then found by imposing the stationarity of $a(\bar{t})$ and $\gamma(\bar{t})$ (i.e., $\dot{a}(\bar{t}) = 0 = \dot{\gamma}(\bar{t})$). The ensuing system includes two nonlinear algebraic equations in the unknowns $a(\bar{t})$ and $\gamma(\bar{t})$. These two equations can be solved for $\sin\gamma(\bar{t})$ and $\cos\gamma(\bar{t})$ to obtain the bifurcation equation involving only the amplitude $a(\bar{t})$, the detuning σ, and the mechanical parameters of the system; this is provided by imposing the trigonometric identity $\sin^2\gamma(\bar{t}) + \cos^2\gamma(\bar{t}) = 1$. Therefore, for fixed values of the strain amplitude e_0 and damping factor ζ, it is then possible to obtain, in closed form, the bifurcation curve represented by solid and dashed lines in Fig. 4.3a where the black lines refer to the fifth-order asymptotic analysis while the grey lines show the solution up to the third-order approximation. The red squares depicted in Fig. 4.3a represent the amplitudes of the stable oscillations calculated by brute-force time integration of the equation of motion given by Eq. (4.2), whose approximate solution was found as the combination of the lowest nine membrane modes $\bar{w}(\bar{x}_1, \bar{x}_2, \bar{t}) = 2\sum_{m=1}^{3}\sum_{n=1}^{3} q_{m,n}(\bar{t}) \sin m\,\pi\,\bar{x}_1 \sin n\,\pi\,\bar{x}_2$.

The stability is ascertained by monitoring the eigenvalues λ of the Jacobian of the bifurcation equations governing the slow dynamics of the amplitude and relative phase; in particular, Fig. 4.3b shows the path of the eigenvalues associated with the amplitude $a(\bar{t})$ in which two pitchfork bifurcation points delimiting the frequency range in which the parametric resonance arises are found when λ vanishes (namely, A and B in Fig. 4.3a, b, indicating supercritical and subcritical pitchfork bifurcations, respectively). On the other hand, a fold bifurcation point C, identifying the boundary between stable (solid line) and unstable (dashed line) branches, is found as the conditions where the change of the eigenvalue sign takes place.

By setting to zero the modal amplitude $a(\bar{t})$ in the equations providing the periodic solutions (i.e., $\dot{a}(\bar{t}) = 0 = \dot{\gamma}(\bar{t})$), it is then possible to derive the stability equation which allows to study the effect of the actuation amplitude e_0 on the stability of the membrane. In particular, the perturbation treatment allows to obtain closed form expressions of the transition curves (i.e., the paths of the pitchfork bifurcation points) with the limitation given by the fifth-order approximation of the asymptotic expansion. These expressions are obtained from the stability equation by finding the roots of the fourth-order polynomial in e_0 representing the stability equation.

To assess the range of e_0 for which the fifth-order asymptotic expansion gives a suitable approximation of the stability curves, numerical continuation of the periodic solution obtained from the nonlinear modal equation given by Eq. (4.3) was performed by means of a Matlab-based continuation toolbox called COCO [7]. To delve more into the details of the numerical continuation procedure, starting from a parametric response calculated via time integrating the equation of motion of the (m, n)th mode, the path of the nonresonant dynamic response having $2\omega_{m,n}$ frequency is followed to determine the period doubling (PD) bifurcations marking the onset of the parametric response having $\omega_{m,n}$ frequency. In particular, the toolbox provides the bifurcation analysis by solving simultaneously the first variational equations for the monodromy matrix associated with the periodic solutions and the corresponding

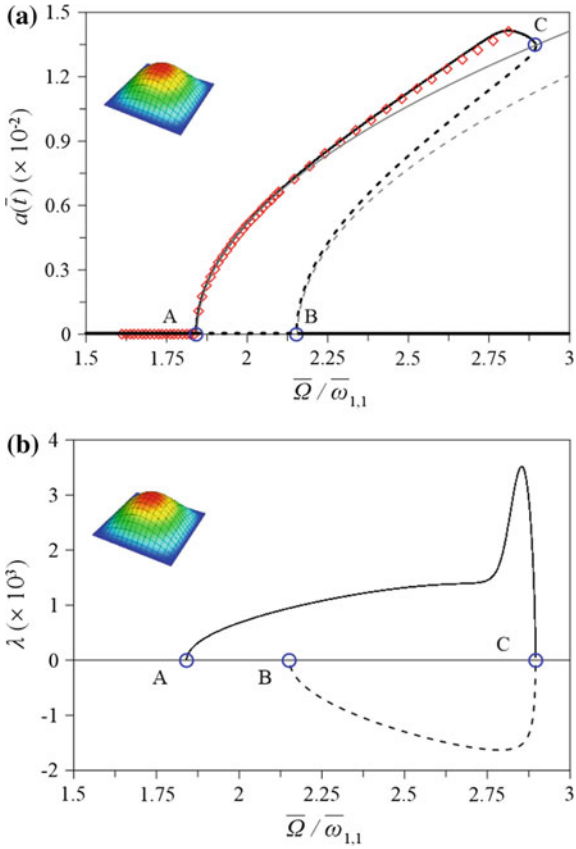

Fig. 4.3 **a** Bifurcation curve of the lowest membrane mode for $e_0 = 1.5 \times 10^{-4}$ and $\zeta = 2 \times 10^{-3}$: stable branch (solid line), unstable branch (dashed line), amplitudes of the stable parametric oscillations via numerical integration (red squares). The black lines refer to fifth-order approximation, while the grey lines refer to third-order approximation. **b** Path of the eigenvalues associated with the amplitude $a(\bar{t})$

eigenvalues (i.e., the Floquet multipliers). Once the PD bifurcation points are determined for a given value of e_0, the continuation of the PD points is performed in a selected range of strain amplitudes e_0. Figure 4.4 shows the resonance tongues for the lowest two modes of the membrane (i.e., $(m, n) = (1, 1)$ and $(m, n) = (1, 2)$) and the results obtained with the perturbation approach up to the third-order approximation (grey dashed-dotted-dotted lines), up to fifth-order approximation (black dashed-dotted lines), are compared to the numerical continuation curves (black solid lines). The comparisons confirm that, up to moderately high values of the actuation strain, $e_0 < 1.4 \times 10^{-3}$, the predictions of the perturbation treatment up to fifth order is in excellent agreement with the numerical results.

Finally, from direct time integrations of the nonlinear equation of motion of modes (1, 1) and (1, 2), performed in the range of excitation frequency $\bar{\Omega}$ near the parametric resonance and for selected values of the strain e_0, the bifurcation points (i.e., where the stable response loses the 2 $\left(2\pi/\bar{\omega}_{m,n}\right)$ periodicity) were calculated and are reported in Fig. 4.4 as red circles to show the agreement with the stability curves obtained via numerical continuation.

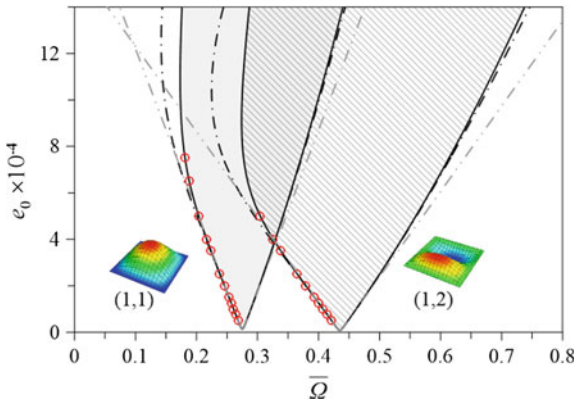

Fig. 4.4 Stability regions of the parametric resonance of the lowest two modes for $\zeta = 2 \times 10^{-3}$. Comparison between asymptotic approach via MMS up to fifth-order approximation (black dashed-dotted line) and numerical continuation (black solid line). The grey dashed-dotted-dotted lines provide the results for third-order asymptotic approximation

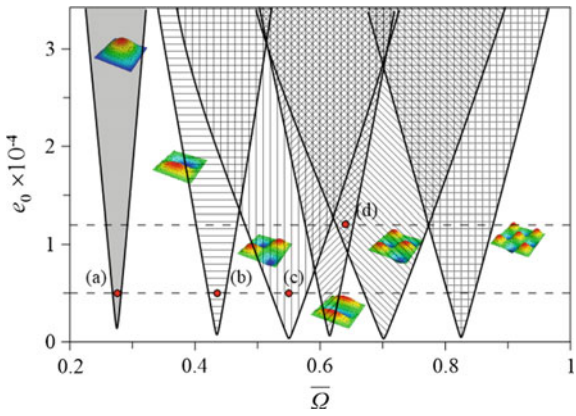

Fig. 4.5 Strutt diagram of the actuated elastic membrane for the lowest six modes

Figure 4.5 shows the Strutt diagram for the lowest six membrane modes obtained via numerical continuation of the nonlinear modal equations (here, the curves for the modes (2, 1), (3, 1), and (3, 2) are not reported). In particular, Fig. 4.5 allows to appreciate the bandwidth frequency where the resonance tongues (shaded regions) overlap and multi-mode responses are expected to arise. To show the multi-mode response in the overlapped instability regions, a direct time integration of the membrane equation of motion was performed by projecting Eq. (4.2) into the basis of trial functions given by the lowest nine membrane modes (i.e., all the modes investigated in the perturbation analysis, including the companion modes (2, 1), (3, 1), and (3, 2)). The results of the numerical simulations are depicted in Fig. 4.6, where the time histories and the fast Fourier transforms (FFTs) were obtained upon varying the excitation frequency to seek parametric response involving single- or multi-mode oscillations. In particular, the membrane morphing through single-mode motion is shown in Fig. 4.6a–c, while mixed-mode motions are shown Fig. 4.6d.

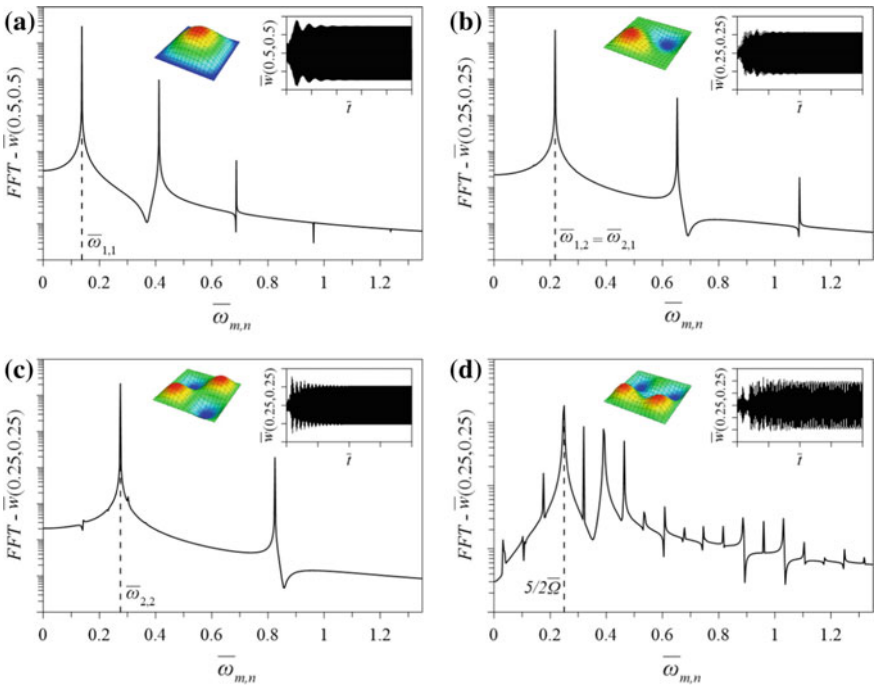

Fig. 4.6 FFTs and time histories of the deflection at selected resonant conditions for parametric excitation given at the excitation frequency for the case (**a**), (**b**), (**c**) and (**d**), indicated in Fig. 4.5

4.4 Conclusions

The investigated parametric resonances of strain-actuated elastic membranes show that the ensuing mixed-mode motions can be exploited for dynamic morphing of flexible skins. In the overlapped Mathieu tongues, mode mixing due to two simultaneous parametric resonances can give rise to complex morphing motions. The ongoing investigations into the parametric resonances of individual modes show that there is great flexibility and richness in driving dynamic morphing with complex mode mixing.

Acknowledgements This work was partially supported by the European Office of Aerospace Research and Development/Air Force Office of Scientific Research (AFOSR) Grant No. 12141951, project title: "Highly reconfigurable, multistable composite with tunable morphing capability".

References

1. Thill, C., Etches, J., Bond, I., Potter, K., Weaver, P.: Morphing skins. Aeronaut. J. **112**, 117–139 (2008)
2. Javidinejad, A.: Vibration modal solutions developing of the elastic circular membrane in polar coordinates based on the Fourier-Bessel series. J. Theor. Appl. Mech. **43**, 19–26 (2013)
3. Arena, A., Lacarbonara, W.: Free vibration of micromembranes subject to prestress and pressure. In: Proceedings of the ASME Design Engineering Technical Conference, ASME IDETC/CIE 2015, Vol. 4, Boston, United States, 2–5 Aug 2015
4. Lacarbonara, W., Antman, S.S.: Parametric instabilities of the radial motions of non-linearly viscoelastic shells under pulsating pressures. Int. J. Nonlinear Mech. **47**, 461–472 (2012)
5. Lacarbonara, W., Arena, A., Antman, S.S.: Flexural vibrations of nonlinearly elastic circular rings. Meccanica **5**(3), 689–705 (2015)
6. Formica, G., Arena, A., Lacarbonara, W., Dankowicz, H.: Coupling FEM with parameter continuation for analysis of bifurcations of periodic responses in nonlinear structures. J. Comput. Nonlinear Dyn. **8**, 1–8 (Art. No. 021013) (2013)
7. Dankowicz, H., Schilder, F.: An extended continuation problem for bifurcation analysis in the presence of constraints. J. Comput. Nonlinear Dyn. **6**(3), 1–8 (Art. No. 031003) (2011)
8. Lacarbonara, W.: Nonlinear Structural Mechanics. Theory, Dynamical Phenomena and Modeling, 1st edn. Springer (2013)
9. Lacarbonara, W., Rega, G.: Resonant non-linear normal modes. Part II: activation/orthogonality conditions for shallow structural systems. Int. J. Nonlinear Mech. **38**(6), 873–887 (2003)
10. Nayfeh, A.H.: Nonlinear Interactions. Wiley Classics, New York (2000)

Chapter 5
Nonlinear Dynamics as a Tool in Selection of Working Conditions for Radial Ball Bearing

Ivana D. Atanasovska, Dejan B. Momcilovic, Radivoje M. Mitrovic, Natasa D. Soldat and Nikola Nesic

Abstract This paper contains elements of a comprehensive research devoted to the dynamic behavior of radial ball bearings in real working conditions. The general motivation for this topic comes from the requirements for high performance operation of bearings within complex mechanical systems, defined in many industrial branches during the last decades. The discussion of the fundamental postulates of the approach used for analyzing the vibration response of rolling ball bearings in order to select the optimal working conditions is given. The certain simplifications and reductions used for analyzing the radial ball bearings are explained. The developed procedure can be used for research of influence of different damages and variable operation conditions on the rolling bearings dynamics. The detail analyses of the dynamic behavior of rolling bearings are performed for particular types of radial ball bearings in two case studies: for the damaged outer raceway surface in accordance with real fatigue damage shapes and dimensions and, for variable working temperature. Obtained results are shown by comparative diagrams of vibration and phase plane portraits. Presented results could be a base for more widely research of nonlinear dynamics of radial ball bearings with different damages and for the application of phase plane analysis in order to choose the optimal operation conditions.

Keywords Nonlinear dynamics · Radial ball bearings · Damages · Stiffness

I. D. Atanasovska (✉) · N. Nesic
Mathematical Institute of the Serbian Academy of Sciences and Arts, Kneza Mihaila 36, Belgrade, Serbia
e-mail: iatanasovska@mi.sanu.ac.rs

D. B. Momcilovic
Institute for Testing of Materials, Bulevar Vojvode Misica 43, Belgrade, Serbia

R. M. Mitrovic · N. D. Soldat
Faculty of Mechanical Engineering, University of Belgrade, Kraljice Marije 16, Belgrade, Serbia

I. Kovacic and S. Lenci (eds.), *IUTAM Symposium on Exploiting Nonlinear Dynamics for Engineering Systems*, IUTAM Bookseries 37,
https://doi.org/10.1007/978-3-030-23692-2_5

5.1 Introduction

The increased requirements for lightweight design and overload reduction lead to necessity for developing the power transmission systems as complex systems of elements designed with optimal load capacity. Consequently, the systems for monitoring and maintenance of these elements should be defined very carefully in order to provide a steady operation state of the certain system. One of the most critical parts of every power transmission system is bearings. Therefore, during last decade researchers are dedicated to analysis of different tasks related with correct operating state of rolling bearings, but research in this area is still required because of their complex mechanics.

The developing both of experimental methods and theoretical approaches are in the focus of contemporary research of dynamics of rolling bearings. Within the experimental research, the special attention is given to the methods for signal monitoring and analysis [1], and verification of analytical models of bearings vibration [2]. The comprehensive consideration of the impact of different parameters and working conditions on the failure occurrence is also very important in order to predefine the expected changes in the monitored vibrations shortly before failure. This research path could leads to the diminishing occurrence of catastrophic failures. These postulates are the basis of extensive research which part is presented in this paper.

The complexity of the design of roller bearings, which have a character of multibody contact system [3] and have the very high values of contact stresses, and in same time operate in conditions of complex external loads and/or the existence of damages at raceway surfaces and/or inclusions in the material and other causes of discontinuity in the load distribution, leads to a significant number of parameters which have the influence on the complex load distribution within the bearing, as well as the complex kinematics and dynamics behavior. Although it is very important to simultaneously consider as much of the influential variables as possible, the authors mainly analyze one or few impact parameters and introduce the additional assumptions and simplifications in order to make the dynamic problem solvable. Through years a significant number of research are dedicated to the studying of clearance as the one of the most strongly influenced factors in load distribution and dynamic behavior of rolling bearings. Mitrovic gave the analytical consideration of the influence of internal radial clearance on the load distribution and stress capacity for radial ball bearings [4], while Kappaganthu and Nataraj few decades later considered the influence of the same parameter as a source of excitation of nonlinear dynamics of the rotor-bearing system [5]. In last few years, the research projects dedicated to the ball bearings, take in first place the modeling of different defects on the contact surfaces. One of the comprehensive researches of this type of problem is given by Rafsanjani et al. [6]. Special attention also should be dedicated to the research of Dougdad et al. [7], who presented an experimental verification of a simplified model of the nonlinear ball bearing behavior and gave an approach for considering the defects simulation. Also, it must be pointed that the significant number and effort in research dealing with the dynamics of rolling bearings with micro-damages at

raceways is still up-to-date [8–11]. In accordance with this and with the possibilities provided by the theories of nonlinear dynamics in this kind of research, there is a big space for new improvements in this area. Thus, Kostek [12] analyzed the dynamics of deep groove ball bearing by analyzing the phenomena associated with non-linear dynamics and chaos and used this approach for discussion of the influence of internal clearance, while De Moerlooze et al. [13] used the theory of non-linear dynamics and discussed a ball bearing dynamics as a case of the complex task of dynamics of ball rolling between two planes. The research and results presented in this paper are on this track, and presents a part of extensive research still in progress. The main goal of this research is to develop the unique methodology for studying the dynamics of ball bearings, which will be sufficiently simple and time-consuming limited, and can be widely applied for relative quantification of impact of different operating parameters on the dynamic behavior of rolling bearings as a part of complex mechanical systems. The uniqueness of the presented methodology consists in the fact that roller bearings are regarded as a "Multi-body contact" [3].

5.2 Theoretical Consideration

The rolling bearing vibration can be analyzed using well-known mathematical model explained by Lim and Singh [14] and improved by Atanasovska [15], which describes a machine system that consists of a flexible shaft and a flexible casing coupled with a rolling bearing and mounted on a flexible support. This system is usually a part of various real mechanical systems and machines.

The discrete vibration model of this system is given with the following equation in matrix form:

$$[M]\{\ddot{q}(t)\} + [D(\mu)]\{\dot{q}(t)\} + [C(q, \mu, t)]\{q(t)\} = \{F(c, t)\} \tag{5.1}$$

where $[M]$, $[D(\mu)]$ and $[C(q, \mu, t)]$ are the system mass, damping and stiffness matrices respectively, and $\{q(t)\}$ and $\{F(c, t)\}$ are the generalized displacement and applied load vectors. Some assumptions and simplifications are required in order to make Eq. (5.1) solvable. The detail description of reduction of Eq. (5.1) in the case of radial rolling bearings is explained by Atanasovska [15]. This reduction procedure assumes the time dependent periodic stiffness of rolling element bearings and non-existence of damages and defects on contact surfaces. If the radial ball bearing is presented with freely suspended mechanical system [14, 15], the matrix Eq. (5.1) can be reduced to the vibration model with one degree of freedom with reduced mass of shaft and housing and the general complex function which defines the radial stiffness for radial bearings with and without damages and/or irregularities at contact surfaces:

$$m_{red}\ddot{x} + d(\mu)\dot{x} + c(x, \mu, t)x = F \tag{5.2}$$

The determination of total bearing stiffness as a function of: time (which reflects the variable number and position of rolling elements in contact), contact deformation (which reflects the geometrical and material characteristics of contact surfaces without or with defects and/or irregularities) and coefficient of friction (which depends of the lubricant)—$c(x, \mu, t)$ is the most important task for solving the nonlinear dynamics of rolling bearings with damages. Meanwhile, the external load is assumed to stay constant.

It is important to point up the significance of the developed procedure as a part of fully new approach in solving the real problems of complex mechanical systems with two or more deformable bodies in contact, named "Multi-body contact" and presented by Atanasovska [3]. One of the most important postulates of this approach is definition of total stiffness of multi-body contact, which analyzed the real mechanical system with two or more deformable bodies in contact as a separated part of big machines.

The total radial stiffness of radial ball bearings defined in this way can be successfully determined by the numerical finite elements method (Finite Elements Analysis—FEA) explained in previous works [10, 15]. The radial ball bearing stiffness is characteristic of the ball bearing assembly and in general can be calculated as ratio of external load and deformation:

$$c_b(x, \mu, t) = F/\delta(x, \mu, t) \tag{5.3}$$

In this equation the F is the constant external radial load and $\delta(x, \mu, t)$ is the elastic displacement of bearing axis that is equal to the total deformation of ball bearing in the radial direction, i.e. total radial displacement of axis of bearing in radial direction.

The time varying radial stiffness can be calculated analytically [16], by different experimental procedures of measuring of ball bearing displacement in terms of predefined external loads [11, 17], or by Finite Element Analysis [18]. The quasi-static Finite Element Analysis for one time varying period of one ball passing along the contact period (period during one ball is continuously in contact) is used in the calculations presented in this paper. The definition and analytical procedure for calculation of one contact period angle is given in [4] and has the following form:

$$2\psi_0 = 2arccos(1 - 2\varepsilon),\ \varepsilon = \frac{1}{2}\left(\frac{\delta_0}{\delta_0 + \frac{e}{2}}\right) \tag{5.4}$$

where: 2ψ is the angle that correspond to one contact period, ε is the load zone parameter, δ_0 is total contact deformation of bearing parts in start point of contact on the most loaded ball and e is radial clearance of radial ball bearing.

The developed Finite Element Model (FEM) is used for calculation the radial ball bearing stiffness (5.3) by calculation the total radial displacement of axis of bearing in radial direction and assumption that the external load remains constant.

5.3 Results—Case Studies

A particular type of radial ball bearing is chosen for analysis of influence of damages at raceway surface on nonlinear dynamics of radial ball bearings. The main characteristics of chosen 6206 type of rolling bearing are: diameter of outer ring—62 mm, diameter of inner ring—30 mm, number of balls—9, radial clearance—0 μm. The FEA is performed and total radial stiffness is calculated for the case of bearing without damages and for bearing with damage at the contact surface of outer ring raceway (groove shape and dimensions: width of 0.3 mm and depth of 50 μm) [10]. The shape and dimension of modeled damage is chosen in accordance with real fatigue damages on raceways found by inspection of dismounted bearings, presenting in detail by FAG (bearing producer) [19]. Calculations are performed for few different external loads within the predefined load capacity range, with constant values of: 500, 1000, 2000 and 5000 N.

The obtained time-dependent functions of radial stiffness for radial bearing with damage are shown on Fig. 5.1 for different external loads. In order to minimize the calculation time, only few main contact position within a ball contact period are analyzed in this point. Therefore, some of presented results can look unexpectedly.

These periodical function are incorporated in Eq. (5.2) and numerical solutions are obtained by numerical Runge–Kutta method and MatLab software for following conditions: $m_{red} = 0.5$ kg, $n = 1000$ rpm, neglected damping, initial conditions: $x = 0$, $\dot{x} = 0$ and time period of twenty rotations. The calculations have been performed for both of the cases: with and without damages. The results of the differential equation of ball bearing vibration are presented by time-dependent diagrams at Fig. 5.2, for four different values of external load.

In order to verify the developed procedure for research of nonlinear dynamics of radial ball bearings, the obtained results for bearings without damages are compared and verified with the results obtained experimentally for the same ball bearing type [20].

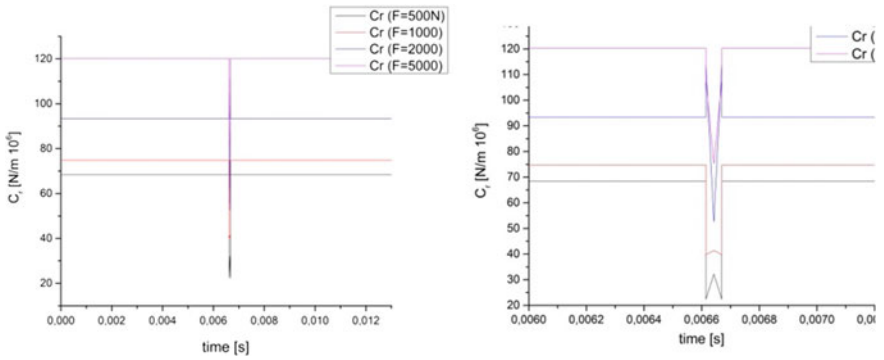

Fig. 5.1 The comparative diagrams of time-dependent function of total radial stiffness for radial ball bearing with damage for different external load values—with zoom in detail around damage

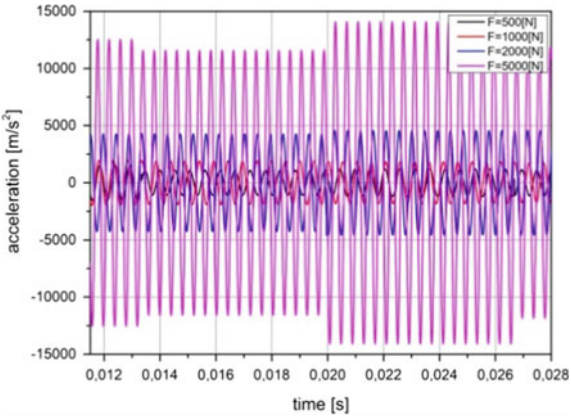

Fig. 5.2 The vibration response of the radial ball bearing with damage at outer ring raceway surface—comparative diagrams for different values of external load

5.4 Discussion

The obtained results are also presented by velocity-displacement diagrams for three values of external load for the period of two rotations, comparative for bearings with and without damage (Figs. 5.3, 5.4 and 5.5).

It is easy to conclude that the phase portrait diagrams created for bearings without damages (red lines at Figs. 5.3, 5.4 and 5.5) show a character of linear dynamic systems with periodic motion, while those for radial ball bearing with damage (black lines at Figs. 5.3, 5.4 and 5.5) show the nonlinear character of dynamics behavior.

The comparative presentation of the results obtained for different external loads (Fig. 5.6) could be used for selection of optimal range of external loads, which is in the particular case is about 1000 N.

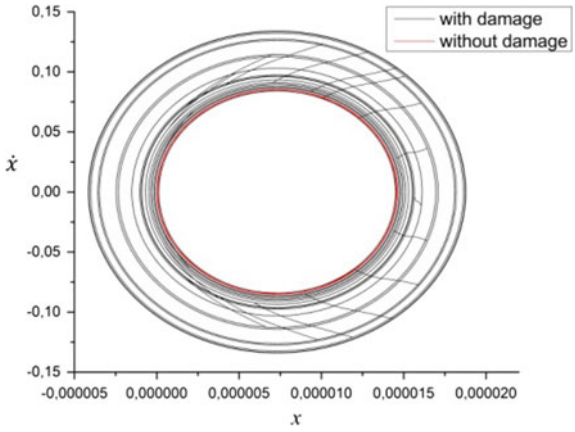

Fig. 5.3 The comparative diagrams for radial ball bearings with and without damage at outer ring raceway, for external load of 500 N for the period of two rotations

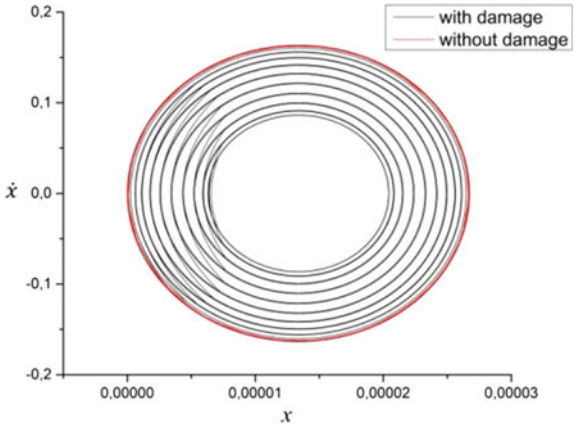

Fig. 5.4 The comparative diagrams for radial ball bearings with and without damage at outer ring raceway, for external load of 1000 N for the period of two rotations

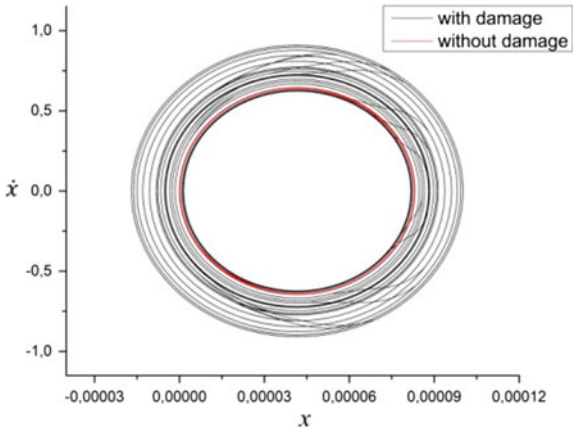

Fig. 5.5 The comparative phase portraits for radial ball bearings with and without damage at outer ring raceway, for external load of 5000 N for the period of two rotations

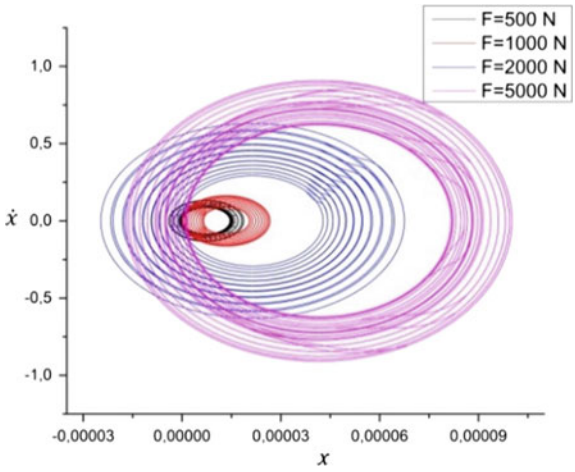

Fig. 5.6 The comparative phase portraits for different external loads for radial ball bearing with damage at outer ring raceway for the period of two rotations

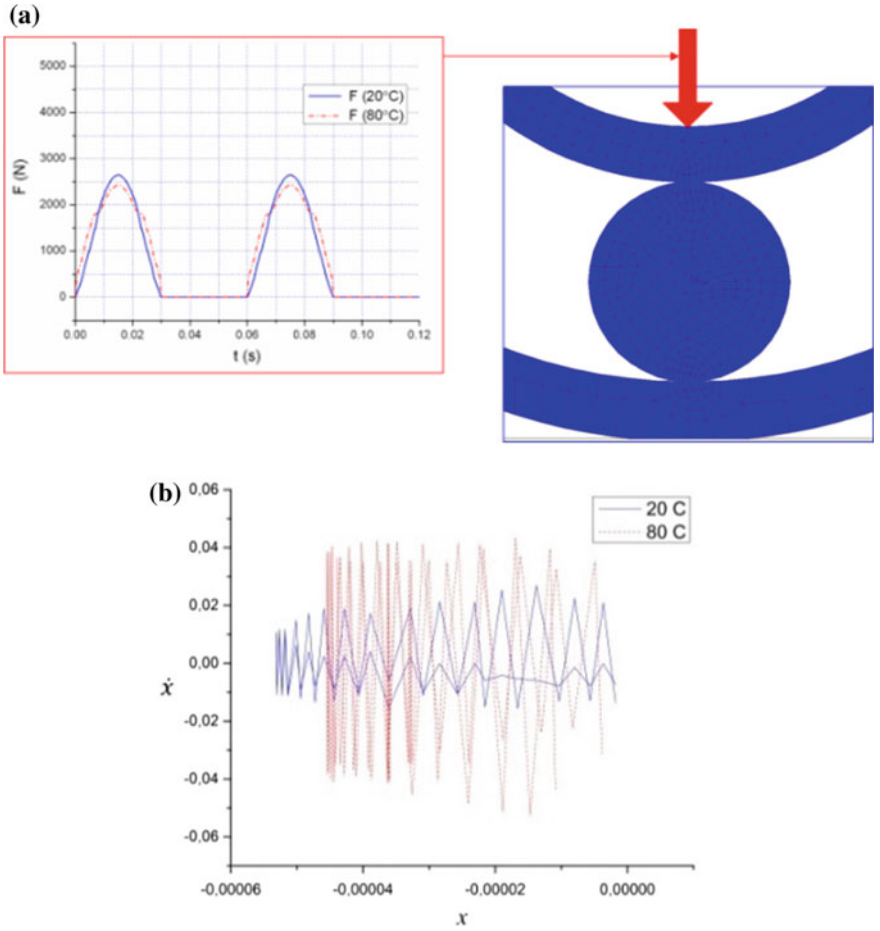

Fig. 5.7 **a** Model for transient dynamic FEA; **b** velocity-displacement diagrams for different working temperatures

In the second performed case study, for investigation of the influence of working temperature on dynamic behavior of rolling bearings, a radial ball bearing of 6310 type is analyzed. The appropriate FEM is developed for quasi-static calculations of load distribution function [21], which is then used in the transient dynamic FEA, Fig. 5.7a.

For the external load of 5000 N and two different working temperatures, obtained results are shown in the comparative diagram on Fig. 5.7b [21]. The comparative presentation of the results for different working temperature (Fig. 5.7) could be used for selection of optimal range of working parameters with influence on the bearing temperature.

5.5 Conclusions

This paper describes the capacity of the theory of the nonlinear dynamics in the selection of the values of working parameters for the mechanical systems with radial roller bearings. The approach used for solving the rolling bearings dynamics and creating the phase portraits is explained in detail. The developed procedure provides a tool for simplified application even for those who are not familiar with the basics of the theory of nonlinear dynamics. This is enabled by visual analysis of obtained comparative presentation of phase portraits.

As illustration, two case studies for particular types of radial ball bearings and defined working parameters are performed. The presented results shown that the visual qualitative and/or qualitative analyses of the results obtained by explained approaches are appropriate for selection the optimal ranges of the investigated working parameters. In the first of the analyzed case studies, the analysis is performed for a particular radial ball bearing with certain damage at outer ring raceway as an excitation for nonlinear dynamics behavior. It is obviously that the optimal range of external load is about 1000 N and that the external loads near the limit value of the bearings load capacity are not recommended from the viewpoint of bearing dynamics behavior. The second case study shows the negative impact of the operating temperature increasing due to friction or other sources.

Acknowledgements Parts of this research were supported by the Ministry of Sciences and Technology of Republic of Serbia through Mathematical Institute of SASA, Belgrade, Projects: OI 174001 and TR35029.

References

1. Cong, F., Chen, J., Dong, G., Pecht, M.: Vibration model of rolling element bearings in a rotor-bearing system for fault diagnosis. J. Sound Vib. **332**, 2081–2097 (2013)
2. Guo, W., Tse, P.W.: A novel signal compression method based on optimal ensemble empirical mode decomposition for bearing vibration signals. J. Sound Vib. **332**, 423–441 (2013)
3. Atanasovska, I.: Multi-body contact in non-linear dynamics of real mechanical systems, procedia engineering, ISSN:1877-7058. In: Vestroni, F., Romeo, F., Gattulli, V. (eds.) X International Conference on Structural Dynamics, EURODYN 2017, Rome, Italia, 10–13 Sept 2017, vol. 199, pp. 510–515 (2017)
4. Mitrovic, R.: Analysis of the influence of elastic deformation and internal radial clearance of ball bearing on the load distribution and stress capacity. M.Sc. Thesis, Faculty of Mechanical Engineering, University in Belgrade (in Serbian) (1988)
5. Kappaganthu, K., Nataraj, C.: Nonlinear modeling and analysis of a rolling element bearing with a clearance. Commun. Nonlinear Sci. Numer. Simul. **16**, 4134–4145 (2011)
6. Rafsanjani, A., Abbasion, S., Farshidianfar, A., Moeenfard, H.: Nonlinear dynamic modeling of surface defects in rolling element bearing systems. J. Sound Vib. **319**(3), 1150–1174 (2009)
7. Dougdag, M., Ouali, M., Boucherit, H., Titouche, N.E., Djaoui, M.: An experimental testing of a simplified model of a ball bearing: stiffness calculation and defect simulation. Meccanica **47**, 335–354 (2012)

8. Ding, W., Zhang, Z., Zhao, F.: Vibration response of ball bearings with different defect sizes in the outer raceway: simulation with a 3-D finite element model. The 14th IFToMM World Congress, Taipei, Taiwan, 20–30 Oct 25–30, pp. 1–4 (2015)
9. Liu, J., Shao, Y., Zhu, W.D.: A new model for the relationship between vibration characteristics caused by the time-varying contact stiffness of a deep groove ball bearing and defect sizes. J. Tribol. ASME **137**, 031101-1–031101-15 (2015)
10. Atanasovska, I., Mitrovic, R., Soldat, N.: Influence of load distribution in ball bearings with defects on the dynamic behavior of gear transmissions systems. In: International Conference on GEARS 2015, Garching (near Munich), Germany, pp. 1065–1068 (2015)
11. Behzad, M., Abbas, R.B., David, M.: A new model for estimating vibrations generated in the defective rolling element bearings. J. Vib. Acoust. ASME **133**, 041011-1–041011-8 (2011)
12. Kostek, R.: Simulation and analysis of vibration of rolling bearing. Key Eng. Mater. **588**, 257–265 (2014)
13. De Moerlooze, K., Al-Bender, F., Van Brussel, H.: Modeling of the dynamic behavior of systems with rolling elements. Int. J. Non-Linear Mech. **46**, 222–233 (2011)
14. Lim, T.C., Singh, R.: Vibration transmission through rolling element bearing, part ii: system studies. J. Sound Vib. **139**(2), 201–225 (1990)
15. Atanasovska, I.: The mathematical phenomenological mapping in nonlinear dynamics of spur gear pair and radial ball bearing due to the variable stiffness. Int. J. Non-Linear Mech. **73**, 114–120 (2015)
16. Kang, Y., et al.: A modification of the Jones-Harris method for deep-groove ball bearings. Tribol. Int. **39**, 1413–1420 (2006)
17. Ali, N.J., García, J.M.: Experimental studies on the dynamic characteristics of rolling element bearings. Proc. Inst. Mech. Eng. Part J J. Eng. Tribol. **224**, 659–698 (2010)
18. Guo, Y., Parker, R.G.: Stiffness matrix calculation of rolling element bearings using a finite element/contact mechanics model. Mech. Mach. Theory **51**, 32–45 (2012)
19. FAG: Rolling bearing damage—recognition of damage and bearing inspection, Publ. No. WL 82 102/3 EA, Status 2001, http://www.skama.gr/UsersFiles/admin/-entypa%20katalogoi/biomixania/wl_82102_3_de_en.pdf (2010)
20. Tomovic, R., Miltenovic, V., Banic, M., Miltenovic, A.: Vibration response of rigid rotor in unloaded rolling element bearing. Int. J. Mech. Sci. **52**(9), 1176–1185 (2010). Elsevier
21. Mitrovic, R., Atanasovska, I., Soldat, N., Momcilovic, D.: Effects of operation temperature on thermal expansion and main parameters of radial ball bearings. Therm. Sci. **19**(5), 1835–1844 (2015)

Chapter 6
On a Geometrically Exact Beam Model and Its Finite Element Approximation

Enrico Babilio and Stefano Lenci

Abstract A geometrically exact beam model is considered along with a total lagrangian finite element approximation. Basic details about kinematics, dynamics and constitutive assumptions on both continuous and discretized models are given. Results of numerical simulations, both in statics and dynamics, are reported and, whenever possible, compared to existing literature findings.

Keywords Geometrically exact beam · Total lagrangian approach · Finite element · Nonlinear dynamics

6.1 Introduction

Beams, as well as structures that can be effectively modelled as such, are used in many engineering fields, spanning from civil engineering and architecture to mechanical and aerospace engineering and even to nanotechnology and bio-inspired applications. Therefore, beam theories able to catch specific aspects have been developed over the years till to current days. Furthermore, since geometric non-linearities often play a relevant role, theories taking into account effects of large displacements and rotations are desirable. It is noteworthy that a beam model, which is one-dimensional (1D), is simpler to develop and also to face numerically in comparison with 2D and 3D models, especially in the nonlinear realm, where the latter two are very cumbersome. Moreover, when the beam is slender enough (as real beams often are), beam theories are also sufficiently accurate (see [1], for instance).

E. Babilio (✉)
Department of Structures for Engineering and Architecture (DiSt), University of Naples "Federico II", via Forno Vecchio 36, 80134 Naples, Italy
e-mail: enrico.babilio@unina.it

S. Lenci
Department of Civil and Building Engineering, and Architecture (DICEA), Polytechnic University of Marche, via Brecce Bianche, 60131 Ancona, Italy
e-mail: lenci@univpm.it

I. Kovacic and S. Lenci (eds.), *IUTAM Symposium on Exploiting Nonlinear Dynamics for Engineering Systems*, IUTAM Bookseries 37,
https://doi.org/10.1007/978-3-030-23692-2_6

In [2], a geometrically exact beam has been deduced and, among others, it becomes part of the list of models initiated by Reissner in [3], originally restricted to the plane static problem and then generalized to the fully three-dimensional dynamical case by Simo in [4]. Both the approaches in [2] and [3] rely on the principle of virtual work, the differences between them depending on the fact that virtual strains are computed from given displacements and generalized stresses are then obtained, as their work conjugate, in the former, while in the latter arbitrary stresses are introduced in advance and conjugate virtual strains are computed, further obtaining strains in terms of displacements. Actually, since deducing generalized stresses or strains, when either one of the two sets is assigned, is possible through the principle of virtual work [5], both approaches are legitimate.

Equations of motion in [2] are written in a not-centroidal, general frame of reference and to investigate their behaviour and features some work has already been done, even by using different numerical approaches. Numerical computations based on a finite difference technique are performed in [2], concerning, for simplicity, the static analysis of beams that are unshearable, homogeneous and with double symmetric uniform cross sections. In [6], the possibility to derive a hierarchy of approximated models from the geometrically exact parent theory is discussed. Some hypotheses adopted in there are recalled in [7] to simplify equations and finally achieve a reduced order model through a single mode Galerkin approximation. Then, the whole set of equations of motion is attacked in [8], through the method of lines. However, the approach experienced some difficulties in dynamics and, therefore, we decided to implement the finite element (FE) approximation, which this contribution is devoted to. It is noteworthy that, being FEs very general tools, many FE-based codes are already available, as proprietary commercial, open-source research-oriented and even courseware-designed programs. However, in working with existing codes, a proper choice of models and parameters requires not only the knowledge of the problem under investigation, but also skills and a suitable understanding of specific aspects of the software chosen for the analysis. Therefore, in order to control any single step in passing from the partial differential equations derived in [2] to their numerical counterpart, we preferred to consider a home-made implementation. The present contribution is organized as follows. We give some details on the beam model and on its discretization in Sect. 6.2, in terms of kinematics, dynamics and constitutive relationships. In Sect. 6.3, applications in statics and dynamics are reported. Finally, some brief remarks close the contribution.

6.2 The Continuous Model and Its Discretization

For the sake of brevity, we report here only basics about the model we are dealing with and refer to [2] for further detail. The finite element approximation we derive is compared strictly to its continuous parent, in a step by step fashion.

6.2.1 Kinematics

Let us accept henceforth the vague definition of a beam as a deformable line, called the beam-centerline or the axis, whose points are equipped each with a flat rigid body, the cross-section $\mathcal{S}_0$, and assume that the length L_0 of the undeformed axis prevails on the largest dimension of the cross section. To locate points of the beam in space, a reference Cartesian frame, of axes x, y and z, is adopted. We restrict the analysis to beams which are straight in their undeformed reference configuration, with the beam axis laying down x and the cross-sectional principal axes set along y and z. In terms of deformation map, the axis is allowed to bend and stretch and cross sections may rotate under a different angle with respect to the tangent to the deformed axis, with the restriction that displacement and rotation functions are sufficiently regular and invertible. So far, apart from the limitation implying that the deformation map cannot induce volume annihilation or infinite expansion, no further assumption is made on the magnitude of displacements and rotations. However, to deal with the simplest case of commutative rotations, we assume the beam deform in $xy-$plane undergoing twist-free configurations only. At the continuous model level, the displacement components $u = u(x,t)$ and $v = v(x,t)$, along x and y respectively, the cross-sectional rotation $\theta = \theta(x,t)$ and the beam axis rotation $\varphi = \varphi(x,t)$, are introduced. We accept $\theta \neq \varphi$, in general. Generalized strains, that is axial strain $\varepsilon = \varepsilon(x,t)$, mechanical bending curvatures $\kappa = \kappa(x,t)$ and shear angle $\gamma = \gamma(x,t)$, are defined as

$$\varepsilon = u' + \frac{u'^2}{2} + \frac{v'^2}{2}, \qquad \kappa = \theta', \qquad \gamma = \theta + \arctan\left(\frac{v'}{1+u'}\right), \tag{6.1}$$

prime standing for differentiation with respect to the space variable x.

It is noteworthy that, besides κ as here defined, other possibilities exist for suitable curvatures (see [2] for a discussion on the subject and references therein).

In order to develop the discretized version of the model, we formulate a finite element approximation, by replacing first the real beam with a discretization made of n_e one-dimensional elements, for simplicity assumed of the same initial length $l_e = L_0/n_e$, with linearly varying displacements and rotations along the generic element e, leading to approximate actual displacement and rotation functions over the beam with C^0-continuous functions. Hence, for the finite element e, spanning from the initial to the final abscissas x^i and x^f, re-mapped onto the interval $-1 \leq \xi \leq 1$, the discretized counterparts of Eqs. (6.1) are

$$\begin{aligned} \varepsilon_e &= \frac{U_e^f - U_e^i}{l_e} + \frac{\left(U_e^f - U_e^i\right)^2 + \left(V_e^f - V_e^i\right)^2}{2\, l_e^2}, \qquad \kappa_e = \frac{\Theta_e^f - \Theta_e^i}{l_e}, \\ \gamma_e &= \frac{\Theta_e^i + \Theta_e^f}{2} + \arctan\left(\frac{V_e^f - V_e^i}{U_e^f - U_e^i + l_e}\right), \end{aligned} \tag{6.2}$$

being U_e^i, V_e^i, Θ_e^i, U_e^f, V_e^f and Θ_e^f the values of displacements and rotations of the element endpoints, collected in a six-dimensional vector defined as

$$\mathbf{U} := \left(U_e^i \quad V_e^i \quad \Theta_e^i \quad U_e^f \quad V_e^f \quad \Theta_e^f\right)^{\mathrm{T}} . \tag{6.3}$$

Notice that approximating the shear strain over the finite element with a constant function (same order as ε_e and κ_e) allows getting convergent results with a number of elements significantly smaller than choosing linear γ_e (which indeed induces locking phenomenon), as shown in [9], through numerical examples.

6.2.2 Equations of Motion

In the present contribution, with slight loss of generality, we consider the simplest case of a homogeneous beam with $\mathcal{S}_0$ held constant along the beam length. On stipulating the principle of virtual work among generalized stresses N, T and M and their work-conjugate virtual variations of ε, γ and κ, as well as among external, inertial and dissipative forces and the corresponding virtual displacements, the equations of motion are got as

$$m_0\,\ddot{u} + c_0\,\dot{u} = (N(2\varepsilon+1)\cos\varphi - T\sin\varphi)' + q_x\,, \tag{6.4}$$

$$m_0\,\ddot{v} + c_0\,\dot{v} = (-N(2\varepsilon+1)\sin\varphi + T\cos\varphi)' + q_y\,, \tag{6.5}$$

$$m_2\,\ddot{\theta} + c_2\,\dot{\theta} = M' - T\sqrt{2\varepsilon+1} + q_\theta\,, \tag{6.6}$$

that must be complemented by properly imposed boundary conditions. Terms in Eqs. (6.4–6.6) are given per unit length, being m_0 and c_0 axial and transverse inertia and damping; m_2 and c_2 rotary inertia and damping; q_x, q_y and q_θ external loads. Prime, as before, and superimposed dot stand for differentiation with respect to the space variable x and time t, respectively. For any element e, we may deduce the six equations of motion by requiring the virtual work equation

$$\delta W_e^{\text{internal strain}} = \delta W_e^{\text{external load}} - \delta W_e^{\text{inertial forces}} - \delta W_e^{\text{dissipative forces}} \tag{6.7}$$

be satisfied for every $\delta\mathbf{U}$, which is the virtual variation of $\mathbf{U}$, defined in Eq. (6.3).

It is noteworthy that the approximation of the model we are dealing with leads to a system of nonlinear equations, with a stiffness matrix dependent on $\mathbf{U}$. From the virtual work due to internal strain, the tangent stiffness matrix, at any $\mathbf{U} = \mathbf{U}^*$, can be deduced as

$$\mathbf{K}_e = \left[\frac{\partial^2}{\partial\delta\mathbf{U}\,\partial\mathbf{U}}\left(\delta W_e^{\text{internal strain}}\right)\right]_{\mathbf{U}=\mathbf{U}^*} . \tag{6.8}$$

In the case of non-uniform beams, also masses and damping matrices vary and, similarly to Eq. (6.8), they are related to virtual works of inertial and dissipative forces, respectively. However, instead of writing $\mathbf{K}_e$ from Eq. (6.8), we numerically compute its entries with *Mathematica*® exploiting the robust methods implemented in and designed to solve systems of algebraic or differential nonlinear equations (as Newton-Raphson, Runge-Kutta, or others, depending on the nonlinear problem to solve).

For the homogeneous uniform beam we are dealing with (however the generalization to the more general non-homogeneous and non-uniform case being quite straightforward) terms in Eq. (6.7) comment as

$$\delta W_e^{\text{internal strain}} = \frac{l_e}{2} \int_{-1}^{1} \left(\left(N_e \delta \varepsilon_e + T_e \delta \gamma_e \right) \sqrt{2\varepsilon_e + 1} + M_e \delta \kappa_e \right) \mathrm{d}\xi \,, \tag{6.9}$$

$$\delta W_e^{\text{inertial forces}} = \frac{l_e}{2} \int_{-1}^{1} \left(m_0 \left(\ddot{u}_e \delta u_e + \ddot{v}_e \delta v_e \right) + m_2 \ddot{\theta}_e \delta \theta_e \right) \mathrm{d}\xi \,, \tag{6.10}$$

$$\delta W_e^{\text{dissipative forces}} = \frac{l_e}{2} \int_{-1}^{1} \left(c_0 \left(\dot{u}_e \delta u_e + \dot{v}_e \delta v_e \right) + c_2 \dot{\theta}_e \delta \theta_e \right) \mathrm{d}\xi \,, \tag{6.11}$$

$$\delta W_e^{\text{external load}} = \frac{l_e}{2} \int_{-1}^{1} \left(q_{xe} \delta u_e + q_{ye} \delta v_e + q_{\theta e} \delta \theta_e \right) \mathrm{d}\xi \,. \tag{6.12}$$

Finally, in order to build the whole system of equations for the original beam discretized in n_e elements, motion equations specialized for every element e of the discretization must be properly assembled with suitable boundary conditions enforced, as well.

6.2.3 Constitutive Relationships

For further development, we assume elastic constitutive assumptions between generalized strains and stresses. In particular, we adopt here without further justification, the relationships deduced in [2], and (coherently with what we have done for equations of motion) specialize them to the simplest case of a homogeneous beam with $\mathcal{S}_0$ held constant along the beam axis. Furthermore, on assuming that γ remains small enough, as confirmed by previous numerical experiences with finite difference approaches [9], we achieve

$$N = \frac{1}{\sqrt{2\varepsilon+1}}\left(K_0\,\varepsilon + \frac{3}{2}K_2\,\kappa^2\right), \qquad M = \left(K_2\,(3\varepsilon+1) + \frac{1}{2}\,\kappa^2\,K_4\right)\kappa\,, \tag{6.13}$$
$$T = \sqrt{2\varepsilon+1}\left(K_S - K_2\,\kappa^2\right)\gamma\,,$$

where K_0, K_2, K_4 and K_S are cross-sectional stiffnesses. Thanks to Eqs. (6.2), the discretization of Eqs. (6.13) is straightforward.

6.3 Numerical Results

The present section is devoted to describe some numerical results obtained using *Mathematica*® based codes. For the sake of comparison, we consider, first, the static problem from [10] that is a thick cantilever beam 2 m long, with uniform rectangular cross section 0.5 m height and 0.1 m width, undergoing large displacements under a combined static load, which is a downward tip force of 125×10^6 N plus a counter-clockwise tip moment of 160×10^6 N m. The beam is made of a material characterized by a Young's modulus of 207 GPa and vanishing Poisson's ratio. Basically, in [10], the beam is of Reissner's type and it is analysed through an absolute nodal coordinate formulation (ANCF) and a fully three-dimensional computation with linear hexahedral finite elements (3D FE).

In Table 6.1, values of non-vanishing parameters used in the present computations are reported. In Table 6.2 and in Fig. 6.1, results are shown. In particular, in Table 6.2, tip (axial and transversal) displacements are compared with results from [10]. Also rotation and shear angle are reported, although the latter two are not reported in [10]. Further, because of different sign assumptions, axial displacements appear positive-signed in [10]. Figure 6.1 collects graphics of axial and transverse displacements at the axis height, cross-sectional rotations and deformed shape of the beam.

By virtue of the good agreement between present results and comparison literature findings, we may infer that our (indeed quite simple) finite element approximation is reliable. Furthermore, we emphasize that the beam model itself, as introduced in [2] is as predictive as the Reissner's one, at least in the analysed case. However, since the two models slightly differ from each other, there's still room to understand in what those differences play role. We leave this for future work.

Table 6.1 Stiffnesses adopted in computations

K_S (N)	K_0 (N)	K_2 (N m^2)	K_4 (N m^4)
43.125×10^8	10.350×10^9	215.625×10^6	808.594×10^4

Table 6.2 Comparison of our results, from the present finite element formulation (FEM) and 2nd and 4th order finite difference approaches (FDM), with available literature findings

Type	# els	u (m)	v (m)	θ (rad)	γ (rad)
FEM	16	−0.02783	0.09211	0.35873	0.02798
	32	−0.02803	0.09311	0.35894	0.02874
	64	−0.02808	0.09336	0.35900	0.02893
FDM (2nd)	16	−0.02916	0.10665	0.34988	0.02909
	32	−0.02892	0.09382	0.35959	0.02900
	64	−0.02955	0.09043	0.36307	0.02878
FDM (4th)	16	−0.02916	0.10665	0.34988	0.02909
	32	−0.02892	0.09382	0.35959	0.02900
	64	−0.02891	0.09292	0.36028	0.02901
ANCF [10]	16	−0.02932	0.09136	–	–
ANCF [10]	32	−0.02938	0.09256	–	–
3D FE [10]	256	−0.02948	0.09030	–	–
3D FE [10]	4096	−0.02958	0.09043	–	–

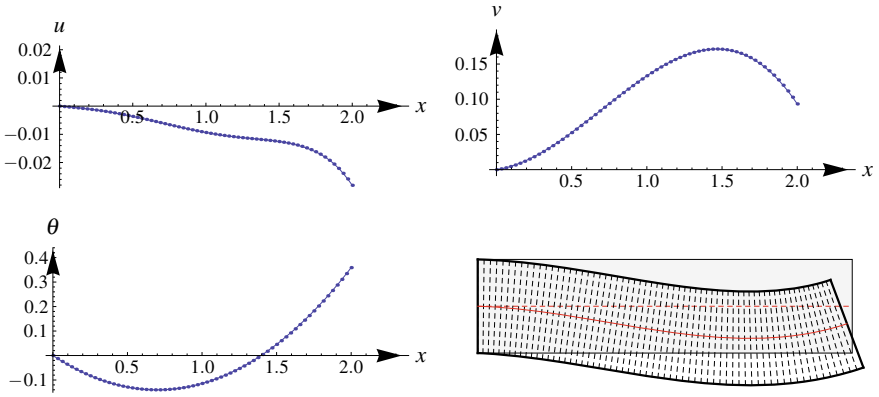

Fig. 6.1 Results for a 64-element discretized beam. Top panels: axial (left) and transverse (right) displacements. Bottom panels: rotation (left) and deformed shape superimposed to undeformed configuration (displacements and rotations are not amplified)

The next set of examples, for which at the moment we do not present comparison, is aimed at testing the present finite element approach in the more challenging and time consuming dynamical case.

We consider a beam hinged at the both ends, of initial length $L_0 = 1$ m, whose mechanical data are reported in Table 6.3 (the parameters that do not appear here or there are set to zero). The beam is subjected to a midspan dynamic point load $Q(t) = P\cos\Omega t$. The amplitude of load is set as a fraction of the axial stiffness, namely $P = K_0/100$. The angular frequency Ω is set as the bifurcation parameter. Results

Table 6.3 Parameters adopted for computations in dynamics (not reported ones are set to zero)

K_S (N)	K_0 (N)	K_2 (N m^2)	K_4 (N m^4)	m_0 (kg m^{-1})	m_2 (kg m)	c_0 (N s m^{-2})
5.25×10^8	1.05×10^9	2.19×10^5	82.03	39.25	8.18×10^{-3}	2.89×10^3

are computed by choosing 240 equally spaced values Ω_i ($i = 1, 2, \ldots, 240$) in the interval

$$0.8\,\omega \leq \Omega \leq 1.2\,\omega\,, \tag{6.14}$$

ω being the first linear angular frequency

$$\omega = \frac{\pi^2}{L_0^2}\sqrt{\frac{K_2}{m_0}} \tag{6.15}$$

of the beam. At every Ω_i the integration of the equations of motion is performed over the time interval spanning from $t_0 = 0$ to the final time $t_{\max}$ defined as

$$t_{\max} = \min\left(N_C, \tau\right)\frac{2\pi}{\Omega_i}\,, \tag{6.16}$$

where N_C and τ are the maximum number of load cycles for each integration (here we choose $N_C = 200$) or the number of cycles that is necessary to the τ-periodic solution to return on itself (under the obvious limitation $\tau < N_C$). In other words, the i-th integration stops soon after a periodic solution is found or after 200 cycles of load are done. Initial displacements and rotations of the first computation, i.e. $i = 1$ (with $\Omega_1 = 0.8\,\omega$) correspond to the static equilibrium of the beam under the midspan static force of magnitude P. Initial velocities are set to zero. For any further computation, i.e. $i \geq 2$, initial data are taken form the final state of the previous $(i-1)$-th simulation.

In simulations we report, the beam is discretized with 4 elements, that is, after hinged boundary conditions are properly imposed, with 11 degrees of freedom, leading to a non-autonomous system of 22 first order ordinary differential equations. Some results are reported in Figs. 6.2 and 6.3. In particular, Fig. 6.2 shows solutions for three selected load frequencies, namely Ω set to $0.8\,\omega$, $0.9\,\omega$ and ω. The first and third solutions are periodic, with period equal to 1 and 3 times the period of the load, respectively, while the second one is chaotic. Figure 6.3 collects these and other solutions in terms of a bifurcation diagram, built in a brute force fashion by using a code running in *Mathematica*® and already applied in [11], with specific changes introduced for the problem here considered.

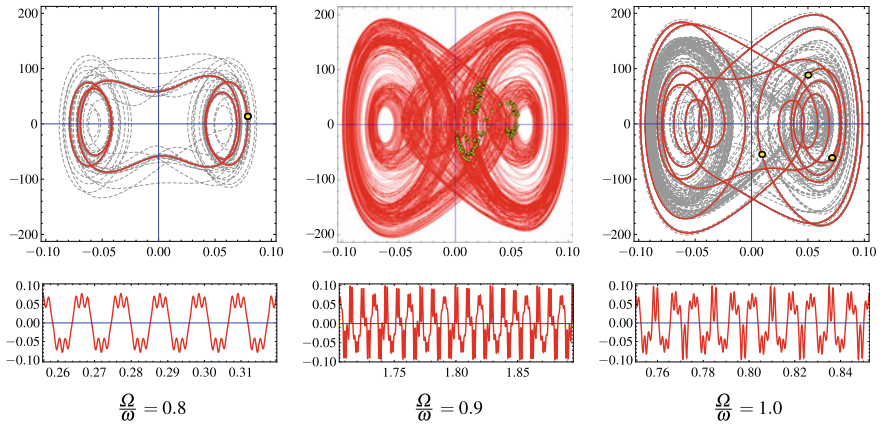

Fig. 6.2 Three solutions for selected load frequencies. Top panels: transient (dashed gray) and steady (red) phase trajectories with superimposed Poincaré return map (yellow dots). Bottom panels: steady state time histories (only few load-cycles time-interval shown)

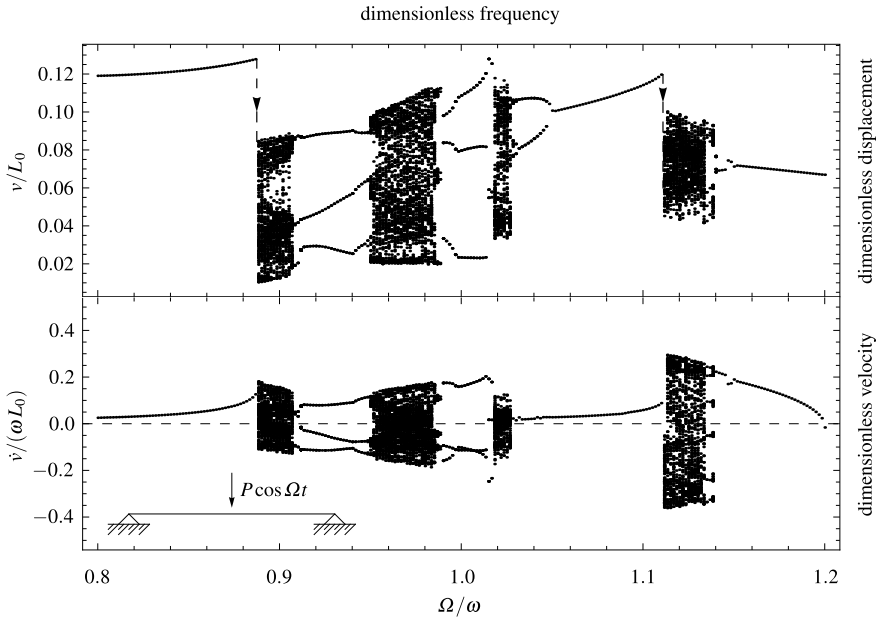

Fig. 6.3 Dimensionless midspan displacement v/L_0 (top panel) and velocity $\dot{v}/(\omega L_0)$ (bottom panel) *vs* dimensionless angular frequency Ω/ω of load. Initial state of the beam is deformed under the static force $P = K_0/100$, K_0 being the axial stiffness of the beam. Each numerical integration is stopped whenever a periodic solution is found or after 200 cycles of force. The diagram is plotted discarding the transient phase

6.4 Conclusions

Basic details of a geometrically exact beam model, both at the continuous and at an approximated formulation levels, are presented. The set of three second-order partial differential equations is discretized through a total lagrangian finite element formulation. The functions approximating displacements and rotations are linear along the generic finite element, and as such enter in the definition of approximated axial and bending strains. However, to avoid locking phenomena, rotation is held constant in approximating shear strain. Results from simulations, both in statics and dynamics, are reported. Solutions of a static benchmark problem are compared with literature results. The good agreement, which has been found, validates both the theoretical beam model and its finite element approximation. Results from dynamic analysis, in terms of phase trajectories, time histories, Poincaré return maps and bifurcation diagrams contain typical feature found in analysing nonlinear systems. As expected, from a computational viewpoint, the discretized dynamic problem, held by ordinary differential equations, was significantly more expensive in comparison with the static counterpart, held by algebraic equations. We conclude by emphasizing that the kinematically-consistent model we are dealing with, in which 1D constitutive relationships (at the beam level) are deduced from continuum-based (point level) stress-strain assumptions, straightforwardly applies to examples more general than those considered in the present contribution, as beams with variable cross sections and material space gradation. Of course, since different kinematic formulations can be employed, many other models to compare with do exist, and for any model several numerical approximation strategies can be adopted. Hence, the choice of the most convenient approximation of any suitable theoretical model relies on many interrelated aspects and, indeed, it may be problem-dependent.

References

1. Bathe, K.-J., Bolourchi, S.: Large displacement analysis of three-dimensional beam structures. Int. J. Numer. Meth. Eng. **14**(7), 961–986 (1979)
2. Babilio, E., Lenci, S.: On the notion of curvature and its mechanical meaning in a geometrically exact plane beam theory. Int. J. Mech. Sci. **128–129**, 277–293 (2017)
3. Reissner, E.: On one-dimensional finite-strain beam theory: the plane problem. Z. Angew. Math. Phys. **23**(5), 795–804 (1972)
4. Simo, J.C.: A finite strain beam formulation. The three-dimensional dynamic problem. Part I. Comput. Method Appl. M **49**(1), 55–70 (1985)
5. Krenk, S.: Non-linear Modeling and Analysis of Solids and Structures. Cambridge University Press (2009)
6. Babilio, E., Lenci, S.: The role of parameters of smallness in deduction of approximated theories for deterministic dynamics of beams. MATEC Web Conf. **83** (2016)
7. Babilio, E., Lenci, S.: Consequences of different definitions of bending curvature on nonlinear dynamics of beams. Procedia Eng. **199**, 1411–1416 (2017)
8. Babilio, E., Lenci, S.: A nonlinear model for design of beams operating in largely deformed configurations. Paper ID 182. In: Stépán, G., Csernák, G. (eds.) Proceedings of 9th European

Nonlinear Dynamics Conference (ENOC 2017), Budapest (2017). Congressline Ltd. ISBN: 978-963-12-9168-1
9. Babilio, E., Lenci, S.: A simple total-lagrangian finite-element formulation for nonlinear behavior of planar beams. In: Proceedings of the ASME Design Engineering Technical Conference, 6 (2018). DETC2018-85622. Quebec City, Quebec. 26–29 August 2018
10. Irschik, H., Gerstmayr, J.: A continuum-mechanics interpretation of Reissner's non-linear shear-deformable beam theory. Math. Comp. Model Dyn. **17**(1), 19–29 (2011)
11. Babilio, E.: Nonlinear dynamics of a slender axially graded beam embedded in a viscoelastic medium. In: Proceedings of the ASME Design Engineering Technical Conference, 6 (2017). DETC2017-68464. Cleveland OH, USA. 6–9 August 2017

Chapter 7
Targeted Nonlinear Energy Transfer for Electroacoustic Absorbers

D. Bitar, A. Ture Savadkoohi, C.-H. Lamarque, E. Gourdon and M. Collet

Abstract In order to investigate the effects of coupling a nonlinear electrical shunt circuit to a loudspeaker terminal, a representative two degrees of freedom (dof) system has been considered. It consists of a main system describing the displacement of the loudspeaker membrane, which is linearly coupled to a Nonlinear Energy Sink (NES) with a small mass compared to the principal one. An analytical treatment enabling the analysis of the behaviour of the system around the 1:1 resonance at different time scales is endowed. This methodology enables the detection of equilibrium and singular points, corresponding to periodic and modulated regimes, respectively. The analytical developments prepare necessary design tools for tuning parameters of the NES.

Keywords Electroacoustic absorber · Passive control · Nonlinear energy sink · Targeted energy transfer

D. Bitar (✉) · A. Ture Savadkoohi · C.-H. Lamarque · E. Gourdon
LTDS-UMR CNRS 5513, Ecole Nationale des Travaux Publics de l'Etat (ENTPE),
Univ. Lyon, 3 rue Maurice Audin, 69120 Vaulx-en-Velin Cedex, France
e-mail: diala.bitar@entpe.fr

A. Ture Savadkoohi
e-mail: alireza.turesavadkoohi@entpe.fr

C.-H. Lamarque
e-mail: Claude-Henri.Lamarque@entpe.fr

E. Gourdon
e-mail: emmanuel.gourdon@entpe.fr

M. Collet
LTDS-UMR CNRS 5513, Ecole Centrale de Lyon (ECL),
36 avenue Guy de Collongue, 69134 Ecully Cedex, France
e-mail: manuel.collet@ec-lyon.fr

I. Kovacic and S. Lenci (eds.), *IUTAM Symposium on Exploiting Nonlinear Dynamics for Engineering Systems*, IUTAM Bookseries 37,
https://doi.org/10.1007/978-3-030-23692-2_7

7.1 Introduction

Audible sound is a combination of direct sound flowing from a source and indirect reflections. In order to improve the quality of sound in a room, the control of noise reverberations at the propagation and reception paths is essential. Among the various employed sound absorption technologies, we are interested in the active absorption approach. For instance, an electrodynamic loudspeaker can be turned into an electroacoustic absorber by connecting a convenient passive electrical shunt circuit to the transducer terminal. This approach permits to dissipate sound power of incident waves [1]. The concept of energy pumping from a primary source to a NES was introduced in several domains of engineering sciences with two main applications namely passive control and energy harvesting (see for example [2–4]).

Nonlinear systems are well known for their ability to improve the performance of the control and increasing frequency range of absorption [5]. For this purpose, a passive nonlinear shunt circuit has been connected to the loudspeaker terminal. Then, the whole structure can be represented by a two dof system, including the main linear system describing the displacement of the loudspeaker membrane which is linearly coupled to an electrical NES.

In order to solve the system analytically, an extended version of complex variables of Manevitch [6] is introduced, taking into account higher harmonics. It permits a better prediction of system behaviors, especially during bifurcations. The multiple-scale method [7] is employed enabling to detect the behavior of the system at different time scales. This approach allows the identification of the system invariant at fast time scale and equilibrium and singular points at slow times scales [8, 9].

7.2 System Representation

The dynamics of an electroacoustic loudspeaker, shunted with an electrical nonlinear circuit and subjected to an external periodically varying sound pressure can be described by the following differential system:

$$\begin{cases} M_{ms}\ddot{x}(t) + R_{ms}\dot{x}(t) + C_{mc}^{-1}x(t) - CBl\dot{V}(t) = SA_m \cos(\Omega t), \\ C(L_e + L_c)\ddot{V}(t) + C(R_e + R_c)\dot{V}(t) + kV^3 + Bl\dot{x}(t) = 0. \end{cases} \tag{7.1}$$

where x and V describe respectively the small displacement of the loudspeaker membrane and the electric potential in the nonlinear shunt circuit. The dot notation indicates the derivative with respect to time t i.e. $\dot{x} = dx/dt$. M_{ms}, R_{ms} and C_{mc} are the mass, the mechanical resistance of the moving bodies and the equivalent compliance of the enclosed loudspeaker. Bl is the force factor of the transducer with B representing the magnetic field magnitude and l standing for the length of the wire in the voice coil. A_m is the pressure amplitude, Ω is the angular frequency and S stands for the diaphragm surface. R_e and L_e are respectively the DC resistance

and the inductance of the voice coil with $Bl\dot{x}(t)$ describing the back electromotive force. R_c, L_c and C are the inductance, resistance, and capacitance of the corresponding nonlinear shunt circuit with k the nonlinear coefficient related to the multiplier connections.

After introducing the non-dimensional time variable $T = \omega_0 t$ with $\omega_0 = \sqrt{1/(M_{ms}C_{mc})}$ the natural angular frequency, the physical two degree of freedom system of Eqs. (7.1) can be expressed by the following scaled system

$$\begin{cases} \ddot{y}_1 + \varepsilon\lambda\dot{y}_1 + y_1 - \varepsilon\alpha\dot{y}_2 = \varepsilon f\cos(\omega T), \\ \varepsilon\left(\ddot{y}_2 + \gamma\dot{y}_2 + \xi y_2^3 + \eta\dot{y}_1\right) = 0. \end{cases} \tag{7.2}$$

The dot notation indicates now the derivative with respect to time T. y_1 and y_2 stand for x and V in the new time domain. The scaled parameters used in Sys. (7.2) are $\varepsilon = L_e + L_c$, $R_{ms}C_{mc}\omega_0 = \varepsilon\lambda$, $CBlC_{mc}\omega_0 = \varepsilon\alpha$, $SA_mC_{mc} = \varepsilon f$, $(R_e + R_c)/\omega_0 = \varepsilon\gamma$, $k/(C\omega_0^2) = \varepsilon\xi$, $\omega = \Omega/\omega_0$ and $Bl/(C\omega_0) = \varepsilon\eta$.

7.3 Analytical Treatment

In order to analyze the dynamical behavior of the system around the 1:1 resonance by letting $\omega = 1 + \varepsilon\sigma$ with σ a detuning parameter, Manevitch's complex variables [6] can be introduced as

$$\begin{cases} \dot{y}_1 + i\omega y_1 = \psi_1(T)e^{i\omega T} \\ \dot{y}_2 + i\omega y_2 = \psi_2(T)e^{i\omega T} \end{cases} \tag{7.3}$$

Before introducing the complex variables (7.3) into the scaled Sys. (7.2), we choose to investigate on the contribution of harmonics in both variables $\dot{y}_n + i\omega y_n$ with $n \in \{1, 2\}$. Then, we plot in Fig. 7.1 the modulus of $\dot{y}_1 + i\omega y_1$ and $\dot{y}_2 + i\omega y_2$ according to scaled time T for the following parameters: $\varepsilon = 0.01, \eta = \alpha = \lambda = 0.2$, $\gamma = 0.3, \xi = 0.5$ and $f = 0$. The corresponding numerical results obtained by direct numerical integration of Eqs. (7.2) using a Runge-Kutta scheme with the corresponding initial conditions as $y_1(0) = y_2(0) = \dot{y}_2(0) = 0$ and $\dot{y}_1(0) = 3.7$.

Remarkably, for the first modulus represented in Fig. 7.1a, it can be clearly seen that the first harmonic is sufficient enough to qualify the energy level of the primary system. Thus, for the energy amplitude of the NES represented in Fig. 7.1b the addition of the third harmonic has remarkable effects on its behavior the individual presence of the first harmonic.

7.3.1 Dynamical Behavior Around 1:1 Resonance

An extended version of Manevitch's complex variables is introduced in the present study, taking into account the effect of the first harmonic for the principal system and

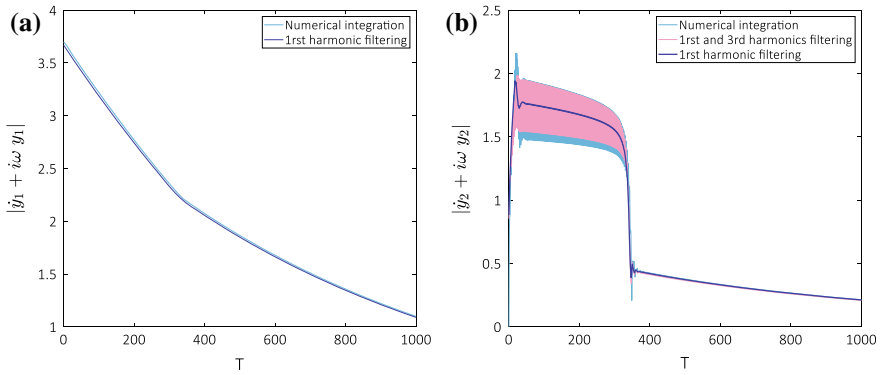

Fig. 7.1 Time histories of $|dy_1/dT + i\omega y_1| = N_1$ and $|dy_2/dT + i\omega y_2|$ obtained by the direct integration of Sys. (7.2) under free oscillations; i.e. $f = 0$

both first and third harmonics for the NES. In addition, we apply a multiple scales approach by introducing a fast time scale τ_0 and slower ones $(\tau_1, \tau_2, \dots)$ as:

$$T = \tau_0, \tau_1 = \varepsilon\tau_0, \tau_2 = \varepsilon^2\tau_0 \dots \tag{7.4}$$

The new complex variables are introduced as in the following relationship:

$$\begin{cases} \dot{y}_1 + i\omega y_1 = \psi_1(\tau_1, \tau_2, \dots)e^{i\omega\tau_0} \\ \dot{y}_2 + i\omega y_2 = \psi_2(\tau_1, \tau_2, \dots)e^{i\omega\tau_0} + \psi_3(\tau_1, \tau_2, \dots)e^{3i\omega\tau_0} \end{cases} \tag{7.5}$$

After introducing the complex variables presented in Eq. (7.5) into Eqs. (7.2) we obtain the system below

$$\begin{cases} \left[\dot{\psi}_1 - i\dfrac{(1-\omega^2)}{2\omega}\psi_1 + \varepsilon\dfrac{\lambda}{2}\psi_1 - \varepsilon\dfrac{\alpha}{2}\psi_2 - \varepsilon\dfrac{f}{2}\right]e^{i\omega\tau_0} - \varepsilon\dfrac{\alpha}{2}\psi_3 e^{3i\omega\tau_0} + c.c. = 0 \\ \left[\dot{\psi}_2 + i\dfrac{\omega}{2}\psi_2 + \dfrac{\gamma}{2}\psi_2 + \dfrac{\eta}{2}\psi_1 - i\dfrac{3\xi}{8\omega^3}\left(\psi_2|\psi_2|^2 - \psi_3\psi_2^{*^2} + 2\psi_2|\psi_3|^2\right)\right]e^{i\omega\tau_0} \\ \quad + \left[\dot{\psi}_3 + i\dfrac{5\omega}{2}\psi_3 + \dfrac{\gamma}{2}\psi_3 - i\dfrac{\xi}{8\omega^3}\left(3\psi_3|\psi_3|^2 - \psi_2^3 + 6\psi_3|\psi_2|^2\right)\right]e^{3i\omega\tau_0} \\ \quad + i\dfrac{3\xi}{8\omega^3}\psi_2\psi_3^2 e^{7i\omega\tau_0} + i\dfrac{3\xi}{8\omega^3}\left[\psi_2^2\psi_3^3 - \psi_3^2\psi_2^*\right]e^{5i\omega\tau_0} + c.c. = 0, \end{cases} \tag{7.6}$$

where $c.c.$ stands for the complex conjugate of the rest of the arguments. The complex variables ψ_n describe the slow modulation of fast vibrations at the frequency ω.

Using the Galerkin technique [9], we keep the first harmonic of the main system and the first and the third harmonics of the NES and truncate higher ones. In applying the method, we suppose that ψ_1, ψ_2, ψ_3 are independent of the fast time τ_0. Then, we obtain an averaged system composed of three first order differential equations in terms of ψ_1, ψ_2 and ψ_3 as:

$$\dot{\psi}_1 - i\frac{(1-\omega^2)}{2\omega}\psi_1 + \varepsilon\frac{\lambda}{2}\psi_1 - \varepsilon\frac{\alpha}{2}\psi_2 = \varepsilon\frac{1}{2}f \tag{7.7}$$

$$\dot{\psi}_2 + i\frac{\omega}{2}\psi_2 + \frac{\gamma}{2}\psi_2 + \frac{\eta}{2}\psi_1 - i\frac{3\xi}{8\omega^3}\left(\psi_2|\psi_2|^2 - \psi_3\psi_2^{*^2} + 2\psi_2|\psi_3|^2\right) = 0 \tag{7.8}$$

$$\dot{\psi}_3 + i\frac{5\omega}{2}\psi_3 + \frac{\gamma}{2}\psi_3 - i\frac{\xi}{8\omega^3}\left(3\psi_3|\psi_3|^2 - \psi_2^3 + 6\psi_3|\psi_2|^2\right) = 0 \tag{7.9}$$

This methodology enables the detection of the system invariant at the fast time scale τ_0, which allows the detection of the system behaviors at the slower time scales.

7.3.1.1 The System Behavior at τ_0 Time Scale

At the order ε^0, resonant terms at τ_0 time scale in Eq. (7.7) give

$$\frac{\partial\psi_1}{\partial\tau_0} = 0 \Rightarrow \psi_1 = \psi_1(\tau_1, \tau_2, \dots) \tag{7.10}$$

Then ψ_1 is constant according to the fast time scale τ_0 winch validates our hypotheses during using the Galerkin method. However, Eqs. (7.8) and (7.9) can be expressed as in the following form

$$\begin{cases} \dfrac{\partial\psi_2}{\partial\tau_0} + H_1(\psi_1, \psi_2, \psi_3, \psi_2^*, \psi_3^*) = 0, \\ \dfrac{\partial\psi_3}{\partial\tau_0} + H_2(\psi_2, \psi_3, \psi_2^*, \psi_3^*) = 0, \end{cases} \tag{7.11}$$

where H_1 and H_2 define the ε^1 order functions of Eqs. (7.8) and (7.9). System (7.11) presents an asymptotic equilibrium governed by a manifold called Slow Invariant Manifold (SIM), which is in fact a geometrical representation of the fixed points of the system i.e.,

$$\tau_0 \longrightarrow \infty \Rightarrow \begin{cases} \dfrac{\partial\psi_2}{\partial\tau_0} \longrightarrow 0, \\ \dfrac{\partial\psi_3}{\partial\tau_0} \longrightarrow 0. \end{cases} \tag{7.12}$$

or we can set

$$\mathscr{H}(\delta_1, N_1, \delta_2, N_2, \delta_3, N_3) = 0 \equiv \begin{cases} H_1(\psi_1, \psi_2, \psi_3, \psi_2^*, \psi_3^*) = 0, \\ H_2(\psi_2, \psi_3, \psi_2^*, \psi_3^*) = 0. \end{cases} \tag{7.13}$$

Writing the complex variables in the polar form as $\psi_j = N_j e^{i\delta_j}$ with $j = 1, 2, 3$, Sys. (7.13) can be expressed and reduced to the following form after separating its real and imaginary parts:

$$h_1 = N_2\big[\gamma + \frac{3}{4}\xi \sin(3\delta_2 - \delta_3)N_2N_3\big] + \eta\cos(\delta_1 - \delta_2)N_1 = 0 \tag{7.14}$$

$$h_2 = N_2\big[1 - \frac{3}{4}\xi(N_2(N_2 + \cos(3\delta_2 - \delta_3)N_3) - 2N_3^2)\big] + \eta\sin(\delta_1 - \delta_2)N_1 = 0 \tag{7.15}$$

$$h_3 = 4\gamma N_3 - \xi\sin(3\delta_2 - \delta_3)N_2^3 = 0 \tag{7.16}$$

$$h_4 = 4N_3\big[-5 + \frac{3}{2}\xi N_2^2 + \frac{3}{4}\xi N_3^2\big] - \xi\cos(3\delta_2 - \delta_3)N_2^3 = 0 \tag{7.17}$$

Replacing Eqs. (7.16) and (7.17) into Eqs. (7.14) and (7.15) respectively, the SIM can be expressed as it follows:

$$\begin{cases} N_1 = \dfrac{N_2}{\eta}\sqrt{\gamma^2\big(1 + 3\dfrac{N_3^2}{N_2^2}\big)^2 + \big(1 - \dfrac{3}{4}\xi N_2^2 - 15\dfrac{N_3^2}{N_2^2} + 3\xi N_3^2 + \dfrac{9}{4}\xi\dfrac{N_3^4}{N_2^2}\big)^2}, \\ \xi^2 N_2^6 = 16N_3^2\big[\gamma^2 + (-5 + \dfrac{3}{2}\xi N_2^2 + \dfrac{3}{4}\xi N_3^2)^2\big]. \end{cases} \tag{7.18}$$

Under free oscillations, we plot in Fig. 7.2 the numerical result obtained by a direct integration of the scaled Sys. (7.2) compared to the SIM obtained by solving Sys. (7.18). The classical SIM driven by employing the first harmonics only is represented in dashed dot line can be obtained after replacing N_3 by 0 in Eq. (7.18). Remarkably, the addition of the third harmonic managed to adjust the gap between the numerical integration and analytical developments, mainly at the bifurcation.

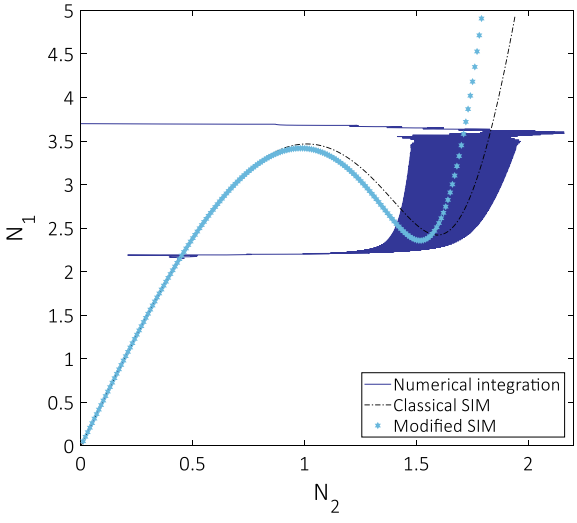

Fig. 7.2 A comparison between the classical (− − −) and modified (∗) SIM together with the direct numerical integration (_____) of the scaled Sys. (7.2) under free oscillations; i.e. $f = 0$

7.3.1.2 The System Behavior at τ_1 Time Scale

Treating Eq. (7.7) at the order ε^1, we can analytically identify the equilibrium points and singularities leading to the presence of periodic or quasi-periodic regimes. Equation (7.7) at ε^1 reads:

$$\frac{\partial \psi_1}{\partial \tau_1} = f(\psi_1, \psi_2) = -(\frac{\lambda}{2} + i\sigma)\psi_1 + \frac{\alpha}{2}\psi_2 + \frac{f}{2} \tag{7.19}$$

Writing Eq. (7.19) into its polar form and separating its real and imaginary parts we obtain the following system

$$\begin{cases} \dfrac{\partial \delta_1}{\partial \tau_1} = f_1(\delta_1, N_1, \delta_2, N_2) = -\dfrac{\lambda}{2}N_1 + \dfrac{\alpha}{2}N_2\cos(\delta_2 - \delta_1) + \dfrac{f}{2}\cos(\delta_1) \\ \dfrac{\partial N_1}{\partial \tau_1} = f_2(\delta_1, N_1, \delta_2, N_2) = \dfrac{1}{N_1}\big(\dfrac{\alpha}{2}N_2\sin(\delta_2 - \delta_1) - \sigma N_1 - \dfrac{f}{2}\sin(\delta_1)\big). \end{cases} \tag{7.20}$$

Combining Eqs. (7.13) and (7.20), the system behavior at slow time scale τ_0 around its invariant can be studied using following equation

$$\begin{pmatrix} \frac{\partial h_1}{\partial \delta_1} & \frac{\partial h_1}{\partial N_1} & \frac{\partial h_1}{\partial \delta_2} & \frac{\partial h_1}{\partial N_2} & \frac{\partial h_1}{\partial \delta_3} & \frac{\partial h_1}{\partial N_3} \\ \frac{\partial h_2}{\partial \delta_1} & \frac{\partial h_2}{\partial N_1} & \frac{\partial h_2}{\partial \delta_2} & \frac{\partial h_2}{\partial N_2} & \frac{\partial h_2}{\partial \delta_3} & \frac{\partial h_1}{\partial N_3} \\ \frac{\partial h_3}{\partial \delta_1} & \frac{\partial h_3}{\partial N_1} & \frac{\partial h_3}{\partial \delta_2} & \frac{\partial h_3}{\partial N_2} & \frac{\partial h_3}{\partial \delta_3} & \frac{\partial h_3}{\partial N_3} \\ \frac{\partial h_4}{\partial \delta_1} & \frac{\partial h_4}{\partial N_1} & \frac{\partial h_4}{\partial \delta_2} & \frac{\partial h_4}{\partial N_2} & \frac{\partial h_4}{\partial \delta_3} & \frac{\partial h_4}{\partial N_3} \end{pmatrix} \begin{pmatrix} \frac{\partial \delta_1}{\partial \tau_1} \\ \frac{\partial N_1}{\partial \tau_1} \\ \frac{\partial \delta_2}{\partial \tau_1} \\ \frac{\partial N_2}{\partial \tau_1} \\ \frac{\partial \delta_3}{\partial \tau_1} \\ \frac{\partial N_3}{\partial \tau_1} \end{pmatrix} = \begin{pmatrix} 0 \\ 0 \\ 0 \\ 0 \\ 0 \\ 0 \end{pmatrix} \tag{7.21}$$

Equation (7.21) can be arranged to be written in the following form

$$\underbrace{\begin{pmatrix} \frac{\partial h_1}{\partial \delta_2} & \frac{\partial h_1}{\partial N_2} & \frac{\partial h_1}{\partial \delta_3} & \frac{\partial h_1}{\partial N_3} \\ \frac{\partial h_2}{\partial \delta_2} & \frac{\partial h_2}{\partial N_2} & \frac{\partial h_2}{\partial \delta_3} & \frac{\partial h_1}{\partial N_3} \\ \frac{\partial h_3}{\partial \delta_2} & \frac{\partial h_3}{\partial N_2} & \frac{\partial h_3}{\partial \delta_3} & \frac{\partial h_3}{\partial N_3} \\ \frac{\partial h_4}{\partial \delta_2} & \frac{\partial h_4}{\partial N_2} & \frac{\partial h_4}{\partial \delta_3} & \frac{\partial h_4}{\partial N_3} \end{pmatrix}}_{\mathscr{M}} \begin{pmatrix} \frac{\partial \delta_2}{\partial \tau_1} \\ \frac{\partial N_2}{\partial \tau_1} \\ \frac{\partial \delta_3}{\partial \tau_1} \\ \frac{\partial N_3}{\partial \tau_1} \end{pmatrix} = - \begin{pmatrix} \frac{\partial h_1}{\partial \delta_1} & \frac{\partial h_1}{\partial N_1} \\ \frac{\partial h_2}{\partial \delta_1} & \frac{\partial h_2}{\partial N_1} \\ 0 & 0 \\ 0 & 0 \end{pmatrix} \begin{pmatrix} f_1(\delta_1, N_1, \delta_2, N_2) \\ f_2(\delta_1, N_1, \delta_2, N_2) \end{pmatrix} \tag{7.22}$$

Then, equilibrium points of the system, can be obtained by solving the following system [10]

$$\begin{cases} \mathscr{H} = 0 \\ f_1 = f_2 = 0 \\ det(\mathscr{M}) \neq 0. \end{cases} \tag{7.23}$$

However, fold singularities are reached when

$$\begin{cases} \mathscr{H} = 0 \\ f_1 = f_2 = 0 \\ det(\mathscr{M}) = 0. \end{cases} \tag{7.24}$$

7.4 Some Results and Discussion

Let us consider a system with $f = 0.3$ and the detuning parameter $\sigma = 0$, Sys. (7.23) is validated with $f_1 = f_2 = 0$, $\mathscr{H} = 0$ and $det(\mathscr{M}) \neq 0$, which indicates the existence of an equilibrium point. Figure 7.3a shows the modified SIM compared to the numerical integration of the scaled Sys. (7.2). This later oscillates around the upper branch of the SIM, then once reaching the stability border, it jumps to follow the small amplitude level to be finally attracted by an equilibrium point. The existence of an equilibrium point indicates the existence of a periodic regime, which is verified in Fig. 7.3b once reaching the permanent regime.

Solving Sys. (7.23) for $f = 0.3$ and $\sigma = 0$, we can deduce the existence of the equilibrium point $(N_2, N_1) = (0.274, 1.3959)$. Then, we can deduce that the analytical predictions are in good agreement with the numerical results depicted in Fig. 7.4,

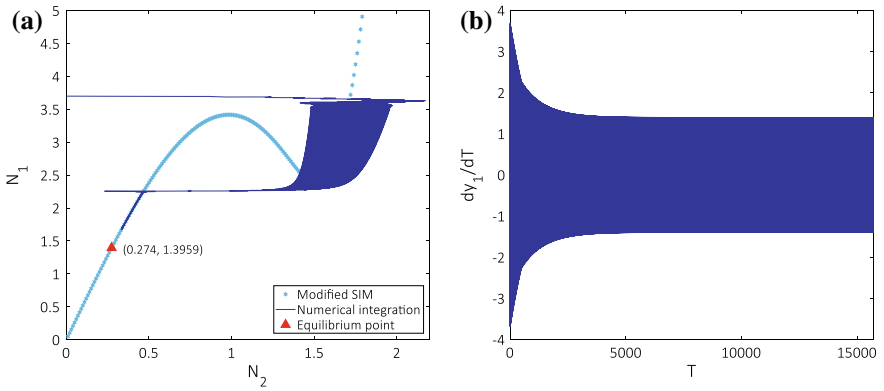

Fig. 7.3 **a** SIM of the system with the numerical integration of the scaled Sys. (7.2) under small forced oscillations with $f = 0.3$ and the detuning parameter $\sigma = 0$. **b** Time histories of the velocity dy_1/dT

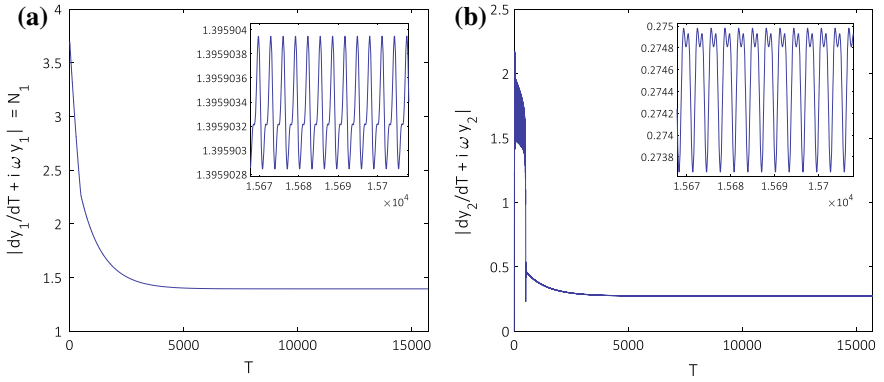

Fig. 7.4 Time histories of both amplitudes $|dy_1/dT + i\omega y_1| = N_1$ and $|dy_2/dT + i\omega y_2|$ obtained by the direct integration of Sys. (7.2) under small forced oscillations with $f = 0.3$ and the detuning parameter $\sigma = 0$

where we plot the histories of $N_1 = |\frac{dy_1}{dT} + i\omega y_1|$ and $|\frac{dy_2}{dT} + i\omega y_2|$. In this given example, the NES is able to control the primary system against periodic external forces by presenting small amplitudes during periodic regimes.

7.5 Conclusions

In order to reduce noise at the propagation and reception paths, an electroacoustic loudspeaker has been turned into a passive absorber by coupling to its terminal a nonlinear electrical shunt circuit. The nonlinear behavior of the system was described by a rescaled two degrees of freedom system, which consists of a linear master structure under sinusoidal forcing that is linearly coupled to a nonlinear energy sink. The study was carried out using an extended version Manevitch's complex variables, including first and third harmonics. The complex system was treated analytically using a multiple-scale method, allowing the detection of the system invariant at the fast time scale. A predictive tool enabling the identification of the dynamical regime (periodic or modulated regimes) is given for the purpose of passive control of the main system.

Acknowledgements This work was conducted in the framework of the LABEX CeLyA ("Centre Lyonnais d'Acoustique"), ANR-10-LABX-60.

References

1. Lissek, H., Boulandet, R., Fleury, R.: Electroacoustic absorbers: bridging the gap between shunt loudspeakers and active sound absorption. JASA **129**, 2968–2978 (2011)
2. Gourdon, E., Alexander, N.A., Taylor, C.A., Lamarque, C.-H., Pernot, S.: Nonlinear energy pumping under transient forcing with strongly nonlinear coupling: theoretical and experimental results. JSV **300**, 522–551 (2007)
3. Bellet, R., Cochelin, B., Herzog, P., Mattei, P.O.: Experimental study of targeted energy transfer from an acoustic system to a nonlinear membrane absorber. JSV **329**, 2768–2791 (2010)
4. Vakakis, A.F., Gendelman, O.V., Bergman, L.A., McFarland, D.M., Kerschen, G., Lee, Y.S.: Nonlinear Targeted Energy Transfer in Mechanical and Structural Systems. Springer, Netherlands (2009)
5. Roberson, R.E.: Synthesis of a nonlinear dynamic vibration absorber. J. Franklin Inst. **254**, 205–220 (1952)
6. Manevitch, L.I.: The description of localized normal modes in a chain of nonlinear coupled oscillators using complex variables. Nonlinear Dyn. **25**, 95–109 (2001)
7. Nayfeh, A., Mook, D.: Nonlinear Oscillations. Wiley, New York (1979)
8. Weiss, M., Chenia, M., Ture Savadkoohi, A., Lamarque, C.-H., Vaurigaud, B., Hammouda, A.: Multi-scale energy exchanges between an elasto-plastic oscillator and a light nonsmooth system with external pre-stress. Nonlinear Dyn. **83**, 109–135 (2016)
9. Lamarque, C.-H., Ture Savadkoohi, A.: Dynamical behavior of a Bouc Wen type oscillator coupled to a nonlinear energy sink. Meccanica **49**, 1917–1928 (2014)
10. Ture Savadkoohi, A., Lamarque, C.-H., Weiss, M., Vaurigaud, B., Charlemagne, S.: Analysis of the 1:1 resonant energy exchanges between coupled oscillators with rheologies. Nonlinear Dyn. **86**, 2145–2159 (2016)

Chapter 8
Using Symbolic Computational Dynamics as an Aid to Design

Matthew P. Cartmell and Niloufar Motazedi

Abstract The topic of Symbolic Computational Dynamics, as presented here, has been motivated by the utility of approximate analytical solutions for reduced order models, and the power of computers to cope with the challenges of both problem scale and automation. Application has traditionally been limited by the algebra needed for problems of more than a few coupled coordinates, making such problems excellent candidates for automation through symbolic computation. But there is a lot of useful information that is naturally lost when doing this, due to the on-going processes of algebraic simplification, the different mathematical-physical processes behind the small parameter, and defining relative strengths of physically based terms. We offer a novel symbolic computational process that applies a semi-automated asymptotic method for solution that also retains all information, leading to a first generation approach to the global visualisation of problems in dynamics.

Keywords Nonlinear dynamics · Perturbation methods · Symbolic computation · Design

8.1 Introduction

Research into *Symbolic Computational Dynamics* (SCD) by Cartmell and Khanin began in 1997 under this title and owes something of its heritage to earlier work carried out by others, notably Rand et al., over a period going back to the early nineteen eighties, mainly on the computation of perturbation methods for approximate analytical solutions to reduced order differential equation models. There are several

M. P. Cartmell (✉)
Department of Mechanical and Aerospace Engineering, University of Strathclyde, Glasgow G1 1XJ, UK
e-mail: matthew.cartmell@strath.ac.uk

N. Motazedi
Bombardier Transportation UK Ltd., Litchurch Lane, Derby DE24 8AD, UK
e-mail: motazedi.n@gmail.com

I. Kovacic and S. Lenci (eds.), *IUTAM Symposium on Exploiting Nonlinear Dynamics for Engineering Systems*, IUTAM Bookseries 37,
https://doi.org/10.1007/978-3-030-23692-2_8

asymptotic methods that can be very usefully applied to nonlinear dynamics problems when they are represented in differential equation form, including the method of Struble, the Lindstedt–Poincaré method, applications of the Volterra series, Harmonic Balance, the method of multiple scales, and the method of direct separation of motions, amongst others. So, in general, approximate analytical solutions can usually be found for reasonably set up reduced-order differential equation models, given certain conditions and constraints. Such solutions can accurately represent the dynamics of the problem—within the limitations of the approximations made. Ease of application of these potentially powerful methods is often limited by the sheer scale of algebraic manipulation needed for nonlinear problems that involve more than a few coupled coordinates. On this basis they are excellent candidates for semi-automation through symbolic computation. The first published research on the formal use of computers to solve symbolic problems in nonlinear dynamics is attributable to Rand [1] in 1984 who introduced the MACSYMA language for this purpose, and then to Rand and Keith who explored normal forms and centre manifold calculations using MACSYMA in 1985 [2], noting that there are several other significant and relevant publications by Rand et al. from around this time. By 1987 Rand and Armbruster had successfully brought together bifurcation theory, perturbation methods, and computer algebra in a major new book [3]. Rand continued to add to this pioneering body of work with a further book on computer algebra applied to nonlinear dynamics in 1994 [4]. Through these seminal works Rand effectively pioneered, and then firmly established, the formal application of symbolic computation to the principal mathematical topics that are used right across the general area of applied dynamics. Recently Professor Rand has issued a comprehensive treatment of nonlinear vibration in the form of published lecture notes, from which virtually all the theories and treatments required for nonlinear analysis are usefully and practically summarised for the practitioner [5].

The long-standing motivation behind the research presented in this paper is an acknowledgement that certain forms of mathematical information are naturally lost when analytically solving the nonlinear differential equations that realistically describe problems encountered in dynamics. This lost information has potential use because of what it can mean physically. One example of this loss is simply that which occurs due to the on-going processes of algebraic simplification. Another is due to the different mathematical-physical reasoning processes that underpin, say, the use of the small perturbation parameter, as it appears and then re-appears throughout an analysis. A third is the way in which we define the relative strengths of physically based terms when they are first introduced into the equations of motion, and the repercussions of getting this partially, or even completely wrong. So, the objective in this research has been to create a symbolic computational process that efficiently applies a semi-automated asymptotic method in a correct, consistent, and adaptable manner. The process was also intended to provide a facility for the identification and retention of all the mathematical-physical information generated that could finally be represented back to the user in an easy-to-interpret visualisation.

The origins of the research specifically reported here go back to a series of lengthy second order multiple scales analyses undertaken by Cartmell and completed in 1984

[6]. That work stimulated many informal and independent experiments in the symbolic codification of perturbation schemes, in the intervening period up to 1997. This led to the award to Cartmell, then based at the University of Edinburgh, of the first of several research grants from 1997 onwards. New forms of symbolic software in *Mathematica*™ emerged from the work done by Cartmell and Khanin under this funding, enabling both serial and parallel computation [7–10]. The work was transferred to the University of Glasgow in 1998 with further research funding awarded from 2000 and this led to the next generation of programs and the burgeoning idea of 'term-tracking' [11–13]. Funded research continued up to 2008. The work was then transferred in 2012 to the University of Sheffield, by which time relatively advanced symbolic solution codes had been developed by Khanin, Forehand, and Cartmell, all written in the *Mathematica*™ language. In addition preliminary research had also been undertaken by Cartmell and Forehand on understanding the challenges inherent in the visualisation of the new information generated by this sort of computation. Motazedi joined the project in 2013 and she subsequently revised and developed the solver software and created an entirely new *term-tracker* package initially based on some of the ideas that had been proposed by Cartmell, Khanin, and Forehand. Motazedi then went on to devise, build, and test new software for visualisation of symbolic data [14, 15], again in *Mathematica*™. Motazedi also took on the substantial problem of writing semi-automated symbolic code for the treatment of the modulation equations that arise naturally within the perturbation method of multiple scales, and she devised a *generic and adaptable* computational structure for handling these important equations systematically in order to complete the solution procedure [14]. These activities have since led to the identification by the authors of *Symbolic Computational Dynamics* (SCD) as a convenient umbrella term for their approach to this general area of research. The authors make no claim for any wider uptake of this term in this context, as yet.

The choice of *Mathematica*™ as the preferred programming language was strategic and made by Cartmell back in the mid 1990s. The thinking behind this decision was generally influenced by the very powerful high-level nature of this language, the fact that it's always been aimed fundamentally at symbolic programming, and because of the many specific features of the language that have lent themselves directly to logical implementations for SCD. The current generation of programs operate as digital interactive notebooks within the *Mathematica*™ interface. This provides an essential level of flexibility for the user so that s/he can apply any assumption or simplification when it is required. The current generations of code allow considerable user interaction and customisation of the core solver and term-tracker, to the extent that differential equations can be added at will, and the internal solution procedures themselves can be customised easily if necessary. This offers a great deal of generality and flexibility in use.

8.2 Symbolic Computational Dynamics

8.2.1 The Process of Symbolic Computational Dynamic Solution

The principles behind SCD are that the problem should be representable in differential equation form and that the equation(s) should lend themselves to asymptotic analysis, also that the analysis method should be adaptable yet algorithmic enough in structure to enable a symbolic computer code to be written to do all the mathematics reliably and accurately yet also adaptively. In addition SCD, as we define it, requires a facility for identifying, encoding uniquely, and then tracking all the mathematical-physical operations within the solution procedure so that a record of the whole process can be generated from which useful visualisations and information can be extracted. The end result is, for example, a typical perturbation analysis in equation form, which is supplemented by a graphic that shows the interconnectedness of the stages within the analysis—in the context of the system variables, operators, constants, and parameters. A detailed mathematical study has been provided by Motazedi [14] and in summarised form in [15], and these two references provide the principal sources for what follows. The utility of the SCD approach depends strongly on the format of the graphic, and this remains an open topic for research with current ideas summarised later. The architecture of an SCD solver is given in Fig. 8.1.

The term-tracker module is based on the authors' *Source and Evolution Encoding Method* (SEEM) and the encoding strategy is summarised in Table 8.1.

An example of how this encoding logic is applied in practice is given in Eqs. (8.1)–(8.5) in which the governing differential equation of motion for a parametrically excited pendulum and the associated multiple scales expansions are all shown in encoded form,

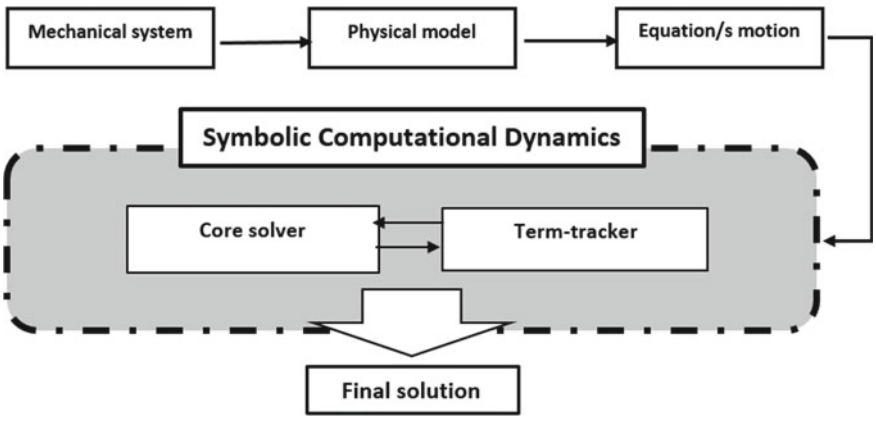

Fig. 8.1 SCD solver architecture [14]

Table 8.1 SEEM logic summary [14]

Encoding level	Description	Visualisation
First level	Origin of the equation and the perturbation order	(i, j)
Second level	First level + equation number in which it becomes explicit	(i, j, k)
Third level	Second level + equation number in which the explicit form is modified	(i, j, k, l)
Compound-I	When two quantities such as e and i subsume, two or more individual e and i terms	$(*, i)$
Compound-II	$(i, j, k, l)_1\, expadd^*(i, j, k, l)_2$	$(*, k_{latest})$
	$(i, j, k, l)_3\, expadd(i, j, k, l)_4$	$(\#, k_{latest})$
	$(i, j, k, l)_5\, expadd(i, j, k, l)_6$	$(\$, k_{latest})$
	$(i, j, k, l)_7\, expadd(i, j, k, l)_8$	$(£, k_{latest})$
Encoding of signs	Signs are not normally encoded unless they are created as the result of an algebraic operation. The divisor is not encoded as well	(i, j, k, l)

$$\ddot{\theta} + \underbrace{2\varepsilon\beta}_{(1,1)}\dot{\theta} + \left(\underbrace{1}_{(1,0)} - \underbrace{\varepsilon q\omega^2}_{(1,1)}\cos(\underbrace{\omega}_{(1,0)} T_0)\right)\theta + \underbrace{\varepsilon\gamma}_{(1,1)}\theta^3 = 0 \tag{8.1}$$

$$\theta(\tau, \varepsilon) = \underbrace{\theta_0}_{(2,0)} + \underbrace{\varepsilon\theta_1}_{(2,1)} + O\left(\varepsilon^2\right) \tag{8.2}$$

$$\frac{d}{dt} = \underbrace{D_0}_{(3,0)} + \underbrace{\varepsilon D_1}_{(3,1)} + O\left(\varepsilon^2\right) \tag{8.3}$$

$$\frac{d^2}{dt^2} = \underbrace{D_0^2}_{(4,0)} + \underbrace{2\varepsilon D_0 D_1}_{(4,1)} + O\left(\varepsilon^2\right) \tag{8.4}$$

$$\theta^3 = \underbrace{\theta_0^3}_{(2,0,5)} + O(\varepsilon). \tag{8.5}$$

The time domain solution is given by Eq. (8.6), with full SEEM encoding shown,

$$\theta\,(\tau, \varepsilon) = \underbrace{a[T_1]}_{(20,0,31)}\, cos\Bigg(\Bigg[\underbrace{1}_{(9,0,31)} - \frac{\overbrace{2}^{(13,0,34)}}{\underbrace{2}_{(21,0)}}\Bigg]\tau + \underbrace{\frac{1}{2}}_{(21,0)}\Bigg[\Big(\underbrace{2}_{(13,0)} - \underbrace{2}_{(9,0)} + \underbrace{\omega}_{(14,0,34)}\Big)\tau + \underbrace{\psi}_{(24,0)}\Bigg]\Bigg)$$
$$- \frac{\overbrace{\varepsilon}^{(2,1)}\ \overbrace{\varepsilon}^{(1,1,19)}}{\underbrace{\varepsilon}_{(2,1,19)}}\ \underbrace{\frac{1}{2^3}}_{(20,0)}\ \underbrace{\frac{1}{8}}_{(19,0)}\ \underbrace{\gamma}_{(1,1,19)}\ \underbrace{a[T_1]^3}_{(20,0)}\cos(\underbrace{3}_{(1,0,10,19)}\ \tau$$

$$
+\frac{\overbrace{3}^{}}{\underbrace{\frac{\overbrace{(20,0,36)}^{}}{\underbrace{2}_{(21,0)}}}_{}}\left[\left(\underbrace{2}_{(13,0)}\underbrace{-2}_{(9,0)}-\underbrace{2}_{(13,0,34)}\underbrace{\omega}_{(14,0,34)}\right)\tau-\underbrace{\psi}_{(24,0)}\right])
$$

$$
+\frac{\overbrace{\varepsilon}^{}\overbrace{\varepsilon}^{}}{\underbrace{\varepsilon}_{(2,1,19)}}\underbrace{q\omega^2}_{(1,1,19)}\underbrace{\frac{1}{2}}_{(1,0,11,19)}\underbrace{\frac{1}{8}}_{(19,0)}\underbrace{\frac{1}{2}}_{(20,0)}\cos
$$

$$
\left[\left(\underbrace{2}_{(13,0,19)}+\underbrace{1}_{(9,0,19)}+\frac{\overbrace{2}^{}}{\underbrace{2}_{(21,0)}}-\frac{\overbrace{2}^{}}{\underbrace{2}_{(21,0)}}-\frac{\overbrace{2}^{}}{\underbrace{2}_{(21,0)}}-\underbrace{2}_{(13,0,34)}\right)\tau\right.
$$

$$
\left.+\left(\underbrace{\omega}_{(14,0,34)}+\frac{\overbrace{\omega}^{}}{\underbrace{2}_{(21,0)}}\right)\tau+-\frac{\overbrace{\psi}^{}}{\underbrace{2}_{(21,0)}}\right]+O\left(\varepsilon^2\right) \tag{8.6}
$$

In order to generate Eq. (8.6) an appropriate form of the method of multiple scales for this problem is run automatically by the solver so that every symbolic and numerical computation can be picked up and recorded by the term-tracker, running in parallel, to generate a completely encoded approximate solution in the time domain, supplemented by the modulation equations from which amplitudes and phases can be obtained. The time domain solution for a first order multiple scales expansion with encoding is given in Eq. (8.6). The as-generated encoding data is clearly quite unwieldy in form but it can still be used to identify the sources of each term, and to make a connection back to the physical conceptualisation of the problem. The specific meaning of the encoding information is directly dependent on the solution procedure and the way that has been introduced mathematically. The complexity of the SEEM generated encodings invariably increases significantly as the problem solution develops. The cancellation of parameters with the solution procedure that would naturally take place in an efficient and elegant algebraic process is deliberately avoided in SEEM, unless both the quantity and the first two encoding digits are identical. The small parameters that are introduced at different points early in a multiple scales perturbation analysis do not necessarily have the same numerical value, and the encoding reflects this. However the reverse may be true where different instances of the small parameter end up being encoded differently (because of their historical treatment) but where in fact these are the same small parameter numerically. SEEM accommodates all such possibilities in all the necessary contexts. The programming strategy for a generic SEEM analysis is given in full in [14] and summarised in [15], and is based on 28 different algorithms which have been created and then coded in *Mathematica*™ in order to implement the solver/tracker.

8.2.2 *Visualisation*

There are two requirements for an SCD visualiser, these being the need to represent the complete form of information and also the practical requirement for this information to be immediately readable, understandable and assimilable. As there is a fundamental conflict between these requirements a series of pragmatic decisions ultimately led to the *visualisation graph* format of Fig. 8.2. This relates directly to Eqs. (8.1)–(8.5) and shows the user the equations in a layered sequential form together with the *link* between Eqs. (8.2) and (8.5), via encoding (2,0,5). The software has since been configured to allow selective viewing of the analysis with zoom and converge features providing concentrated visualisation of the finest detail, together with controllable zoom-out for the bigger picture. Automated colour and line thickness features have been included to differentiate between links based on information flows based on different perturbation order and systematic definitions of term complexity. A statistical package has also been devised to provide a *strength factor* metric visualised in the form of shaded circles of different diameter. This allows comparisons to be made between the relative importance of terms within the same equation and also with terms as they relate to other terms in other equations, travelling forwards or backwards through the analysis. This is shown in Fig. 8.3.

The visualisations of Figs. 8.2 and 8.3 are based on a sequential hierarchy, in which the analysis proceeds graphically from top right to bottom left, however Fig. 8.4 shows an example from one highly promising avenue of research in which the sequential constraint is dropped in favour of an alternative algorithm which presents the problem three dimensionally and emphasises the *interconnectedness* as a dominant feature. This visualisation could be more useful than the sequential approach, when combined with the strength factor metric and full three dimensional positioning and automated rotation about a user specifiable axis. The left hand image in Fig. 8.4 is a plan view of the interconnectedness visualisation showing two distinct regions, which relate to the two parts of the analysis of a 2 DoF autoparametric oscillator (physically representing a pair of coupled beams).

Most of the analysis connected with the primary beam is in and around the upper left area and conversely for the secondary beam in the lower right area. The right hand

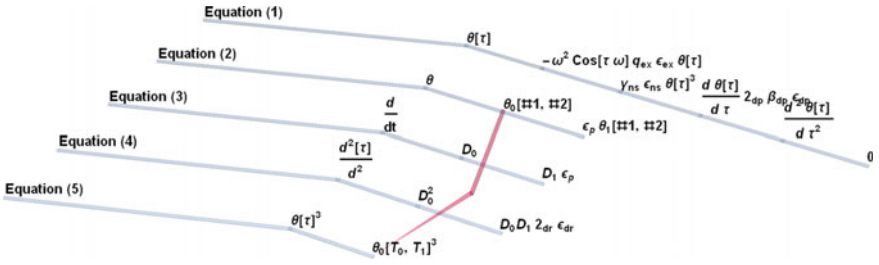

Fig. 8.2 Visualisation graph for the first five equations of the parametrically excited pendulum example (refer to Eqs. (8.1)–(8.5)) [14]

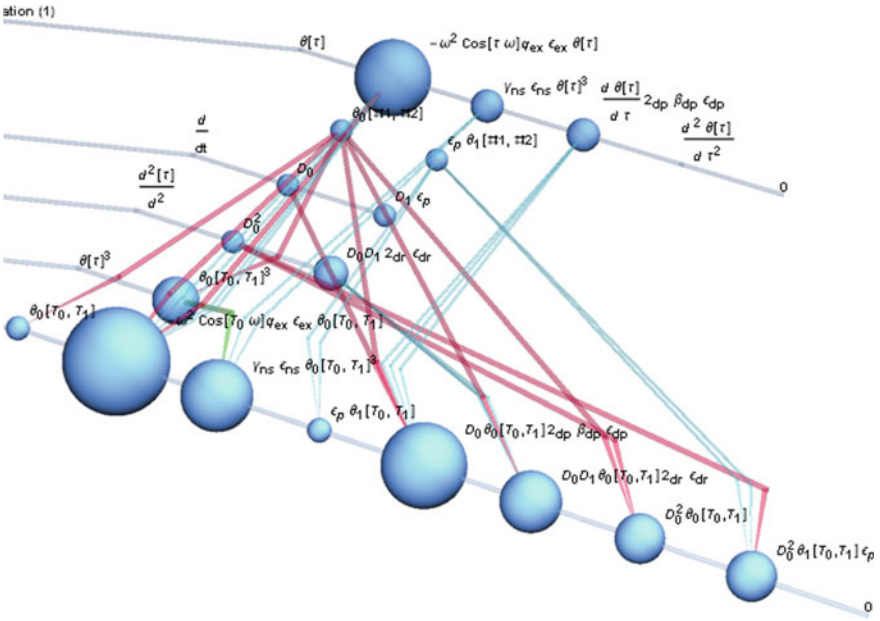

Fig. 8.3 An implementation of the strength factor metric in the early stages of the parametrically excited pendulum example [14]

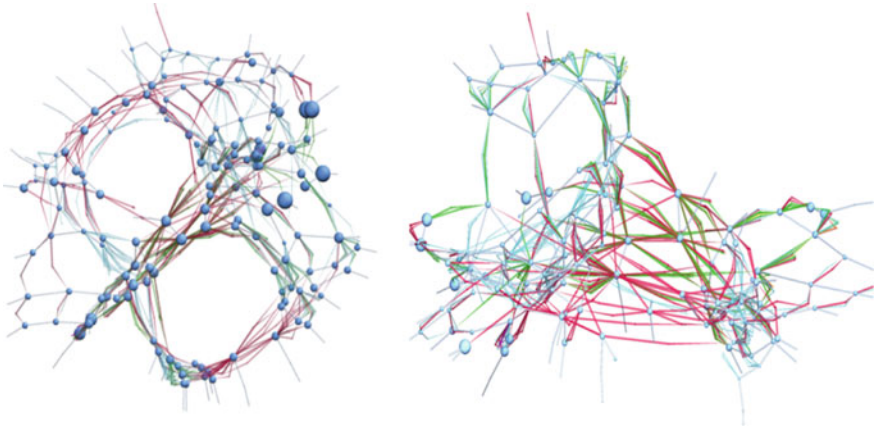

Fig. 8.4 Two images of typical SCD output for a 2 DoF autoparametric oscillator in two different elevations [14]

image shows the same graphic when rotated into a side elevation (noting that these definitions of elevation do not relate in any obvious way to any physical aspects of the problem, they are simply convenient terms for distinguishing between the views shown). Closer investigation of the two images reveals a cylindrical structure emerging for each physical part of the problem.

8.3 Conclusions

This research has taken place over a long period and has led to a series of computational strategies which can generate user graphics for the dynamics. The rules of interpretation are evolving and have not been stated here in detail. The work confirms that the fundamental mathematical model contains a richness of information that is normally not seen, and if this is converted into an explicit form it can be used to provide a supplement to the conventional symbolic and/or numerical solution to the problem. This could offer insights into interrelationships within the mathematical and physical representations of the system, provided the graphics can be interpreted meaningfully and quickly. These remaining challenges of user interpretation are currently under intensive study.

Acknowledgements The authors wish to acknowledge the pioneering research of Professor Richard H. Rand of Cornell University and his colleagues, also the support of Engineering and Physical Sciences Research Council grants EP/C530446/1, GR/N32334/02, GR/N32334/01, GR/N32280/01, GR/L30749/02, and GR/L30749/01, and the support made available to Motazedi by the University of Sheffield.

References

1. Rand, R.H.: Computer Algebra in Applied Mathematics: An Introduction to MACSYMA, Research Notes in Mathematics, vol. 94, p. 181. Pitman Publishing Inc. (1984)
2. Rand, R.H., Keith, W.L.: Normal forms and center manifold calculations on MACSYMA. In: Pavelle, R. (eds.) Applications of Computer Algebra, pp. 309–328. Kluwer Academic Publishers (1985)
3. Rand, R.H., Armbruster, D.: Perturbation Methods, Bifurcation Theory and Computer Algebra, Applied Math Sciences, vol. 65, p. 243. Springer, Berlin (1987)
4. Rand, R.H.: Topics in Nonlinear Dynamics with Computer Algebra, p. 229. Gordon and Breach (1994)
5. Rand, R.H.: Lecture Notes in Nonlinear Vibrations. Published online via http://ecommons.library.cornell.edu/handle/1813/28989 (2012)
6. Cartmell, M.P.: Combination instabilities and nonlinear vibratory interactions in beam systems. Ph.D. thesis, University of Edinburgh (1984)
7. Khanin, R., Cartmell, M.P., Gilbert, A.: Applying the perturbation method of multiple scales. Math. Educ. Res. **8**(2), 19–26 (1999)
8. Khanin, R., Cartmell, M.P.: A computerised implementation of the multiple scales perturbation method using *Mathematica*. Comput. Struct. **76**, 565–575 (2000)

9. Khanin, R., Cartmell, M.P.: Parallelisation of perturbation analysis: application to large-scale engineering problems. J. Symb. Comput. **31**, 461–473 (2001)
10. Cartmell, M.P., Ziegler, S.W., Khanin, R., Forehand, D.I.M.: Multiple scales analyses of the dynamics of weakly nonlinear mechanical systems. Trans. ASME Appl. Mech. Rev. **56**(5), 455–492 (2003)
11. Forehand, D.I.M., Khanin, R., Cartmell, M.P.: A Lagrangian multibody code for deriving the symbolic state-space equations of motion for open-loop systems containing flexible beams. Math. Comput. Simul. **67**(1/2), 85–98 (2004)
12. Forehand, D.I.M., Cartmell, M.P., Khanin, R.: Initial development towards an integrated fully symbolic-analytical multibody code. Int. J. Mech. Eng. Educ. **33**(2), 149–176 (2005)
13. Forehand, D.I.M., Cartmell, M.P.: The implementation of an automated method for solution term-tracking as a basis for symbolic computational dynamics. Proc. Inst. Mech. Eng. Part C J. Mech. Eng. Sci. **225**(1), 40–49 (2011)
14. Motazedi, N.: The development of solvers for symbolic computational dynamics. Ph.D. thesis, University of Sheffield (2017)
15. Motazedi, N., Cartmell, M.P., Rongong, J.A.: Extending the functionality of a symbolic computational dynamics solver by using a novel term-tracking method. Proc. Inst. Mech. Eng. Part C J. Mech. Eng. Sci. (2017) https://doi.org/10.1177/0954406217737104

Chapter 9
Theorem and Observation About the Nature of Perpetual Points in Conservative Mechanical Systems

Fotios Georgiades

Abstract Perpetual points have been defined recently and they have been associated with hidden attractors. The significance of these points for the dynamics of a system is ongoing research. Herein, a theorem is presented, describing the nature of the perpetual points in linear natural conservative mechanical systems and as it is shown they are defining the rigid body motions and vice versa. Subsequently, the perpetual points of two conservative nonlinear mechanical systems are determined. The first one is a two degrees of freedom nonlinear natural mechanical system and, as it is shown there are two sets of perpetual points which are associated with the rigid body motions. The other system is a non-natural conservative system, a flexible spinning shaft with non-constant rotating speed and, as it is shown, there are also three sets of perpetual points, and all of them are associated with the rigid body motions. In all examined nonlinear systems, the same observation made, that the perpetual points are associated with the rigid body motions, but formal proofs with the associated conditions as future work should be considered to generalise this observation. This work is essential to understand the nature of perpetual points in mechanical systems and opens new horizons for new operational modes and new design processes, targeting the ultimate operational modes of many mechanical systems which are the rigid body motions without having any vibrations.

Keywords Perpetual points · Rigid-body motion · Theorem for perpetual points

9.1 Introduction

In [1], the notion of perpetual points (PPs) is defined, as special points for the dynamics of a system, by setting accelerations and jerks as zero (like fixed points), restricted to cases of non-zero set of velocities. Initially, in [1] it was suggested, that the PPs can be used as indicators for dissipative dynamical systems, but in [2] with counterex-

F. Georgiades (✉)
School of Engineering, University of Lincoln, Lincoln, UK
e-mail: fgeorgiadis@lincoln.ac.uk

I. Kovacic and S. Lenci (eds.), *IUTAM Symposium on Exploiting Nonlinear Dynamics for Engineering Systems*, IUTAM Bookseries 37,
https://doi.org/10.1007/978-3-030-23692-2_9

amples it was showed that this is not the case. In [3], the experimental investigation of the PPs in a pendulum has been done. The general trend nowadays is to develop methods for identification of hidden attractors in dynamical systems, and the definition of the PPs is one of them [4]. The significance of the PPs in the dynamic analysis of systems is still under investigation [1–4].

In this work, a theorem about the nature of PPs in linear natural mechanical systems is presented and then the PPs in two nonlinear mechanical systems are determined. The first nonlinear system is a two degree of freedom (DOF) system of coupled oscillators with linear and nonlinear springs. The second nonlinear system is a conservative non-natural mechanical system, by means of a mechanical system with gyroscopic effects. It is a flexible spinning shaft with non-constant rotating speed. Finally, in the numerical section, the theoretical findings for both nonlinear mechanical systems are validated by examining the responses.

9.2 Theorem About Perpetual Points in Linear Mechanical Systems

On this section, a theorem about PPs in linear conservative natural mechanical systems is presented. In linear mechanical systems, in case that the stiffness matrix is positive semidefinite, then there is a rigid body mode with mode shape the rigid body motions (not unique) which correspond to a nondeformable configuration of the flexible parts [5]. Therefore, in rigid body motions, all the moving parts have the same values of positions and velocities.

Theorem *The perpetual points in linear conservative natural mechanical systems are defined by the rigid body motions and the inverse.*

Direct proof;

The equations of motion of a linear conservative natural mechanical system are given by [5],

$$[M_{ns}]\{\ddot{x}\} + [K]\{x\} = 0, \tag{9.1}$$

whereas, in general the stiffness matrix (K) it can be positive semi-definite and the mass matrix (M_{ns}) for natural systems it can be only positive definite [5], therefore,

$$[M_{ns}]\{\ddot{x}\} = 0 \Leftrightarrow \{\ddot{x}\} = 0. \tag{9.2}$$

In PPs from Eqs. (9.1) and (9.2) arise,

$$[K]\{x\} = 0, \tag{9.3}$$

which is true in case of a semi-definite stiffness matrix.

The equations of jerks arise by differentiation of Eq. (9.1) and they are given by,

$$[M_{ns}]\{\dddot{x}\} + [K]\{\dot{x}\} = 0. \tag{9.4}$$

Similarly, since the mass matrix is positive definite then,

$$[M_{ns}]\{\ddot{x}\} = 0 \Leftrightarrow \{\ddot{x}\} = 0, \tag{9.5}$$

Therefore, in PPs,

$$[K]\{\dot{x}\} = 0, \tag{9.6}$$

with non-zero solutions in velocities only in the case of positive semi-definite stiffness matrix that is associated with the rigid body motions. Therefore, the three conditions in defining PPs; (i) zero accelerations, (ii) zero jerks, (iii) nonzero set of velocities, are leading to rigid body motions.

Inverse proof;

Starting from Eq. (9.1) and considering that in the case of rigid body motions the 2nd term is eliminated (due to Eq. 9.3) and this leads to Eq. (9.2). Then, considering Eq. (9.4) and, taking into account that in rigid body motions the 2nd term is eliminated (due to Eq. 9.6), and this leads to Eq. (9.5). Therefore, the rigid body motions define PPs.

Example 1 A two DOF linear system is considered. The configuration is shown in Fig. 9.1a (as an example a car connected with a trailer through a flexible connector) with masses m_1, m_2, stiffness of coupling spring k and, equations of motion and jerks, given by,

$$m_1\ddot{x}_1 = -k(x_1 - x_2) \Leftrightarrow m_1\dddot{x}_1 = -k(\dot{x}_1 - \dot{x}_2), \tag{9.7a-b}$$

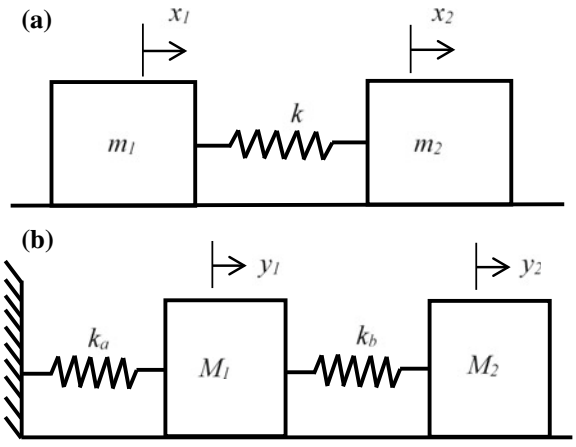

Fig. 9.1 Configurations of linear natural conservative mechanical systems: **a** Example 1, **b** Example 2

$$m_2\ddot{x}_2 = -k(x_2 - x_1) \Leftrightarrow m_2\dddot{x}_2 = -k(\dot{x}_2 - \dot{x}_1), \tag{9.7c-d}$$

which is clear that the PPs are $x_{1,p} = x_{2,p}$ and $\dot{x}_{1,p} = \dot{x}_{2,p}$ (all over the article the index p indicates the PPs) and, corresponds to the rigid body motions.

Example 2 A second two DOF linear system is considered. The configuration is shown in Fig. 9.1b, with masses M_1, M_2, stiffnesses of coupling springs k_a, k_b and, the equations of motion and jerks are given by,

$$M_1\ddot{y}_1 = -k_a y_1 - k_b(y_1 - y_2) = 0 \Leftrightarrow M_1\dddot{y}_1 = -k_a\dot{y}_1 - k_b(\dot{y}_1 - \dot{y}_2), \tag{9.8a-b}$$

$$M_2\ddot{y}_2 = -k_b(y_2 - y_1) \Leftrightarrow M_2\dddot{y}_2 = -k_b(\dot{y}_2 - \dot{y}_1), \tag{9.8c-d}$$

which, lead to positions $y_{1,p} = y_{2,p} = 0$ and velocities $\dot{y}_{1,p} = \dot{y}_{2,p} = 0$. In this example, there are no PPs since all velocities are zero, and, there are no rigid body motions too.

Therefore, the PPs are existing even in very simple conservative mechanical dynamical systems such as linear oscillators and, they are associated with manifolds, that are not necessarily hidden attractors, such as the rigid body motion.

9.3 Case Study About Perpetual Points of a Nonlinear Natural Mechanical System

In this section, a conservative natural nonlinear mechanical system of 2 DOF is considered. The two masses (m_x, m_y) are coupled together with a linear (k_1) and a nonlinear spring (k_2) as shown in Fig. 9.2. As an example, it could be a car connected with a trailer through a flexible connector that exhibits stiffness nonlinearities. The equations of motion are given by,

$$m_x\ddot{x} = -k_1(x - y) - k_2(x - y)^3 = -(x - y)\left(k_1 + k_2(x - y)^2\right), \tag{9.9a}$$

$$m_y\ddot{y} = k_1(x - y) + k_2(x - y)^3 = (x - y)\left(k_1 + k_2(x - y)^2\right). \tag{9.9b}$$

The associated equations of the jerks are given by,

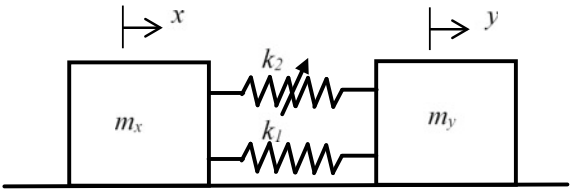

Fig. 9.2 Configuration of the nonlinear natural mechanical system

$$m_x \dddot{x} = -(\dot{x} - \dot{y})\left(k_1 + 3k_2(x - y)^2\right), \tag{9.9c}$$

$$m_y \dddot{y} = (\dot{x} - \dot{y})\left(k_1 + 3k_2(x - y)^2\right). \tag{9.9d}$$

The PPs on this system can be determined, by setting the accelerations and the jerks equal to zero, which leads to

(1) $x_p = y_p$ and for $\dot{x}_p = \dot{y}_p \neq 0$,
(2) $x_p = \sqrt{-k_1/k_2} + y_p$ (only in case that $k_2 < 0$, by means of softening nonlinear effects) and for $\dot{x}_p = \dot{y}_p \neq 0$.

Both sets are valid for any values of position and nonzero velocities. The 1st PP is clearly associated with the rigid body motions of the system. Although, it is not obvious also the 2nd PP is associated with rigid body motion, since the two masses are moving together with a constant distance and this is becoming more obvious in the numerical section of this article. An additional observation based on the condition of the existence of the second PP is a qualitative difference of softening and hardening nonlinear effects.

9.4 Case Study About Perpetual Points of a Nonlinear Non-natural Conservative Mechanical System

In this section, a non-natural conservative mechanical system is considered, a spinning shaft with non-constant rotating speed.

In [6], the modal equations of a spinning shaft with non-constant rotating speed (neglecting any non-conservative loads) have been derived. The configuration is shown in Fig. 9.3, whereas the generalized coordinates; rigid body angular position (θ), rigid body angular velocity ($\dot{\theta}$), the modal displacements (q_v, q_w in lateral bending and q_φ in torsion) of the considered system, including their associated deformations (v, w, φ), are indicated. The equations of motion are given by,

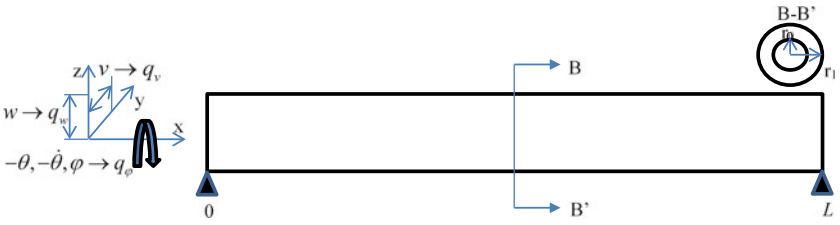

Fig. 9.3 Configuration and generalized coordinates of the spinning shaft

$$\begin{bmatrix} M_\theta & q_w & -q_v & -2F \\ q_w & (1-M) & 0 & 0 \\ -q_v & 0 & (1-M) & 0 \\ -F & 0 & 0 & 1 \end{bmatrix} \begin{Bmatrix} \ddot{\theta} \\ \ddot{q}_v \\ \ddot{q}_w \\ \ddot{q}_\varphi \end{Bmatrix}$$

$$= [M_{tot}] \begin{Bmatrix} \ddot{\theta} \\ \ddot{q}_v \\ \ddot{q}_w \\ \ddot{q}_\varphi \end{Bmatrix} = \begin{Bmatrix} -2\dot{\theta}\dot{q}_v q_v - 2\dot{\theta}\dot{q}_w q_w - 4\dot{\theta}\dot{q}_\varphi q_\varphi \\ \left[\dot{\theta}^2 - \omega_b^2(1-M)\right] q_v - 2\dot{\theta}\dot{q}_w \\ \left[\dot{\theta}^2 - \omega_b^2(1-M)\right] q_w + 2\dot{\theta}\dot{q}_v \\ \left(\dot{\theta}^2 - \omega_T^2\right) q_\varphi \end{Bmatrix} = \begin{Bmatrix} h_1 \\ h_2 \\ h_3 \\ h_4 \end{Bmatrix}, \tag{9.10}$$

with $M_\theta = 2IL + q_v^2 + q_w^2 + 2q_\varphi^2$. Also, $M = -\frac{I_1 \pi^2}{mL^2}$, $F = \frac{2}{\pi}\sqrt{2I_1 L}$, $I_1 = \pi\rho\left(\frac{D_o^4 - D_i^4}{64}\right)$, $m = \pi\rho\left(\frac{D_o^2 - D_i^2}{4}\right)$, with D_o and D_i the external and internal diameters, ρ the density of the shaft and also E, G are the Young's and shear modulus respectively. Also, $\omega_b = \sqrt{\frac{\pi^4 EI}{L^2\pi^2 I_1 + L^4 m}}$ and, $\omega_T = \frac{\pi}{2L}\sqrt{\frac{GI}{I_1}}$ [6].

The mode shapes are given by [6],

$$y_k(x) = \sqrt{\frac{2}{mL}} sin\left(\frac{k\pi}{L}x\right), \tag{9.11a}$$

$$Y_k(x) = \sqrt{\frac{2}{I_1 L}} sin\left(\frac{(2k-1)\pi}{2L}x\right). \tag{9.11b}$$

The deformations are given by [6],

$$v(x,t) = y_1(x) q_v(t), \tag{9.12a}$$

$$w(x,t) = y_1(x) q_w(t), \tag{9.12b}$$

$$\varphi(x,t) = Y_1(x) q_\varphi(t), \tag{9.12c}$$

whereas the first two correspond to lateral bending motions and the last one in torsion (Fig. 9.3).

The equations of jerks can be derived with differentiation of (Eq. 9.10),

$$\left[\dot{M}_{tot}\right] \begin{Bmatrix} \ddot{\theta} \\ \ddot{q}_v \\ \ddot{q}_w \\ \ddot{q}_\varphi \end{Bmatrix} + [M_{tot}] \begin{Bmatrix} \dddot{\theta} \\ \dddot{q}_v \\ \dddot{q}_w \\ \dddot{q}_\varphi \end{Bmatrix} = \begin{Bmatrix} \dot{h}_1 \\ \dot{h}_2 \\ \dot{h}_3 \\ \dot{h}_4 \end{Bmatrix} = \begin{Bmatrix} G_1 \\ G_2 \\ G_3 \\ G_4 \end{Bmatrix}$$

$$\Leftrightarrow \begin{Bmatrix} \dddot{\theta}_p \\ \dddot{q}_{v,p} \\ \dddot{q}_{w,p} \\ \dddot{q}_{\varphi,p} \end{Bmatrix} = [M_{tot,p}]^{-1} \begin{Bmatrix} G_{1,p} \\ G_{2,p} \\ G_{3,p} \\ G_{4,p} \end{Bmatrix} = [M_{tot,p}]^{-1} \begin{Bmatrix} -2\dot{\theta}_p \dot{q}_{v,p}^2 - 2\dot{\theta}_p \dot{q}_{w,p}^2 - 4\dot{\theta}_p \dot{q}_{\varphi,p}^2 \\ \left[\dot{\theta}_p^2 - \omega_b^2(1-M)\right] \dot{q}_{v,p} \\ \left[\dot{\theta}_p^2 - \omega_b^2(1-M)\right] \dot{q}_{w,p} \\ \left(\dot{\theta}_p^2 - \omega_T^2\right) \dot{q}_{\varphi,p} \end{Bmatrix}, \tag{9.13}$$

whereas, the right hand-side has been derived considering that in PPs the accelerations are zero (to avoid confusion the index p is used in all associated components). The inverse of the mass matrix ($[M_{tot}]^{-1}$), always exist and as it is shown in [7], it is given by,

$$[M_{tot}]^{-1} = \frac{1}{\delta}\begin{bmatrix} (1-M) & -q_w & q_v & 2(1-M)F \\ -q_w & M_\theta - \frac{q_v^2}{(1-M)} - 2F^2 & -\frac{q_v q_w}{(1-M)} & -2Fq_w \\ q_v & -\frac{q_v q_w}{(1-M)} & M_\theta - \frac{q_w^2}{(1-M)} - 2F^2 & 2Fq_v \\ F(1-M) & -Fq_w & Fq_v & (1-M)M_\theta - q_v^2 - q_w^2 \end{bmatrix}, \tag{9.14}$$

with,

$$\delta = 2(1-M)\big(I_1 L - F^2\big) - Mq_v^2 - Mq_w^2 + 2(1-M)q_\phi^2 > 0, \tag{9.15}$$

as shown in [7].

To find the PPs, the equations of the jerks (Eq. 9.13) are set to zero and lead to the following algebraic system:

$$(1-M)G_{1,p} - q_{w,p}G_{2,p} + q_{v,p}G_{3,p} + 2(1-M)FG_{4,p} = 0, \tag{9.16a}$$

$$-q_{w,p}G_{1,p} + \left(2\big(I_1 L - F^2\big) - \frac{Mq_{v,p}^2}{(1-M)} + q_{w,p}^2 + 2q_{\phi,p}^2\right)G_{2,p} - \left(\frac{q_{v,p}q_{w,p}}{(1-M)}\right)G_{3,p} - 2Fq_{w,p}G_{4,p} = 0, \tag{9.16b}$$

$$q_{v,p}G_{1,p} - \left(\frac{q_{v,p}q_{w,p}}{(1-M_1)}\right)G_{2,p} + \left(2\big(I_1 L - F^2\big) - \frac{Mq_{w,p}^2}{(1-M)} + q_{v,p}^2 + 2q_{\phi,p}^2\right)G_{3,p} + 2Fq_{v,p}G_{4,p} = 0, \tag{9.16c}$$

$$F(1-M)G_{1,p} - Fq_{w,p}G_{2,p} + Fq_{v,p}G_{3,p} + \big(2(1-M)I_1 L - Mq_{v,p}^2 - Mq_{w,p}^2 + 2(1-M)q_{\phi,p}^2\big)G_{4,p} = 0. \tag{9.16d}$$

The multiplication of Eq. (9.16a) with F and using it in Eq. (9.16d), it emerges that,

$$\big\{2(1-M)\big(I_1 L - F^2\big) - Mq_{v,p}^2 - Mq_{w,p}^2 + 2(1-M)q_{\phi,p}^2\big\}G_{4,p} = 0 \Leftrightarrow \delta G_{4,p} = 0, \tag{9.17}$$

and using Eqs. (9.13) and (9.15) this is true when,

$$\dot{\theta}_p^2 = \omega_T^2 \quad \text{or,} \quad \dot{q}_{\phi,p} = 0. \tag{9.18a-b}$$

Then, using Eq. (9.17) in Eq. (9.16a) arise that,

$$G_{1,p} = \frac{q_{w,p}}{(1-M)} G_{2,p} - \frac{q_{v,p}}{(1-M)} G_{3,p}, \tag{9.19}$$

which can be used in Eq. (9.16b) and after some manipulations lead to,

$$\left(2\left(I_1 L - F^2\right) - \frac{M q_{v,p}^2}{(1-M)} - \frac{M q_{w,p}^2}{(1-M)} + 2q_{\phi,p}^2\right) G_{2,p} = 0 \Leftrightarrow \frac{\delta}{(1-M)} G_{2,p} = 0, \tag{9.20}$$

and using Eqs. (9.13) and (9.15), this is true (Eq. 9.20) when,

$$\dot{\theta}_p^2 = \omega_b^2 (1-M) \text{ or } , \dot{q}_{v,p} = 0. \tag{9.21a-b}$$

Similarly, using Eq. (9.19) in Eq. (9.16c) and after some manipulations one gets,

$$\left(2\left(I_1 L - F^2\right) - \frac{M q_{w,p}^2}{(1-M)} - \frac{M q_{v,p}^2}{(1-M)} + 2q_{\phi,p}^2\right) G_{3,p} = 0 \Leftrightarrow \frac{\delta}{(1-M)} G_{3,p} = 0, \tag{9.22}$$

considering Eqs. (9.13), (9.15) in Eq. (9.22) lead to,

$$\dot{\theta}_p^2 = \omega_b^2 (1-M) \text{ or } , \dot{q}_{w,p} = 0. \tag{9.23a-b}$$

Setting the accelerations (Eq. 9.12) equal to zero, the following system of algebraic equations is arising:

$$(1-M)h_1 - q_w h_2 + q_v h_3 + 2(1-M)F h_4 = 0, \tag{9.24a}$$

$$\begin{aligned} &- q_w h_1 + \left(2\left(I_1 L - F^2\right) - \frac{M q_v^2}{(1-M)} + q_w^2 + 2q_\phi^2\right) h_2 \\ &- \left(\frac{q_v q_w}{(1-M)}\right) h_3 - 2F q_w h_4 = 0, \end{aligned} \tag{9.24b}$$

$$\begin{aligned} &q_v h_1 - \left(\frac{q_v q_w}{(1-M_1)}\right) h_2 + \left(2\left(I_1 L - F^2\right) - \frac{M q_w^2}{(1-M)} + q_v^2 + 2q_\phi^2\right) h_3 \\ &+ 2F q_v h_4 = 0, \end{aligned} \tag{9.24c}$$

$$\begin{aligned} &F(1-M)h_1 - F q_w h_2 + F q_v h_3 \\ &+ \left(2(1-M)I_1 L - M q_v^2 - M q_w^2 + 2(1-M)q_\phi^2\right) h_4 = 0. \end{aligned} \tag{9.24d}$$

Multiplication of Eq. (9.24a) with F and replacement in Eq. (9.24d) lead to,

$$\left\{2(1-M)\left(I_1 L - F^2\right) - Mq_v^2 - Mq_w^2 + 2(1-M)q_\phi^2\right\}h_4 = 0 \Leftrightarrow \delta h_4 = 0, \tag{9.25}$$

after considering Eqs. (9.10), (9.13) then (Eq. 9.25) is true when,

$$\dot{\theta}_p^2 = \omega_T^2 \text{ or, } q_{\varphi,p} = 0, \tag{9.26a-b}$$

then using Eq. (9.25) in Eq. (9.24a), emerges that,

$$h_1 = \frac{q_w}{(1-M)}h_2 - \frac{q_v}{(1-M)}h_3, \tag{9.27}$$

then using Eq. (9.27) in Eq. (9.24b) and after some manipulations arise that,

$$\left(2\left(I_1 L - F^2\right) - \frac{Mq_v^2}{(1-M)} - \frac{Mq_w^2}{(1-M)} + 2q_\phi^2\right)h_2 = 0 \Leftrightarrow \frac{\delta}{(1-M)}h_2 = 0, \tag{9.28}$$

whereas considering Eqs. (9.10), (9.13) and (9.23) lead to,

$$\dot{\theta}_p^2 = \omega_b^2(1-M) \text{ with } \dot{q}_{w,p} = 0 \text{ or } q_{v,p} = 0 \text{ with } \dot{\theta}_p^2 \neq \omega_b^2(1-M). \tag{9.29a-d}$$

Then using Eq. (9.27) in Eq. (9.24c) and after some manipulations, emerges that,

$$\left(2\left(I_1 L - F^2\right) - \frac{Mq_w^2}{(1-M)} - \frac{Mq_v^2}{(1-M)} + 2q_\phi^2\right)h_3 = 0 \Leftrightarrow \frac{\delta}{(1-M)}h_3 = 0, \tag{9.30}$$

and considering Eqs. (9.10), (9.13) and (9.21) lead to,

$$\dot{\theta}_p^2 = \omega_b^2(1-M) \text{ with } \dot{q}_{v,p} = 0 \text{ or } q_{w,p} = 0 \text{ with } \dot{\theta}_p^2 \neq \omega_b^2(1-M). \tag{9.31a-d}$$

Considering Eqs. (9.28) and (9.30) in Eq. (9.27), lead to,

$$h_1 = 0 \Leftrightarrow -2\dot{\theta}\dot{q}_v q_v - 2\dot{\theta}\dot{q}_w q_w - 4\dot{\theta}\dot{q}_\varphi q_\varphi = 0, \tag{9.32}$$

which is always true, since all the modal velocities should be zero.

Also, whereas $\dot{\theta}_p^2 = \omega_T^2$ and considering Eq. (9.19) with Eqs. (9.21b) and (9.23b) it arises that,

$$G_{1,p} = 0 \Leftrightarrow \dot{q}_{\phi,p} = 0. \tag{9.33}$$

Summarizing the results of Eqs. (9.18a-b, 9.21a-b, 9.23a-b, 9.26a-b, 9.29a-d, 9.31a-d, 9.33) lead to the following three sets of PPs:

(1) $$q_{v,p,1} = q_{w,p,1} = q_{\varphi,p,1} = \dot{q}_{v,p,1} = \dot{q}_{w,p,1} = \dot{q}_{\varphi,p,1} = 0 \text{ and,}$$
$$\left(\theta_{p,1}, \dot{\theta}_{p,1}\right) \in S^1 \times \mathbb{R}, \tag{9.34a}$$

(2) $$q_{\varphi,p,2} = \dot{q}_{v,p,2} = \dot{q}_{w,p,2} = \dot{q}_{\varphi,p,2} = 0, \quad \dot{\theta}_{p,2} = \pm\omega_b\sqrt{1-M} \text{ and,}$$
$$\left(\theta_{p,2}, q_{v,p,2}, q_{w,p,2}\right) \in S^1 \times \mathbb{R}^2, \tag{9.34b}$$

(3) $$q_{v,p,3} = q_{w,p,3} = \dot{q}_{v,p,3} = \dot{q}_{w,p,3} = \dot{q}_{\varphi,p,3} = 0, \quad \dot{\theta}_{p,3} = \pm\omega_T \text{ and,}$$
$$\left(\theta_{p,3}, q_{\varphi,p,3}\right) \in S^1 \times \mathbb{R}. \tag{9.34c}$$

The only non-zero velocities are the rigid body angular velocities and, although it is not obvious, all the PPs are associated with the rigid body rotation of the shaft and this is evident with the plots in the numerical section. In [7], the rigid body motions of the shaft are determined, and they coincide with those defining the PPs in Eq. (9.34).

9.5 Numerical Results for Natural Mechanical System

On this section, a natural mechanical system is considered and using direct numerical integration of the set (Eq. 9.8a-b) the responses are determined. In this section, the following mass values $m_x = m_y = 1$ kg and stiffness values $k_1 = 1000$ N/m, $k_2 = -500$ N/m in (Eq. 9.8a-b) are used. Two sets of initial conditions (ICs) have being considered; (a) $x_p = y_p = 1$ m, $\dot{x}_p = \dot{y}_p = 1$ m/s which belongs to the 1st set of PPs and (b) $y_p = 1$ m, $\dot{x}_p = \dot{y}_p = 1$ m/s, $x_p = \sqrt{-k_1/k_2} + y_p = 2.4142$ m which belongs to the 2nd set of PPs. The choice of the ICs can be done arbitrarily since as it is shown they lead to rigid body motions and, in this particular case considering a car with a trailer they have sensible values (the defined parameters corresponds, to masses of the vehicles and, stiffnesses of the connections scaled by 1/1000 which can be done due to the form of the Eqs. 9.8a-b). Figure 9.4 depicts the responses arising from the 1st set of initial conditions and it is obvious that the two masses are moving together in a rigid body motion. Figure 9.5 is depicting the displacements using the 2nd set of initial conditions. Initially, the two masses are moving together with constant distance but after around the 5th second, the solution jumps (it seems that it is an unstable PP) to another non-periodic motion. After the 5th second, it seems that the two responses are comprised by the same periodic term in antiphase combined with the same linearly increasing amplitude, as indicated by the displacements depicted in Fig. 9.5a. Based on Figs. 9.4 and 9.5, both PPs on this system are associated with the rigid body motions.

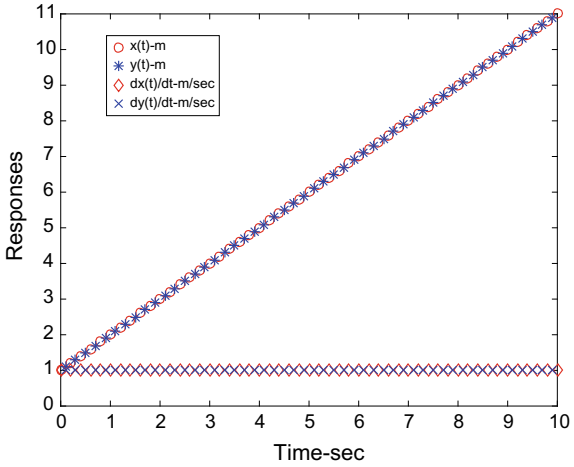

Fig. 9.4 Responses of the natural mechanical system associated with ICs belonging in 1st set of PPs

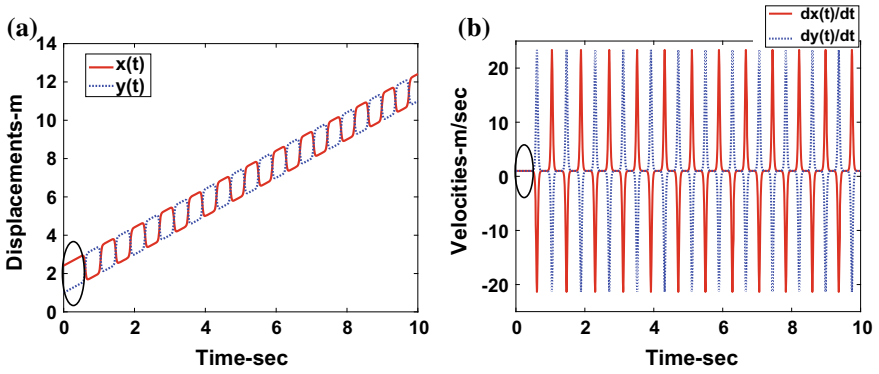

Fig. 9.5 Responses of the natural mechanical system associated with ICs belonging in 2nd set of PPs; **a** displacements, **b** velocities

9.6 Numerical Results for Non-natural Mechanical System

On this section, using direct numerical integration of Eq. (9.10) the responses of the non-natural mechanical system (spinning shaft) are determined. A 1-m length steel shaft with external and internal radii, $r_o = 0.03$ m $r_i = 0.028$ m, respectively, is considered. The material properties of the shaft are; density $\rho = 7850$ kg/m^3, Poisson's ratio $\nu = 0.3$, Young's and shear modulus, $E = 200$ GPa and $G = 76.9$ GPa, respectively.

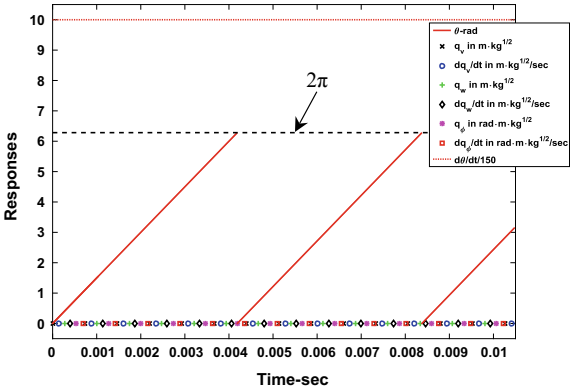

Fig. 9.6 Responses of the non-natural mechanical system, with ICs belonging in 1st set of PPs

Using the provided formulae, the rest parameters are; $M = -0.0042$, $\omega_b\sqrt{1-M} = 1022.165$ rad/s and, $\omega_T = 4916.411$ rad/s.

The following three sets of ICs (one for each set of PP) are considered:

(1) $\left(\theta_{p,1}, q_{v,p,1}, q_{w,p,1}, q_{\varphi,p,1}, \dot{\theta}_{p,1}, \dot{q}_{v,p,1}, \dot{q}_{w,p,1}, \dot{q}_{\varphi,p,1}\right) =$
$(0, 0, 0, 0, 1500, 0, 0, 0)$,

(2) $\left(\theta_{p,2}, q_{v,p,2}, q_{w,p,2}, q_{\varphi,p,2}, \dot{\theta}_{p,2}, \dot{q}_{v,p,2}, \dot{q}_{w,p,2}, \dot{q}_{\varphi,p,2}\right) =$
$(0, 15, 20, 0, 1022.165, 0, 0, 0)$,

(3) $\left(\theta_{p,3}, q_{v,p,3}, q_{w,p,3}, q_{\varphi,p,3}, \dot{\theta}_{p,3}, \dot{q}_{v,p,3}, \dot{q}_{w,p,3}, \dot{q}_{\varphi,p,3}\right) =$
$(0, 0, 0, 10, 4916.411, 0, 0, 0)$.

Rearranging (Eq. 9.12) and using (Eq. 9.11) then the units for the modal displacements in lateral bending (q_v, q_w) are in $\mathrm{m}\sqrt{\mathrm{kg}}$, for the modal displacement in torsion (q_φ) is in $\mathrm{rad\,m}\sqrt{\mathrm{kg}}$, and also the units for rigid body angular position and velocity are in rad and rad/s respectively. Considering the proof in [7] that these sets of ICs correspond to rigid body motions, the initial conditions have been chosen arbitrarily large to have close values to 2π and also to become evident the difference with the zero values of the other displacements on the plots.

In Fig. 9.6 the responses associated with the 1st set of ICs are depicted which is obvious that the shaft is just spinning without any deformation. In Fig. 9.7 the responses associated with the 2nd set of ICs are depicted, and it is evident that the shaft is just spinning with nonzero but constant lateral bending deformation.

Figure 9.8 depicts the responses associated with the 3rd set of ICs, and the shaft is spinning with nonzero but constant torsional deformation in a rigid body motion. Therefore, all the sets of PPs of the spinning shaft are associated with the rigid body motions.

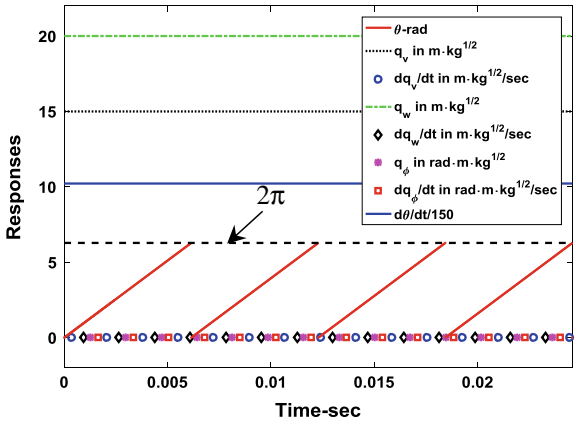

Fig. 9.7 Responses of the non-natural mechanical system with ICs belonging in 2nd set of PPs

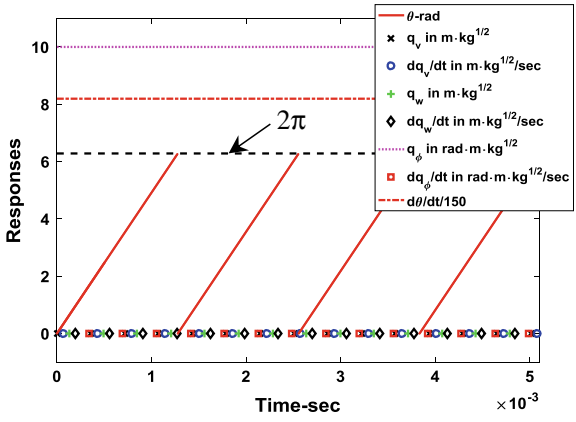

Fig. 9.8 Responses of the non-natural mechanical system with ICs belonging in 3rd set of PPs

9.7 Conclusions

In this article, the nature of perpetual points in several types of conservative mechanical systems is examined. A theorem about the nature of the perpetual points in linear natural mechanical systems is given, by means that the PPs are defined only by rigid body motions, and that the rigid body motions are defined by the PPs. Also, two cases of nonlinear mechanical systems; (a) a natural system and (b) a non-natural system, are examined, and in both systems, the same observation made, that the perpetual points are defined by the rigid body motions. This work gives insight into the nature of perpetual points in mechanical systems. The fact that the perpetual points are defined by the rigid body motions accompanied with the provided relevant formalism of PPs, open horizon for a new mechanical design for specific configurations of mechanical systems that lead to stable attracting perpetual points (the stability analysis of PPs has been developed in [1]), which eliminate vibrational motions that might be caused by perturbations. This is the ultimate operational mode for many

mechanical systems. Further work should be done in all these directions and, also, in deriving formal proofs (with the associated conditions) that the perpetual points are defined by the rigid body motions for more general cases e.g. non-natural linear, nonlinear etc. mechanical systems.

References

1. Prasad, A.: Existence of perpetual points in nonlinear dynamical systems and its applications. Int. J. Bifurc. Chaos **25**, 1530005 (2015)
2. Jafari, S., Nazaimehr, F., Sprott, J.C., Golpayegani, S.M.R.H.: Limitation of perpetual points for confirming conservation in dynamical systems. Int. J. Bifurc. Chaos **25**, 1550182 (2015)
3. Brzeski, P., Virgin, L.N.: Experimental Investigation of perpetual points in mechanical systems. Nonlinear Dyn. **90**, 2917–2928 (2017)
4. Dudkowski, D., Jafari, S., Kapitaniak, T., Kuznetsov, N.V., Leonov, G.A., Prasad, A.: Hidden attractors in dynamical systems. Phys. Rep. **637**, 1–50 (2016)
5. Meirovitch, L.: Fundamental of Vibrations. Waveland Press, Long Grove, IL (2001)
6. Georgiades, F.: Nonlinear dynamics of a spinning shaft with non-constant rotating speed. Nonlinear Dyn. **93**, 1–30 (2018)
7. Georgiades, F.: Equilibrium points with their associated normal modes describing nonlinear dynamics of a spinning shaft with non-constant rotating speed. J. Vib. Test. Syst. Dyn. **2**(4), 327–373 (2018)

Chapter 10
Energy Flow Considerations in Nonlinear Systems on the Basis of Interesting Experiments with Three Paradigmatic Physical Systems in Engineering

Ioannis T. Georgiou

Abstract Nonlinear dynamical systems host types of central dynamics-phenomena whose phase space dynamic structure allows potentially the appearance of motions underlined by irreversible energy flow among the physical system components or the perpendicular projections of the vector dynamics. Motions exhibiting irreversible energy flow are a very important feature, and their potential existence could be addressed by either a mathematical model or a physical one, both endowed with coexisting central phenomena to form the dynamics environment for irreversible energy flow. Here we present experimental evidence that indeed irreversible energy flow-motions are observed in physical laboratory nonlinear systems possessing by design either coexisting static equilibria or coexisting chaotic and regular attractors. The observation of irreversible energy flow-motions in physical paradigmatic systems forms a basis for targeted-and-effective nonlinear modification of flexible elastic continua for vibration isolation and energy harvesting by inserting nonlinearities to create irreversible energy flow. From the scientific point of view, advanced considerations of nonlinear systems at the levels of energy or power flow is fundamental and potentially paves, as the present work indicates, an avenue for systematic exploitations of nonlinearities in mechanical-structural-electrical engineering applications.

Keywords Irreversible energy flow · Multiple attractors · Reduced models · Multi-physics dynamics · Data-driven analysis · POD transform · Physical model-based studies · Slow-fast dynamics

I. T. Georgiou (✉)
School of Naval Architecture and Marine Engineering,
National Technical University of Athens, Athens, Greece
e-mail: georgiou@central.ntua.gr

School of Mechanical Engineering, Purdue University, West Lafayette, IN, USA

I. Kovacic and S. Lenci (eds.), *IUTAM Symposium on Exploiting Nonlinear Dynamics for Engineering Systems*, IUTAM Bookseries 37,
https://doi.org/10.1007/978-3-030-23692-2_10

10.1 Introduction

Smart exploitation of well-understood bifurcation-chaos phenomena in nonlinear dynamical systems [1, 2] can lead to innovations in broad scope engineering in reference to barriers-limitations inherent in linear and weakly nonlinear systems. For example, coexisting regular and chaotic attractors can be turned from harmful features into beneficial ones as manipulators of energy flow. Vibration isolation, noise reduction, energy harvesting, and sensing-actuation are some dynamical processes that can potentially be enhanced by introducing nonlinearities in a system or extending its operation in the intrinsic nonlinear regime. The simplest way, yet very fundamental in paving ways for a systematic study, to create *exploitable* nonlinear phenomena in linear or weakly nonlinear continuum mechanical structures is to augment a mother flexible structure properly by attaching bi-stable mechanical oscillators [3] and in general by attaching a multi-stable flexible continuum [4, 5]. Desirable nonlinear phenomena, for exploitation, are motions characterized by irreversibly energy transfer, in the time averaged sense [6]. For the motion to be exploitable, the energy flow feature should take place between the separate-and-interacting components of the system, or between the perpendicular resultants of the system coupled vector dynamics. The coexistence of multiple attractors can form topology features in phase space that allow paths supporting motions with irreversibility features in energy or power flow. In general, the creation of coexisting nonlinear central phenomena can be traced systematically by using the geometric concepts of global Slow and local transversal Fast Invariant Manifold (SIM, FIM). Being static equilibria for the local fast dynamics, the global SIM potentially undergoes many qualitative changes-since it admits, as a nonlinear geometric object, tangent bifurcations at folding points, leading to the creation of motion-paths taking the system from one steady state (attractor) to another one with irreversible energy flow dynamics [5, 6]. Coexisting multiple attractors means the coexistence of many low-dimensional stable-and-unstable invariant manifolds [1, 2]. Perhaps for the first time, an interesting energy irreversible-nonlinear phenomenon—was observed in numerical and experimental studies in a coupled structural-mechanical system composed of a cantilevered flexible beam modified with a planar pendulum [3], a classical bi-stable nonlinear oscillator. In this system, a forced motion where the beam vibrates at large amplitude and the pendulum at small amplitude transforms naturally into a motion where the beam vibrates at smaller amplitude whereas the pendulum settles into a vibration of considerably larger amplitude. *Clearly, energy had flown irreversibly from the flexible beam subsystem to the nonlinear pendulum one*. This phenomenon was formed because of the coexistence of multiple attractors in a bi-stable continuum-rigid system. This observation has attracted the attention of several researchers in nonlinear mechanics-dynamics as they have considered the basic problem which is the dynamic modification of a linear oscillator with a nonlinear one [7]. Herein presented is a physical model-based experimental study with subject three paradigmatic systems which are flexible continua modified dynamically to introduce nonlinear phenomena that disrupt the uniformity of the phase space flow structure of

the uncoupled continuum system. *The creation of hills, valleys and whirls dynamics structures in the phase space potentially creates a critical dynamics environment for the creation of motions characterized by irreversible energy transverse.* In particular, we explore whether a phase space flow topology, as formed by the presence of coexisting equilibria either pure static or steady state dynamic, allows the appearance of motions with irreversible energy flow between two coupled subsystems. The work is organized as follows: Sect. 3 presents a flexible continuum with multiple static equilibria introduced by boundary conditions. Section 4 presents a cantilevered beam modified by a highly degenerate oscillator, the eccentric rotor. And Sect. 5 presents a cantilevered flexible beam interacting over a finite area with a basic electromagnetic system. All systems are viewed as dynamic nonlinear modifications of a core flexible structure. The core structure is used as a reference in a physical-model approach study of the coupled system into which the core system is modified.

10.2 The Physical Model-Based Methodology and the POD Transform

The present study involves laboratory physical models. Thus, it is a pure experimental data-driven analysis. Distributed experimental acceleration data are turned into modal like features to enable analysis. Given a reliable vibration measuring system, well-designed physical models provide an efficient way to initially discover and then exploit nonlinear phenomena. On a basis of well-understood phenomena in bi-stable mechanical structural systems, the physical models studied here possess by design the necessary constituents to introduce coexisting phenomena as the means to create motions with desirable energy flow properties, such as irreversibility in the average sense. *These are the coexisting equilibria and coexisting chaotic and regular attractors. The existence of multiple attractors disrupts semantically the flow structure of a dynamical system since some of them have unstable invariant manifolds contained in a bounded region of the phase space.*

Regarding the availability of physical databases, we are using a state-of-the-art vibration measurement system to sample in high resolution the motions of flexible structures in space and time. The sensors are embedded in the system and thus we acquire natural, in local coordinates, measurements of the acceleration field. The acquired data sets are analyzed with advanced proper orthogonal decomposition (POD) tools to form a basis for analytics. The reader can consult reference [8] dealing with the POD transform of geometry consistent experimental measurements of acceleration in beam like structures viewed as Cosserat continua [9] to model geometrically exactly the coupled vector dynamics. The POD modal structure of the sampled motions is used as a basis to detect and quantify irreversible energy flow phenomena. Specifically, to compute the rate of irreversible energy flow, the dominant POD modal amplitude is transformed into RMS-per-cycle information, revealing how POD modal vibration decays as a function of sequential time frames,

their duration being equal to a natural period of oscillation. It turns out that a motion-induced irreversible energy flow has a completely differed *RMS-per-cycle character* than that of a naturally, irreversibly dissipated mechanical energy in the limit of weakly nonlinear continuum dynamics.

10.3 Dynamic Modification of a Continuum by Boundary Constraints

Figure 10.1 depicts a high strength steel beam constrained in such a way at its boundaries to effectively-and-naturally introduce multiple static equilibria, coexisting at specific values of the control parameter (distance of pin bearing locations). This basic technique of structural modification disrupts greatly the topology of the phase space flow of the reference structure, defined as the one possessing a single static equilibrium. The pinned-pinned boundary constraint controls the number of multiple static equilibria. Specifically, although three static equilibria are visible, many more could coexist, depending on the magnitude of compression imposed the axial boundary displacement constraint [10]. Because the system possesses many equilibrium states, it is easy to store strain energy in bending mode by applying slowly transverse forces or bending moments about the pin axes. This is an exploitable feature for vibration isolation and energy harvesting [11]. We hope that the modified phase space structure is allowing the appearance of motions with irreversible energy transfer from bending into axial stretching and lateral bending with shearing, *thus exploiting in full the three-dimensional flexibility of the structure*. Motivated by considerations and results in works [4, 5], the present multi-stable beam structure as well as the scope of the present study are quite different from the classical studies of the buckled beam-column under the action of a dead load [12]. The present study, thanks to the physical model approach, reveals how strong the coupling among three-dimensional dynamics is: In-plane bending, axial stretching accompanied by torsion and out-of-plane bending accompanied by shearing are nonlinearly coupled and thus quite interesting phenomena may take place.

The presence of multiple stable-and-unstable equilibrium states along with the pinned-pinned boundary conditions forms physics mechanisms allowing naturally the occurrence of transverse displacements of considerable magnitude by applying slowly transverse forces or moments about the pin bearing axes. The important fact is that both the transverse forces and the bending moments are of small magnitudes. This means that the multi-stable continuum can be used to store strain energy statically and dynamically in the bending mode of motion. This cannot happen to the same extent if the beam has a single static equilibrium. In view of the above fact, we concentrate our study in understanding the coupled dynamics initiated by static or dynamic initial bending. We performed a series of systematic experiments to investigate whether the interaction of near homoclinic motions with the multiple static equilibria causes vibrations with interesting properties, such as fast mechanical energy dissipation.

Fig. 10.1 A lab set-up of a thin beam constrained at the boundaries by pin bearing supports to introduce-and-control coexisting multiple equilibrium states. An array of sixteen sensors samples the transverse acceleration field in local coordinates for a POD-based modal analysis of the dynamics

These motions are created by displacing slowly one of the static equilibria to approach at nearly zero velocity the unstable equilibrium [11]. Figure 10.2 reveals that such an excited free motion possesses remarkable features: (1) It processes a quite broad POD energy spectrum in comparison to that of a beam with a single equilibrium; and (2) is decomposed into intrinsic *slow* and *fast* POD modal vibration patterns characterized by *ultra-fast decay*. The term intrinsic points to the stationary geometric features formed by the database when viewed as a geometric object, data cloud, sitting in the linear hyperspace of measurements [8].

The multi-stable continuum is very flexible in almost all possible modes of motion and thus we wonder whether the *ultra-fast decay* of bending vibration, Fig. 10.2, stems from interactions-in a multi-stable environment-of bending with axial stretching and lateral bending accompanied, among others. Figure 10.3 presents a measurement of the acceleration tri-axial orthogonal components at the middle point of the beam. We see that the coupled vibrations are of the same order and that besides the slow vibration present are fast vibrations in all orthogonal components of the motion. *It is clear that a certain physics mechanism triggers irreversible energy flow from slow bending vibration to coupled slow and fast vibrations in axial stretching and lateral bending*. This interaction triggers irreversible flow of mechanical energy, initially stored mainly as bending strain energy in low frequencies, into higher frequencies of bending; and low and high frequencies motions in the axial and lateral directions. The irreversible energy flow from the slow invariant manifold (SIM) to slow and fast coupled vibrations manifests itself as an *ultra-fast decay* of the transverse acceleration component as well as in the two coupled orthogonal components [11], as Fig. 10.3 reveals. In the presence of multiple static equilibria, strong interactions among the components of the coupled transverse-axial-lateral vibrations are possible mainly due to the fact that the axial stretching interacts with the hills and valleys of the elastic strain potential. In creating near homoclinic motions, the strain energy

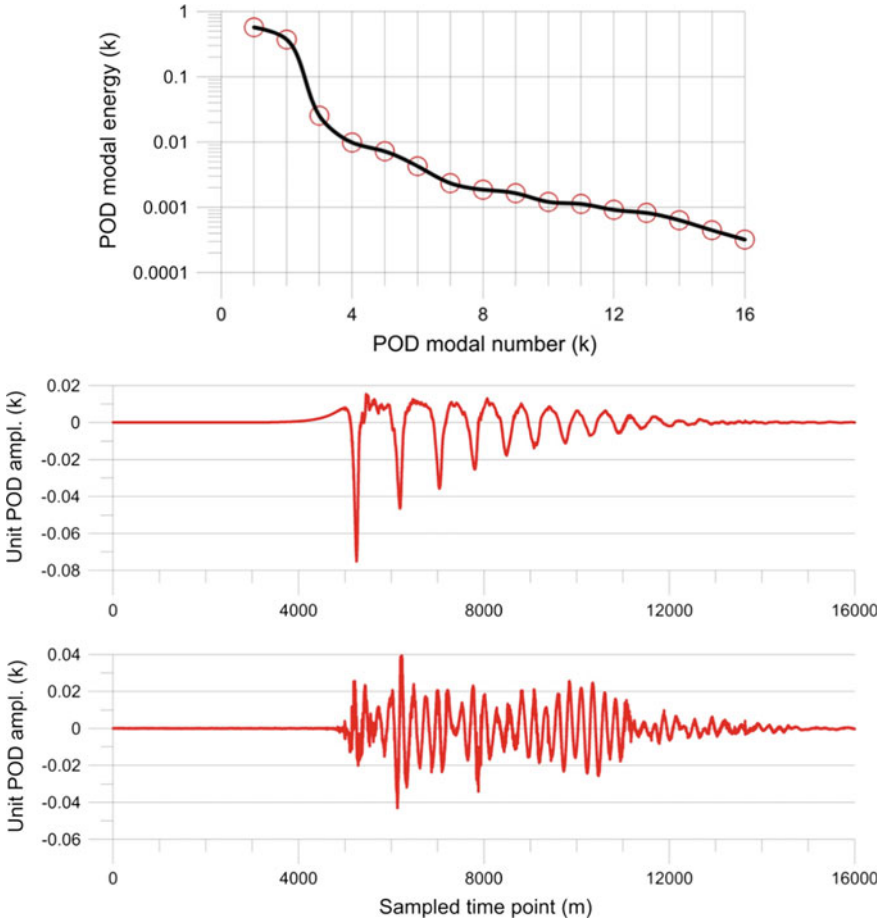

Fig. 10.2 POD-based modal analysis of a near homoclinic motion. The broad POD energy spectrum (top) characteristic of irreversible energy flow. Slow dominant (middle) and secondary fast (bottom) POD modal amplitudes with fast decay, quite different from natural free vibration decay

is initially stored in a shape that belongs to the space of slow bending motions. We conjecture that the irreversibility of energy flow occurs because the SIM undergoes transverse bifurcations and thus potential heteroclinic and homoclinic connections lurk. Because of the presence of coupled three-dimensional motions, the SIM of the multi-stable continuum is a quite complicated dynamics structure embedded in a high-dimensional space. Thus the near heteroclinic slow motions interact with slow and fast multi-dimensional coupled dynamics. This has been seen in a coupled system composed of a pendulum coupled to a stiff elastic rod [13]. The irreversible spread of mechanical energy from slow vibrations to fast ones should speed up its natural dissipation by internal frictional forces, thus possibly explaining the observed *ultra-fast decay* of vibrations.

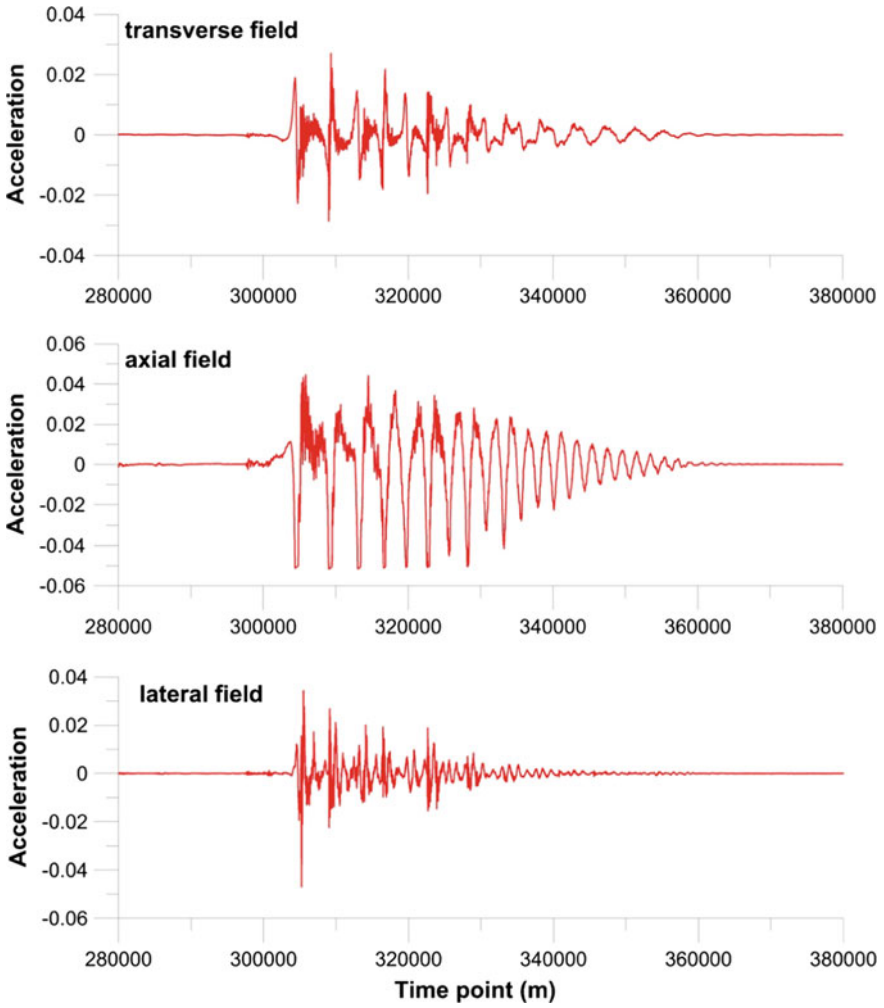

Fig. 10.3 Experimental time series of the acceleration orthogonal components in local coordinate system (in volts) of the middle point of the constrained beam, Fig. 10.1, during a near homoclinic motion

10.4 Dynamic Modification of a Flexible Cantilevered Beam with an Eccentric Rotor System

Figure 10.4 depicts a lab mechanical system composed of a high strength steel beam with attached at its free end an eccentric rotor. This coupled structural-mechanical system is endowed with a coexisting continuum of neutral equilibrium states, introduced naturally by the interacting eccentric rotor. We have conducted several experiments aimed at detecting motions transferring irreversibly-in the average sense-strain

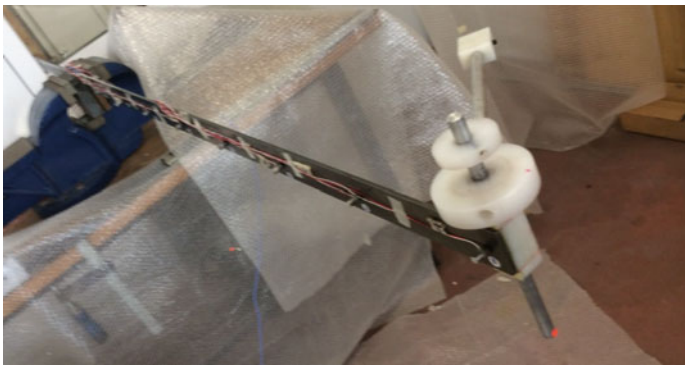

Fig. 10.4 A lab set-up of a flexible beam-eccentric rotor system as a paradigm of a coupled dynamical system with a continuum of coexisting equilibrium static states of neutral character. The phase space flow of the flexible beam is disturbed semantically with a whirl dynamics structure introduced by the eccentric rotor

energy from the flexible cantilevered beam to the freely rotating eccentric rotor. Specifically, the steel beam is released abruptly-with nearly zero velocity-from an initial displacement reached by applying slowly a transverse force, thus controlling the amount of strain energy stored initially in the flexible beam. The following phenomenon is observed: while the beam is vibrating in bending, the initially at rest rotor starts rotating to burst into a spin motion. As the rotor is accelerating, the beam motion decays fast. Eventually, the rotor comes into a rest state while the beam continues vibrating at its fundamental natural bending frequency. The motions are sensitive to the initial conditions: the rotor reaches different rest positions when started form different initial conditions.

An array of eight sensors was installed (Fig. 10.4) to acquire high resolution samples of the bending motion of the beam as it is exchanging energy with the eccentric rotor. The dynamics of the coupled beam-rotor system are dominated by a single POD mode whose shape remains the same as the bending deflection increases, see Fig. 10.5. The eccentric rotor drains continuously in time mechanical energy from the elastic beam because it is under the action of an inertia-induced torque due to the acceleration differential between the eccentric mass and the rotor center. Possessing a continuum of neutral static equilibria, the rotor absorbs very effectively work done from this no alternating torque. This mechanism, which is clearly nonlinear, allows the rotor to drain continuously energy from the oscillating beam. *We find that the rotor motion is quite sensitive to the initial conditions, a clear sign that heteroclinic or homoclinic connections have been introduced by the interacting eccentric rotor.* For completeness, we mention that we have noticed a phenomenon where the beam drains irreversibly energy, in an average sense, from the moving rotor since the latter

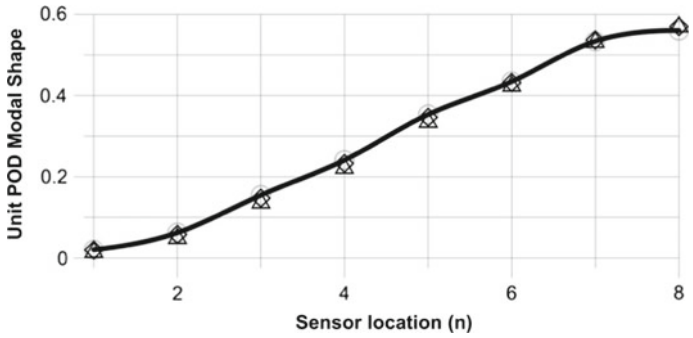

Fig. 10.5 The shape of the dominant POD mode of the beam-rotor system, Fig. 10.4, in free vibrations. The rotor motion does not affect the shape of the dominant POD mode. A reduced dynamical system is present. The accompanying time modulation of the dominant POD mode is used to analyze the experimental dynamics

gives rise to an internal force with frequency close to the resonance frequency of the beam + mass of rotor system. This is the well-known phenomenon of passage through resonance. This amount of energy is very small compared to that flows irreversibly form the flexible beam to the eccentric rotor.

10.4.1 Experimental Evidence of Energy Flow: Computation and Quantification

The rate of mechanical energy flow from the flexible beam into the rigid eccentric rotor can be estimated accurately when comparing the dominant POD modal amplitude of a motion with the rotor unlocked to that of a similar motion with the rotor locked. For both cases, nearly the same amount of strain energy was stored in the cantilevered steel beam. Figure 10.6 (bottom) presents the beam bending dynamic (dominant POD mode) when its energy flows irreversibly into the eccentric rotor dynamics: The beam oscillation undergoes a forced-like decay being quite different from that occurring naturally in the beam when the rotor subsystem is locked, Fig. 10.6 (top). The natural decay, being irreversible energy flow into heating, is due to the internal material friction. We quantify the rate of irreversible energy flow from the flexible beam into the rotor by computing the RMS-per-cycle quantity contained in the dominant POD modal amplitude. This energy like quantity is computed by dividing the observed time interval into a sequence of time intervals, each equal in length to the natural fundamental period of the beam-locked rotor structure. It turns out that the RMS-per-cycle quantity of a motion with the rotor locked is an exponential function of the sequence of natural time frames, revealing the fact that the frictional internal force is proportional to the velocity. Figure 10.7 (top) shows qualitatively the rate by which the stored energy at macro-scales is transformed irreversibly

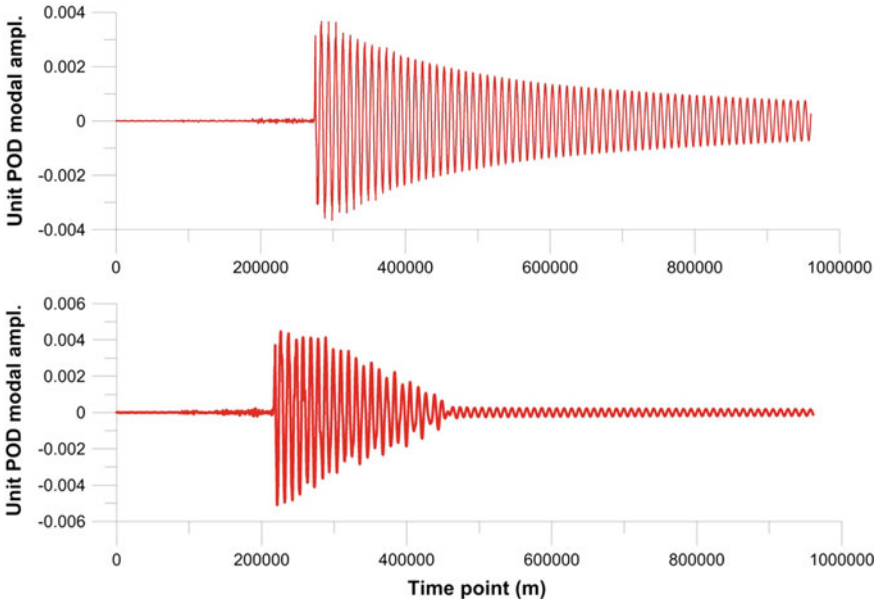

Fig. 10.6 Waveform of dominant experimental POD modal amplitude of bending motion of the beam-rotor coupled system, Fig. 10.4. Evolution of motion (top) with natural dissipation (rotor locked) of beam strain energy (top). Evolution of motion (bottom) with irreversible energy flow from the flexible beam into rotational kinetic energy flow of the rigid eccentric rotor

into heat, being the random micro motion of the molecule-level microstructure of the steel material. Figure 10.7 (bottom) reveals that this picture changes dramatically when energy flows irreversibly from the flexible beam into the rotor. *Clearly, natural irreversible energy flow would not materialize if the rotor were counteracted by a restoring moment*, *a fact impossible here due to the coexisting continuum of neutral static equilibria*. Figure 10.7 (bottom) reveals that the rate of flow of strain energy to the eccentric rotor is fast linear compared to the slow exponential one, when the rotor is locked, see Fig. 10.7(top). Figure 10.8 presents a measurement of the local tangential acceleration component of the acceleration of the eccentric mass. It possesses a large nonzero mean value indicating the fact the kinetic energy of the rotor increases as the beam vibration decays linear fact. This verifies independently the fact that mechanical energy flows irreversibly from the flexible continuum to the eccentric rotor.

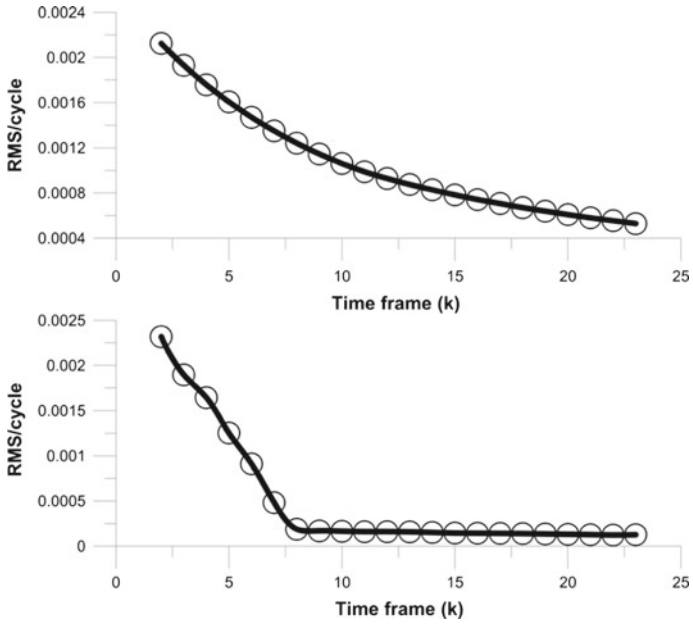

Fig. 10.7 RMS-based quantification of irreversible energy flow from the flexible beam. Natural slow dissipation (top) of strain energy due to internal frictional forces. Increased energy dissipation (bottom) due to motion-induced irreversible flow of energy from the flexible beam into the eccentric rotor (bottom)

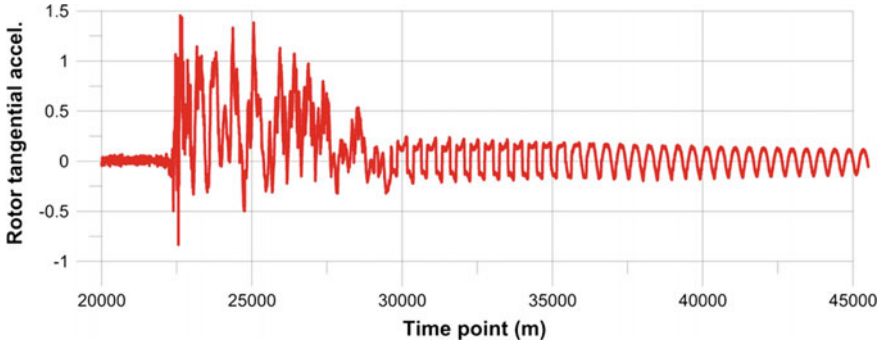

Fig. 10.8 Experimental time series, recorded by wireless MEMES sensor, of the tangential component of the acceleration of the eccentric mass of the rotor. After time point 30,000 the rotor has reached equilibrium for rotation. The RMS-per-cycle is nearly constant, a fact meaning that the rotor has given away all its rotational kinetic energy

10.5 Coupled Flexible Structural-Electromagnetic System: Multi-physics Complex and Extreme Dynamics

Figure 10.9 depicts a lab set-up of a representative coupled structural-electromagnetic system for an important class of multi-physics nonlinear systems encounter in aero and marine engineering applications. Motivated by the results of theoretical work [14] and the results of the mechanical systems studied above, we conducted a series of systematic experiments aimed at discovering the possibility that this system is the host of extreme nonlinear dynamics phenomena with potential irreversible energy flow. To this end, when forced harmonically by a voltage source, this coupled system exhibits coexisting multiple chaotic-and-regular attractors with a wide magnitude spectrum [15].

Figure 10.9 shows the transition of the flexible beam from a large amplitude steady state motion to a coexisting one of very low amplitude. At these particular values of the system parameters, we have detected at least five coexisting regular and chaotic attractors [15]. The coexisting chaotic and regular attractors stem from the distortion and disintegration of the SIM (slow invariant manifold) [14]. Over a relatively small region of the phase space, the SIM is computed analytically as a function of the slow variables. The analytic approximations to the SIM do not converge exactly at

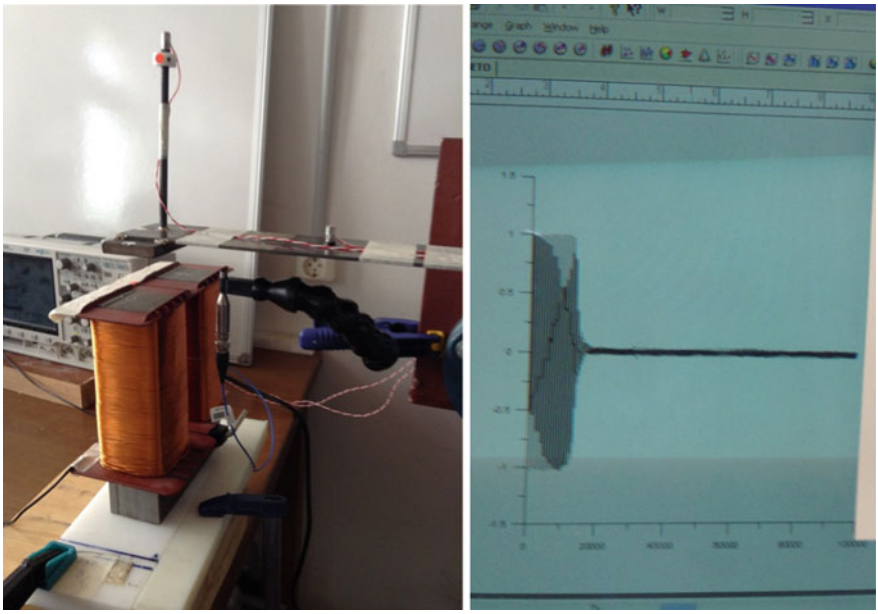

Fig. 10.9 Lab set-up of a prototypical structural-electromagnetic system at the NTUA nonlinear dynamics lab (left photo). Experimental time series of a transition of the vibrating flexible beam from a large amplitude attractor to a coexisting one of smaller amplitude (computer screen graph) for voltage excitation frequency at 12.80 Hz and magnet-to-mass gap = 36.6 mm

the phase space point where the manifold stops being described by a single-valued function. At this critical point, the SIM manifold admits folding and potential tangent bifurcations lurk to create out of the blue coexisting actuators with homoclinic and heteroclinic connections. In a series of recently published papers, the complexity of the dynamics is studied with Poincare sections, and the continuation methods [16]. Indeed, pictures of very complex chaotic-regular dynamics have been computed indicating that this complicated system, coupled multi-physics with infinite degrees-of-freedom, is an interesting physical system paradigm to search for phenomena with irreversible energy flow. It is reasonable to conjecture that the coexistence of multiple chaotic attractors-of wide spectrum of magnitude-potentially allows the existence of motions that drain energy from the electromagnetic system to the structural system and vice versa. We have seen this clearly in the dynamics of the cantilevered flexible beam modified at its free end by an eccentric rotor.

The author wishes to add here the fact that the present work, centered on the notion of irreversible energy flow in nonlinear dynamics systems, has its roots-motivation in a past experimental-theoretical work [17] that he conducted at Purdue University over a period of four years (1987–1991), and where he designed an experimental method to measure the temperature rise in thermoplastic composite materials subjected to cyclic fatigue load. It these experiments chaotic stress-strain curves were detected in unidirectional coupons fixed at an immovable grip and subjected to unidirectional periodic forcing. Furthermore, it was found that the temperatures rise, measure of irreversible energy flow from macro-micro-motion into fast molecular motion, was a highly nonlinear phenomenon since the systematic experiments revealed that the measured temperature rise is a cubic function of the stress or strain squared for all orientations of the carbon fibres embedded in a thermoplastic polymeric resin. We have irreversible transformation of mechanical energy input at the continuum mechanics lever (slow time scale) into heat, a measure of the kinetic energy of the random fast motions of the molecules. We contrast this natural irreversible energy flow from macro-scales to molecule scales with the spirit and results of the present study, where we have detected in coupled mechanical-structural systems irreversible flow of energy from natural slow time scales to natural fast time scales and then the natural transformation of the scattered mechanical energy in many natural time scales into heat.

10.6 Conclusions

We have studied to some extent the experimental dynamics of three paradigmatic, physical nonlinear systems in an effort to learn how nonlinear phenomena can be exploited in designing engineering systems with desired features, such as the fast decay of unwanted vibrations, for example. *The nonlinear phenomenon that we wish to understand and exploit is motions with irreversible energy flow among the components of a coupled multi-body system or among the components of the vector dynamics of a flexible one-dimensional continuum*. The three systems studied here

are nonlinear modifications of core systems in order to introduce coexisting nonlinear phenomena which in turn modify the phase space flow with hills, valleys and whirls as critical structures to support the formation of heteroclinic and homoclinic connections, among other motion types. It seems that the coexistence of multiple static equilibrium states or that of multiple chaotic-and-regular attractors create a dynamic environment where the creation of motion paths with irreversible energy is possible. In a future work, the above paradigmatic physical systems shall be explored systematically in a unified nonlinear dynamics approach to isolate and understand the type of motions that support irreversible energy flow. The studied systems are infinite-dimensional and derivation of optimum reduced order models, via a POD-based method of a high fidelity mathematical model, shall be very useful to map in parameter space sets of coexisting attractors. Poincare sections and continuation methods can be used to compute holistic bifurcation and attractor diagrams in parameter space. Indeed, a very elementary reduced order model for the multi-physics paradigmatic system reveals very complicated attractor and bifurcation diagrams. The irreversible energy flow characteristic of nonlinear systems is a very important feature and should be studied appropriately for realistic exploitation of nonlinearities and the fact that this adds to the production of entropy in general. From the scientific point of view, research considerations of nonlinear systems at the levels of energy-and-power flow is fundamental and as such shall pave the way for the exploitation of nonlinearities in engineering for energy harvesting and transmission of information. The multi-physics system draws our attention for further systematic study of its coupled structural-thermal-electromagnetic dynamics via a programmatic research program with emphasis on the detection of irreversible energy flow.

References

1. Guckenrheimer, J., Holes, P.: Nonlinear Oscillations, Dynamical Systems, and Bifurcations of Vector Fields. Springer, New York (1983)
2. Goldstein, H., Poole, C.P., Safko, J.: Classical Mechanics, 3rd edn. Addison Wesley, San Francisco, CA (2002)
3. Georgiou, I.T., Schwartz, I.B., Emace, E., Vakakis, A.: Interaction between slow and fast oscillations in an infinite degree-of-freedom linear system coupled to a nonlinear system: theory and experiment. J. Appl. Mech. **66**(2), 448–459 (1999)
4. Georgiou, I.T.: Nonlinear dynamics and chaotic motions of a singularly perturbed nonlinear viscoelastic beam. Ph.D. thesis, Purdue University, Aeronautics & Astronautics School, West Lafayette (1993)
5. Georgiou, I.T., Corless, M.J., Bajaj, A.K.: Dynamics of nonlinear structures with multiple equilibria: a singular perturbation-invariant manifold approach. A. Z. Angew Math. Phys. **50**, 892–924 (1999)
6. Georgiou, I.T.: On the global geometric structure of the dynamics of the elastic pendulum. Nonlinear Dyn. **18**, 51–68 (1999)
7. Kerchen, G., Lee, Y.S., Vakakis, A.F., McFarland, D.M., Bergman, L.A.: Irreversible passive energy transfer in coupled oscillators with essential nonlinearities. SIAM. J. Appl. Math. **66**, 648–679 (2006)

8. Georgiou, I.T.: A single pair-of-sensors technique for geometry consistent sensing of acceleration vector fields in beam structures: damage detection and dissipation estimation by POD modes. Meccanica **50**, 1303 (2015). https://doi.org/10.1007/s11012-014-0091-y
9. Rubin, M.B.: Cosserat Theories: Shells, Rods and Points. Kluwer Academic Publishers, Dordrecht, The Netherlands (2000)
10. Gabutti, B., Lepora, P., Merlo, G.: A bifurcation problem involving the elastica. Meccanica 154–165 (1980)
11. Georgiou, I.T., Bajaj, A.K.: Experimental nonlinear phenomena in structures with multiple equilibria controlled by boundary displacements: ultra-fast decay of coupled vibrations. In: ENOC2017, Budapest, Hungary, 25–30 June 2017
12. Goss, V.G.A.: The history of the planar elastica: insights into mechanics and scientific method. Sci. Educ. 1057–1082 (2009)
13. Georgiou, I.T., Schwartz, I.B.: The nonlinear slow normal mode and stochasticity in the dynamics of a conservative flexible rod/pendulum configuration. J. Sound Vib. **220**(3), 383–411 (1999)
14. Georgiou, I.T., Romeo, T.: Multi-physics dynamics of a mechanical oscillator coupled to an electro-magnetic circuit. Int. J. Nonlinear Mech. **70**, 153–164 (2015)
15. Georgiou, I.T., Romeo, F.: Nonlinear dynamic interactions in a coupled electro-magneto-mechanical system: experimental study. In: Nonlinear Dynamics. Conference Proceedings of the Society for Experimental Mechanics Series, vol. 1 (2016)
16. Romeo, F., Georgiou, I.T.: Multiphysics chaotic interaction in a coupled electro-magneto-mechanical system. In: Volume 4B: Dynamics, Vibration, and Control: V04BT04A018. ASME International Mechanical Engineering Congress and Exposition, Montreal, Quebec, Canada, 14–20 Nov 2014. https://doi.org/10.1115/imece2014-38714
17. Georgiou, I.T., Sun, C.T.: Temperature rise due to mechanical energy dissipation in unidirectional thermoplastic composites (AS4/PEEK). NASA Langley Research Center; Hampton, VA, United States, Technical Report and in Developments in theoretical and applied mechanics; Southeastern Conference on Theoretical and Applied Mechanics, 16th, Nashville, TN, 12–14 Apr 1992. A95-93700, pp. II.7.1–II.7.9. The University of Tennessee Space Institute (SECTAM, Vol. 16), Tullahoma, TN, United States. https://ntrs.nasa.gov/search.jsp?R=19950062118 (1992)

Chapter 11
Energy Harvesting in a Duffing Oscillator with Modulated Delay Amplitude

Zakaria Ghouli, Mustapha Hamdi and Mohamed Belhaq

Abstract We study periodic and quasi-periodic (QP) vibration-based energy harvesting (EH) in a delayed Duffing harvester device in which a piezoelectric component is considered. It is supposed that the delay feedback is inherently present in the system and it is modulated with a certain frequency around a mean value. We focus attention on the case of delay parametric resonance for which the frequency of the modulation is near twice the natural frequency of the oscillator. The method of multiple scales is applied to approximate the amplitude of periodic vibrations and the corresponding power output of the harvester device. The amplitude of the QP response and the corresponding power output are determined using numerical integration. Results show that for fixed values of amplitude and frequency of the modulated delay amplitude and small values of the unmodulated delay amplitude, only periodic vibrations can be exploited to extract energy. For large values of unmodulated delay amplitude, periodic solution may turn to unstable in certain ranges of time delay and only QP vibrations can be used to extract energy with good performance.

Keywords Energy harvesting · Delayed duffing oscillator · Quasi-periodic vibrations · Piezoelectric coupling.

11.1 Introduction

A monostable piezoelectric nonlinear EH device has been widely studied in the literature [1–4]. It is well known that, for appropriate choice of the nonlinearity, damping,

Z. Ghouli (✉) · M. Belhaq
Faculty of Sciences Ain Chock, University Hassan II Casablanca, Casablanca, Morocco
e-mail: ghoulizakaria@gmail.com

M. Belhaq
e-mail: mbelhaq@yahoo.fr

M. Hamdi
University Mohammed I Oujda, FST-Al Hoceima, El Hoceima, Morocco
e-mail: hamustapha2000@yahoo.fr

I. Kovacic and S. Lenci (eds.), *IUTAM Symposium on Exploiting Nonlinear Dynamics for Engineering Systems*, IUTAM Bookseries 37,
https://doi.org/10.1007/978-3-030-23692-2_11

and excitation amplitude, such a harvester may exhibit a relatively broadband frequency interval around the resonance in which the amplitude of the response and voltage can be exploited to extract energy. However, bistability and jump phenomena may occur in the system. This problem induced by the non linearity can pose a serious limitation of the harvester performance. Such a limitation can be overcome using QP vibrations away from the resonance.

A recent investigation showed that introducing a modulated delay amplitude in a van der Pol oscillator, QP vibrations having large amplitude performing in large range of parameters may occur away from the resonance [5]. Taking advantage of this result, it was reported [6] that in a delayed van der Pol oscillator with modulated delay amplitude coupled to an electromagnetic energy harvester, such QP vibrations can be exploited to scavenge energy in broadband of parameters. In [6] the time delay is introduced in the mechanical subsystem. The case where the time delay is introduced in both mechanical component and electrical circuit was studied in [7]. More recently, QP vibration-based EH in a delayed nonlinear MEMS device consisting of a delayed Mathieu-van der Pol-Duffing oscillator coupled to a delayed piezoelectric coupling mechanism was investigated [8]. It was shown that QP vibrations can be exploited to extract energy with good performance compared to periodic vibrations.

The time delay has also been used in a Duffing-type monostable harvester device subject to a harmonic excitation and coupled to a piezoelectric circuit [9]. The obtained QP vibrations have been exploited for improving EH performance in the case where the time delay is unmodulated. It was shown that for appropriate values of delay parameters, QP vibration-based EH may be exploited to scavenge energy over a large interval of frequencies far from the resonance with good efficiency. As result, bistability and jump phenomena occurring near the nonlinear frequency response can be circumvented when considering QP vibrations.

Motivated by such a performance of time delay in improving EH, the purpose of the present work is to study the EH performance in the case of a delayed Duffing harvester device with modulated delay amplitude and coupled to an electric circuit through a piezoelectric mechanism. This study can be useful in certain applications in which time delay is inherently present in the mechanical attachment of the harvester. In this case, the time delay is not considered as an additional power input introduced into the system.

The difference between the current work and the one given in [9] is that in [9] the Duffing harvester is subject to a periodic external forcing and the time delay is unmodulated, while in the present study the external excitation is absent and the time delay is modulated around a mean value with certain amplitude and frequency.

The rest of the paper is structured as follows. Section 11.2 describes the piezoelectric EH system. Using the multiple scales method and numerical simulations, periodic and QP responses and the corresponding powers are derived. In Sect. 11.3 the effect of parameters of the system on the EH performance is examined. The last section concludes the work.

11.2 The Harvester and Perturbation Analysis

The system we consider consists of a delayed Duffing equation as the mechanical subsystem and a piezoelectric device as the electrical component. We study the case for which the delay is time-dependant and is introduced in the position. The schematic of the system is presented in Fig. 11.1.

The governing equation for the system can be written in the dimensionless form as

$$\ddot{x}(t) + \delta\dot{x}(t) + x(t) + \gamma x(t)^3 - \chi v(t) = \alpha x(t-\tau), \tag{11.1}$$

$$\dot{v}(t) + \beta v(t) + \kappa\dot{x}(t) = 0, \tag{11.2}$$

where $x(t)$ is the relative displacement of the rigid mass m, $v(t)$ is the voltage across the load resistance, δ is the mechanical damping ratio, γ is the stiffness parameter, χ is the piezoelectric coupling term in the mechanical attachment, κ is the piezoelectric coupling term in the electrical circuit, β is the reciprocal of the time constant of the electrical circuit, α and τ are, respectively, the delay amplitude and time delay. As pointed out before, it is emphasized that the delay may not be considered as an power input into the system. For instance, in cutting operations, the delay phenomenon is imposed by the system itself [10–12]. In this case, the delay can be considered as proportional to the external forcing supplied to the harvester by a host structure such as a milling machine.

We assume that the delay amplitude α is modulated around a mean value such that

$$\alpha = \alpha_1 + \alpha_2 \cos(\omega t), \tag{11.3}$$

where α_1 is the unmodulated delay amplitude and α_2, ω are, respectively, the amplitude and the frequency of the modulation. Note that the case of forced and unmodulated time delay ($\alpha_2 = 0$) was studied in [9]. From mechanical point of view, the modulation of the time delay present in milling and cutting operations can be generated for instances in machining a mechanical tool with modulated surface in which a rolling motion of a special cam is involved.

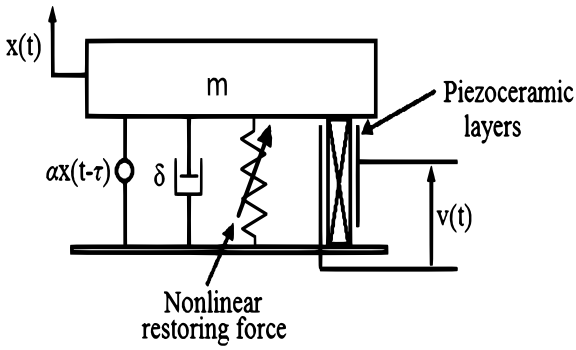

Fig. 11.1 Schematic description of the EH system

We investigate the response of the system near the delay parametric resonance by introducing the resonance condition $1 = \frac{\omega^2}{4} + \sigma$ where σ is a detuning parameter. Introducing a bookkeeping parameter ε, scaling parameters as $\delta = \varepsilon\tilde{\delta}$, $\gamma = \varepsilon\tilde{\gamma}$, $\chi = \varepsilon\tilde{\chi}$, $\alpha_1 = \varepsilon\tilde{\alpha_1}$, $\alpha_2 = \tilde{\alpha_2}$, $\sigma = \varepsilon\tilde{\sigma}$, and applying the method of multiple scales [13], Eqs. (11.1) and (11.2) take the form

$$\ddot{x}(t) + \frac{\omega^2}{4}x = \varepsilon[-\tilde{\delta}\dot{x}(t) - \tilde{\gamma}x(t)^3 + \tilde{\chi}v(t) - \tilde{\sigma}x(t) + (\tilde{\alpha_1} + \tilde{\alpha_2}\cos(\omega t))x(t-\tau)], \tag{11.4}$$

$$\dot{v}(t) + \beta v(t) + \kappa\dot{x}(t) = 0. \tag{11.5}$$

A solution to Eqs. (11.4) and (11.5) can be sought in the form

$$x(t) = x_0(T_0, T_1) + \varepsilon x_1(T_0, T_1) + O(\varepsilon^2), \tag{11.6}$$

$$v(t) = v_0(T_0, T_1) + \varepsilon v_1(T_0, T_1) + O(\varepsilon^2), \tag{11.7}$$

where $T_0 = t$, and $T_1 = \varepsilon t$. In terms of the variables T_i, the time derivatives become $\frac{d}{dt} = D_0 + \varepsilon D_1 + O(\varepsilon^2)$ and $\frac{d^2}{dt^2} = D_0^2 + \varepsilon^2 D_1^2 + 2\varepsilon D_0 D_1 + O(\varepsilon^2)$ where $D_i^j = \frac{\partial^j}{\partial^j T_i}$. Substituting (11.6) and (11.7) into (11.4) and (11.5) and equating coefficient of like powers of ε, one obtains:

$$D_0^2 x_0 + \frac{\omega^2}{4}x_0 = 0, \tag{11.8}$$

$$D_0 v_0 + \beta v_0 + \kappa D_0 x_0 = 0, \tag{11.9}$$

$$D_0^2 x_1 + \frac{\omega^2}{4}x_1 = -2D_0 D_1 x_0 - \tilde{\delta}D_0 x_0 - \tilde{\sigma}x_0 - \tilde{\gamma}x_0^3 + \tilde{\chi}v_0 + (\tilde{\alpha_1} + \tilde{\alpha_2}\cos(\omega t))x_{0\tau}, \tag{11.10}$$

$$D_0 v_1 + \beta v_1 = -D_1 v_0 - \kappa D_0 x_1 - \kappa D_1 x_0. \tag{11.11}$$

Up to the first order the solution is given by

$$x_0(T_0, T_1) = A(T_1)e^{i\frac{\omega T_0}{2}} + \bar{A}(T_1)e^{-i\frac{\omega T_0}{2}}, \tag{11.12}$$

$$v_0(T_0, T_1) = \frac{-\kappa i\omega A(T_1)}{2\beta + i\omega}e^{i\frac{\omega T_0}{2}} + \frac{\kappa i\omega\bar{A}(T_1)}{2\beta - i\omega}e^{-i\frac{\omega T_0}{2}}, \tag{11.13}$$

where $A(T_1)$ and $\bar{A}(T_1)$ are unknown functions. Substitution of Eqs. (11.12) and (11.13) into (11.10) and (11.11) and removing the secular terms lead to

$$-i\omega(D_1 A) - \frac{i\tilde{\delta}A\omega}{2} - \tilde{\sigma}A - 3\tilde{\gamma}A^2\bar{A} - \frac{\kappa i\omega\tilde{\chi}A}{2\beta + i\omega} + \tilde{\alpha_1}Ae^{-\frac{i\omega\tau}{2}} + \frac{\tilde{\alpha_2}}{2}\bar{A}e^{\frac{i\omega\tau}{2}} = 0. \tag{11.14}$$

Expressing $A = \frac{1}{2}ae^{i\theta}$ where a and θ are the amplitude and the phase, we obtain up to the first order the modulation equations

$$\begin{cases} \dfrac{da}{dt} = S_1 a + S_2 a\cos(2\theta) + S_3 a\sin(2\theta), \\ a\dfrac{d\theta}{dt} = S_4 a + S_5 a^3 + S_3 a\cos(2\theta) - S_2 a\sin(2\theta), \end{cases} \tag{11.15}$$

where $S_1 = \frac{-\delta}{2} - \frac{2\chi\kappa\beta}{4\beta^2+\omega^2} - \frac{\alpha_1}{\omega}\sin\frac{\omega\tau}{2}$, $S_2 = \frac{\alpha_2}{2\omega}\sin\frac{\omega\tau}{2}$, $S_3 = -\frac{\alpha_2}{2\omega}\cos\frac{\omega\tau}{2}$, $S_4 = \frac{\sigma}{\omega} + \frac{\chi\kappa\omega}{4\beta^2+\omega^2} - \frac{\alpha_1}{\omega}\cos\frac{\omega\tau}{2}$ and $S_5 = \frac{3\gamma}{4\omega}$. The solution to the first order given by (11.12) and (11.13) can be written as $x_0(T_0, T_1) = a\cos(\frac{\omega t}{2} + \theta)$ and $v_0(T_0, T_1) = V\cos(\frac{\omega t}{2} + \theta + \arctan\frac{2\beta}{\omega})$ where the voltage amplitude V is given by

$$V = \frac{\kappa\omega}{\sqrt{4\beta^2+\omega^2}}a. \tag{11.16}$$

The steady-state response of system (11.15), corresponding to periodic oscillations of Eqs. (11.4) and (11.5), are determined by setting $\frac{da}{dt} = \frac{d\theta}{dt} = 0$. Eliminating the phase, we obtain the following sixth-order algebraic equation in a

$$(S_1 a)^2 + (S_4 a + S_5 a^3)^2 = (S_2^2 + S_3^2)a^2. \tag{11.17}$$

An expression for the average power is obtained by integrating the dimensionless form of the instantaneous power $P(t) = \beta v(t)^2$ over the period of the delay modulation T. This is given by

$$P_{av} = \frac{1}{T}\int_0^T \beta v^2 dt, \tag{11.18}$$

where $T = \frac{4\pi}{\omega}$. Then, the average power expressed by $P_{av} = \frac{\beta V^2}{2}$ reads

$$P_{av} = \frac{1}{2}\left(\frac{\beta\kappa^2\omega^2}{4\beta^2+\omega^2}\right)a^2, \tag{11.19}$$

where the amplitude a is obtained from Eq. (11.17). Using the maximization procedure, one obtains the maximum power response as

$$P_{max} = \left(\frac{\beta\kappa^2\omega^2}{4\beta^2+\omega^2}\right)a^2. \tag{11.20}$$

Hereafter, we fix the parameters as $\delta = 0.1$, $\gamma = 0.25$, $\kappa = 0.5$, $\beta = 0.05$ and $\chi = 0.05$. The time delay is fixed as $\tau = 2.7$, except in the stability chart reported below.

11.3 Main Results

Next, the influence of different parameters of the system on vibration and power amplitudes is examined. Equation (11.17) is used for periodic solutions and Eq. (11.20) is exploited to calculate the power response. The amplitude of the QP response and the corresponding power extracted from QP vibrations are obtained numerically by using `dde23` algorithm [14].

In Fig. 11.2 is shown the variation of the amplitudes of periodic and QP responses (Fig. 11.2a) as well as the maximum power output amplitudes (Fig. 11.2b) versus the unmodulated delay amplitude α_1 and $\alpha_2 = 0.2$. The analytical prediction (solid lines for stable and dashed line for unstable) of periodic solutions are compared to numerical simulation (circles) obtained by using `dde23` algorithm [14]. The QP modulation envelope (circles connected by vertical line) is obtained numerically [14]. The boxes inset in the figures show time histories of the amplitudes (Fig. 11.2a) and the power responses (Fig. 11.2b) in the periodic and QP regions.

It can be seen from Fig. 11.2b that for negative values of α_1, energy can be extracted from QP vibration with better performance comparing to the periodic power output.

Figure 11.3 shows the variation of the amplitude of the responses (Fig. 11.3a) and the powers (Fig. 11.3b) versus the modulated delay amplitude α_2 for $\alpha_1 = -0.9$. It can be observed that periodic and QP vibration-based EH can be extracted over large band of the modulation delay amplitude α_2. It is worth noting that the ratio $\frac{\alpha_2}{\alpha_1}$ plays a crucial role rather than the individual quantities themselves. For instance, from Figs. 11.2 and 11.3, it is seen that the QP response can be observed when this ratio is approximately greater than $-\frac{1}{2}$.

Figures 11.4 and 11.5 show, respectively, the variation of the amplitude of the responses (Figs. 11.4a, 11.5a) as well as the powers (Figs. 11.4b, 11.5b) versus the frequency ω for $\alpha_1 = -0.1$ (Fig. 11.4) and $\alpha_1 = -0.9$ (Fig. 11.5). Figure 11.4 shows

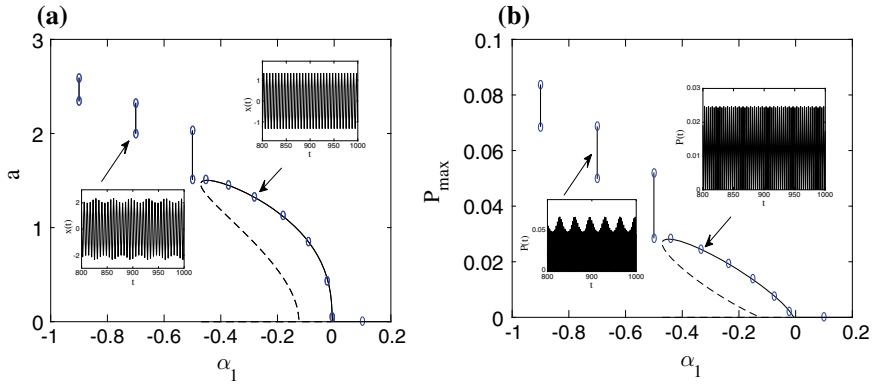

Fig. 11.2 Vibration and powers amplitudes versus α_1 for $\alpha_2 = 0.2$ and $\omega = 2$. Analytical prediction (solid lines for stable and dashed line for unstable) and numerical simulation (circles) for periodic solution; connected circles for QP solutions

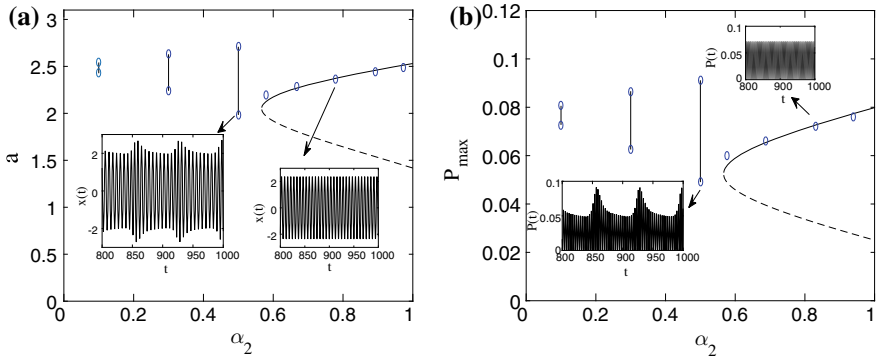

Fig. 11.3 Vibration and powers amplitudes versus α_2 for $\alpha_1 = -0.9$ and $\omega = 2$. Analytical prediction (solid lines for stable and dashed line for unstable) and numerical simulation (circles) for periodic solution; connected circles for QP solutions

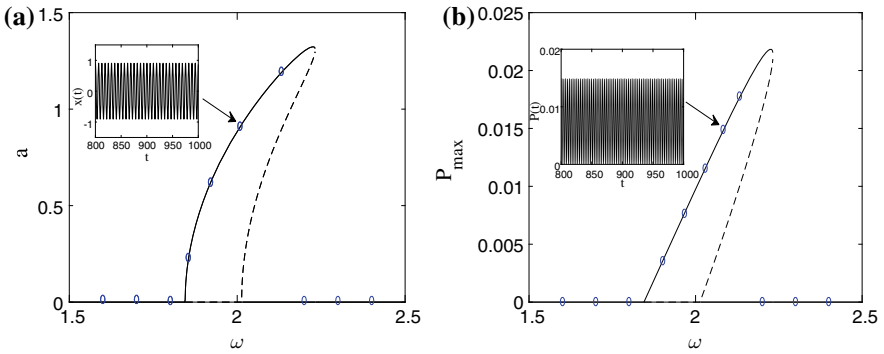

Fig. 11.4 Vibration and powers amplitudes vs ω for $\alpha_1 = -0.1$ and $\alpha_2 = 0.2$. Analytical prediction (solid lines for stable and dashed line for unstable) and numerical simulation (circles)

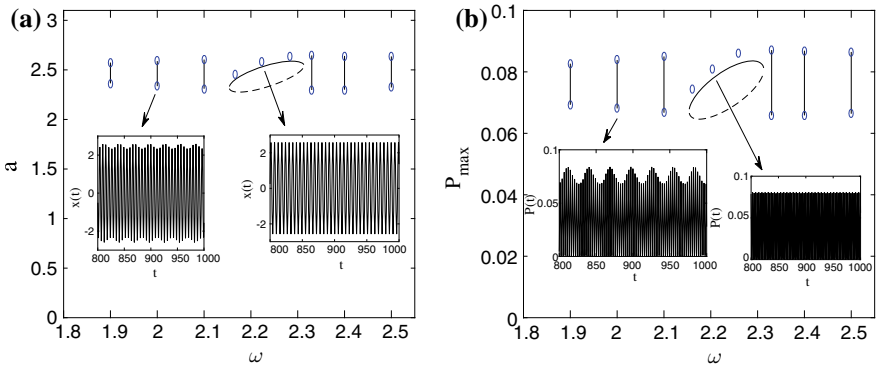

Fig. 11.5 Vibration and powers amplitudes vs ω for $\alpha_1 = -0.9$ and $\alpha_2 = 0.2$. Analytical prediction (solid lines for stable and dashed line for unstable) and numerical simulation (circles) for periodic solution; connected circles for QP solutions

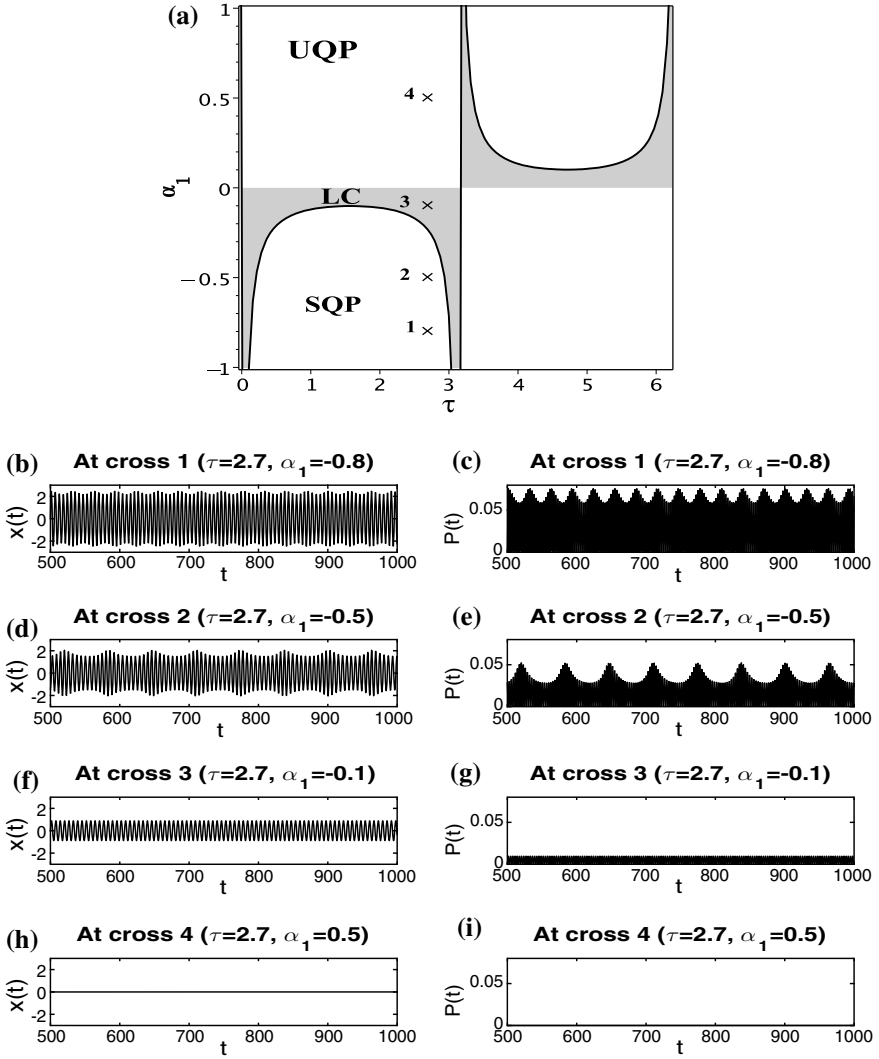

Fig. 11.6 **a** Stability chart in the plane (α_1, τ) and time histories: **b**, **c** at cross 1; **d**, **e** at cross 2; **f**, **g** at cross 3 and **h**, **i** at cross 4. LC: limit cycle, SQP: stable QP, UQP: unstable QP for fixed parameters $\omega = 2$ and $\alpha_2 = 0.2$

that for $\alpha_1 = -0.1$, power can be generated only from periodic oscillations. For $\alpha_1 = -0.9$, energy can be harvested from both periodic and QP vibrations. In the periodic regime a small range of frequencies can be exploited (solid line in the power response, Fig. 11.5b), while in the QP one a broadband of frequencies away from the resonance can be used to extract energy, as depicted inset in Fig. 11.5b.

Finally, to ensure the stability of vibrations during operation, the stability chart is determined in the parameter plane (α_1, τ). This can be obtained by considering the Jacobian matrix $\mathbf{J}$ of the slow flow (11.15). The curves delimiting the regions of stability of solutions are given by the conditions ($Tr(\mathbf{J}) = 2S_1 < 0$ and $Det(\mathbf{J}) = 4a^2 S_4 S_5 + 4a^4 S_5^2 > 0$). The grey regions of stable limit cycle (LC) are depicted in Fig. 11.6a. The stable QP (SQP) and unstable QP (UQP) responses are also shown in this chart. In Fig. 11.6b–i are shown time histories and power responses corresponding to crosses 1, 2, 3 and 4 in Fig. 11.6a. From cross 3 to 2 the system response changes behavior in a secondary Hopf bifurcation from LC to SQP oscillations with slight amplitude modulation offering a better performance of the power output. It can be observed that when the negative unmodulated delay amplitude increases, the power output performance is improved, as clearly shown in Fig. 11.6b, c corresponding to cross labelled 1 in Fig. 11.6a.

It is interesting to point out that modulating the delay amplitude α around a negative value of α_1 gives a stable behavior in the range $0 < \tau < \pi$ and modulating it around a positive value of α_1 gives a stable behavior in the range $\pi < \tau < 2\pi$. This result is illustrated in the stability chart (Fig. 11.6a).

11.4 Conclusions

In this paper we have studied periodic and QP vibration-based EH in a delayed Duffing oscillator coupled to an electric circuit through a piezoelectric mechanism in the case where the delay amplitude is modulated. It is supposed that the delay in the harvester is induced by the system itself and should not be considered as an additional power input. Application of the method of multiple scales enables the approximation of the amplitude of the periodic vibration and the corresponding power output. The QP response and the corresponding power output were obtained by numerical simulation. These periodic and QP vibrations are used to extract the corresponding power from the harvester device. It was shown that the modulation of the delay amplitude gives rise to large-amplitude QP vibration which can be exploited to extract energy with good performance away from the resonance. Depending on the modulated delay amplitude, energy can be harvested from periodic vibrations in a small interval of the frequency near the resonance or from QP vibrations over broadband of frequencies away from the resonance. Also, the results indicated that the power output performance can be enhanced substantially by increasing negative values of the unmodulated delay amplitude. From engineering application point of view, the modulation of the time delay can be used in milling and cutting operations for machining mechanical tools with a modulated surface considering a rolling motion of a special cam.

References

1. Hu, Y., Xue, H., Yang, J., Jiang, Q.: Nonlinear behavior of a piezoelectric power harvester near resonance. IEEE Trans. Ultrason. Ferroelectr. Freq. Control **53**, 1387–1391 (2006)
2. Mann, B.P., Sims, N.D.: Energy harvesting from the nonlinear oscillations of magnetic levitation. J. Sound Vib. **19**, 515–530 (2009)
3. Barton, D., Burrow, S., Clare, L.: Energy harvesting from vibrationswith a nonlinear oscillator. ASME J. Vib. Acoust. **132**, 021009 (2010)
4. Erturk, A., Inman, D.J.: Piezoelectric Energy Harvesting. Wiley (2011)
5. Hamdi, M., Belhaq, M.: Quasi-periodic vibrations in a delayed van der Pol oscillator with time-periodic delay amplitude. J. Vib. Control (2015). https://doi.org/10.1177/1077546315597821
6. Belhaq, M., Hamdi, M.: Energy harversting from quasi-periodic vibrations. Nonlinear Dyn. **86**, 2193–2205 (2016)
7. Ghouli, Z., Hamdi, M., Belhaq, M.: Energy harvesting from quasi-periodic vibrations using electromagnetic coupling with delay. Nonlinear Dyn. **89**, 1625–1636 (2017)
8. Belhaq, M., Ghouli, Z., Hamdi, M.: Energy harvesting in a Mathieu-van der Pol-Duffing MEMS device using time delay. Nonlinear Dyn. **94**, 2537–2546 (2018)
9. Ghouli, Z., Hamdi, M., Lakrad, F., Belhaq, M.: Quasiperiodic energy harvesting in a forced and delayed Duffing harvester device. J. Sound Vib. **407**, 271–285 (2017)
10. Stepan, G., Kalmr-Nagy, T.: Nonlinear regenerative machine tool vibrations. In: Proceedings of the 1997 ASME Design Engineering Technical Conferences, 16th ASME Biennial Conference on Mechanical Vibration and Noise (Sacramento, 1997), DETC97/VIB-4021, 1–11 (1997)
11. Kalmr-Nagy, T., Stepan, G., Moon, F.C.: Subcritical Hopf bifurcation in the delay equation model for machine tool vibrations. Nonlinear Dyn. **26**, 121–142 (2001)
12. Rusinek, R., Weremczuk, A., Warminski, J.: Regenerative model of cutting process with nonlinear Duffing oscillator. Mech. Mech. Eng. **15**, 129–143 (2011)
13. Nayfeh, A.H., Mook, D.T.: Nonlinear Oscillations. Wiley, New York (1979)
14. Shampine, L.F., Thompson, S.: Solving delay differential equations with dde23, PDF (2000). https://www.radford.edu/~hompson/webddes/tutorial.pdf

Chapter 12
Rotary Speed Modulation to Improve the Stability of Steady Drilling

Sunit K. Gupta and Pankaj Wahi

Abstract In this work, we investigate the effect of periodic modulations in the rotary speed of the top table on the drill-string dynamics of rotary drilling. The analysis is presented for the lumped-parameter model corresponding to the axial-trosional modes. The regenerative effect due to the axial vibration is included through the functional description of the cut surface instead of a traditional state-dependent delay model. This further results in the coupled ODE-PDE model with time periodic coefficients, defining the axial-trosional dynamics with modulating rotary speed. The rotary speed modulation causes the emergence of number of possible solutions for steady-drilling states. In particular, the case wherein the steady depth of cut remains constant even with periodically varying steady twist of the drill-string has been considered in the current work. We observe the significant improvement in the stability of the system as the modulation frequency reaches towards the natural frequency corresponding to trosional mode.

Keywords Rotary drilling · Axial-torsional model · Stability · Rotary speed modulation

12.1 Introduction

One of the popular methods in the exploration of oil and natural gas is the rotary deep drilling. Rotary deep drilling systems consist of a rotary table at the top to transmit the rotary power required for drilling through a series of drill-pipes, also known as drill-string, to the bottom hole assembly (BHA) which further carries the drill-bit to cut the rock formation [2]. Drill-string is also used for the transmission of the drilling-fluid which acts as the lubricant for the drill-bit. Thus, drill-string plays

S. K. Gupta · P. Wahi (✉)
Mechanical Department, Indian Institute of Technology Kanpur, Kanpur 208016, India
e-mail: wahi@iitk.ac.in

S. K. Gupta
e-mail: guptasunit1987@gmail.com

I. Kovacic and S. Lenci (eds.), *IUTAM Symposium on Exploiting Nonlinear Dynamics for Engineering Systems*, IUTAM Bookseries 37,
https://doi.org/10.1007/978-3-030-23692-2_12

an important role in the drilling operation and any failure of drill-string causes the shut down of the entire drilling operation and economic loss to drilling industry. One of the major causes of the drill-string failure is the self-exciteyeard axial, torsional and lateral vibrations and the coupling between them. These self-excited vibrations further manifest to bit-bounce, stick-slip and whirling motions in axial, torsional and lateral directions, respectively. These manifested form of the self-excited vibrations are detrimental to the system and eventually lead to the failure of drill-string. Hence, it is necessary to understand the behavior of drill-string under different operating conditions to improve the performance of drilling. In the current work, we present one of the methods to enhance the stability of the system by modulating the rotary speed around a mean value.

There are different methods available in the literature proposed by the researchers to control or suppress these self-excited vibrations. These methods can be broadly classified into three categories: (1) proper analysis of drilling apparatus at the design stage itself along with the optimum choice of operating parameters [4, 9]; (2) passive control of drill-string vibrations through the use of shock absorbers (shock subs) [6, 21]; and (3) the use of active controllers [3, 22].

Further, in machining processes, modulation in rotary speed is also considered as one of the effective methods to control/suppress excessive machine tool vibrations (chatter) [10, 19]. However, the incorporation of modulating rotary speed with the regenerative effect in machining processes leads to variable delay differential equation (VDDE). It is noted that the stability analysis of the VDDE model is not as straightforward as that of the constant DDE models. Several studies have been done for the stability analysis of these VDDE using different methods [11, 15, 17, 18]. With the same motivation, Alzibdeh [1] implemented the rotary speed modulation in the torsional-lateral vibration of the drill-string and observed the effectiveness of modulation in the attenuation of the vibration.

We implement the modulation in the rotary speed of the top table in axial-torsional model of rotary drilling with the regenerative effect. However, traditional model to include regenerative effect in drilling leads to implicit state-dependent delay differential equation (SDDDE) and we have observed that SDDDE model to be rather cumbersome for this purpose. Instead we have modified the recently proposed alternate approach to model the axial-torsional dynamics of rotary drilling [8] to include rotary speed modulation. We start with a brief description of a mathematical model for rotary drilling with speed modulation.

12.2 Mathematical Model

We first start with the mathematical description of the rotary drilling process with the speed modulation. Rotary drilling typically involves two user-controlled operating parameters viz. top table rotary speed, Ω_0, and the effective weight on bit (WOB), W_0. In the current work, we will allow the possibility of having modulations in the W_0 which will be synchronous with the rotary speed modulations. Drill-string vibrations

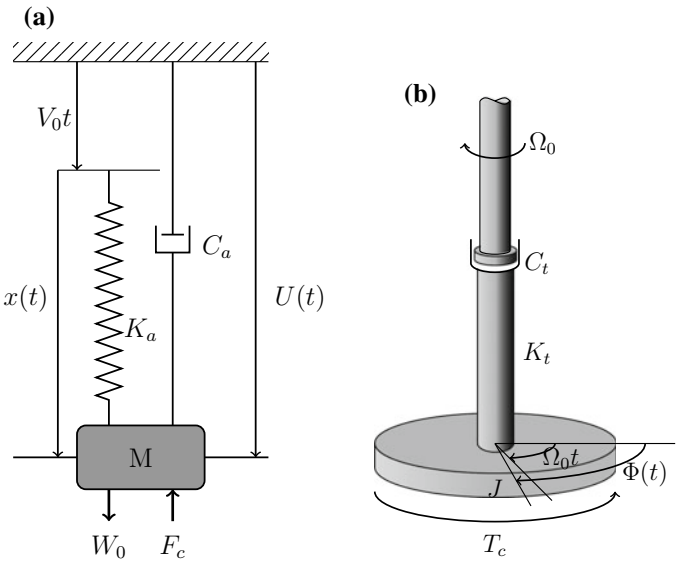

Fig. 12.1 Schematics of **a** axial and **b** torsional dynamics of drill-string

have been studied extensively using continuum models, lumped parameter models and finite element models [5, 13, 14] but to avoid complexity and focusing on the formulation we are considering the lumped parameter model [8]. For the sake of completeness and convenience of readability, we briefly outline the mathematical model of rotary drilling [8] which is being used in the current work. The schamatics of axial and torsional modes of drill-string are shown in Fig. 12.1. In the axial direction, the drill-string is modeled as a spring-mass-damper system with spring stiffness (K_a), viscous damping coefficient (C_a) and the combined mass (M) of the drill-pipes and the bottom hole assembly (BHA) lumped at the end (Fig. 12.1a). For torsional oscillations, the drill-string is modeled as a system with torsional spring stiffness (K_t), torsional viscous damping coefficient (C_t) and the combined rotary inertia of the drill-pipes and the BHA (J) about the rotational axis (Fig. 12.1b).

Equations of motion for this system in the axial and torsional directions are [8]

$$M\ddot{U}(t) + C_a\dot{U}(t) + K_a\left(U(t) - V_0t\right) = W_0 - \xi\varepsilon a d(t) H(\dot{\Phi}) H(d(t))\,, \quad \text{(12.1a)}$$

$$J\ddot{\Phi}(t) + C_t\dot{\Phi}(t) + K_t\left(\Phi(t) - \Omega_0 t\right) = -\varepsilon a^2 d(t)/2 H(\dot{\Phi}) H(d(t))\,. \quad \text{(12.1b)}$$

where $H(.)$ represents the Heaviside step function. The other quantities are: ξ is the cutter inclination coefficient, ε is the rock specific strength, a is the radius of the drill-bit, $d(t)$ is the instantaneous depth of cut per revolution [16]. Note that under variable Ω_0 and W_0, the rate of progression V_0 will be also time-varying and hence, the above equations of motion will be modified to

$$M\ddot{U}(t) + C_a\dot{U}(t) + K_a\left(U(t) - \int_0^t V_0\left(\tilde{t}\right)\mathrm{d}\tilde{t}\right) = W_0(t) - \xi\varepsilon a d(t) H(\dot{\Phi}) H(d(t))\,, \tag{12.2a}$$

$$J\ddot{\Phi}(t) + C_t\dot{\Phi}(t) + K_t\left(\Phi(t) - \int_0^t \Omega_0\left(\tilde{t}\right)\mathrm{d}\tilde{t}\right) = -\varepsilon a^2 d(t)/2 H(\dot{\Phi}) H(d(t))\,. \tag{12.2b}$$

As a result of the rotary speed modulation, the change of variables from $U(t)$ and $\Phi(t)$ to $x(t)$ and $\theta(t)$, in a frame of reference translating with the feed velocity $V_0(t)$ and rotating with an angular velocity $\Omega_0(t)$ will be $U(t) = \int_0^t V_0\left(\tilde{t}\right)\mathrm{d}\tilde{t} + x(t)$, $\Phi(t) = \int_0^t \Omega_0\left(\tilde{t}\right)\mathrm{d}\tilde{t} + \theta(t)$. Therefore the equations of motion, i.e., Eq. (12.2) in the new variables are

$$M\ddot{x}(t) + C_a\left(\dot{x}(t) + V_0(t)\right) + K_a x(t) = W_0(t) - \xi\varepsilon a d(t)\,, \tag{12.3a}$$

$$J\ddot{\theta}(t) + C_t\left(\dot{\theta}(t) + \Omega_0(t)\right) + K_t\theta(t) = -\varepsilon a^2 d(t)/2\,. \tag{12.3b}$$

Note that, we have replaced $H(\Omega_0 + \dot{\theta}) = 1$ and $H(d(t)) = 1$ in Eq. (12.3) as the main emphasis of the study is to obtain steady states and their stability and hence, free from any self-interruption. Equation (12.3) represents the lumped parameter axial-torsional model of rotary drilling with modulating rotary table speed for the continuous cutting condition. We next present the necessary modifications in the alternate model for the depth of cut [8] during rotary speed modulation (Fig. 12.2).

For an alternate model for the depth of cut, we represent the cut surface by a function $L(\phi, t)$ with $\phi \in (0, 2\pi/n]$. It should be noted here that the domain of ϕ, i.e., $(0, 2\pi/n]$ is measured in a reference frame rotating with the drill-bit, i.e., $\Omega_0(t) + \dot{\theta}(t)$. If $L(0, t)$ and $L(2\pi/n, t)$ represent the points on the cut surface at the two adjacent cutter locations, then the depth of cut per cutter is

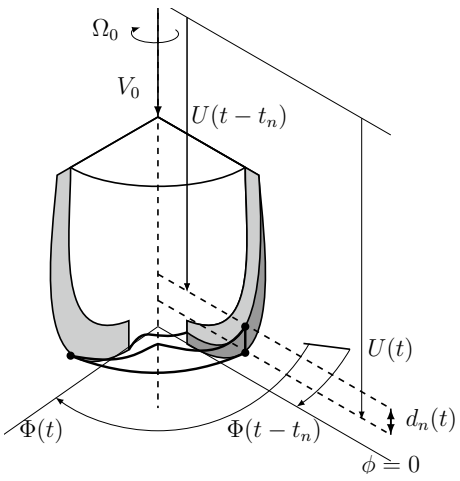

Fig. 12.2 Schematic of the section between two successive cutters

$$d_n(t) = L\left(\frac{2\pi}{n}, t\right) - L(0, t), \tag{12.4}$$

which is related to depth of cut per revolution, $d(t)$, by $d(t) = nd_n(t)$. Following [8] we get the evolution of L to be governed by the partial differential equation (PDE)

$$\frac{\partial L}{\partial t} + \left(\Omega_0(t) + \frac{\mathrm{d}\theta}{\mathrm{d}t}\right)\frac{\partial L}{\partial \phi} = 0\,. \tag{12.5}$$

Equation (12.5) is a first order nonlinear partial differential equation (PDE) with a time-dependent parametric forcing and to solve it we need an initial and boundary condition. The initial condition for this PDE can arbitrarily be set to $L(\phi, 0) = 0$ (an initial flat surface). Since we are interested in operating conditions where the bit is always in contact with the cut surface, i.e., the engaged position, the boundary condition, $L(0, t)$ will be specified by the axial location of the cutter. In the presence of axial vibrations of the drill string, the actual position of the cutter and consequently $L(0, t)$ is

$$L(0,t) = L(0,0) - \int_0^t V_0\left(\tilde{t}\right)\mathrm{d}\tilde{t} - x(t) = -\int_0^t V_0\left(\tilde{t}\right)\mathrm{d}\tilde{t} - x(t) \quad (\text{by } L(0,0) = 0). \tag{12.6}$$

Accordingly, the instantaneous depth of cut can be written as

$$d_n(t) = L\left(\frac{2\pi}{n}, t\right) + \int_0^t V_0\left(\tilde{t}\right)\mathrm{d}\tilde{t} + x(t). \tag{12.7}$$

The first order PDE given by Eq. (12.5) with Eq. (12.6) acting as the boundary condition governs the evolution of the cut surface for arbitrary t and $\phi \in (0, 2\pi/n]$. For ease of further algebra, we introduce the function $\bar{L}$ ([8, 20]) as

$$\bar{L}(\phi, t) = L(\phi, t) + \int_0^t V_0\left(\tilde{t}\right)\mathrm{d}\tilde{t}\,.$$

Accordingly, the PDE governing the evolution of cut surface and the boundary condition get modified to

$$\frac{\partial \bar{L}}{\partial t} + \left(\Omega_0(t) + \frac{\mathrm{d}\theta}{\mathrm{d}t}\right)\frac{\partial \bar{L}}{\partial \phi} - V_0(t) = 0\,, \tag{12.8}$$

$$\text{B.C.} \quad \bar{L}(0, \tau) = -x(t)\,. \tag{12.9}$$

With this function, the instantaneous depth of cut $d_n(t)$ from Eq. (12.7) becomes

$$d_n(t) = \bar{L}\left(\frac{2\pi}{n}, t\right) + x(t)\,. \tag{12.10}$$

Equations (12.3), (12.8)–(12.10) represent the complete mathematical model for rotary drilling with modulating rotary speed and WOB during cutting, free from any kind of self-interruption. We now utilize the equations of motion for rotary drilling with modulations in the WOB and angular velocity of the top table to study the effect of rotary speed variation on the steady drilling states and use this information to non-dimensionlize the equations of motion.

12.3 Steady States

In this section, we will discuss the various possible steady drilling states and non-dimensionlize our equations after shifting about the practically relevant steady state. For the current work we have used the modulation in the form of

$$\Omega_0(t) = \Omega_{0s} \left[1 + m \cos\left(\omega_m t\right)\right] , \tag{12.11}$$

with Ω_{0s} as the mean rotary speed, m as the percentage amplitude modulation and ω_m as the frequency of the modulation. We will further consider a synchronous modulation in the effective WOB (the other operating parameter) of the form

$$W_0(t) = W_{0s} + W_1 \sin\left(\omega_m t\right) + W_2 \cos\left(\omega_m t\right) . \tag{12.12}$$

Note that we have not assumed any particular values of W_1 and W_2 and hence, have allowed for a phase difference between the rotary speed modulation and the modulation in the WOB. Under these operating conditions, we assume that the various relevant quantities defining the steady drilling state are also synchronous with the variations in the rotary speed and can be defined as

$$\begin{aligned} &d(t) = d_s + d_1 \sin\left(\omega_m t\right) + d_2 \cos\left(\omega_m t\right) , \; x(t) = x_s + x_1 \sin\left(\omega_m t\right) + x_2 \cos\left(\omega_m t\right) \\ &\theta(t) = \theta_s + \theta_1 \sin\left(\omega_m t\right) + \theta_2 \cos\left(\omega_m t\right) , \; V_0(t) = V_{0s} + V_1 \sin\left(\omega_m t\right) + V_2 \cos\left(\omega_m t\right) , \\ &\bar{L}(\phi, t) = \bar{L}_{0s}(\phi) + \bar{L}_1(\phi) \sin\left(\omega_m t\right) + \bar{L}_2(\phi) \cos\left(\omega_m t\right) . \end{aligned} \tag{12.13}$$

In the above mentioned variables, the subscript s represents the mean component of the steady state values. Substituting these variables in Eqs. (12.3),(12.8)–(12.10) and using harmonic balance, we will get 15 equations which can be used to obtain the 15 unknowns involved in Eq. (12.13) in terms of the quantities involved in Eqs. (12.11) and (12.12). We will have multiple possible steady drilling states which arises from the fact that while modulating the rotary speed, we can either choose to modulate the WOB or not. For the same rotary speed modulation, different synchronous modulations of the WOB could lead to different steady drilling states. In the current work, we have considered the steady drilling state which does not accompany any axial vibrations and has a steady depth of cut per revolution. This steady state is of practical relevance as axial vibrations during drilling operation are not desirable. Accordingly, the various quantities of interest can be written

$$
\begin{aligned}
&d(t) = d_s,\ x(t) = 0,\ \bar{L}(\phi, t) = \bar{L}_s(\phi),\\
&\theta(t) = \theta_s + \theta_1 \sin(\omega_m t) + \theta_2 \cos(\omega_m t) = \tilde{\theta}_s(t)\,,\\
&V_0(t) = V_{0s} + V_1 \sin(\omega_m t) + V_2 \cos(\omega_m t) = V_s(t)\,.
\end{aligned} \tag{12.14}
$$

The equations governing the axial and torsional motion of the drill-string and the PDE governing the cut surface along with its boundary condition for this steady state are

$$M\dot{V}_s(t) + C_a V_s(t) = W_0(t) - \xi a \varepsilon d_s\,, \tag{12.15a}$$

$$J\left(\dot{\Omega}_0(t) + \ddot{\tilde{\theta}}_s(t)\right) + C_t\left(\Omega_0(t) + \dot{\tilde{\theta}}_s(t)\right) + K_t\tilde{\theta}_s(t) = -\varepsilon a^2 d_s/2\,. \tag{12.15b}$$

$$\left(\Omega_0(t) + \dot{\tilde{\theta}}_s(t)\right)\frac{\partial \bar{L}_s}{\partial \phi} - V_s(t) = 0\,,\quad \bar{L}_s(0, t) = -x(t) = 0\,. \tag{12.15c}$$

Substituting $\Omega_0(t)$, $W_0(t)$, $\theta_s(t)$ and $V_s(t)$ in Eq. (12.18) solving for the unknowns using harmonic balance, we get

$$
\begin{aligned}
&V_{0s} = \frac{W_{0s} + \xi\varepsilon a d_s}{C_a},\ \theta_s = \frac{-\varepsilon a^2 d_s - C_t\Omega_{0s}}{2K_t},\ \bar{L}_s = \frac{d_s\phi}{2\pi},\\
&\theta_1 = -\frac{{C_t}^2\omega_m\, m\Omega_{0s}}{{C_t}^2{\omega_m}^2 + {K_t}^2 - 2\,K_t\,J{\omega_m}^2 + J^2{\omega_m}^4},\ \theta_2 = \frac{\left(-K_t + J{\omega_m}^2\right)C_t\, m\Omega_{0s}}{{C_t}^2{\omega_m}^2 + {K_t}^2 - 2\,K_t\,J{\omega_m}^2 + J^2{\omega_m}^4},\\
&V_1 = -\frac{d_s\theta_2\omega_m}{2\pi},\ V_2 = \frac{d_s}{2\pi}\left(\theta_1\omega_m + m\Omega_{0s}\right),\ W_1 = V_1 C_a,\ W_2 = V_2 C_a\,.
\end{aligned} \tag{12.16}
$$

Having obtained the steady state solution, we can study its stability by linearizing our system of equations around this solution along with the non-dimensionlization to reduce the effective number of parameters.

12.4 Linearization and Nondimensionlization

Having obtained all the quantities corresponding to the steady drilling state, we provide small perturbations to the various states viz. $x(t)$, $\theta(t)$, $d(t)$ and $L(\phi, t)$ as

$$x(t) = \eta_x\,,\ \theta(t) = \tilde{\theta}_s(t) + \eta_\theta(t) d(t) = d_s + \eta_{ds}(t)\,,\ \bar{L}(\phi, t) = \bar{L}_s(\phi) + \eta_{\bar{L}}(\phi, t)$$

where $\left\{\eta_x,\ \eta_\theta,\ \eta_{ds},\ \eta_{\bar{L}}\right\} \ll 1$. On substituting these in Eqs. (12.3) and (12.8), utilizing the steady state relations given by Eq. (12.18) and ignoring all higher order terms involving $\left\{\eta_x,\ \eta_\theta,\ \eta_{ds},\ \eta_{\bar{L}}\right\}$, we get the linearized system of equations as

$$M\ddot{\eta}_x + C_a\dot{\eta}_x + K_a\eta_x = -\xi\varepsilon a\eta_{ds}\,, \tag{12.17a}$$

$$J\ddot{\eta}_\theta + C_t\dot{\eta}_\theta + K_t\eta_\theta = -\varepsilon a^2\eta_{ds}/2\,, \tag{12.17b}$$

$$\frac{\partial \eta_{\bar{L}}}{\partial t} + \left\{\Omega_0(t) + \dot{\tilde{\theta}}_s(t)\right\} \frac{\partial \eta_{\bar{L}}}{\partial \phi} + \dot{\eta}_\theta \frac{d_s}{2\pi} = 0\,. \tag{12.17c}$$

It should be noted that all the four perturbations $\left\{\eta_x,\ \eta_\theta,\ \eta_{ds},\ \eta_{\bar{L}}\right\}$ are not independent. In particular, Eq. (12.9) gives us $\eta_{\bar{L}}(0,t) = -\eta_x$ while we have $\eta_{ds} = n(\eta_x + \eta_{\bar{L}}(2\pi/n, t))$ from Eq. (12.10). Using these two relations in conjunction with Eq. (12.17c) completely determines the linearized system of equations. Now, we non-dimensionalize our system using following nondimensional variables:

$$\tilde{L} = \frac{2K_t}{\varepsilon a^2},\ \psi = \frac{\xi a \varepsilon J}{M K_t},\ \tilde{\eta}_x = \frac{\eta_x}{\tilde{L}},\ \tilde{a} = \frac{a}{\tilde{L}},\ \tilde{\eta}_{\bar{L}} = \frac{\eta_{\bar{L}}}{\tilde{L}},\ \tilde{\eta}_{\delta ns} = \frac{\eta_{ds}}{n\tilde{L}},\ \tau = \sqrt{\frac{K_t}{J}}t,\ \delta_s = \frac{d_s}{\tilde{L}},$$
$$\zeta = \frac{C_a}{2\sqrt{K_a M}},\ \kappa = \frac{C_t}{2\sqrt{K_t J}},\ \omega_{0s} = \frac{\Omega_{0s}}{\sqrt{\frac{K_t}{J}}},\ \tilde{\omega}_m = \frac{\omega_m}{\sqrt{\frac{K_t}{J}}},\ \beta = \frac{\sqrt{\frac{K_a}{M}}}{\sqrt{\frac{K_t}{J}}}\,.$$

Using these the nondimensional linearized equations can be written as

$$\ddot{\eta}_x + 2\zeta\beta\dot{\eta}_x + \beta^2\eta_x = -n\psi\eta_{\delta ns}\,, \tag{12.18a}$$

$$\ddot{\eta}_\theta + 2\kappa\dot{\eta}_\theta + \eta_\theta = -n\eta_{\delta ns}\,, \tag{12.18b}$$

$$\frac{\partial \eta_{\bar{L}}}{\partial \tau} + \left\{\omega_{0s}\left(1 + m\cos\left(\omega_m\tau\right)\right) + \dot{\theta}_s(\tau)\right\} \frac{\partial \eta_{\bar{L}}}{\partial \phi} + \dot{\eta}_\theta \frac{\delta_s}{2\pi} = 0\,, \tag{12.18c}$$

with $\theta_s(\tau)$

$$\dot{\theta}_s = \frac{-\omega_{0s}\left(-1 + 1\,{\omega_m}^2 + 4\kappa^2\right) m{\omega_m}^2\cos\left(\omega_m\,\tau\right) + 2\,\kappa\,\omega_{0s}\,m\sin\left(\omega_m\,\tau\right)\omega_m}{1 + {\omega_m}^4 + \left(-2 + 4\,\kappa^2\right){\omega_m}^2}\,. \tag{12.19}$$

In the above, we have dropped the tilde from the nondimensional variables for the sake of notational convenience. Furthermore, the solution for $\theta_s(\tau)$ has been obtained from Eq. (12.14) after substituting Eq. (12.16) followed by nondimensionalization. Since our linearized equations involve a PDE and time-periodic coefficients, we first need to discretize the system to obtain reduced order system of ODEs, presented in the next seciton, which can be used to obtain the stability curves using the Floquet theory [7, 12].

12.5 Reduced Order System

For the discretization of Eq. (12.18c), we approximate the perturbation $\eta_{\bar{L}}(\phi, \tau)$ as

$$\eta_{\bar{L}}(\phi,\tau) = a_0(\tau)\left(1 - \frac{n\phi}{2\pi}\right) + a_1(\tau)\frac{n\phi}{2\pi} + \sum_{k=1}^{N-1} a_{k+1}(\tau)\sin\left(\frac{nk\phi}{2}\right)\,, \tag{12.20}$$

with N representing the number of terms in the approximation and $a_i(\tau)'s$ for $i = 0, \cdots, N$ represent the undetermined functions of τ that define the variation in the cut surface from the steady linear profile. From the above approximation for $\eta_{\bar{L}}(\phi, \tau)$, we have $\eta_{\bar{L}}(0, \tau) = a_0(\tau) = -\eta_x(\tau)$ (using the boundary condition at $\phi = 0$) and $\eta_{\bar{L}}(2\pi/n, \tau) = a_1(\tau)$. Hence, the perturbation to the steady depth of cut can be written as

$$\eta_{\delta ns} = a_1(\tau) + \eta_x(\tau). \tag{12.21}$$

Since, $\eta_{\bar{L}}$ is not the exact solution of Eq. (12.18), we will get the residue on substituting $\eta_{\bar{L}}$ in Eq. (12.18) and defined by

$$\begin{aligned} R_e = &- \dot{\eta}_x(\tau)\left(1 - \frac{n\phi}{2\pi}\right) + \dot{a}_1(\tau)\frac{n\phi}{2\pi} + \sum_{k=1}^{N-1} \dot{a}_{k+1}(\tau)\sin\left(\frac{nk\phi}{2}\right) \\ &+ \left(\omega_0(\tau) + \dot{\theta}_s\right)\left\{\eta_x(\tau)\frac{n}{2\pi} + a_1(\tau)\frac{n}{2\pi} + \sum_{k=1}^{N-1}\frac{a_{k+1}(\tau)nk}{2}\cos\left(\frac{nk\phi}{2}\right)\right\} \\ &+ \dot{\eta}_\theta\frac{\delta_s}{2\pi}\,. \end{aligned} \tag{12.22}$$

This residual R_e is minimized in the Galerkin projection approach by making it orthogonal to the shape functions corresponding to the unknown variables $a_i(t)$ for $i = 1, \cdots, N$. This results in the following N ODEs governing the evolution of $a_i(\tau)$:

$$\int_0^{2\pi/n} R_e\frac{n\phi}{2\pi}\mathrm{d}\phi = 0\,, \quad \int_0^{2\pi/n} R_e\sin\left(\frac{nk\phi}{2}\right)\mathrm{d}\phi = 0\,, \quad \text{for } k = 1, \ldots, N-1\,. \tag{12.23}$$

The complete set of linear ODEs for the always cutting condition is given by $N + 4$ first order ODEs obtained from Eqs. (12.18a), (12.18b) along with (12.23). We next present the stability curves in the δ_s-ω_{0s} plane for different values of modulation amplitude m and frequencies ω_m using the Floquet theory.

12.6 Stability Curves

The complete set of linear ODEs from Eqs. (12.18a), (12.18b) along with (12.23) can be written in a compact form as $\dot{\mathbf{X}}(\tau) = \mathbf{A}(\tau)\mathbf{X}(\tau)$, with $\mathbf{A}(\tau)$ as a Jacobian matrix with time-periodic coefficients and $\mathbf{X}(\tau)$ as a state vector with components $\mathbf{X}(\tau) = \{a_1(\tau), a_2(\tau)...a_N(\tau), \eta_x(\tau), \dot{\eta}_x(\tau), \eta_\theta(\tau), \dot{\eta}_\theta(\tau)\}$. To study the stability characteristics of this system, we obtain the Floquet multipliers (as per the Floquet theory).

To generate the stability curves, we divide the chosen range of operating parameters into 4000×500 subregions with 4000 discrete points along the ω_{0s} axis and 500 discrete points along the δ_s axis. We next run the algorithm for generating the

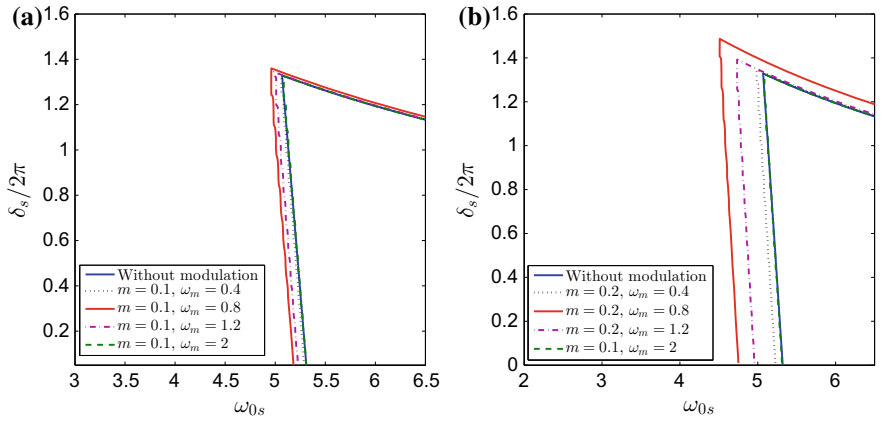

Fig. 12.3 Stability curves with modulation amplitude **a** 10% and **b** 20% of imposed angular velocity and different modulation frequencies. The other system parameters are $\beta = 1.5816$, $\psi = 13.8943$, $\zeta = 0.01$, $\kappa = 0.01$ and $n = 4$

fundamental matrix and obtain the Floquet multipliers, λ_i, as the eigenvalues of this matrix for each point. We check the magnitude of the dominant Floquet multiplier, if the dominant Floquet multiplier is less than 1 in magnitude, the system is stable whereas if it is greater that 1, the system is unstable. Hence, the stability boundary is obtained as the locus of the points corresponding to the dominant Floquet multiplier having a magnitude of 1. After evaluating the Floquet multipliers at every point, the boundary between the stable region and the unstable region is plotted in Fig. 12.3 for different modulation frequency for modulation amplitude of $m = 0.1$ and $m = 0.2$, respectively.

From Fig. 12.3 we can observe that as the modulation frequency approaches 1, i.e., the nondimensional frequency corresponding to the torsional mode, there is significant improvement in the stability of steady drilling. However, modulating frequency very close to 1 also causes a deterioration in the stability because of the resonance between the modulation and the torsional mode which could lead to stick-slip oscillations in the steady state itself. Furthermore, higher the m value, larger is the improvement in the stability property of the system. Again we should not use very high values of modulation amplitude as the combined effect of the modulation and the resulting forced torsional oscillations can set the system into stick-slip motions which are detrimental to the drill-string.

12.7 Conclusion

In this work, we present the effect of modulation of the turntable speed on the appearance of axial vibrations during rotary drilling. It has been observed that for a given value of modulation amplitude, the stable regime increases as the modula-

tion frequency approaches the nondimensional natural frequency corresponding to the torsional mode. Furthermore, modulation frequencies smaller than the torsional frequencies have been found to be more effective in suppressing axial vibrations.

References

1. Al-Zibdeh, A., AlQaradawi, M., Balachandran, B.: Effects of high frequency drive speed modulation on rotor with continuous stator contact. Int. J. Mech. Sci. **131**, 559–571 (2017)
2. Berlioz, A., Hagopian, J.D., Dufour, R., Draoui, E.: Dynamic behavior of a drill-string: experimental investigation of lateral instabilities. J. Vib. Acoust. **118**, 292–298 (1996)
3. Christoforou, A.P., Yigit, A.S.: Active control of stick-slip vibrations: The role of fully coupled dynamics. In: SPE Middle East Oil Show, Society of Petroleum Engineers (2001)
4. Dareing, D.W.: Drill collar length is a major factor in vibration control. J. Pet. Technol. **36**, 637–644 (1984)
5. Dunayevsky, V.A., Abbassian, F., Judzis, A.: Dynamic stability of drill-strings under fluctuating weight on bit. SPE Drill. Complet. **8**(2), 84–92 (1993)
6. Elsayed, M.A., Aissi, C.: Analysis of shock absorber characteristics for drill-strings. In: ASME 8th Biennial Conference on Engineering Systems Design and Analysis, pp. 93–101 (2006)
7. Farkas, M.: Periodic motions. Applied Mathematical Sciences. Springer, New York (1994)
8. Gupta, S.K., Wahi, P.: Global axialtorsional dynamics during rotary drilling. J. Sound Vib. **375**, 332–352 (2016)
9. Gupta, S.K., Wahi, P.: Tuned dynamics stabilizes an idealized regenerative axial-torsional model of rotary drilling. J. Sound Vib. **412**, 457–473 (2018)
10. Inamura, T., Sata, T.: Stability analysis of cutting under varying spindle speed. Int. J. Jpn. Soc.Preci. Eng. **33**, 13–29 (1975)
11. Insperger, T., Stepan, G.: Stability analysis of turning with periodic spindle speed modulation via semi-discretization. J. Vib. Control **10**, 1835–1855 (2004)
12. Jordan, D.W., Smith, P.: Nonlinear Ordinary Differential Equations: An Introduction to Dynamical Systems. Oxford University Press, Oxford Applied and Engineering Mathematics (1999)
13. Khulief, Y.A., Al-Naser, H.: Finite element dynamic analysis of drill-strings. Finite Elem. Anal. Des. **41**(13), 1270–1288 (2005)
14. Kreisle, L.F., Vance, J.M.: Mathematical analysis of the effect of a shock sub on the longitudinal vibrations of an oil well drill string. Soc. Pet. Eng. J. **10**(04), 349–356 (1970)
15. Pakdemirli, M., Ulsoy, A.: Perturbation analysis of spindle speed variation in machine tool chatter. J. Vib. Control **3**, 261–278 (1997)
16. Richard, T., Germay, C., Detournay, E.: A simplified model to explain the root cause of stick-slip vibrations in drilling systems with drag bits. J. Sound Vib. **305**(3), 432–456 (2007)
17. Sastry, S., Kapoor, S.G., DeVor, R.E., Dullerud, G.E.: Chatter stability analysis of the variable speed face-milling process. J. Manuf. Sci. Eng. **123**, 753–756 (2001)
18. Sexton, J.S., Milne, R.D., Stone, B.J.: A stability analysis of single-point machining with varying spindle speed. Appl. Math. Modell. **1**, 310–318 (1977)
19. Takemura, T., Kitamura, T., Hoshi, T., Okushima, K.: Active suppression of chatter by programmed variation of spindle speed. Ann. CIRP **23**, 121–122 (1974)
20. Wahi, P., Chatterjee, A.: Self-interrupted regenerative metal cutting in turning. Int. J. Non-linear Mech. **43**, 111–123 (2008)
21. Warren, T.W., Oster, J.H., Sinor, L.A., Chen, D.C.K.: Shock sub performance tests. In: IADC/SPE Drilling Conference, Society of Petroleum Engineers (1998)
22. Zamanian, M., Khadem, S.E., Ghazavi, M.R.: Stick-slip oscillations of drag bits by considering damping of drilling mud and active damping system. J. Pet. Sci. Eng. **59**, 289–299 (2007)

Chapter 13
Comparative Analysis of NES and TMD Performance via High-Dimensional Invariant Manifolds

Giuseppe Habib and Francesco Romeo

Abstract A comparative study between a tuned mass damper (TMD) and a nonlinear energy sink (NES), attached to a linear two-degree-of-freedom (DoF) mechanical system under impulsive excitation, is performed. The analysis involves different scenarios; namely, we consider the cases in which only one or both modes of the primary system are initially excited. First, exploiting a harmonic balance approach, the invariant manifolds describing the slow dynamics of the system are identified. Then, introducing the so-called relative dissipation power, the performance of the two absorbers is carefully compared, based on analytical computations. Results illustrate that the two absorbers have similar performance, albeit resorting to different mechanical properties: the NES achieve a broad frequency band of operation exploiting nonlinearity, while the TMD by increasing damping. An interesting feature, highlighted by the invariant manifold, is that the NES is generally unable to resonate with more than one mode of the primary system at the same time, rather, it experiences a sort of modal cascade.

Keywords Nonlinear energy sink · Tuned mass damper · Multi-modal vibration absorber · Impulsive energy dissipation

13.1 Introduction

Resonance vibrations have since ever aroused great concern in the engineering community due to their harmful consequences on mechanical and structural systems. Countless mitigation strategies, each with its pros and cons, have been so far proposed

G. Habib (✉)
Department of Applied Mechanics, Budapest University of Technology and Economics, Műegyetem rkp. 5., Budapest 1111, Hungary
e-mail: habib@mm.bme.hu

F. Romeo
Department of Structural Engineering and Geotechnics, Sapienza University of Rome, via Gramsci 53, 00197 Rome, Italy
e-mail: francesco.romeo@uniroma1.it

I. Kovacic and S. Lenci (eds.), *IUTAM Symposium on Exploiting Nonlinear Dynamics for Engineering Systems*, IUTAM Bookseries 37,
https://doi.org/10.1007/978-3-030-23692-2_13

in the literature; a common classification distinguishes between active, semi-active, passive and hybrid techniques which, in turn, can rely on devices characterized by linear and nonlinear behaviours. Among the passive linear vibration absorbers, tuned mass dampers (TMDs) are undoubtedly an established benchmark for mitigation of resonances [1, 2]. As known, their effectiveness lies in the tuning of their own natural frequency with that of the resonance to be mitigated, which implies that a single TMD can be used to optimally damp only one resonance of the host structure. Such intrinsic limitation of TMDs has prompted the engineering challenge of expanding the absorbers bandwidth of operation, giving the start to an extensive and multifaceted research activity. Among the proposed passive linear strategies, multiple tuned mass dampers (MTMDs) and spatially distributed MTMDs have been considered in literature, as reported in the recent review article [3]. Alternatively, willing to keep a single device in the control system, nonlinear absorbers designed to resonate for broad frequency band have been recently proposed. This brought the development of the nonlinear energy sink (NES), consisting of a small mass connected to the primary system by an essential nonlinear spring [4, 5]. Given the inherent different dynamic regimes involved in the passive linear and nonlinear absorbers during the vibration mitigation processes, a comparison between the performance of the two families of devices is not straightforward. Moreover, the variety of excitations, host structure typology, design constraints and objectives have so far lead to partial and incomplete performance comparisons between the two families of devices. In [6] it is illustrated that, in some specific conditions, the NES can outperform the TMD for resonance mitigation of a single-degree-of-freedom (DoF) linear primary system, exploiting quasiperiodic motions. In [7], a comparative analysis about the relevance of damping for NES and TMD revealed that, for low damping of the absorber, the NES can be more effective than the TMD also in narrow-band energy dissipation; increasing damping, the TMD behaves better than the NES. A comparison between NES and TMD performance in a periodically excited linear beam is performed in [8].

In this work, an attempt is made to qualitatively and quantitatively compare the TMD and the NES capabilities for the mitigation of broadband impulsive energy, considering various engineering scenarios. By exploiting the high-dimensional invariant manifold of a two-DoF host system, an effective performance measure is introduced, the so-called relative dissipation power.

13.2 Mathematical Model and Invariant Manifold Derivation

We consider the simple model shown in Fig. 13.1. The dynamics of this system is governed by the equations

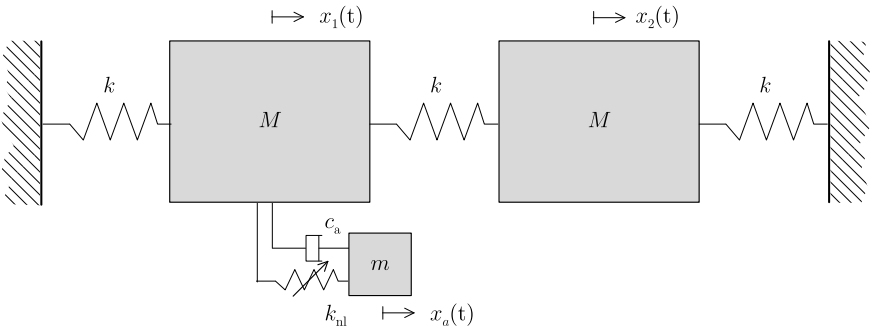

Fig. 13.1 A three-DoF system consisting of two coupled symmetric linear oscillators and an NES connected to one of them

$$\begin{aligned} &Mx_1'' + kx_1 + k\left(x_1 - x_2\right) + k_{nl}\left(x_1 - x_a\right)^3 + c_a\left(x_1' - x_a'\right) = 0 \\ &Mx_2'' + kx_2 + k\left(x_2 - x_1\right) = 0 \\ &mx_a'' + k_{nl}\left(x_a - x_1\right)^3 + c_a\left(x_a' - x_1'\right) = 0 \end{aligned} \tag{13.1}$$

where x_1 and x_2 refer to the displacements of the primary 2 DoF system, while x_a refers to the displacement of the absorber; m is assumed much smaller than M and the prime denote differentiation with respect to time t. The choice of considering an undamped hosting structure reflects results obtained in previous works [9], where it is illustrated that small damping in the primary system does not affect the overall qualitative dynamics.

We divide the system of Eqs. (13.1) by M, introduce the dimensionless time $T = \omega_n t$ and dimensionless variables $y_1 = \sqrt{\lambda_3}\left(x_1 + x_2\right)/2$, $y_2 = \sqrt{\lambda_3}\left(x_1 - x_2\right)/2$ and $y_3 = \sqrt{\lambda_3}\left(x_1 - x_a\right)$, where $\omega_n = \sqrt{k/M}$ and $\lambda_3 = k_{nl}/\left(m\omega_n^2\right)$, obtaining the governing equations in primary system dimensionless modal coordinates, i.e.

$$\begin{aligned} &\ddot{y}_1 + y_1 = \varepsilon\left(-\frac{y_3^3}{2} - \mu_a\dot{y}_3\right) \\ &\ddot{y}_2 + 3y_2 = \varepsilon\left(-\frac{y_3^3}{2} - \mu_a\dot{y}_3\right) \\ &\ddot{y}_3 + y_1 + 3y_2 + (1+\varepsilon)\left(y_3^3 + 2\mu_a\dot{y}_3\right) = 0 \end{aligned} \tag{13.2}$$

where $\varepsilon = m/M$, $\mu_a = c_a/\left(2m\omega_n\right)$ and the overdots denote differentiation with respect to T. Starting from Eqs. (13.2), by considering $\varepsilon \ll 1$ as a perturbation parameter, an analytical framework enabling to design the NES and to optimize its performance is derived.

In order to study the slow dynamics of the system, we collect terms of order ε^0, reducing the system to

$$\ddot{y}_1 + y_1 = 0 \tag{13.3}$$
$$\ddot{y}_2 + 3y_2 = 0 \tag{13.4}$$
$$\ddot{y}_3 + 2\mu_a \dot{y}_3 + y_3^3 = -y_1 - 3y_2. \tag{13.5}$$

We define an approximate solution by adopting the harmonic balance method [10, 11], assuming 1:1 resonance between the primary system and the absorber. The solutions of Eqs. (13.3) and (13.4) are $y_1 = A_1 e^{iT} + \text{c.c.}$ and $y_2 = A_2 e^{\sqrt{3}iT} + \text{c.c.}$, where A_1 and A_2 are complex and c.c. stands for complex conjugate. The approximate solution of Eq. (13.5) is expressed by $y_3 = B_1(t_1)\, e^{iT} + B_2(t_1)\, e^{\sqrt{3}iT} + \text{c.c.}$

We substitute the approximate solutions of y_1, y_2 and y_3 into Eq. (13.5) and collect harmonics of e^{iT} and $e^{\sqrt{3}iT}$, obtaining

$$\begin{aligned} \left(e^{iT}\right) &: -B_1 + A_1 + 3B_1^2\bar{B}_1 + 6B_1B_2\bar{B}_2 + 2\mu_a i B_1 = 0 \\ \left(e^{\sqrt{3}iT}\right) &: -3B_2 + 3A_2 + 3B_2^2\bar{B}_2 + 6B_1\bar{B}_1B_2 + 2\sqrt{3}\mu_a i B_2 = 0. \end{aligned} \tag{13.6}$$

By defining $B_1 = 1/2 b_1 e^{i\beta_1}$, $B_2 = 1/2 b_2 e^{i\beta_2}$, $A_1 = 1/2 a_1 e^{i\alpha_1}$ and $A_2 = 1/2 a_2 e^{i\alpha_2}$, and separating real and imaginary parts of the first equation of (13.6), we have

$$\begin{aligned} \frac{1}{2}a_1 \cos\alpha_1 &= \frac{1}{2}b_1\left(1 - \frac{3}{4}b_1^2 - \frac{3}{2}b_2^2\right)\cos\beta_1 + \mu_a b_1 \sin\beta_1 \\ \frac{1}{2}a_1 \sin\alpha_1 &= \frac{1}{2}b_1\left(1 - \frac{3}{4}b_1^2 - \frac{3}{2}b_2^2\right)\sin\beta_1 - \mu_a b_1 \cos\beta_1. \end{aligned} \tag{13.7}$$

We calculate the squares of the two equations of (13.7) and we sum them up attaining

$$a_1^2 = b_1^2\left(1 - \frac{3}{4}b_1^2 - \frac{3}{2}b_2^2\right)^2 + 4\mu_a^2 b_1^2. \tag{13.8}$$

Repeating the same operation with the second equation of (13.6) we obtain

$$a_2^2 = b_2^2\left(1 - \frac{1}{4}b_2^2 - \frac{1}{2}b_1^2\right)^2 + \frac{4}{3}\mu_a^2 b_2^2. \tag{13.9}$$

Equations (13.8) and (13.9) describe the invariant manifold that relates the slow dynamics of y_3 with respect to y_1 and y_2. A detailed analysis of the obtained manifold is performed in the following sections by considering separately the cases in which the excitation involves either a single or both modes.

We notice that, although the absorber is characterized by the three parameters ε, μ_a and λ_3, thanks to the performed non-dimensionalization the only parameter left in the manifold equation is μ_a. λ_3 simply scales the amplitude of the variables, while ε is proportional to the energy dissipation rate, but, if it is kept small, it has no

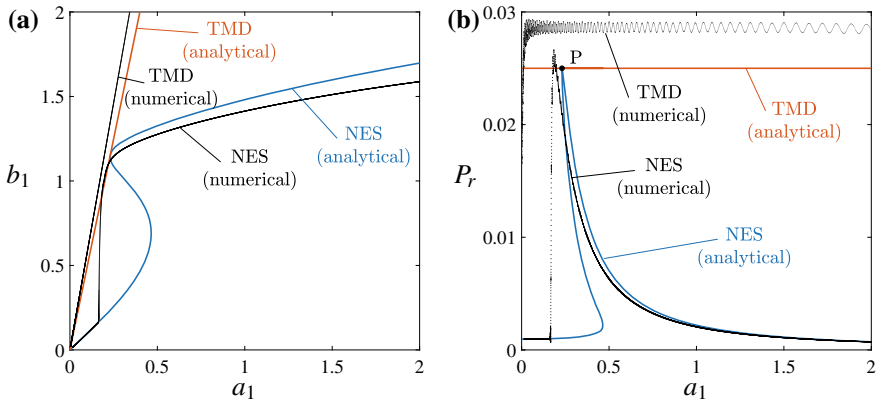

Fig. 13.2 **a** Invariant manifold for the first mode ($\mu_a = 0.1$, $\gamma = 1$ for TMD); **b** Estimated relative dissipation power based on the invariant manifold ($\mu_a = 0.1$, $\varepsilon = 0.01$, $\gamma = 1$ for TMD). Blue and orange lines refer to analytical results of NES and TMD, respectively, black lines refer to numerical results

qualitative effect on the slow dynamics of the system, which can be captured by the adopted approach.

13.3 Single Mode Dynamics

We consider at first the case when only the first mode of the primary system is initially excited. In this case, y_2 is assumed of order ε, therefore the invariant manifold is defined only by Eq. (13.8), with $b_2 = 0$, i.e.

$$a_1^2 = b_1^2 \left(1 - \frac{3}{4} b_1^2\right)^2 + 4\mu_a^2 b_1^2. \tag{13.10}$$

The relative manifold is illustrated in Fig. 13.2a for $\mu_a = 0.1$. The black line in the figure is the result of a numerical simulation, which qualitatively confirms analytical results. Modal amplitudes were obtained through a wavelet transformation of the system time series. Although stability of the manifold was not studied, it can be guessed that, if for a single a_1 value there are three different b_1 values, the middle one is unstable.

The invariant manifold enables one to predict the amplitude of oscillation of y_3 depending on the oscillation amplitude y_1. Large values of y_3 (i.e. b_1) correspond to high dissipation power. Adopting the hypothesis of single harmonic response, dissipation power in one period is given by $\varepsilon \mu_a b_1^2$. However, from an engineering point of view, it is more significant to indicate the energy dissipated in one period with respect to the energy present in the primary system, that is (if only the first mode

is activated) $P_r = \varepsilon\mu_a b_1^2/a_1^2$. This curve is illustrated in Fig. 13.2b for $\mu_a = 0.1$ and $\varepsilon = 0.01$.

The shape of the P_r function gives important information about the performance of the NES. For very high values of a_1, P_r is very low (P_r tends to zeros for $a_1 \to \infty$); however, at large amplitudes additional harmonics, overlooked by the adopted analytical approach, might become more relevant. Reducing a_1, P_r increases until it reaches a high peak (called P in the figure), whose exact position can be calculated and it is $\mathrm{P} = \left(4\mu_a/\sqrt{3}, \varepsilon/(4\mu_a)\right)$. For $a_1 < 4\mu_a/\sqrt{3}$, P_r has a sudden decrease and it reaches an almost constant plateau until $a_1 = 0$ (for $a_1 \to 0$, $P_d = \varepsilon\mu_a/(1 + 4\mu_a^2)$). This lower limit corresponds to the minimum energy threshold below which the NES is not activated, a feature which has been extensively studied [5]. Numerical results, represented by black dots in the figure, agree very well with the analytical prediction. The main difference consists in the slightly mismatching position of the peak.

During the design of an NES, the position of point P is clearly a key parameter for defining the performance of the device and the range of operation. Since the amplitude was normalized with respect to $\sqrt{\lambda_3}$, this parameter can be tuned to adjust the energy level of optimal operation. Furthermore, the a_1-coordinate of point P grows linearly with μ_a. Increases of μ_a also enlarge the peak and lower P, reducing the maximal dissipation power, but widening the amplitude range of operation.

The same procedure performed for the NES, can be analogously computed for the TMD, in order to compare the two absorbers. The analysis leads to the invariant manifold described by the equation

$$a_1^2 = b_1^2\left(1-\gamma^2\right)^2 + 4\mu_a^2 b_1^2 \quad \text{or} \quad a_1 = b_1\sqrt{\left(1-\gamma^2\right)^2 + 4\mu_a^2}, \tag{13.11}$$

where γ is the ratio between the natural frequency of the TMD and of the primary system. Orange lines in Fig. 13.2a and b illustrate the manifold and the relative dissipation power for the TMD, which can be directly compared with the NES. It is particularly interesting that, if $\gamma = 1$, the relative dissipation power of the TMD is always equal to the maximum P_r of the NES. This clearly highlights the superiority of the TMD over the NES when it is properly tuned and only one mode is involved. Also in this case, numerical results qualitatively confirm analytical predictions.

13.4 Two Modes Dynamics

In the hypothesis that both modes of the primary system are activated, Eqs. (13.8) and (13.9) form a unique system of equations. This defines the invariant manifold, that is a 2-dimensional surface in the 4-dimensional space (a_1, a_2, b_1, b_2). Figure 13.3 illustrates the manifold exploiting two projections: x- and y-axes mark the modal amplitude in the primary system of the first (a_1) and second (a_2) mode, respectively; z-axis indicates the modal amplitude related to the first (b_1, Fig. 13.3a) and to the second mode (b_2, Fig. 13.3b) in the NES.

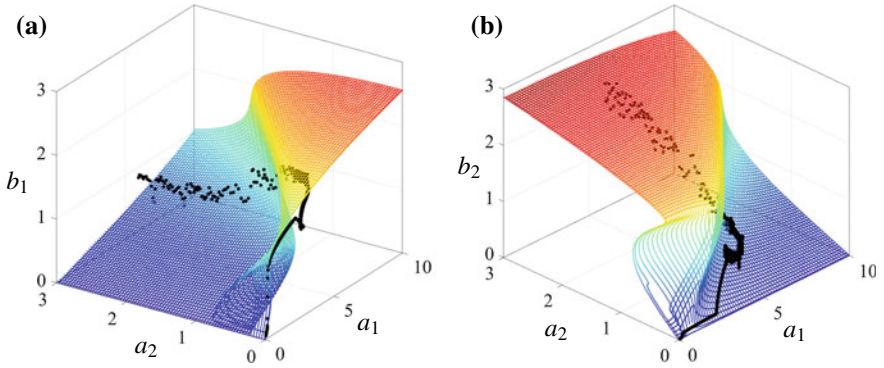

Fig. 13.3 Invariant manifold projected on the (a_1, a_2, b_1) (**a**) and on the (a_1, a_2, b_2) (**b**) spaces for $\mu_a = 0.1$. The black dots mark the instantaneous modal amplitude of the time series in Fig. 13.4 calculated through a wavelet transformation. Subplots **c** and **d** offer top views of subplots **a** and **b**, respectively

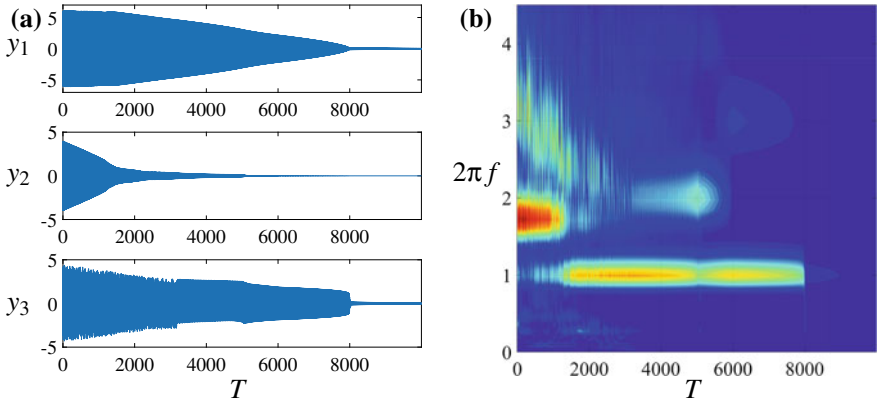

Fig. 13.4 **a** Time series for system (13.2) with $\mu_a = 0.1$ and $\varepsilon = 0.01$; **b** wavelet transformation of y_3

We notice the interesting feature that, for given a_1 and a_2 values, either b_1 is large and b_2 is small, or the opposite is verified. An ideal line, splitting in two the a_1, a_2 space, divides the two regions where either b_1 or b_2 is larger. This consideration has important practical consequences, indeed it means that the NES, although is able to interact with modes at different frequencies, it works well with only one at a time.

A numerical validation of this phenomenon is illustrated in Fig. 13.4. Figure 13.4a shows time series for the three system coordinates, while Fig. 13.4b depicts the instantaneous frequency of the NES motion (y_3), obtained through a wavelet transformation. For $T < 1500$, Fig. 13.4b clearly illustrates that the NES has a strong coupling with the second mode (at 1.732 rad/s), while it does not interact with the first one. This is consistent with the manifold in Fig. 13.3; in fact, for the adopted

initial conditions ($y_1(0) = 6$ and $y_2(0) = 4$), b_1 is relatively small, while b_2 is much larger. This causes a relatively rapid dissipation of energy on the second mode of the primary system, while the first one is almost unaffected by the absorber, as it can be verified from the time series in Fig. 13.4a. At $T \approx 1500$, the NES abruptly disengages from the second mode and it couples with the first one, forming a sort of modal cascade. In terms of invariant manifold, this coincides to reach the boundary dividing the regions where either b_1 or b_2 is large. The correspondence between analytical and numerical results is given by the black dots in Fig. 13.3a and b: although the black dots, indicating the modal amplitude in the NES b_1 and b_2, do not exactly lie on the manifold, the transition between second and first modes is well predicted in terms of modal amplitudes a_1 and a_2. For $1500 < T < 8000$ the energy decreases on both modes; however, the dissipation rate for the second mode is significantly diminished, in virtue of the discussed modal transition. At $T \approx 8000$ the NES disengages also from the first mode, causing a sudden drop of its oscillation amplitude and of the energy dissipation on the first mode. Considering that at this point most of the energy was only on the first mode, this phenomenon practically coincides with the drop illustrated in Fig. 13.2 for the case of single mode dynamics. Super- and sub-harmonic resonances, visible in Fig. 13.4b, are overlooked by the analytical framework adopted.

We notice that, if the system is initially in the region where the first mode is prevalent but there is some energy also on the second mode, the NES will have a stronger coupling with the first mode, but it will still dissipate some energy on the second mode. This cancels the modal cascade, which seems to occurs only from higher modes to lower ones. We also remark that the ideal line dividing the two regions of modal coupling follows a somehow different trend for low amplitude. The minimum energy threshold of each mode and the S shape observed in Fig. 13.2a is dominant over the interaction between the two modes, causing a drop of modal amplitude for the first mode at $a_1 = 0.23$ and for the second mode at $a_2 = 0.23$. Indeed, the best dissipation performance are obtained for a_1 and a_2 only slightly larger than these limits.

13.4.1 NES-TMD Comparison

In the following, we compare the NES and TMD performance while operating on the primary system with both modes activated. We consider the initial conditions $y_1(0) = y_2(0) = 0$, $\dot{y}_1(0) = \dot{y}_2(0) = v_0$ and identify parameters providing the minimum dissipation time, given $\varepsilon = 0.01$. For the NES, the only parameter to be optimized is μ_a as a function of the initial velocity v_0; we remind that the amplitude is scaled with $\sqrt{\lambda_3}$, therefore, in principle, the system can be set to any energy level. For the TMD, optimization is performed tuning μ_a and γ; because of the linearity of the system, dynamics is invariant with respect to v_0.

As optimal conditions, we obtain for the NES that 70% of the initial energy is dissipated in 147 time units for $\mu_a = 0.1248$, if $v_0 = 0.504$. Regarding the TMD,

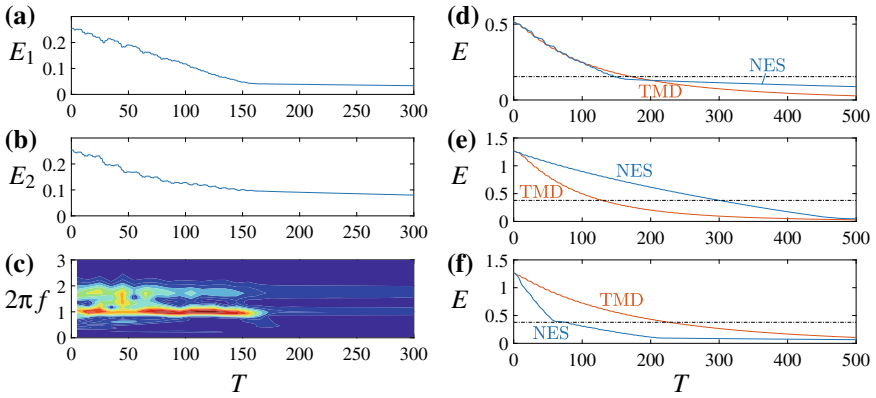

Fig. 13.5 **a**, **b** Energy decrement on the first and on the second mode for system (13.2) with $\mu_a = 0.1248$, $\varepsilon = 0.01$, $\dot{y}_1(0) = \dot{y}_2(0) = 0.504$ and $y_1(0) = y_2(0) = 0$; **c** wavelet transformation of y_3; **d**, **e**, **f** energy decrement comparison with TMD ($\mu_a = 0.204$, $\gamma = 1.04$) for the initial conditions $y_1(0) = y_2(0) = 0$ and $\dot{y}_1(0) = \dot{y}_2(0) = 0.504$ (**d**), $\dot{y}_1(0) = 1$ and $\dot{y}_2(0) = 0.5$ (**e**), $\dot{y}_1(0) = 0.5$ and $\dot{y}_2(0) = 1$ (**f**)

minimum dissipation time of 172 time units is obtained for $\mu_a = 0.204$ and $\gamma = 1.04$. In these conditions the NES outperform the TMD by 17% in terms of dissipation time.

Extensive numerical simulations show that, for optimal parameter values, the NES has a strong interaction with the first mode, keeping, at the same time, a weak interaction with the second one, therefore the modal cascade shown in Fig. 13.4 is no longer present. This can be clearly seen from the wavelet transformation of y_3 in Fig. 13.5c, which refers to the optimal NES. Figure 13.5a and b depict the energy decrement on the first and on the second mode of the primary system, respectively. It can be noted that energy decreases on both modes at a similar rate, until $T \approx 150$, when the NES disengages from both of them almost simultaneously.

Referring to an optimal TMD, because the value of γ is only slightly larger than 1, y_1 oscillation amplitude undergoes a much rapid decrement than y_2; this was verified through direct numerical simulations, not shown here for the sake of brevity. Nevertheless, energy of the second mode is still dissipated thanks to the quite large damping ($\mu_a = 0.204$).

A comparison of the energy decrement obtained by the NES and by the TMD is illustrated in Fig. 13.5d, which shows that the NES only slightly outperforms the TMD. However, after dissipating 70% of the energy, it becomes almost ineffective, while the TMD works also for small amplitude. Figure 13.5e and f, depict the energy decrement adopting the same absorbers, but changing initial conditions. For $\dot{y}_1(0) = 1$ and $\dot{y}_2(0) = 0.5$ (more energy on the first mode, Fig. 13.5e) the NES has a significant deterioration of its performance, while the TMD an improvement. Conversely, increasing the initial energy on the second mode ($\dot{y}_1(0) = 0.5$ and $\dot{y}_2(0) = 1$,

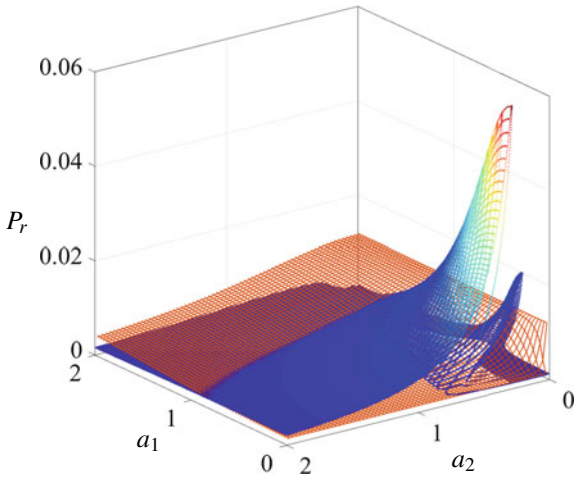

Fig. 13.6 Relative dissipation power for the NES (colored surface) and the TMD (orange surface) with $\varepsilon = 0.01$ and $\mu_a = 0.12$ (NES) or $\gamma = 1.04$ and $\mu_a = 0.204$ (TMD)

Fig. 13.5f), the TMD has slightly worst performance, while the NES has an important improvement.

This behavior can be better understood by plotting the relative dissipation power P_r as a function of a_1 and a_2. This is defined by the equation $P_r = \varepsilon\mu_a \left(b_1^2 + 3b_2^2\right) / \left(a_1^2 + 3a_2^2\right)$ and it is illustrated in Fig. 13.6 (colored surface) for $\varepsilon = 0.01$ and $\mu_a = 0.1248$. In the figure, we notice that there are two peaks; the smaller is related to the first mode and the higher one to the second mode. These correspond to the points with maximum dissipation power (their height is $\varepsilon/(4\mu_a)$ and $3\varepsilon/(4\mu_a)$, respectively, as it can be computed by the hypothesis of single mode dynamics). For the initial conditions $\dot{y}_1(0) = \dot{y}_2(0) = 0.504$ the NES fully exploits the smaller peak, obtaining a good energy dissipation for the first mode. Increasing the initial energy on the first mode ($\dot{y}_1(0) = 1$), the peak of the second mode is still not exploited, while some additional time is required before reaching the peak of the first mode. This results in a deterioration of the performance. On the contrary, increasing the energy on the second mode ($\dot{y}_2(0) = 1$), the NES first exploits the peak relative to the second mode and then the one relative to the first one. This can be recognized observing that the energy decrement approximately consists of three linear segments. These correspond to dissipation of the energy on the second mode, then on the first mode and finally slowly dissipated residual energy.

Overlapping the relative dissipation power surface of the TMD (orange surface in Fig. 13.6) over the one of the NES, we can directly estimate the relative performance of the two absorbers. In general, for the same a_1, a_2 values, the surface with the higher P_r value is the one providing better performance.

13.5 Conclusions

The dynamics of an NES attached to a two-DoF linear oscillator was investigated, evaluating the performance of the absorber against impulsive excitations. Invariant manifolds, describing the slow dynamics of the system, proved to be an effective tool to predict quite accurately the behavior and the performance of the absorber. In particular, they allowed us to explain how the NES couples with the primary system when more than one mode is activated. If the energy content on both modes is sufficient, the NES first dissipates energy on the higher mode and then, once a threshold is reached, it couples with the lower one abruptly decoupling from the higher one. A direct comparison between the NES and the TMD illustrated which conditions are required for the NES to outperform the TMD. Prediction of the comparative behavior based on the invariant manifold was confirmed by direct numerical simulations.

The verification of the existence of the described modal cascade for primary systems with large number of DoF will be the subject of a future study.

Acknowledgements GH acknowledges the financial support of the European Union, H2020 Marie Skłodowska-Curie Individual Fellowship, Grant Agreement 704133. FR acknowledges the financial support of PRIN 2015 N. 2015TTJN95.

References

1. Frahm, H.: Device for damping vibrations of bodies. US Patent 989,958, 18 Apr 1911
2. Den Hartog, J.P.: Mechanical Vibrations. McGraw-Hill, New York (1956)
3. Elias, S., Matsagar, V.: Research developments in vibration control of structures using passive tuned mass dampers. Annu. Rev. Control **44**, 129–156 (2017)
4. Gendelman, O., Manevitch, L., Vakakis, A.F., Mcloskey, R.: Energy pumping in nonlinear mechanical oscillators: part i-dynamics of the underlying Hamiltonian systems. J. Appl. Mech. **68**(1), 34–41 (2001)
5. Kerschen, G., Lee, Y.S., Vakakis, A.F., McFarland, D.M., Bergman, L.A.: Irreversible passive energy transfer in coupled oscillators with essential nonlinearity. SIAM J. Appl. Math. **66**(2), 648–679 (2005)
6. Gendelman, O.V., Gourdon, E., Lamarque, C.-H.: Quasiperiodic energy pumping in coupled oscillators under periodic forcing. J. Sound Vib. **294**(4–5), 651–662 (2006)
7. Starosvetsky, Y., Gendelman, O.: Attractors of harmonically forced linear oscillator with attached nonlinear energy sink. II: optimization of a nonlinear vibration absorber. Nonlinear Dyn. **51**(1–2), 47 (2008)
8. Parseh, M., Dardel, M., Ghasemi, M.H.: Performance comparison of nonlinear energy sink and linear tuned mass damper in steady-state dynamics of a linear beam. Nonlinear Dyn. **81**(4), 1981–2002 (2015)
9. Romeo, F., Sigalov, G., Bergman, L.A., Vakakis, A.F.: Dynamics of a linear oscillator coupled to a bistable light attachment: numerical study. J. Comput. Nonlinear Dyn. **10**(1), 011007 (2015)
10. Luongo, A., Zulli, D.: Dynamic analysis of externally excited nes-controlled systems via a mixed multiple scale/harmonic balance algorithm. Nonlinear Dyn. **70**(3), 2049–2061 (2012)
11. Luongo, A., Zulli, D.: Aeroelastic instability analysis of NES-controlled systems via a mixed multiple scale/harmonic balance method. J. Vib. Control (2013). https://doi.org/10.1177/1077546313480542

Chapter 14
Nonlinear Dynamics of a Planar Hinged-Simply Supported Beam with One End Spring: Higher Order Resonances

Lukasz Kloda, Stefano Lenci and Jerzy Warminski

Abstract The paper addresses the nonlinear dynamics of a hinged simply supported beam with an axial elastic support. The investigation is based on the Multiple Time Scales Method (MTSM) applied directly to the governing partial differential equations of motion, and is focused on the first seven bending resonances of a planar system. The effect of axial spring on hardening/softening phenomena is illustrated. Backbone Curves (BbCs) and Frequency Response Curves (FRCs) for selected cases are shown and compared with their numerical counterpart done with the Finite Element Method (FEM) to cross-checking the reliability of analytical and numerical methods.

Keywords Hardening/softening behaviour · Higher order resonances · Hinged-simply supported beam · Multiple time scales method · Finite element method · Frequency response curve

14.1 Introduction

Nowadays, a lot of attention is paid to nonlinear dynamics of beams under different boundary conditions, like clamped-clamped, cantilever, hinged-hinged, hinged-simply supported and so on. Advanced software mathematical manipulators, and more powerful hardware, allow us to attack analytically more and more

L. Kloda (✉) · S. Lenci
Department of Civil and Building Engineering, and Architecture,
Polytechnic University of Marche, via Brecce Bianche, 60131 Ancona, Italy
e-mail: l.kloda@pollub.pl

S. Lenci
e-mail: lenci@univpm.it

L. Kloda · J. Warminski
Department of Applied Mechanics, Lublin University of Technology, ul. Nadbystrzycka 36,
20-618 Lublin, Poland
e-mail: j.warminski@pollub.pl

I. Kovacic and S. Lenci (eds.), *IUTAM Symposium on Exploiting Nonlinear Dynamics for Engineering Systems*, IUTAM Bookseries 37,
https://doi.org/10.1007/978-3-030-23692-2_14

accurate models of such systems by covering all geometrical effects. However, nonlinear dynamics of higher order modes are frequently omitted in investigations, as the main attention is commonly devoted to principal natural frequencies.

Higher order resonances are presented in [7] for hinged-hinged beams, where it is shown that frequency response curves of the first six bending modes are always hardening. The first three bending modes of a Micro Electro Mechanical System (MEMS) in clamped-clamped configuration are studied analytically and experimentally in [3], again highlighting that the structure is always hardening. In this paper authors present, hitherto unexplored, higher order resonances of a hinged simply supported beam with an elastic longitudinal support for arbitrarily stiffnesses. For varying axial spring stiffness the structure can be softening, hardening or can have a linear backbone curve.

14.2 Beam Model

A planar system composed of a hinged simply supported beam and a linear axial spring attached to the sliding support, see Fig. 14.1, is considered. The beam has a linear elastic material behaviour and performs displacements along three directions (axial Z, transversal X and rotational). Different values of spring stiffness determinate three possible scenarios:

- $k_s = 0$ (i.e. no spring): the beam is *hinged-simply supported*, namely one end is free to move in Z-direction;
- $k_s \to \infty$: the beam end displacement is blocked and the structure is *hinged-hinged*;
- $0 < k_s < \infty$ (which is the most general case): the system is *hinged-simply supported-spring*.

Finite Element Model described in Sect. 14.2.2 requires to work with a dimensional object, whose geometrical and mechanical properties are presented in Table 14.1. However, to better understand forthcoming analytical results, the dimensionless parameter $\kappa = \frac{k_s L}{EA}$ is introduced.

All nonlinearities of the structure are geometric, and are *not* caused by nonlinear material.

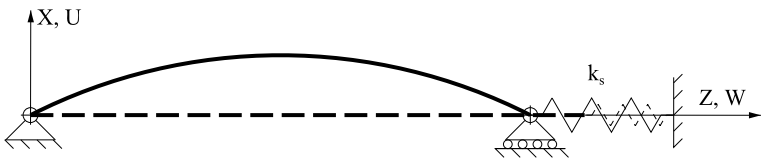

Fig. 14.1 The beam model

Table 14.1 Beam properties

Beam length L (m)	Cross section $B \times H$ (mm)	Density ρ (kg/m^3)	Young modulus E (GPa)	Poisson's ratio ν (-)	Shear factor χ (-)	Spring stiffness κ (-)
0.5	50 × 50	7850	210	0.3	0.85	$0 \leq \cdots \leq \infty$

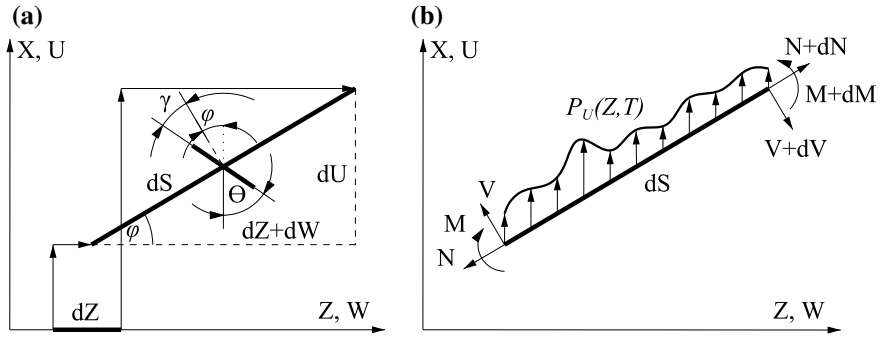

Fig. 14.2 Kinematics (**a**) and coplanar forces (**b**) of the deformed beam element

14.2.1 Analytical Approach

The beam element undergoes large in plane deformations, where beam infinitesimal length in rest (deformed) configuration is dZ (dS). Transversal and axial displacements are denoted by U and W, respectively. Slope angle φ does not coincide with rotation of cross section θ because the beam is shearable. In other words, the angle θ consists of the slope angle φ and Timoshenko angle γ, and in our investigations $\gamma \neq 0$, see Fig. 14.2a. The geometrical curvature is used ($k = d\theta/dS$), as an extensible beam is considered. For more exhaustive information on different curvature definitions we refer to [1, 8].

Combining (linear) material law behaviour, equilibrium (Fig. 14.2b) and kinematics (Fig. 14.2a) of the beam element the following system of partial differential equations of motion is obtained [5]:

$$\left\{ EA\left[\sqrt{(1+W')^2+U'^2}-1\right]\frac{1+W'}{\sqrt{(1+W')^2+U'^2}} + \right.$$
$$\left. + GA\left[\theta - \arctan\left(\frac{U'}{1+W'}\right)\right]\frac{U'}{\sqrt{(1+W')^2+U'^2}} \right\}' = \rho A\ddot{W} + C_W\dot{W}, \quad (14.1)$$

$$\left\{EA\left[\sqrt{(1+W')^2+U'^2}-1\right]\frac{U'}{\sqrt{(1+W')^2+U'^2}}+\right.$$
$$\left.-GA\left[\theta-\arctan\left(\frac{U'}{1+W'}\right)\right]\frac{1+W'}{\sqrt{(1+W')^2+U'^2}}\right\}'=$$
$$=\rho A\ddot{U}+C_U\dot{U}+P_U(Z,T), \tag{14.2}$$

$$\left[EJ\frac{\theta'}{\sqrt{(1+W')^2+U'^2}}\right]'+$$
$$-GA\left[\theta-\arctan\left(\frac{U'}{1+W'}\right)\right]\sqrt{(1+W')^2+U'^2}=\rho J\ddot{\theta}+C_\theta\dot{\theta}, \tag{14.3}$$

where dot ($\dot{}$) and prime ($'$) correspond to partial derivative with respect to time T and coordinate Z. Terms C_θ, C_U and C_W denote linear viscous damping coefficients. We refer to [5] for the definition of the various parameters appearing in Eqs. (14.1)–(14.3) and for further details. Related boundary conditions are:

$$W(0,T)=0,\ U(0,T)=0,\ U(L,T)=0,\ M(0,T)=0,\ M(L,T)=0, \tag{14.4}$$
$$N(L,T)\cos\varphi+V(L,T)\sin\varphi+k_sW(L,T)=0. \tag{14.5}$$

Detailed procedure of applying the MTSM to the exact partial differential equations of motion (14.1)–(14.3) is shown in [5] and will not be repeated here.

14.2.2 Numerical Approach

The finite element beam model is made of 100 (initially) equal length *B31* type elements. Each element undergoes large in plane deformation, and is provided by local coordinate system at each node, that allows to compute the true deformations and stresses. The out of plane displacement is restrained (equals to zero) as well as associated rotations ($RZ=0$, $RX=0$ but $RY\neq 0$). Linear spring is fixed to beam end and axially anchored to the ground. For $\kappa=0$ the spring is eliminated, and for $\kappa=\infty$ the beam end is blocked in the axial direction.

Transient simulations have been set in dynamic explicit module, and the axial and transversal displacements of relevant nodes have been sampled with a frequency that is 40 times of the frequency of excitation, for a time large enough to detect the amplitudes of the steady state motion. Frequency excitation has been gradually swept, forward and backward around the nth natural frequency in order to reconstruct the whole Frequency Response Curve (FRC). More details about this method are presented in [4–6].

14.3 Results

14.3.1 Linear Oscillations

The nth natural circular frequencies depend on geometrical and mechanical properties of the beam and are given by:

$$\omega_n^2 = \frac{\pi^2 n^2 J(E+G) + AGL^2 - \sqrt{\left[AGL^2 + \pi^2 Jn^2(E+G)\right]^2 - 4\pi^4 EGJ^2 n^4}}{2JL^2\rho}, \tag{14.6}$$

while the associated mode shapes are:

$$\hat{U}_n(Z) = \sin\left(\frac{n\pi Z}{L}\right), \quad \hat{\theta}_n(Z) = \frac{\pi^2 n^2 G - L^2\rho\omega_n^2}{\pi GnL}\cos\left(\frac{n\pi Z}{L}\right). \tag{14.7}$$

Note that axial boundary conditions do *not* influence $\hat{U}_n(Z)$, $\hat{\theta}_n(Z)$ and ω_n.

In this paper the ratio between the axial and transversal displacements is assumed to be small, so that the longitudinal linear modes of the beam have not be determined in the analytical part of the work. A set of calculation results is presented in Table 14.2. Numerical computations have been done with displacement normalization by *Eigensolver Lanczos* module of Abaqus_CAE© commercial software. The

Table 14.2 The lowest ten linear natural frequencies and corresponding free vibration mode shapes. Single star (*) corresponds to hinged-simply supported case and two stars (**) describe hinged-hinged beam

Mode No.	Mode shape	FEM frequency (rad/s)	Analytic frequency (rad/s)	Maxima of displacement/rotation vectors	
				FEM (-)/(°)	MTSM: ε^1 (-)/(°)
1	1st bending	2899.50	2899.51	1/6.13	1/6.130
2	2nd bending	11086.68	11087.12	1/11.45	1/11.447
3	1st longitudinal	16248.95* 32496.63**	Not included	1/0	Not included
4	3rd bending	23373.45	23377.34	1/15.53	15.535
5	4th bending	38511.53	38511.84	1/18.41	1/18.382
6	2nd longitudinal	48742.44* 64986.99**	Not included	1/0	Not included
7	5th bending	55501.89	55521.12	1/20.19	1/20.197
8	6th bending	734657.78	73702.39	1/21.20	1/21.223
9	3rd longitudinal	81222.74* 97458.49**	Not included	1/0	Not included
10	7th bending	92526.19	92614.78	1/21.65	1/21.683

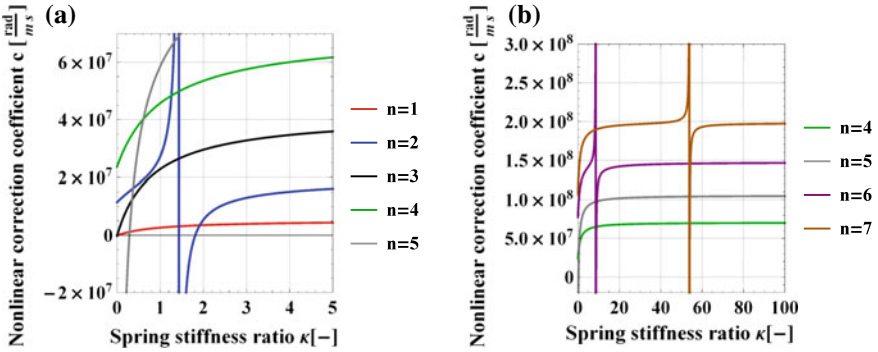

Fig. 14.3 Nonlinear correction coefficient of the first seven bending modes

FEM analysis involves 3×100 degrees of freedom in X-, Z- and RY-directions, as consequence, longitudinal modes are spontaneously covered in outcomes. The influence of boundary conditions on the natural frequencies in the longitudinal direction is shown for 3rd, 6th, and 9th modes. By varying spring stiffnesses from 0 to ∞, natural frequencies in the longitudinal direction can be changed of about 100%, 33.3% and 20%, respectively.

14.3.2 Free Nonlinear Oscillations—Hardening and Softening Behaviors

Free nonlinear oscillations can undergo hardening or softening phenomena. If free oscillations frequency decreases with increasing vibrations amplitude it is called softening, and if the frequency increases it is named hardening. When frequency of oscillations is independent of the amplitude (which occurs only for some specific values of the parameters), the system has a linear nature also in the nonlinear regime.

This behaviour is mathematically described by nonlinear correction coefficient c which is given by

$$\sigma = \frac{c_1}{c_2} a^2 = ca^2, \; c_2 = \rho\omega_n \frac{J\left(Gn^2\pi^2 - L^2\rho\omega_n^2\right)^2 + AL}{G^2 L n^2 \pi^2}, \tag{14.8}$$

and where the real parameter c_1, that depends on mechanical and geometrical properties of the structure, has a long expression that cannot be reported here; it is given in [5].

σ denotes the (additive) detuning parameter with respect to nth natural frequency ω_n (i.e. the actual frequency of oscillation is $\Omega = \omega_n + \sigma$) and a is the amplitude of oscillation. It is easy to observe that $c > 0$ determines hardening behavior, while $c < 0$ softening phenomenon.

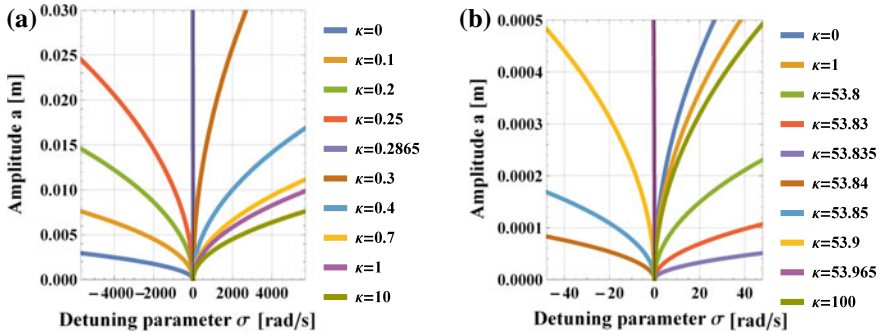

Fig. 14.4 Backbone curves of 5th (**a**) and 7th (**b**) bending modes

For the first seven bending modes the nonlinear correction coefficients are shown in Fig. 14.3a, b. On average, c increases when the order modes growth. All curves have the smallest values for $\kappa = 0$ (simply supported beam) and as spring stiffness increases, they tend to the constant value corresponding to hinged-hinged beam. Astonishing singularities (the parameter c tends to $\pm\infty$) are observed for 2nd, 6th and 7th modes. Softening behavior appears for small spring stiffnesses of the 1st bending mode; also the 5th mode has negative values in range $0 < \kappa < 0.2865$. Examples of BbCs are shown in Fig. 14.4a, b. Nonlinear oscillations of a hinged-simply supported beam ($\kappa = 0$) have softening nature for 5th bending mode. As axial spring stiffness increases the BbCs bends toward right, across linear case ($\kappa = 0.2865$) up to the limit branch, which corresponds to hinged-hinged beam ($\kappa = \infty$). The case of the 7th bending mode is much more different. Beams with hinged and simply supported right end present similar levels of hardening, and even huge changes scarcely influence the nonlinear dynamics, *except* at a singularity, which occurs between $\kappa = 50$ and $\kappa = 60$. The hardening to softening to hardening transition across the singularity is well described in Fig. 14.4b. Linear oscillations appear again for $\kappa = 53.835$.

Numerical verification of BbCs is possible, and can be done as in [2], but to limit the length of the paper this comparative analysis is left for future works. Validation of the singularity of the 2nd bending mode by FEM will be presented in Sect. 14.3.3 in terms of FRC.

14.3.3 Forced Damped Vibrations—Frequency Response Curves

In this section damping factors (in rotational and transversal directions) are equal to 6% and external excitation is assumed to be an harmonic concentrated force p_v, applied to $Z = L/4$ in vertical direction (X). The frequency response curve, determined analytically by the MTSM, is given by [4, 5]

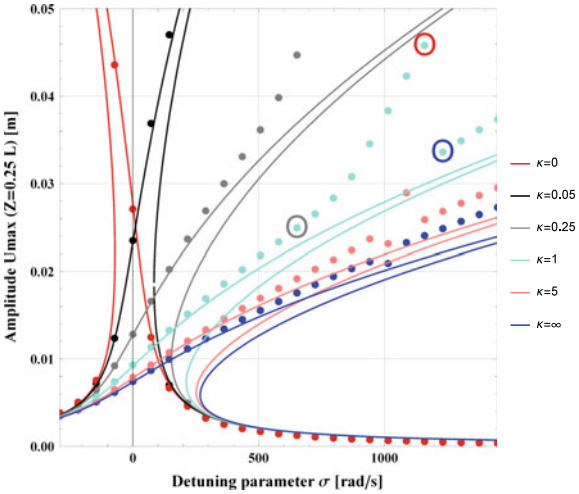

Fig. 14.5 Frequency response curves of the first bending mode. Lines (dots) represent analytical (numerical) solutions

$$\sigma = \frac{c_1 a^2 \pm \sqrt{\frac{p_v^2}{a^2}\sin^2\left(\frac{n\pi}{4}\right) - c_3^2}}{c_2}, \quad c_3 = \omega_n \left[c_\theta \frac{\left(Gn^2\pi^2 - L^2\rho\omega_n^2\right)^2}{2G^2 L n^2 \pi^2} + c_U \frac{L}{2} \right]. \tag{14.9}$$

Frequency response curves for first three bending modes are shown in Figs. 14.5, 14.7, 14.8. In general, numerical and analytical approaches are in very good agreement, even for large amplitudes of oscillations.

Discrepancies occur when the excitation is far from resonant frequencies. This is reasonable, because the MTSM is valid for small values of the detuning parameter, and the solution is sought only up to third order. Higher order analysis could provide more accurate results. Furthermore, Perturbation Method is focused on only one nth bending mode, while FEM covers many modes combination. For example Fig. 14.5 shows results where σ has been swept from $-0.1\omega_1$ to $+0.5\omega_1$, while excellent agreement for $\pm 0.1\omega_1$ is obtained.

The considered excitation, and in particular the fact that the concentrated load is at $Z = L/4$, simultaneously activates the 1st and 2nd bending modes of the system, as shown by the FFT analysis of Fig. 14.6a. Frequencies $\Omega = 1.2\omega_1$ and $\Omega = 1.45\omega_1$ are represented by single picks, while steady state motion for $\Omega = 1.4\omega_1$ consists of two frequencies, which correspond to the frequency of excitation $\Omega_a = 1.4\omega_1$ (1st mode) and its multiplicity $\Omega_b = 3 \times 1.4\omega_1$ (2nd mode). To better explain the results of Fig. 14.6a, the time histories of the corresponding solutions are reported in Fig. 14.6b.

The FRCs for the second bending mode have very good agreement between FEM and MTSM for spring stiffnesses, see Fig. 14.7. The relevant aspect of this figure is that analytical and numerical results qualitatively agree also across the particular spring stiffness where the behavior changes from hardening to softening. For exam-

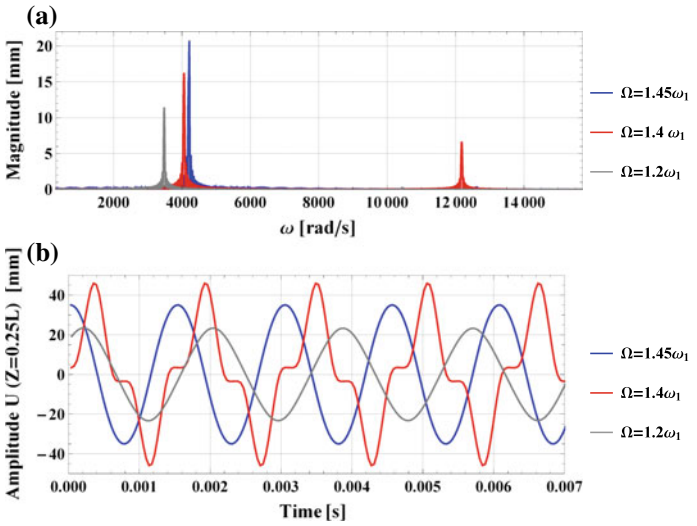

Fig. 14.6 Fast Fourier transform (**a**) and Time history (**b**) of a steady state motion of beam-spring system ($\kappa = 1, n = 1, Z = L/4$). Selected cases are marked by circles in Fig. 14.5

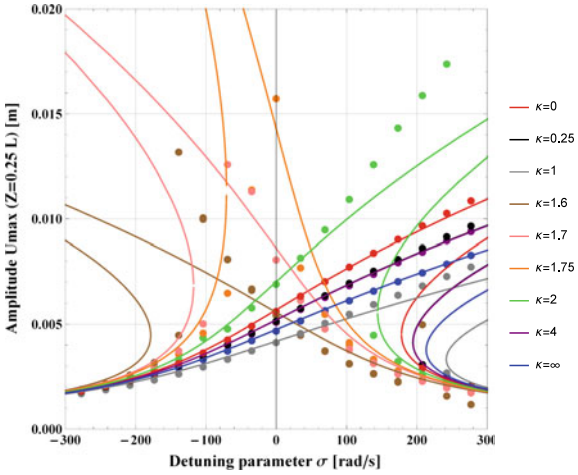

Fig. 14.7 Frequency response curves of the second bending mode. Lines (dots) represent analytical (numerical) solutions

ple, both show softening behaviour for $\kappa = 1.6; 1.7; 1.75$ (these values are in the interval of $c < 0$ in Fig. 14.3a) and hardening behaviour elsewhere. For low amplitudes the agreement is also quantitative, while of course for increasing amplitude—as well as approaching the critical value of κ (see the case $\kappa = 1.6$)—the accuracy decreases.

Figure 14.8 shows qualitatively and quantitatively agreement of the methods for the third bending mode. Relatively small range of detuning parameter as well minor

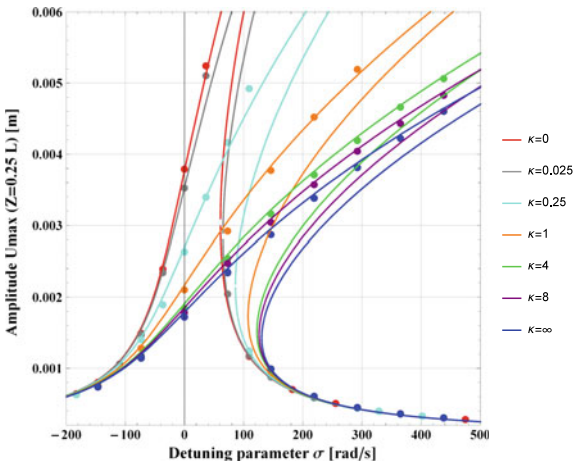

Fig. 14.8 Frequency response curves of the third bending mode. Lines (dots) represent analytical (numerical) solutions

nonlinear correction coefficient variations contribute in this case to perfect overlapping.

14.4 Conclusions and Further Developments

The nonlinear oscillations around the first seven bending modes of a planar beam have been investigated. Results of numerical and analytical comparative analyses for primary, secondary and tertiary nonlinear resonances have been presented, and it is shown that the best agreement is obtained for the 3rd bending mode. At this level of investigation, the MTSM applied to the exact beam model is not able to capture superharmonic and subharmonic resonances, but this can be done in the future. Extended study on singularities is necessary to better understand the nature of the hardening/softening transition phenomenon across these critical points.

Acknowledgements This work is part of the collaboration between Polytechnic University of Marche and Lublin University of Technology, which is aimed at developing a Joined Doctoral Programme.

References

1. Babilio, E., Lenci, S.: Consequences of different definitions of bending curvature on nonlinear dynamics of beams. Procedia Eng. (2017). https://doi.org/10.1016/j.proeng.2017.09.382
2. Clementi, F., Lenci, S., Rega, G.: Cross-checking asymptotics and numerics in the hardening/softening behaviour of Timoshenko beams with axial end spring and variable slenderness. Arch. Appl. Mech. (2017). https://doi.org/10.1007/s00419-016-1159-z

3. Jaber, N., Ramini, A., Carreno, A.A.A., Younis, M.I.: Higher order modes excitation of electrostatically actuated clamped-clamped microbeams: experimental and analytical investigation. J. Micromech. Microeng. **26**(2), 025008 (2016)
4. Kloda, L., Lenci, S., Warminski, J.: Nonlinear dynamics of a planar hinged-supported beam with one end spring system. In: MATEC Web of Conferences (2018). https://doi.org/10.1051/matecconf/201814806004
5. Kloda, L., Lenci, S., Warminski, J.: Nonlinear dynamics of a planar beam-spring system: analytical and numerical approaches. Nonlinear Dyn. (2018). https://doi.org/10.1007/s11071-018-4452-2
6. Kloda, L., Lenci, S., Warminski, J.: Nonlinear dynamics of a planar hinged-supported beam with one end lumped mass and longitudinal elastic support. In: MATEC Web of Conferences (in proceedings)
7. Lacarbonara, W., Camillacci, R.: Nonlinear normal modes of structural systems via asymptotic approach. Int. J. Solids Struct. (2004). https://doi.org/10.1016/j.ijsolstr.2004.04.029
8. Lenci, S., Rega, G.: Nonlinear free vibrations of planar elastic beams: a unified treatment of geometrical and mechanical effects. Procedia IUTAM (2016). https://doi.org/10.1016/j.piutam.2016.03.007

Chapter 15
Helmholtz, Duffing and Helmholtz-Duffing Oscillators: Exact Steady-State Solutions

Ivana Kovacic and Gianluca Gatti

Abstract This work presents an analytic technique aimed at designing the external excitation of linear and nonlinear oscillators so that a prescribed form of their steady-state response can be achieved. The technique exploits the exact analytic solutions of the oscillator response having quadratic and/or cubic nonlinearities. Both single-frequency and multi-frequency responses are considered. Examples of possible applications are provided in terms of virtual experiments.

Keywords Nonlinear oscillator · Quadratic nonlinearity · Cubic nonlinearity

15.1 Introduction

Quadratic and cubic geometric nonlinearities appear in a variety of physical and engineering oscillatory systems. Quadratic nonlinearities are referred to as Helmholtz-type nonlinearities, since it was Helmholtz, who first postulated that the eardrum behaves as an asymmetric oscillator with a restoring force including a linear and a quadratic geometric term [1]. Cubic nonlinearities are referred to as Duffing-type nonlinearities, and are named after Duffing, who investigated pendula with restoring forces containing cubic nonlinearities [2]. Analogously, oscillators that comprise both quadratic and cubic stiffness nonlinearities are referred to as Helmholtz-Duffing oscillators.

During the previous decades, many perturbation and non-perturbation techniques have been developed to obtain the free and forced responses of Helmholtz, Duffing and Helmholtz-Duffing oscillators. All of these techniques are based on approxima-

I. Kovacic
Faculty of Technical Sciences, Centre of Excellence for Vibro-Acoustic Systems and Signal Processing CEVAS, University of Novi Sad, Novi Sad, Serbia

G. Gatti (✉)
Department of Mechanical, Energy and Management Engineering, University of Calabria, Cosenza, Italy
e-mail: gianluca.gatti@unical.it

I. Kovacic and S. Lenci (eds.), *IUTAM Symposium on Exploiting Nonlinear Dynamics for Engineering Systems*, IUTAM Bookseries 37,
https://doi.org/10.1007/978-3-030-23692-2_15

tions [1, 3]. However, recent investigations have considered strategies based on the exact solutions of the steady-state response of nonlinear oscillators, and the design of external excitations to generate them. The idea of a specially designed external excitation to generate a specific form of steady-state response dates back to Hsu [4]. Such an idea has been recently extended to forced one-degree-of-freedom undamped oscillators with cubic or quadratic nonlinearities [5], purely nonlinear oscillators [6], multi-degree-of-freedom purely nonlinear chains [7], as well as to a variety of damped nonlinear oscillators [8, 9].

This study aims at extending the methodology presented in [9], which is limited to oscillators containing a symmetric form of stiffness nonlinearity, to oscillators containing quadratic nonlinearities as well, thus leading to asymmetric force-deflection curves.

15.2 Theoretical Approach

15.2.1 Free Oscillators

The equation of motion of a Helmholtz-Duffing oscillator can be written down as

$$\ddot{x} + c_1 x + c_2 x^2 + c_3 x^3 = 0, \quad x(0) = A, \quad \dot{x}(0) = 0, \tag{15.1}$$

where c_1, c_2 and c_3 are all assumed to be equal or greater than zero. The initial conditions are selected so that the initial velocity is assumed to be zero.

There is no exact solution for the response of the Helmholtz-Duffing oscillator, and the approximate solution for its motion contains odd and even harmonics [3]. However, the exact solution for the response of Helmholtz and Duffing oscillators does exist and is given below.

When $c_3 = 0$, the exact solution for the Helmholtz oscillator includes the square of the Jacobi elliptic sn function [10] and can be written down as follows

$$x = A_0 + A_1 \mathrm{sn}^2(\omega t, k), \tag{15.2}$$

where

$$A_0 = \frac{c_1}{2c_2} \frac{k^2 + 1 - \sqrt{\lambda}}{\sqrt{\lambda}}, \; A_1 = -\frac{3c_1}{2c_2} \frac{k^2}{\sqrt{\lambda}}, \; \omega = \frac{\sqrt{c_1}}{2} \frac{1}{\lambda^{\frac{1}{4}}}, \; \lambda = k^4 - k^2 + 1. \tag{15.3}$$

Note that the Jacobi sn elliptic function has two arguments: the first is a function of the frequency ω, the second is the elliptic modulus k. For $k = 0$ the sn function turns into the sin function. It should be pointed out that the Helmholtz oscillator with positive coefficients has two equilibria: a center point at the origin and a saddle point at $x = -\frac{3c_1}{2c_2}$. The separatrix that passes through the saddle point corresponds to $k =$

1 [10]. The phase trajectories that lie inside the separatrix are closed, and indicate the occurrence of periodic motion. Furthermore, the existence of the constant term in the solution given by Eq. (15.2) implies that the system oscillates around a non-trivial value. The frequency content can be determined based on the Fourier expansion [11, 12], where the sn function can be represented as a sum of odd harmonics of the sin function, as follows

$$\mathrm{sn}(\omega t, k) = \sum_{N=1}^{\infty} S_N \sin\left[(2N-1)\frac{\pi}{2K}\omega t\right], \tag{15.4}$$

where the coefficients S_N are given by

$$S_N = \frac{2\pi}{kK}\frac{q^{N-1/2}}{1-q^{2N-1}}, \tag{15.5}$$

$K = K(k)$ is the complete elliptic integral of the first kind [11, 12], and $q = q(k)$ is the so-called Nome, given by

$$q = \exp\left(-\frac{\pi K\left(\sqrt{1-k^2}\right)}{K(k)}\right). \tag{15.6}$$

The fact that the sn function appears as a squared function in Eq. (15.2) implies that the oscillatory response includes an offset and both odd and even harmonics.

When $c_2 = 0$, Eq. (15.1) corresponds to the equation of motion of the Duffing oscillator, whose exact solution has the form of a Jacobi cn elliptic function

$$x = A\mathrm{cn}(\omega t, k), \tag{15.7}$$

where

$$\omega = \sqrt{c_1 + c_3 A^2}, \quad k^2 = \frac{c_3 A^2}{2\left(c_1 + c_3 A^2\right)}. \tag{15.8}$$

For positive coefficients, i.e. for hardening nonlinearity, such oscillator has one equilibrium, which is a center point at the origin. The frequency content can be determined from a Fourier expansion, which includes odd harmonics of the cos function as follows

$$\mathrm{cn}(\omega t, k) = \sum_{N=1}^{\infty} C_N \cos\left[(2N-1)\frac{\pi}{2K}\omega t\right], \tag{15.9}$$

and the coefficients C_N are given by

$$C_N = \frac{2\pi}{kK}\frac{q^{N-1/2}}{1+q^{2N-1}}. \tag{15.10}$$

When $c_2 = c_3 = 0$, Eq. (15.1) simplifies to a linear oscillator, having the well-known solution for motion given by

$$x = A\cos\left(\sqrt{c_1}t\right). \tag{15.11}$$

15.2.2 Forced Oscillators

Based on the previous discussion, it is possible to determine the exact solution for the steady-state response of a variety of damped and undamped linear and nonlinear oscillators governed by the following generalized equation of motion

$$\ddot{x} + 2\varsigma\dot{x} + c_1 x + c_2 x^2 + c_3 x^3 = F(x_r(t), \dot{x}_r(t)). \tag{15.12}$$

Furthermore, it is possible to design the external excitation of such oscillators to achieve a desired form for their free response $x_r(t)$, as discussed below.

15.2.2.1 Single-Harmonic Response

If it is desirable that the oscillator governed by Eq. (15.12) responds as a free linear oscillator, i.e. with a single harmonic as in Eq. (15.11), then this can be achieved with the external force having the following form

$$F(x_r(t), \dot{x}_r(t)) = 2\varsigma\dot{x}_r(t) + Ex + c_2 x_r^2(t) + c_3 x_r^3(t), \tag{15.13}$$

where E is a constant.

Using Eq. (15.11) as the desired response, the equation of motion can be written as

$$\begin{aligned}\ddot{x} + 2\varsigma\dot{x} + c_1 x + c_2 x^2 + c_3 x^3 &= -2\varsigma\, A\Omega\sin(\Omega t)\\ &+ \frac{1}{4}\left(2A^2c_2 + \left(4AE + 3A^3c_3\right)\cos(\Omega t) + 2A^2c_2\cos(2\Omega t) + A^3c_3\cos(3\Omega t)\right),\end{aligned} \tag{15.14}$$

where $\Omega = \sqrt{c_1 - E}$, and $c_1 \geq E$.

On the one hand, equating c_3 to zero and assuming $E = 0$, gives the equation of motion of an externally excited Helmholtz oscillator, whose steady-state response is harmonic. Such an oscillator is governed by:

$$\begin{aligned}\ddot{x} + 2\varsigma\dot{x} + c_1 x + c_2 x^2 &= -2\varsigma A\sqrt{c_1}\sin\left(\sqrt{c_1}t\right)\\ &+ \frac{1}{4}\left(2A^2c_2 + 2A^2c_2\cos\left(2\sqrt{c_1}t\right)\right).\end{aligned} \tag{15.15}$$

On the other hand, equating c_2 to zero in Eq. (15.14) and assuming $E = 0$, gives the equation of motion of the externally excited Duffing oscillator, whose steady-state response is also harmonic. Such an oscillator is governed by:

$$\ddot{x} + 2\varsigma\dot{x} + c_1 x + c_3 x^3 = -2\varsigma A\sqrt{c_1}\sin\left(\sqrt{c_1}t\right) + \frac{1}{4}\left(3A^3 c_3 \cos\left(\sqrt{c_1}t\right) + A^3 c_3 \cos\left(3\sqrt{c_1}t\right)\right). \tag{15.16}$$

15.2.2.2 Multi-harmonic Response

The same methodology can be applied to design an external excitation for a nonlinear oscillator to make it respond as any other oscillator. Thus, assuming the external force in the form

$$F(x_r(t), \dot{x}_r(t)) = 2\varsigma\dot{x}_r(t) + Bx_r^2(t) + Dx_r^3(t), \tag{15.17}$$

Equation (15.12) becomes

$$\ddot{x} + c_1 x + (c_2 - B)x^2 + (c_3 - D)x^3 = 0. \tag{15.18}$$

If $c_3 = D$, then the system response has the form given by Eq. (15.2), where c_2 in Eq. (15.3) is replaced by $c_2 - B$, and $c_2 > B$. Similarly, for $c_2 = B$ and $c_3 > D$, the system response has the form given by Eq. (15.7), and c_3 in Eq. (15.8) is replaced by $c_3 - D$.

15.3 Numerical Simulations

To validate the previous theoretical considerations, virtual experiments [13] are performed on a mechanical model of the system illustrated in Fig. 15.1. The system consists of one mass m attached to three linear springs of stiffness k, geometrically arranged to achieve the desired stiffness nonlinearity.

In particular, a vertical linear spring is combined with two lateral linear springs, which incline as the oscillating mass moves. The static equilibrium position of the mass from the position where the lateral springs are horizontal is denoted by a, so that the natural spring length is $l_0 = \sqrt{a^2 + b^2}$, where b is labeled in Fig. 15.1. A linear viscous damper c is introduced for dynamic purposes. The expression of the static force-deflection curve of the oscillator in Fig. 15.1 is

$$F = kx + 2k(x + a)\left(1 - \sqrt{\frac{a^2 + b^2}{(a + x)^2 + b^2}}\right), \tag{15.19}$$

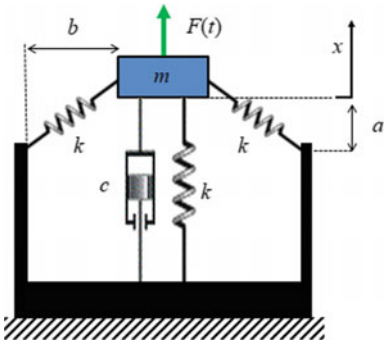

Fig. 15.1 Mechanical implementation of a nonlinear oscillator under consideration

which can be expanded in Taylor series to the third term to give

$$F \sim k\left(1+\frac{2a^2}{a^2+b^2}\right)x+\frac{3kab^2}{\left(a^2+b^2\right)^2}x^2+\frac{k\left(b^4-4a^2b^2\right)}{\left(a^2+b^2\right)^3}x^3. \tag{15.20}$$

It can be noted from Eq. (15.20) that when $a = b/2$, the system behaves as the Helmholtz oscillator, since the cubic stiffness coefficient becomes zero, and when $a = 0$ the system behaves as the Duffing oscillator, since the quadratic stiffness coefficient becomes zero.

Three virtual experiments are then performed on the Helmholtz, Duffing and Helmholtz-Duffing oscillator, respectively, and they are reported below.

15.3.1 Forced Helmholtz Oscillator

In this case, a representation of the system in its static equilibrium configuration is shown in Fig. 15.2a. The geometric system parameters are $a = 0.1$, $b = 0.2$, $k = 100$, $c = 2$, $m = 1$, so that $\varsigma = 1$, $c_1 = 140$ and $c_3 = 480$ in Eq. (15.15). The force-deflection curve given by Eq. (15.19) and its approximation in Eq. (15.20) are plotted in Fig. 15.2b. It can be seen that the Taylor series expansion is a good approximation in the displacement range from -0.1 to 0.1. The curve is clearly asymmetric.

The excitation given by Eq. (15.13), with $c_3 = 0$ and $E = 0$ is applied to the oscillating mass, and is plotted in Fig. 15.3a with a solid line. The excitation is such that the displacement amplitude at the steady-state is 0.1. In Fig. 15.3a, a sinusoidal excitation with an amplitude equal to the first harmonic of the excitation in Eq. (15.13) is plotted as a dashed line. Figure 15.3b shows the Fourier coefficients of the two excitations plotted in Fig. 15.3a with a corresponding line style. Clearly, a second harmonic and an offset are evident from the solid line.

Two virtual experiments are then carried out by exciting the system in Fig. 15.2a with the two excitations described above. The results are presented in Fig. 15.3c.

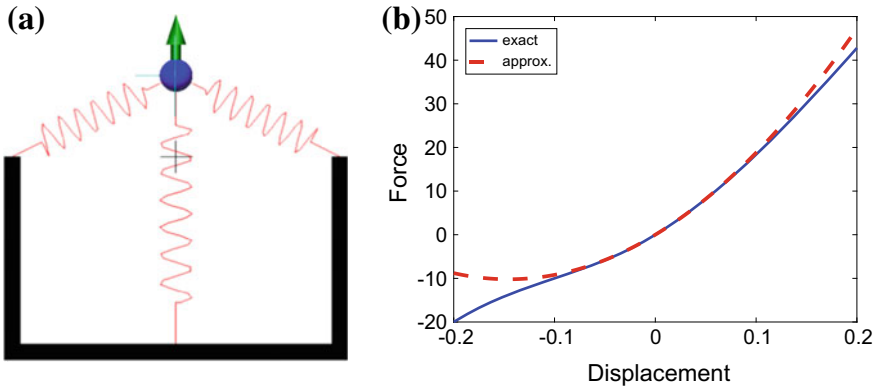

Fig. 15.2 **a** Helmholtz-like oscillator in its static equilibrium configuration. **b** Corresponding force-deflection curve: exact expression from Eq. (15.19) (solid line) and approximate expression from Eq. (15.20) (dashed line)

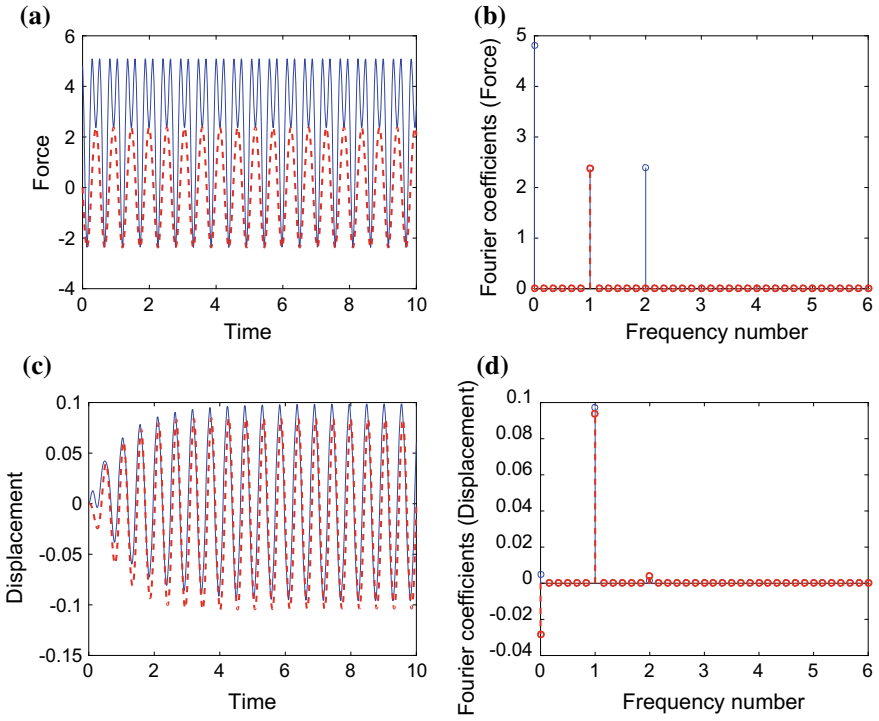

Fig. 15.3 Helmholtz-like oscillator. **a** Force excitation and **b** corresponding Fourier coefficients; **c** displacement response and **d** corresponding Fourier coefficients. Force excitation according to Eq. (15.13) and corresponding response (solid line), harmonic excitation and corresponding response (dashed line)

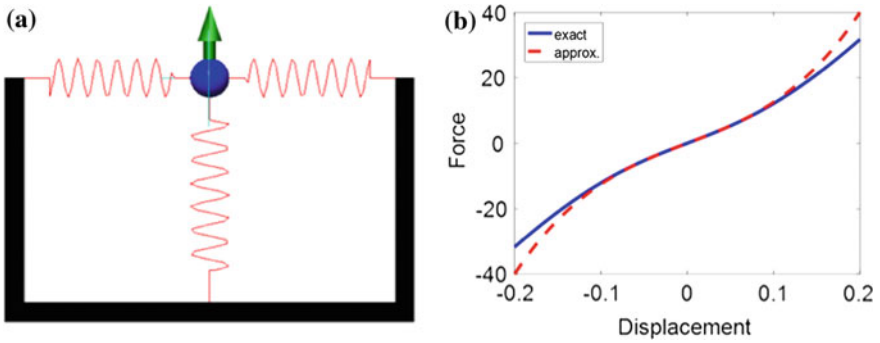

Fig. 15.4 **a** Duffing-like oscillator in its static equilibrium configuration. **b** Corresponding force-deflection curve: exact expression from Eq. (15.19) (solid line) and approximate expression from Eq. (15.20) (dashed line)

It is noted that simulations run from the static equilibrium condition (i.e. $x(t) = \dot{x}(t) = 0$), and after a transient, both responses reach a steady-state that is fairly harmonic. However, as noted in Fig. 15.3d, the Fourier coefficients of the displacement responses in Fig. 15.3c show that the specifically designed excitation in Eq. (15.13) significantly reduces the presence of the offset and also of the second harmonic in the response.

15.3.2 Forced Duffing Oscillator

In this case, a representation of system is shown in Fig. 15.4a. The system parameters are $a = 0$, $b = 0.2$, $k = 100$, $c = 2$, $m = 1$, so that $\varsigma = 1$, $c_1 = 100$ and $c_3 = 2500$ in Eq. (15.16). The force-deflection curve is plotted in Fig. 15.4b and it is now symmetric. Taylor series approximation holds, as in the previous section.

The force excitation given in Eq. (15.13), with $c_2 = 0$ and $E = 0$ is plotted in Fig. 15.5a with a solid line, and a sinusoidal excitation with an amplitude equal to the first harmonic of the excitation in Eq. (15.13) is plotted as a dashed line. Figure 15.5b shows the Fourier coefficients of the two excitations plotted in Fig. 15.5a with a corresponding line style. Clearly, a third harmonic is evident from the solid line.

Two virtual experiments are performed by exciting the system in Fig. 15.4a with the two excitations described above. The results are presented in Fig. 15.5c. It can be noted that after a transient, both responses reach a fairly harmonic steady-state. However, as noted in the close-up of Fig. 15.5d, the Fourier coefficients of the displacement responses in Fig. 15.5c show that the specifically designed excitation in Eq. (15.13) considerably reduces the presence of the third harmonic in the response.

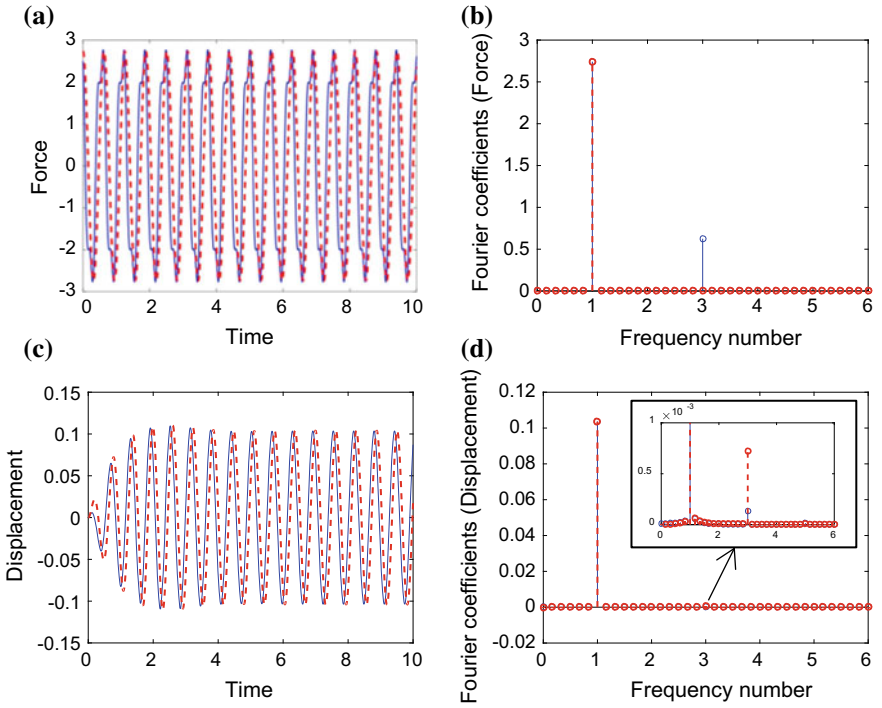

Fig. 15.5 Duffing-like oscillator. **a** Force excitation and **b** corresponding Fourier coefficients; **c** displacement response and **d** corresponding Fourier coefficients. Force excitation according to Eq. (15.13) and corresponding response (solid line), harmonic excitation and corresponding response (dashed line)

15.3.3 Forced Helmholtz-Duffing Oscillator

In this case, a representation of the system is shown in Fig. 15.6a. The system parameters are $a = 0.1$, $b = 0.2$, $k = 100$, $c = 2$, $m = 1$, so that $\varsigma = 1$, $c_1 = 111.7647$, $c_2 = 332.1799$ and $c_3 = 1563.2$ in Eq. (15.14). The asymmetric force-deflection curve is plotted in Fig. 15.6b, together with its Taylor series approximation.

The force excitation given by Eq. (15.13), with $E = 0$, is plotted in Fig. 15.7a with a solid line, and a sinusoidal excitation with an amplitude equal to the first harmonic of the excitation in Eq. (15.13) is plotted as a dashed line. Figure 15.7b shows the Fourier coefficients of the two excitations plotted in Fig. 15.7a. An offset, a second and a third harmonic are evident from the solid line.

Two virtual experiments are carried out as described earlier. The results are presented in Fig. 15.7c, where it is noted that both responses reach a steady-state which is again fairly harmonic. However, as noted in Fig. 15.7d, the Fourier coefficients of the displacement responses from Fig. 15.7c show that the specifically designed

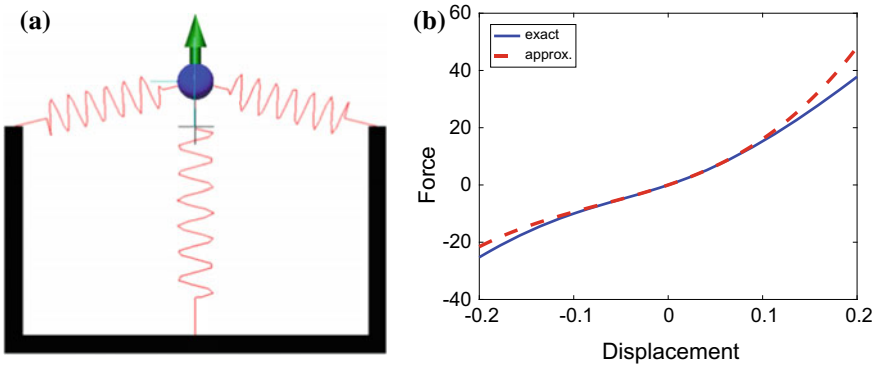

Fig. 15.6 **a** Helmholtz-Duffing-like oscillator in its static equilibrium configuration. **b** Corresponding force-deflection curve: exact expression from Eq. (15.19) (solid line) and approximate expression from Eq. (15.20) (dashed line)

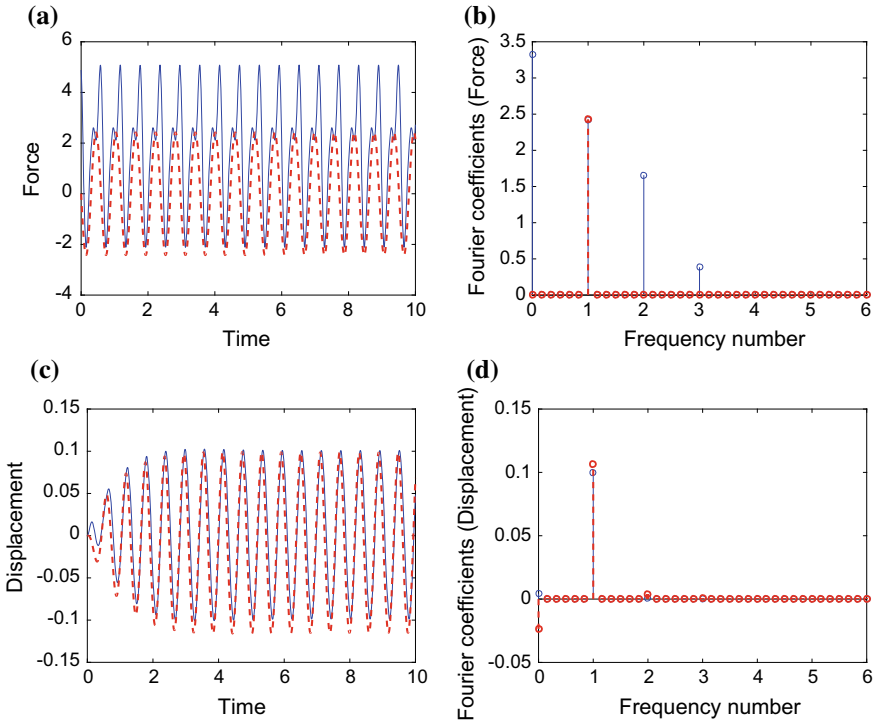

Fig. 15.7 Helmholtz-Duffing-like oscillator. **a** Force excitation and **b** corresponding Fourier coefficients; **c** displacement response and **d** corresponding Fourier coefficients. Force excitation according to Eq. (15.13) and corresponding response (solid line), harmonic excitation and corresponding response (dashed line)

excitation in Eq. (15.13) significantly reduces the presence of the offset and of the second harmonic in the system response.

15.4 Conclusions

Oscillators with quadratic and/or cubic nonlinearities have been considered in this paper. An analytic technique has been presented to properly design a specific external excitation to make them respond as different desired free oscillators. The case where the response contains one single harmonic only, and the case where there is a multi-frequency response, have been considered. Virtual experiments have been performed on a mechanical assembly of the oscillator, and they have shown that the proposed technique can significantly reduce the presence of undesired harmonics in the oscillator response.

Acknowledgements The first author acknowledges support of the Ministry of Education and Science of Serbia, grant ON174028.

References

1. Kovacic, I., Brennan, M.J. (eds.): The Duffing Equations: Nonlinear Oscillators and their Behaviour. Wiley, Chichester (2011)
2. Duffing, G.: Erzwungene Schwingungen bei veränderlicher Eigenfrequenz und ihre technische Bedeutung, Heft 41/42. Vieweg, Braunschweig (1918) (in German)
3. Nayfeh, A.H., Mook, D.: Nonlinear Oscillations. Wiley, New York (1979)
4. Hsu, C.S.: On the application of elliptic functions in nonlinear forced oscillations. Q. Appl. Math. **17**, 393–407 (1960)
5. Rakaric, Z., Kovacic, I., Cartmell, M.P.: On the design of external excitations in order to make nonlinear oscillators respond as free oscillators of the same or different type. Int. J. Nonlinear Mech. **94C**, 323–333 (2017)
6. Kovacic, I.: On the response of purely nonlinear oscillators: an Ateb-type solution for motion and an Ateb-type external excitation. Int. J. Nonlinear Mech. **92**, 15–24 (2017)
7. Kovacic, I., Zukovic, M.: Coupled purely nonlinear oscillators: normal modes and exact solutions for free and forced responses. Nonlinear Dyn. **87**, 713–726 (2017)
8. Kovacic, I.: Externally excited undamped and damped linear and nonlinear oscillators: exact solutions and tuning to a desired exact form of the response. Int. J. Nonlinear Mech. **102**, 72–81 (2018)
9. Kovacic, I., Gatti, G.: Some benefits of using exact solutions of forced nonlinear oscillators: theoretical and experimental investigations. J. Sound Vib. **436**, 310–326 (2018)
10. Rand, R.H.: Using computer algebra to handle elliptic functions in the method of averaging. In: Noor, A.K., Elishakoff, I., Hulbert, G. (eds.) Symbolic Computations and Their Impact on Mechanics, vol. 205, pp. 311–326. American Society of Mechanical Engineers, PVP (1990)
11. Byrd, P., Friedman, M.: Handbook of Elliptic Integrals for Engineers and Scientists. Springer, Berlin (1954)
12. Abramowitz, M., Stegun, I.: Handbook of Mathematical Functions. Dover Publications, New York (1965)
13. Gatti, G., Brennan, M.J.: Inner detached frequency response curves: an experimental study. J. Sound Vib. **396**, 246–254 (2017)

Chapter 16
Tree-like Structures as Hierarchical Coupled Oscillators

Ivana Kovacic, Miodrag Zukovic and Dragi Radomirovic

Abstract This bio-inspired study deals with the dynamics of tree-like models whose main structural part mimics a trunk, while the first- and second-order branches are modelled as pendula coupled to it. Conditions for the existence of modes localized in branches are determined in terms of the system parameters. This is then compared with the behaviour of the system performing large-amplitude vibration. It is found that certain localized modes exist when the system performs both small-amplitude vibration and large-amplitude vibration.

Keywords Bio-inspired structure · Coupled oscillators · Hierarchy · Modes · Localization

16.1 Introduction

Branches of trees are, in general, slender structures, but they cope fairly well with small and large-amplitude vibrations caused by various types of excitation. As such, they are seen as potentially suitable for biomimetic design [1] of man-made hierarchical structures that can rapidly localize external energy, where this energy can be either dissipated or harvested, which opens up new avenues for progress in a variety of engineering applications.

For this purpose, theoretical mechanical and mathematical modelling of trees is needed first. Mechanical models of branched trees that have been formed and investigated so far involve either discrete (lumped) or continuous/elastic systems, with the former having a finite number of degrees of freedom, and the latter having an infinite number of degrees of freedom. The former are of interest for this study as

I. Kovacic · M. Zukovic (✉)
Faculty of Technical Sciences, Centre for Vibro-Acoustic Systems and Signal Processing CEVAS, University of Novi Sad, Novi Sad, Serbia
e-mail: zukovic@uns.ac.rs

D. Radomirovic
Faculty of Agriculture, University of Novi Sad, Novi Sad, Serbia

I. Kovacic and S. Lenci (eds.), *IUTAM Symposium on Exploiting Nonlinear Dynamics for Engineering Systems*, IUTAM Bookseries 37,
https://doi.org/10.1007/978-3-030-23692-2_16

there have been just few multi-degree-of-freedom models of branched trees, whose elements have been particles/discrete masses or rigid bodies. They include: a coupled spring-mass-damper system [2, 3], a system of 13 rigid rods hinged together [4], a Y-shaped system of pendula [5], and symmetric or asymmetric two and three-branch physical pendula [6]. In [2, 3], each structural element of a tree (the trunk and branches of different hierarchy) are treated as oscillating masses, attached mutually via a spring and a damper. The spring on the branches of the same order are arranged in parallel. The springs in the same hierarchical order have the same stiffness properties, which is still an open question as being unrealistic. The model is very simple and its concept corresponds to a model of multiple tuned mass-dampers. In [4], Kerzenmacher and Gardiner developed a mechanical and mathematical model of a spruce tree and compared the results with field measurements. A model of a tall tree whose height was 13 m contains 13 rigid sections hinged together with rotational springs at each joint, while each section has the same length and with the masses concentrated at the center of each segment. The differential equations of motion were derived first for the case of small vibration. The equations of motion with damping included are solved then in the symbolic software package Mathematica Wolfram. The comparison with field measurements enabled one to note the complexity of tree responses to wind excitation and the deficiencies of the mechanical model. The authors pointed out that 'the lack of coupling of the branches and stem is a major weakness of the current model.' To overcome this shortage, in our paper, the influence of coupling is taken into consideration through the stiffness ratio. In [5], a Y-shaped system of pendula coupled with rotational springs is considered. However, although the system has three degrees of freedom, the authors treated it as a two-degree-of-freedom system, assuming that two angles are the same. In this way, they omitted the possibility when the angles of rotation are not the same and are out-of-phase. The same mechanical model is considered in our paper, but no assumption of this kind is introduced and three generalised coordinates are introduced to catch all the modes of vibration. In [6], symmetric and asymmetric two-branch and three-branch physical pendula are investigated. The analytical investigations comprise modal shapes of small free vibrations, which are then represented as oscillating mass coupled via springs. The natural damped frequencies and mode shapes are also determined. The case of large-amplitude vibrations is treated numerically, showing the associated frequency spectra for the points on the trunk and two branches, emphasizing the difference between them. The authors noted that the analytical solution obtained for small-amplitude vibrations breaks down and 'is unable to mimic the (true) numerical solution'. Unlike in [6], the study in [7] includes symmetric two-branch physical pendula, but also six-branch physical pendula, which are analysed both in small- and large-amplitude free and forced vibrations.

This study contributes to the investigations of hierarchical bio-inspired tree-like structures focusing on free small and large-amplitude vibration especially related to localized modes of vibration in terms of the main system parameters.

16.2 Models and Responses

16.2.1 Free Small- and Large-Amplitude Response for First-Order Branching

The tree-like structure under consideration is motivated by the Leeuwenberg tree model [8], which contains symmetric lateral segments at each branching point, but does not include axial segments. The mechanical model contains physical pendula coupled with torsional springs with first-order branches as shown in Fig. 16.1a. The constant branching angle α is the angle of divergence of lateral branches from the axial direction of the previous segment. The lateral branching ratio is defined as the ratio between cross-sectional areas of segments after and before branching, and it is assumed to be $\lambda = 1/2$. The diameter, length, mass and stiffness ratios are defined as the ratios of the corresponding parameters between the subsequent and preceding element, and they are hierarchically reduced. They are, respectively, given by: $D_1/D = \lambda^{1/2}$, $l_1/l = \lambda^{1/3}$, $m_1/m = \lambda^{4/3}$ and $\kappa = k_1/k$ (see [7] and the references cited therein). The system has three degrees of freedom and the corresponding generalized coordinated are taken to be the absolute angles φ, ψ_1 and ψ_2 between each pendula and its position in the static equilibrium, as labelled in Fig. 16.1a.

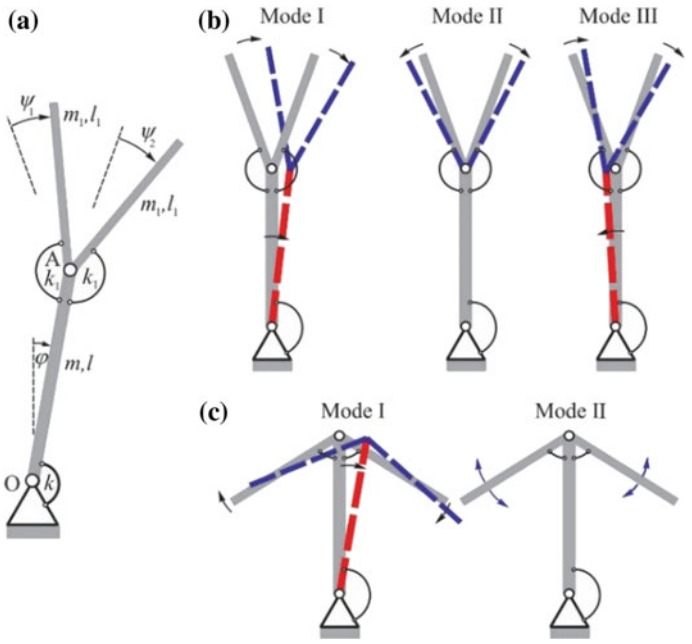

Fig. 16.1 **a** Mechanical model with first-order branching; **b** modes of vibration corresponding to $\alpha = 20°$ and $\kappa = 0.3$; **c** Modes of vibration corresponding to $\bar{\alpha} = 121.947°$ and $\kappa = 0.3$

Equations of motion will be derived by using Lagrange's equations of the second kind. Therefore, the potential energy and the kinetic energy need to be formed first. Neglecting the gravitational potential energy, the overall potential energy V stems from the deflection of the springs and is given by:

$$V = \frac{1}{2}k\varphi^2 + \frac{1}{2}k_1(\varphi - \psi_1)^2 + \frac{1}{2}k_1(\psi_2 - \varphi)^2. \tag{16.1}$$

The trunk performs rotational motion, while the branches are in general plane motion, so that the overall kinetic energy T can be expressed as:

$$T = \frac{1}{2}J_O\dot{\varphi}^2 + \frac{1}{2}m_1v_{C_1}^2 + \frac{1}{2}J_{C_1}\dot{\psi}_1^2 + \frac{1}{2}m_1v_{C_2}^2 + \frac{1}{2}J_{C_2}\dot{\psi}_2^2, \tag{16.2}$$

where the square of the velocities of the centres of mass C_1 and C_2 of the first-order branches are:

$$v_{C_1}^2 = l^2\dot{\varphi}^2 + \frac{1}{4}l_1^2\dot{\psi}_1^2 + ll_1\dot{\varphi}\dot{\psi}_1\cos(\alpha - \varphi - \psi_1). \tag{16.3}$$

$$v_{C_2}^2 = l^2\dot{\varphi}^2 + \frac{1}{4}l_1^2\dot{\psi}_2^2 + ll_1\dot{\varphi}\dot{\psi}_2\cos(\alpha - \varphi + \psi_2). \tag{16.4}$$

Treating the trunk and the branches as rods, their mass moments of inertia are, respectively, $J_O = \frac{ml^2}{3}$, $J_{C_1} = J_{C_2} = \frac{m_1l_1^2}{3}$.

Calculating the kinetic energy (16.2)–(16.4) while the system passes through the equilibrium position, i.e. by putting $\varphi = 0$, $\psi_1 = 0$ and $\psi_2 = 0$ into Eqs. (16.3) and (16.4), and using Lagrange's equation of the second kind for small (linear) vibrations in the form $(d/dt)\big(\partial T(q_i = 0)/\partial\,\dot{q}_i\big) + \partial V/\partial q_i = 0$ [9], where $q_i \in \{\varphi, \psi_1, \psi_2\}$, the following differential equations for linear vibrations are obtained:

$$\varphi'' + \frac{1 + 2\kappa}{1 + 6\lambda^{4/3}}\varphi - \frac{\kappa}{1 + 6\lambda^{4/3}}(\psi_1 + \psi_2) + \frac{3\lambda^{5/3}}{2\big(1 + 6\lambda^{4/3}\big)}\cos(\alpha)\big(\psi_1'' + \psi_2''\big) = 0, \tag{16.5}$$

$$\psi_1'' + \frac{\kappa}{\lambda^2}\psi_1 - \frac{\kappa}{\lambda^2}\varphi + \frac{3}{2\lambda^{1/3}}\cos(\alpha)\varphi'' = 0, \tag{16.6}$$

$$\psi_2'' + \frac{\kappa}{\lambda^2}\psi_2 - \frac{\kappa}{\lambda^2}\varphi + \frac{3}{2\lambda^{1/3}}\cos(\alpha)\varphi'' = 0, \tag{16.7}$$

where the primes stand for the derivatives with respect to non-dimensional time $\tau = t\,\omega^*$, with $\omega^* = \sqrt{3k/ml^2}$. Note that the parameter used for non-dimensionalization of the time has a clear physical meaning—it corresponds to the natural frequency of the trunk itself.

Based on Eqs. (16.5)–(16.7), three natural frequencies are calculated:

$$\omega_{\mathrm{I}}^2 = \frac{2\kappa}{6\kappa\lambda^{5/3}\cos(\alpha) + \sqrt{\Lambda} + 6\kappa\lambda^{4/3} + 2\kappa\lambda^2 + \kappa + \lambda^2}, \tag{16.8}$$

$$\omega_{\mathrm{II}}^2 = \frac{\kappa}{\lambda^2}, \tag{16.9}$$

$$\omega_{\mathrm{III}}^2 = \frac{2\kappa}{6\kappa\lambda^{5/3}\cos(\alpha) - \sqrt{\Lambda} + 6\kappa\lambda^{4/3} + 2\kappa\lambda^2 + \kappa + \lambda^2}, \tag{16.10}$$

where:

$$\Lambda = \kappa\lambda^2\left(9\lambda^{4/3}\cos(2\alpha) - 15\lambda^{4/3} - 4\right) + \left(6\kappa\lambda^{5/3}\cos(\alpha) + 6\kappa\lambda^{4/3} + 2\kappa\lambda^2 + \kappa + \lambda^2\right)^2 \tag{16.11}$$

It is seen that the first and the third natural frequency are influenced both by the stiffness ratio and the branching angle, while the second one depends on the stiffness ratio and the lateral branching ratio but not on the branching angle. There is an interesting special case in which the number of possible natural frequencies and possible modes is reduced: when $\cos(\bar{\alpha}) = -2\lambda^{1/3}/3$, one has $\omega_{\mathrm{II}} = \omega_{\mathrm{III}}$. For the lateral branching ratio used in this study, this condition is satisfied for $\bar{\alpha} = 121.947^{\mathrm{o}}$. The modes that corresponds to $\alpha = 20^{\circ}$ are shown in Fig. 16.1b for the fixed stiffness ratio. They include: Mode I, with the whole structure behaving as a rigid body without the hinge in the branching point and with the angles between the branches staying 2α; Mode II: when the trunk does not oscillate, while the branches move out-of-phase symmetrically, i.e. the mode is localized in the branches; Mode III: when the trunk and the branches move out-of-phase and the angle between the branches stays fixed to 2α. Two modes that corresponds to $\bar{\alpha} = 121.947^{\mathrm{o}}$ are presented in Fig. 16.1c and involve one localized Mode II when the trunk does not move, while the branches behave as two physical pendula that are uncoupled but oscillate with the same frequency. Note that the localized mode can be deduced from the equations of motion (16.5)–(16.7) by substituting $\varphi = 0$.

The next aim is to investigate free large-amplitude (nonlinear) oscillations of the tree-inspired model from Fig. 16.1a. The exact equations of motion are therefore derived based on the exact expressions for the potential and kinetic energy (16.1)–(16.4) by using Lagrange's equation $(d/dt)\left(\partial T/\partial\,\dot{q}_i\right) + \partial T/\partial q_i + \partial V/\partial q_i = 0$ [9], where $q_i \in \{\varphi, \psi_1, \psi_2\}$. These equations can be written down in the following non-dimensional form

$$\begin{aligned}
&\varphi'' + \frac{1+2\kappa}{1+6\lambda^{4/3}}\varphi - \frac{\kappa}{1+6\lambda^{4/3}}(\psi_1+\psi_2) + \frac{3\lambda^{5/3}\cos(\alpha)}{2\left(1+6\lambda^{4/3}\right)}\left(\psi_1'' + \psi_2''\right) \\
&+ \frac{3\lambda^{5/3}}{2\left(1+6\lambda^{4/3}\right)}\sin(\alpha+\varphi-\psi_1)\psi_1'^2 - \frac{3\lambda^{5/3}}{2\left(1+6\lambda^{4/3}\right)}\sin(\alpha-\varphi+\psi_2)\psi_2'^2 \\
&+ \frac{3\lambda^{5/3}}{2\left(1+6\lambda^{4/3}\right)}\cos(\alpha+\varphi-\psi_1)\psi_1'' + \frac{3\lambda^{5/3}}{2\left(1+6\lambda^{4/3}\right)}\cos(\alpha-\varphi+\psi_2)\psi_2'' = 0,
\end{aligned} \tag{16.12}$$

$$\psi_1'' + \frac{\kappa}{\lambda^2}\psi_1 - \frac{\kappa}{\lambda^2}\varphi - \frac{3}{2\lambda^{1/3}}\sin(\alpha + \varphi - \psi_1)\varphi'^2 + \frac{3}{2\lambda^{1/3}}\cos(\alpha + \varphi - \psi_1)\varphi'' = 0, \tag{16.13}$$

$$\psi_2'' + \frac{\kappa}{\lambda^2}\psi_2 - \frac{\kappa}{\lambda^2}\varphi + \frac{3}{2\lambda^{1/3}}\sin(\alpha - \varphi + \psi_2)\varphi'^2 + \frac{3}{2\lambda^{1/3}}\cos(\alpha - \varphi + \psi_2)\varphi'' = 0. \tag{16.14}$$

Note that nonlinearities in these equations exist due to the last terms appearing in the expressions for the squares of the velocities of centres of mas, Eqs. (16.3) and (16.4), involving the coefficients of the quadratic forms in the angular velocities that also have nonlinear and displacement-dependent coefficients.

It is important to note that the mode localized in branches, i.e. Mode II from Fig. 16.1b, c exists when the system performs large-amplitude oscillations. This is confirmed in Fig. 16.2, where time histories for all three angles are shown for the linear and nonlinear system with the initial conditions corresponding to Mode II from Fig. 16.1b—they coincide.

Thus, it should be pointed out that the sympodial tree-like structures from Fig. 16.1a have the following feature potentially useful for biomimetic applications: when perturbed in a way that only their first-order branches oscillate equally but in the opposite direction, such behaviour persists both when branches perform small and large-amplitude oscillations.

Modes I and III do not have this property, but new frequencies are likely to be born in the nonlinear case. To investigate this deeper, the whole tree-like structure is exposed to a pull-and-release test, in which the initial amplitudes of the generalised coordinates are equal as in Mode I, while the initial angular velocities are taken to be zero. The equations of motion (16.12)–(16.14) are solved numerically for large initial angles equal to 0.5 rad = 28.65°. Then, spectral analyses are performed on these solutions for the range of values of the branching angle $\alpha \in (0, 180^o)$. The

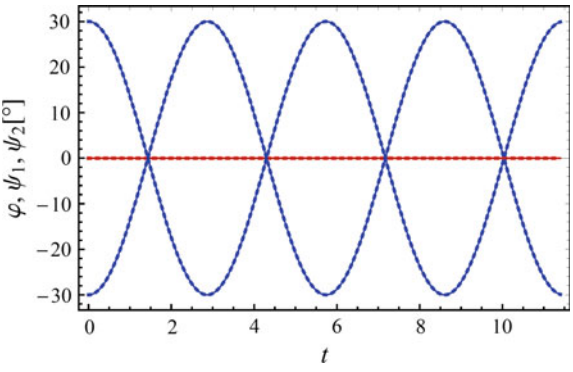

Fig. 16.2 Time-histories for all three angles with the initial conditions corresponding to Mode II from Fig. 16.1b: φ (red line), ψ_1 and ψ_2 (blue line). Solid line—linear case, dashed line—nonlinear case

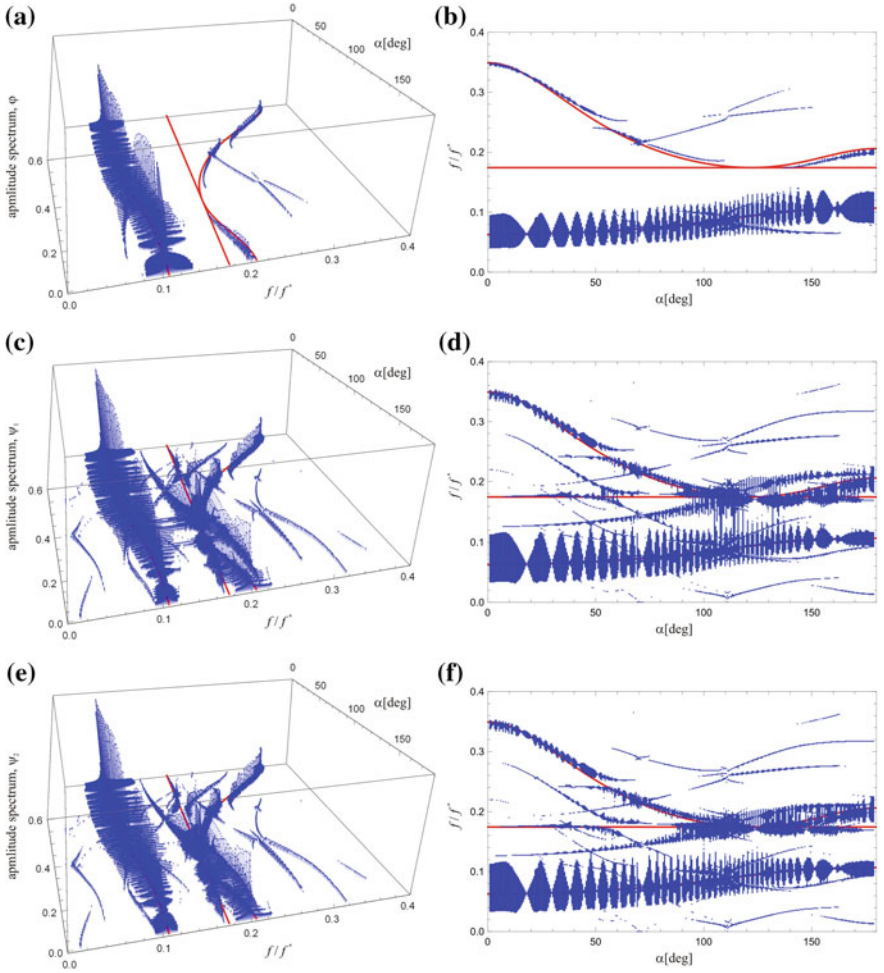

Fig. 16.3 Spectral analyses of large-amplitude vibrations calculated numerically from Eqs. (16.12) to (16.14) for $\kappa = 0.3$ (blue lines): **a**, **b** amplitude of φ; **c**, **d** amplitude of ψ_1; **e**, **f** amplitude of ψ_2. Red line—the frequencies of the linear system

content obtained is shown in blue with respect to the non-dimensional frequency $f/f*$ and the branching angles for all generalised coordinates (Fig. 16.3a, c, e). When viewed from above (Fig. 16.3b, d, f), these graphs can be compared with the plots of the natural frequencies (16.8)–(16.10) plotted as the red solid line. Results for the trunk show that the first frequency is dominant in its response. It is also evident that other frequencies can exist in the response of the first-order branches. For certain values of the branching angle, these frequencies are very dense.

16.2.2 Free Small- and Large-Amplitude Response for Second-Order Branching

The second-order branches are added in a hierarchical way (Fig. 16.4a) with the parameters $D_2/D_1 = \lambda^{1/2}$, $l_2/l_1 = \lambda^{1/3}$, $m_2/m_1 = \lambda^{4/3}$and $\kappa = k_2/k_1$. Four new generalized coordinates are introduced as the absolute angles θ_1–θ_4 between the second-order branches and their positions in the static equilibrium, as labelled in Fig. 16.4a.

The equations of motion are formed first for small vibrations (they are not given here for brevity), and natural frequencies and the corresponding modes are also sought. For the branching angles different from $\bar{\alpha} = 121.947^{\circ}$, seven natural frequencies and the corresponding modes are determined. Note that the corresponding calculated non-dimensional frequencies are presented as a function of the branching angle in Fig. 16.6 as the red solid lines. Further, three associated modes of vibration are found to be characterized by localization. They are presented in Fig. 16.4b: Mode II and VI are localized in the first- and second-order branches, while Mode IV is localized in the second-order branches only. As seen in Fig. 16.6, where the frequency lines are plotted in red, for the branching angle $\bar{\alpha} = 121.947^{\circ}$ some of the frequency lines coincide, so that five different ones exist. It is also obtained that out of the five corresponding modal shapes, two are characterized by localization (Fig. 16.4c). In each of these two modes, the trunk does not move. In Mode II, both the branches of the first- and second-order oscillate, while in Mode IV for which $\omega_{\mathrm{IV}}^2 = \kappa^2/\lambda^4$, only the second-order branches oscillate. Other expressions for the

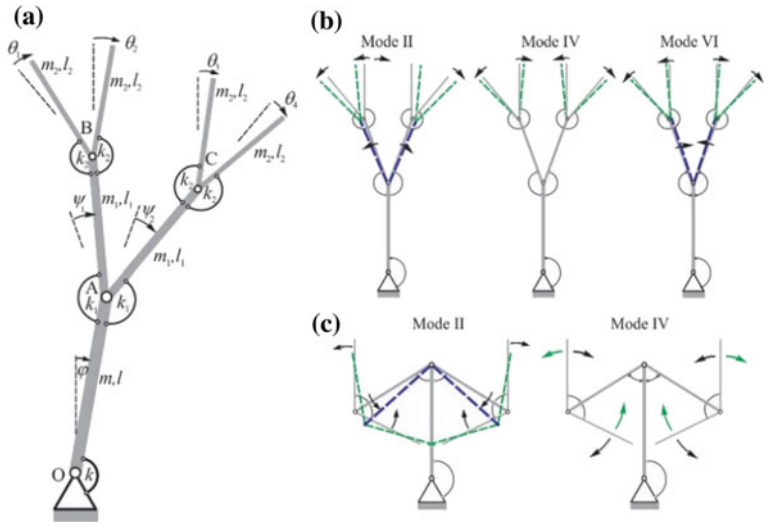

Fig. 16.4 **a** Mechanical model with second-order branching; **b** localized modes of vibration corresponding to $\alpha = 20^{\circ}$ and $\kappa = 0.3$; **c** localized modes of vibrations corresponding to $\bar{\alpha} = 121.947^{\circ}$ and $\kappa = 0.3$

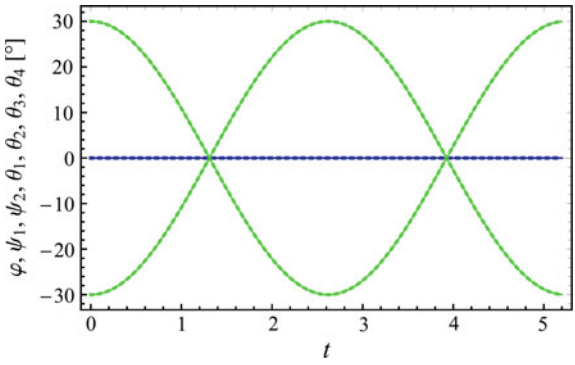

Fig. 16.5 Time-histories for all seven angles with the initial conditions corresponding to Mode IV from Fig. 16.4b: φ (red lines), ψ_1 and ψ_2 (blue lines)), θ_1–θ_4 (green lines). Solid line—linear case, dashed line—nonlinear case

natural frequencies are obtained as well, but they are not given here for brevity. Note that similarly to the natural frequency ω_{II}^2, Eq. (16.9) of the localized mode in the system with first-order branching, this ω_{IV} of the mode localized in the highest-order branching does not depend on the branching angle, but does depend on the stiffness ratio and the lateral branching ratio.

Analogously to the case studied in the previous section, the mode localized in the highest-order branches is also found to exist in the exact (nonlinear) equations for motion. Figure 16.5 illustrates it, showing time-histories for all seven angles with the initial conditions corresponding to Mode IV from Fig. 16.4b. The solutions for the small- and large-amplitude oscillations coincide, confirming the behaviour described.

This fact does not hold when the whole tree-like structure is exposed to a pull-and-release test with the initial conditions corresponding to Mode I. i.e. as a rigid body. This is seen in Fig. 16.6, which shows both the frequencies for the linear case and the frequency spectra obtained numerically for the nonlinear case for different branching angles. The lowest frequency is again dominant for the trunk, while the spectra for the branches are more dense as their order increases.

16.3 Conclusions

This study has been bio-inspired by the behaviour of the trunk and branches of sympodial trees. A hierarchical mechanical model has been formed and investigated for the case of the first-order branches and also for the case of second-order branches. The number of natural frequencies corresponds, respectively, to the number of degrees of freedom (three and seven) if the branching angle is different from a certain special value, which depends on the lateral branching ratio. The expression for this special value has been obtained, as well as the corresponding reduced number of natural frequencies. The modal shapes have been examined in details, and have been found to be associated with the possibility for localization, when the trunk does not move but the

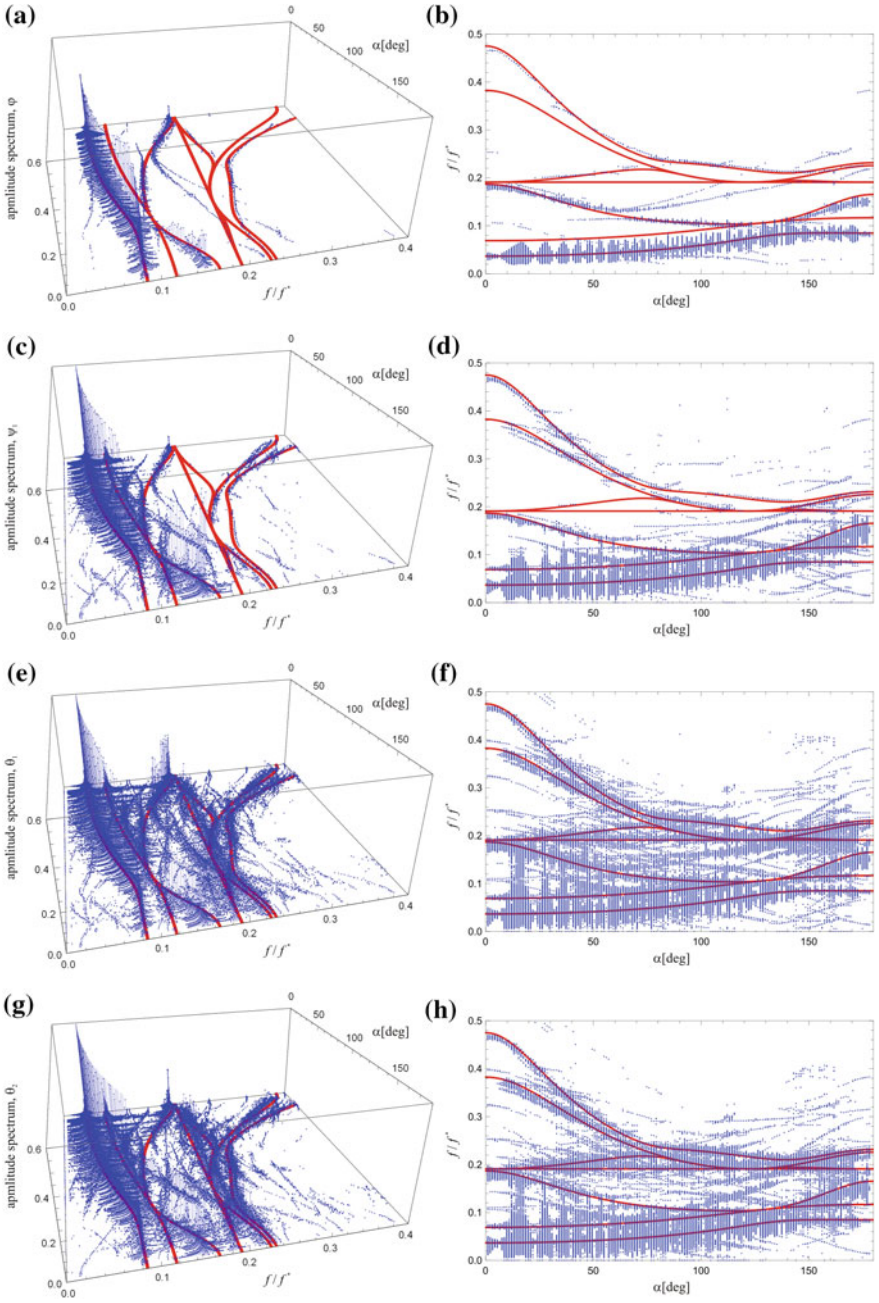

Fig. 16.6 Spectral analyses of large-amplitude vibrations for $\kappa = 0.3$ (blue lines): **a**, **b** amplitude of φ; **c**, **d** amplitude of ψ_1; **e**, **f** amplitude of θ_1; **g**, **h** amplitude of θ_2. Red line—the frequencies of the linear system

branches do oscillate. The modes localized in the highest-order branches have been found to exist both in the system performing small- and large-amplitude vibration. Given the fact that these localized modes can be of interest for biomimetic design, the current research is concerned with the development of an analytical framework for determining localized modes for an arbitrary number of the branching order and their potential bifurcations.

Acknowledgements The authors acknowledge support of the Ministry of Education and Science of Serbia, grant III41007.

References

1. Spatz, H., Theckes, B.: Oscillation damping in trees. Plant Sci. **207**, 66–71 (2013)
2. James, K.: Dynamic loading of trees. J. Arboric. **29**, 165–171 (2003)
3. James, K.R.: A dynamic structural analysis of trees subject to wind loading. Ph.D. thesis. University of Melbourne (2010)
4. Kerzenmacher, T., Gardiner, B.A.: A mathematical model to describe the dynamic response of a spruce tree to the wind. Trees **12**, 385–394 (1998)
5. Theckes, B., de Langre, E., Boutillon, X.: Damping by branching: a bioinspiration from trees. Bioinspiration Biomim. **6**(046010), 11 (2011)
6. Murphy, K.D., Rudnicki, M.: A physics-based link model for tree vibrations. Am. J. Bot. **99**, 1918–1929 (2012)
7. Kovacic, I., Zukovic, M., Radomirovic, D.: Sympodial tree-like structures: from small to large-amplitude vibrations. Bioinspiration Biomim. **13**(026002) (2018)
8. Timonin, A.K.: Botany, vol. 3. Academia, Moscow (2004) (in Russian)
9. Kovacic, I., Radomirovic, D.: Mechanical Vibrations: Fundamentals with Solved Examples. Willey, New York (2017)

Chapter 17
Energy Transport and Localization in Weakly Dissipative Resonant Chains

Agnessa Kovaleva

Abstract In this paper we examine the effect of dissipation on the emergence of resonance in a weakly dissipative Klein-Gordon chain subjected to harmonic forcing applied to the first oscillator. Both asymptotic approximations and numerical simulations prove that weak linear dissipation counteracts resonant oscillations in the entire chain even if a similar undamped array exhibits resonance. Stable resonance may occur either in a short-length chain or in an initial segment of a long-length weakly damped chain but motion of distant oscillators becomes non-resonant. Furthermore, an increase of dissipation diminishes the localization length for resonant oscillations. The conditions of the emergence of resonance as well as an expected length of localization are obtained from the equations for the steady solutions of the system under consideration. The closeness of the approximate solutions to exact (numerical) results is demonstrated.

Keywords Nonlinear oscillations · Asymptotic methods · Energy localization

17.1 Introduction

The emergence of resonance and localization of resonant oscillations in the chain driven by harmonic forcing with constant frequency have been discussed over past decades (see, e.g., [1–5]). It has been concluded that the nonlinearity plays the important role in the emergence and stability of resonance in non-dissipative chains. However, the excitation of resonant oscillations and the development of localized structures in dissipative arrays have not been studied in details. The results have been obtained for particular mechanical applications, such as, for example, dissipative roto-breathers [6], dissipative optical resonators [7], micro- and macro-scale cantilever arrays [5, 8–11].

A. Kovaleva (✉)
Space Research Institute, Moscow 117997, Russia
e-mail: agnessa_kovaleva@hotmail.com

I. Kovacic and S. Lenci (eds.), *IUTAM Symposium on Exploiting Nonlinear Dynamics for Engineering Systems*, IUTAM Bookseries 37,
https://doi.org/10.1007/978-3-030-23692-2_17

The objective of this work is to study nonlinear mechanisms for resonant energy transport and localization in the weakly dissipative Klein-Gordon array consisting of identical weakly linearly coupled Duffing oscillators and driven by external harmonic forcing applied to the first oscillator. It is assumed that the behavior of the array is close to 1:1 (fundamental) resonance, when the responses of all oscillators have a dominant harmonic component with the frequency close to the excitation frequency. The physical effects arising in the resonant chain are studied with the help of the well-developed multiple time scales formalism [12]. The derived asymptotic solutions demonstrate that the presence of dissipation may prevent the occurrence of large-amplitude resonant responses in the entire array even if a similar non-dissipative array is resonant. If dissipation cannot be ignored, then resonant oscillations can be localized only in the initial part of the chain close to the source of energy but the distant particles undergo non-resonant oscillations.

17.2 The Model

In this work we study the resonant dynamics of a weakly dissipative oscillator chain subjected to a harmonic force applied at an edge of the chain. Under the condition of linear coupling between the oscillators, the equations of motion are given by

$$\frac{d^2u_r}{dt^2} + \chi\frac{du_r}{dt} + \omega^2 u_r + \gamma u_r^3 + \kappa\left[\eta_{r,r+1}(u_r - u_{r+1}) + \eta_{r,r-1}(u_r - u_{r-1})\right] = F_r \sin\Omega t, r \in [1, n]. \tag{17.1}$$

In (17.1), the variable u_r depicts the absolute displacement of the rth oscillator; ω^2 is the linear spring stiffness; κ is the linear coupling constant; χ denotes the coefficient of dissipation; γ is the cubic spring stiffness. Since the harmonic excitation is directly applied only to the first particle, we let $F_1 = F$, $\Omega = \omega(1 + d)$, $d \ll 1$ but $F_r = 0$, $r \geq 2$. Note that all coefficients are reduced to the unit mass. The parameters $\eta_{r,k} = \{1, k \in [1, n]; 0, k = 0, k = n + 1\}$ indicate that the end oscillators unilaterally coupled with the neighboring particles.

The chain is assumed to be initially at rest, i.e. $u_r = 0$, $v_r = \frac{du_r}{dt}$ at $t = 0$ for all oscillators. By definition, Eq. (17.1) with zero initial conditions depict the transition from the initial rest state to stable resonant oscillations along the so-called *Limiting Phase Trajectories* (LPTs) corresponding to maximum energy transport from the source of energy to the oscillator [13–15].

We reduce the equations of motion to the dimensionless form. Assuming weak coupling between the oscillator, we define the dimensionless parameter $\varepsilon = \kappa/(2\omega^2) \ll 1$ as a small parameter of the problem. Then, considering weak dissipation, weak nonlinearity, and weak resonant forcing in the resonant chain, we introduce the rescaled parameters by formulas:

$$d = 2\varepsilon s,\ \mu = \frac{1}{s},\ \gamma = 8\varepsilon\alpha\omega^2,\ \chi = 2\varepsilon s\delta\omega,\ \Lambda = \sqrt{\frac{s}{3\alpha}},$$
$$F_r = 2\varepsilon s\Lambda f_r\omega^2,\ U_r = \frac{u_r}{\Lambda}. \tag{17.2}$$

Finally, we introduce the dimensionless fast and slow time variables as $\tau_0 = \omega t$ and $\tau = \varepsilon\tau_0$, respectively. Substituting the rescaled parameters into (17.1), we obtain the dimensionless equations

$$\frac{d^2U_r}{d\tau_0^2} + 2\varepsilon s\delta\frac{dU_r}{d\tau_0} + U_r + \varepsilon s\frac{8U_r^3}{3}$$
$$+ 2\varepsilon s\mu\left[\eta_{r,r+1}(U_r - U_{r+1}) + \eta_{r,r-1}(U_r - U_{r-1})\right] = 2\varepsilon s f_r\sin\theta,$$
$$\frac{d\theta}{d\tau_0} = 1 + 2\varepsilon s, \tag{17.3}$$

where $f_1 = f$ but $f_r = 0$ if $r \in [2, n]$. Equation (17.3) are solved with the help of the multiple scales method [12]. To this end, the following complex-valued change of variables is introduced:

$$\Psi_r = \left(\frac{dU_r}{d\tau_0} + iU_r\right)e^{-i\theta},\quad r \in [1, \ldots, n]. \tag{17.4}$$

By definition, the expressions $\tilde{a}_r = |\Psi_r|$ and $\tilde{\Delta}_r = \arg\Psi_r$ depict the (exact) response amplitude and the phase of the rth particle. After substituting (17.4) into (17.3), we obtain the following equations for the complex variables Ψ_r:

$$\frac{d\Psi_r}{d\tau_0} = -\varepsilon s\delta\Psi_r - \varepsilon si\left\{\left(1 - |\Psi_r|^2\right)\Psi_r - \mu\left[\eta_{r,r+1}(\Psi_r - \Psi_{r+1}) + \eta_{r,r-1}(\Psi_r - \Psi_{r-1})\right]\right.$$
$$\left. + f_r + G_r\right\}, \tag{17.5}$$

with initial conditions $\Psi_r(0) = 0$, $r \in [1, n]$. The coefficients G_r in the right-hand side of (17.5) comprise higher harmonics in θ but explicit expressions of these coefficients are unimportant for the asymptotic analysis.

We deduce from (17.5) that each complex-valued envelope Ψ_r can be presented as $\Psi_r(\tau, \tau_0, \varepsilon) = \psi_r(\tau) + \varepsilon\psi_r^{(1)}(\tau) + \cdots$, $\tau = \varepsilon s\tau_0$, with the main slow term $\psi_r(\tau)$ satisfying the equation:

$$\frac{d\psi_r}{d\tau} = -\delta\psi_r - i\left\{\left(1 - |\psi_r|^2\right)\psi_r - \mu\left[\eta_{r,r+1}(\psi_r - \psi_{r+1}) + \eta_{r,r-1}(\psi_r - \psi_{r-1})\right]\right.$$
$$\left. + f_r\right\} \tag{17.6}$$

with initial conditions $\psi_r(0) = 0$, $r \in [1, n]$. The change of variables

$$\psi_r = a_r e^{i\Delta_r},\ a_r = |\psi_r|,\ \Delta_r = \arg\psi_r \tag{17.7}$$

transforms (17.6) into the following system for the amplitudes a_r and the phases Δ_r:

$$\begin{aligned}
\frac{da_r}{d\tau} &= -\delta a_r + \mu\big[\eta_{r,r-1}a_{r-1} + \eta_{r,r+1}a_{r+1}\sin(\Delta_{r+1} - \Delta_r)\big] - f_r \sin\Delta_r,\\
a_r\frac{d\Delta_r}{d\tau} &= a_r + \mu\big[\eta_{r,r-1}(a_r - a_{r-1}\cos(\Delta_{r-1} - \Delta_r))\\
&\quad +\eta_{r,r+1}(a_r - a_{r+1}\cos(\Delta_{r+1} - \Delta_r))\big]\\
&\quad -\big(1 - a_r^2\big)a_r - f_r\cos\Delta_r
\end{aligned} \tag{17.8}$$

with initial amplitudes $a_r(0) = 0$ and indefinite initial phases $\Delta_r(0)$, $r \in [1, n]$. Note that these initial conditions make the system singular at $\tau_0 = 0$. To avoid this uncertainty, numerical solutions are constructed from regular Eq. (17.6); in the next step, the amplitudes and the phases are found by definition (17.7).

The correctness of asymptotic approximations (17.6)–(17.8) is discussed, e.g., in [12]. In particular, it was proved that $|\tilde{a}_r(\tau, \varepsilon) - a_r(\tau)| \to 0$ as $\varepsilon \to 0$. The accuracy of the resonance approximations may also be checked by the comparison of the exact (numerical) solutions of Eq. (17.3) with their slow approximations (17.8). The results of numerical simulations are discussed below.

17.3 Critical Parameters of the Non-dissipative Chain

In this section we define the parametric boundaries between non-resonant and resonant oscillations in the non-dissipative system.

Since the coupling response can be interpreted as the driving force for the attached oscillator, large-amplitude resonant oscillations of the excited oscillator can be considered as the necessary condition of the emergence of resonance in the neighboring oscillator. This means that the first critical threshold between resonant and non-resonant oscillations can be found from the approximate equations of the excited oscillator, namely,

$$\begin{aligned}
\frac{da_1}{d\tau} &= -f\sin\Delta_1,\\
a_1\frac{d\Delta_1}{d\tau} &= -(1-\mu)a_1 + a_1^3 - f\cos\Delta_1
\end{aligned} \tag{17.9}$$

The initial conditions $a_1(0) = 0$, $\Delta_1(0) = -\pi/2$ corresponds to the LPT of oscillator (17.9) [14]. Equations (17.9) confirm that resonance in oscillator (17.9) may occur if $0 \le \mu < 1$. Furthermore, the number of particles in the attachment does not change (in the main approximation) the resonance condition for the excited oscillator.

It was found [13, 14] that the boundary between non-resonant and resonant oscillations of oscillator (17.9) are expressed as

$$f_{1\mu} = f_1\sqrt{(1-\mu)^3},\ f_{2\mu} = f_2\sqrt{(1-\mu)^3} \tag{17.10}$$

where $f_1 = \sqrt{2/27}$, $f_2 = 2/\sqrt{27}$. It follows from [13] that the LPT depicts an outer boundary for a set of closed trajectories encircling the stable center on the axis $\Delta_1 = -\pi$ at $f < f_{1\mu}$, while at $f > f_{1\mu}$ the LPT characterizes an outer boundary for the trajectories encircling the stable center on the axis $\Delta_1 = 0$. The transition from small to large oscillations takes place through instability of the LPT at $f = f_{1\mu}$.

If the forced oscillator is captured into resonance, then resonant oscillations of the entire chain can emerge if coupling strength μ is sufficient to sustain large-amplitude oscillations of the neighboring oscillator. We recall that the admissible values of the parameter μ, or, by definition, the values of the frequency detuning $s = 1/\mu$ can be found from the equations for the constant steady states amplitudes and phases of the non-dissipative system. The steady states $\bar{a}_\mathrm{r}$, $\bar{\Delta}_\mathrm{r}$ satisfy the conditions

$$\mathrm{d}\bar{a}_\mathrm{r}/\mathrm{d}\tau = 0, \mathrm{d}\bar{\Delta}_\mathrm{r}/\mathrm{d}\tau = 0.$$

The first group of equations yields the following stationary phases of the non-dissipative system:

$$\sin\bar{\Delta}_1 = 0,\ \sin(\bar{\Delta}_r - \bar{\Delta}_{r-1}) = 0,\ r \in [2, n]. \tag{17.11}$$

Equations (17.11) have a pair of solutions, namely, $\bar{\Delta}_r = 0 \pmod{2\pi}$ and $\bar{\Delta}_r = \pi \pmod{2\pi}$, $r \in [1, n]$. The analysis of the variational equations linearized near $\bar{a}_\mathrm{r}$, $\bar{\Delta}_r$ proves that, in analogy to a single oscillator [14], the phases $\bar{\Delta}_\mathrm{r} = 0$ correspond to the stable resonance with the maximal stationary amplitudes. In this case, the stationary amplitudes are defined by the following equations:

$$\begin{gathered}\left(a_1^2 - 1\right)a_1 + \mu(a_1 - a_2) = f,\\ \left(a_r^2 - 1\right)a_r + \mu(2a_r - a_{r-1} - a_{r+1}) = 0, r \in [2, n-1],\\ \left(a_n^2 - 1\right)a_n + \mu(a_n - a_{n-1}) = 0.\end{gathered} \tag{17.12}$$

It is easy to prove that the maximal solutions of Eq. (17.12) are approximated by formulas:

$$\bar{a}_1 = 1 + f/2 + O(\mu f);\ \bar{a}_r = 1 + O\left(\mu^{r-1} f\right), r \in [2, n]. \tag{17.13}$$

Solutions (17.13) formally exist even if the coupling coefficient μ is nearly negligible. The purpose is to find the coupling strength μ, which produces the coupling response sufficient to excite resonance in an arbitrary oscillator under the condition of resonance in all previous oscillators. We begin with the analysis of the nth oscillator. To this end, we rewrite the nth equation in (17.12) in the form

$$a_n^3 - (1-\mu)a_n = \varphi_n,\ \varphi_n = \mu\bar{a}_{n-1}, \tag{17.14}$$

where $\bar{a}_{n-1} = 1$. Following [16], we analyze the roots of Eq. (17.14) through the properties of the discriminant $P_n = 27\varphi_n^2 - 4(1-\mu)^3$. If $P_n < 0$, then Eq. (17.14) has 3 different real roots; if $P_n = 0$, two real roots merge; if $P_n > 0$, there exists a single real and two complex conjugate roots [16].

It is easy to demonstrate that the inequality $P_n > 0$ can be rewritten in the form $\mu > f_{2\mu}$, or

$$\mu > \mu_{cr} = 0.25. \tag{17.15}$$

In the next step, we analyze the steady state of the rth particle under the conditions of resonance in the $(r-1)$th particle and non-resonant oscillations of the $(r+1)$th particle. These conditions imply the following equation for the amplitude a_r:

$$a_r^3 - (1-2\mu)a_r = \varphi_r, \varphi_r = \mu\bar{a}_{r-1}, r \in [2, n-1]. \tag{17.16}$$

Equation (17.16) is studied through the properties of the discriminant $P_r = 27\varphi_r^2 - 4(1-2\mu)^3$ [16]. It is easy to calculate that $P_r > 0$ at $\mu > 0.189$ for $r \in [2, n-1]$. One can conclude from (17.10), (17.15) that an admissible parametric domain for a multi-particle Klein-Gordon chain is determined by the same conditions as for a pair of coupled Duffing oscillators [13], namely,

$$f_{1\mu} = f_1\sqrt{(1-\mu)^3}, \mu > \mu_{cr} = 0.25. \tag{17.17}$$

Conditions (17.17) are illustrated in Fig. 17.1. It is seen from Fig. 17.1 that oscillators with the parameters $(f, \mu) \in D_1$ perform small non-resonant oscillations; if the parameters $(f, \mu) \in D_0$, then the entire chain is captured into resonance and each oscillator perform large-amplitude resonant oscillations; if the $(f, \mu) \in D$, then the excited oscillator is captured into resonance but the dynamics of the attachment should be investigated separately. Note that conditions (17.17) do not correspond to the exact boundaries of the resonant domain, as they have been derived under special assumptions on the dynamics of the chain. However, conditions (17.17) remain in close proximity to the results of direct numerical simulations for the exact non-dissipative system.

Figure 17.2 illustrates the effect of the forcing amplitude on capture into resonance and escape from it for the 2-particle arrays with the coupling strength $\mu = 0.25$. From Fig. 17.2, it follows that both particles exhibit small-amplitude non-resonant oscillations if the parameters $(f = 0.15, \mu = 0.25) \in D_1$; the excited oscillator is captured into large-amplitude resonance but the attachment exhibits small non-resonant oscillations at $(f = 0.2, \mu = 0.25) \in D$; both oscillators are captured into resonance at $(f = 0.3, \mu = 0.25) \in D_0$. It is important to note that the amplitude a_1 in Fig. 17.2b is similar to the LPT of a single oscillator (17.9) but the effect of the attached oscillator in Fig. 17.2c is negligible only in the initial step of motion, and both amplitudes tend to their steady states at large times. This effect remains valid for the chains of arbitrary length.

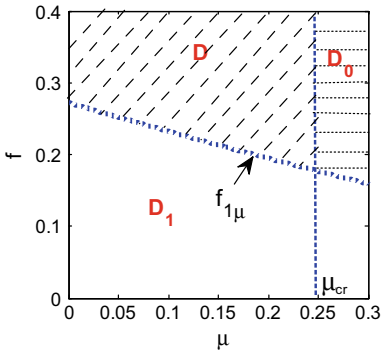

Fig. 17.1 Parametric thresholds (17.17)

Figure 17.2c demonstrates that capture into resonance of both oscillators takes place at large times. This allows excluding the initial interval of irregular motion from the analytical investigation.

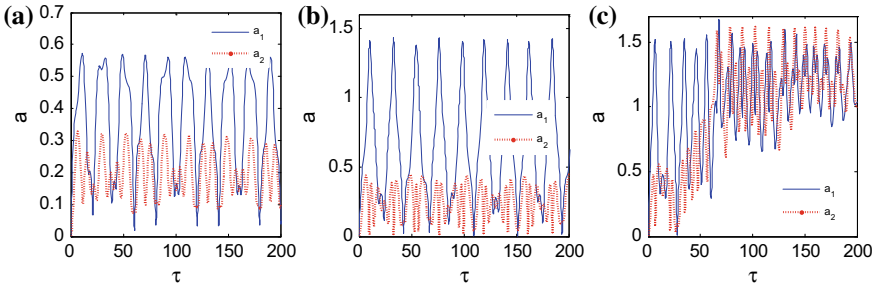

Fig. 17.2 Small-amplitude and large-amplitude oscillations of the 2-particle chain: **a** ($f = 0.15$, $\mu = 0.25$) $\in D_1$; **b** ($f = 0.2$, $\mu = 0.25$) $\in D$; **c** ($f = 0.3$, $\mu = 0.25$) $\in D_0$

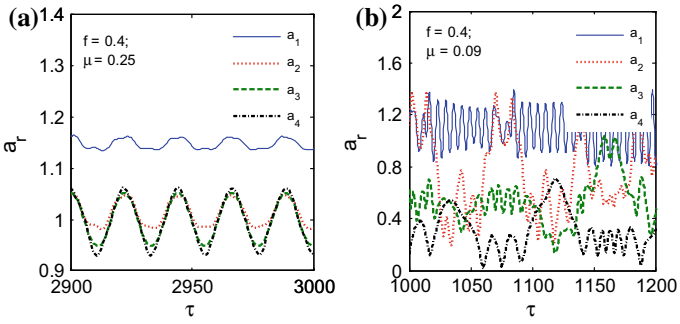

Fig. 17.3 Capture into resonance (**a**) and escape from it (**b**) of the 4-particle undamped chains with coupling stiffness $\mu = 0.25$ and $\mu = 0.09$, respectively

Figure 17.3 depicts the response amplitudes of the 4-particle non-dissipative chains with parameters ($f = 0.4$, $\mu = 0.25$) $\in D_0$ and ($f = 0.4$, $\mu = 0.09$) $\in D$ at large times. It follows from Fig. 17.3a that resonant oscillations in the entire chain can be described as in-phase oscillations near the stationary states (17.13). Figure 17.3b illustrates resonant oscillations of the excited particle, intermittent capture into resonance and escape from it of the second particle, and evident escape from the resonance domain of the distant (third and fourth) particles.

17.4 Resonance Capture in Dissipative Chains

In this part of the paper, we develop an analytical framework to understand the influence of dissipation on the resonant properties of the oscillator array. We show that the resulting process in the weakly dissipative Klein-Gordon chain can be presented as resonant oscillations in the entire short-length chain or in an initial part of the long-length chain against small-amplitude oscillations in the part of the chain far removed from the source of energy. The number p of the resonant oscillators can be interpreted as *localization length*, beyond which resonant oscillations cannot occur.

First, we find the critical coordinates and parameters from the equations for the stationary states $\bar{a}_r$, $\bar{\Delta}_r$ of (17.8). It was shown in the previous section that the solutions $\bar{a}_r$, $\bar{\Delta}_r$ satisfy the conditions $d\bar{a}_r/d\tau = 0, d\bar{\Delta}_r/d\tau = 0$. However, in the weakly damped resonant system the solutions $\bar{a}_r$ are approximated by equalities (17.13). In this case, the following approximate equations for the stationary phases $\bar{\Delta}_r$ are considered:

$$\begin{aligned} &-\delta + \mu \sin(\bar{\Delta}_2 - \bar{\Delta}_1) - f \sin \bar{\Delta}_1 = 0, \\ &-\delta + \mu\big[\sin(\bar{\Delta}_{r-1} - \bar{\Delta}_r) + \sin(\bar{\Delta}_{r+1} - \bar{\Delta}_r)\big] = 0, \ r \in [2, n-1], \\ &-\delta + \mu \sin(\bar{\Delta}_{n-1} - \bar{\Delta}_n) = 0 \end{aligned} \tag{17.18}$$

provided that $\delta \ll 1$, $\left|\sin \bar{\Delta}_1\right| \ll 1$, $\left|\sin(\bar{\Delta}_r - \bar{\Delta}_{r-1})\right| \ll 1$. Starting from the last equation, we obtain

$$\sin \bar{\Delta}_1 = -\frac{n\delta}{f}, \ \sin(\bar{\Delta}_{n-r} - \bar{\Delta}_{n-(r+1)}) = -\frac{(r+1)\delta}{\mu}. \tag{17.19}$$

If the rth oscillator is captured into resonance, then the corresponding phase $\bar{\Delta}_r$ belongs to the interval I: $(-\pi/2, 0)$ (see Figs. 17.4 and 17.5). Non-resonant oscillations of the rth oscillator are accompanied not only by a strong reduction of the amplitude $\bar{a}_r$ but also by the exit of the phase $\bar{\Delta}_r$ from the interval I (Fig. 17.6). The computation of the phase $\bar{\Delta}_r$ by formulas (17.19) yields

$$\sin \bar{\Delta}_1 = -\delta\frac{n}{f}, \ \sin \bar{\Delta}_r = -\delta\left(\frac{n}{f} + \frac{(r-1)(2n-r)}{2\mu}\right) \tag{17.20}$$

under a given value of dissipation δ. The phase $\bar{\Delta}_r$ is defined by formulas (17.20) provided that $\left|\sin \bar{\Delta}_r\right| \ll 1,\ r \in [1, n]$.

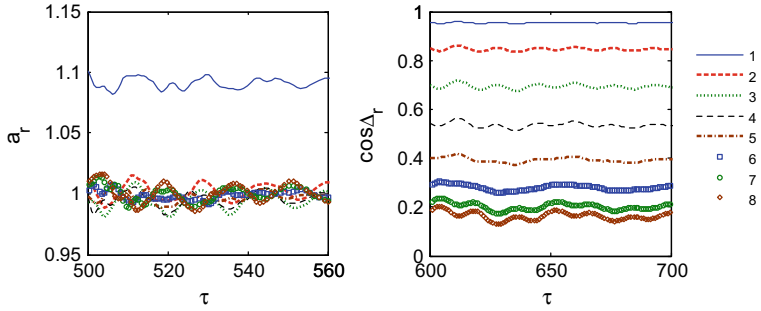

Fig. 17.4 Convergence of the amplitudes a_r and the phases Δ_r to the steady states at $\tau \to \infty$. Initial intervals of chaotic motion are truncated

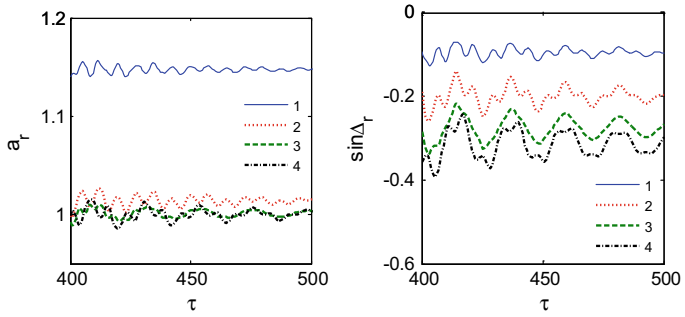

Fig. 17.5 Convergence of the amplitudes a_r and the phases Δ_r to their steady values for the 4-particle chain with parameters $f = 0.4$, $\mu = 0.25$, $\delta = 0.01 < \delta_4$

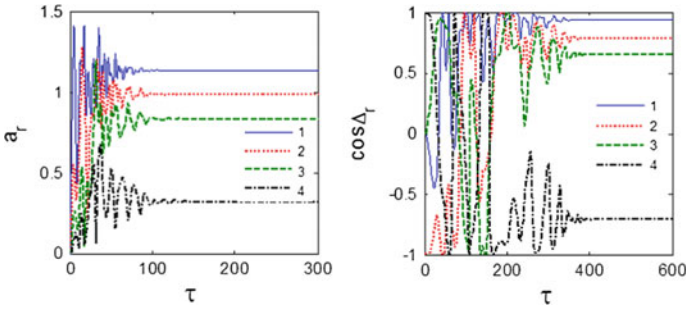

Fig. 17.6 Resonant oscillations in the initial part of the chain ($r = 1, 2, 3$) and escape from resonance of the last oscillator in the 4-dimensional chain with parameters $f = 0.4$, $\mu = 0.25$, $\delta = 0.05 > \delta_4^*$

Localization length for a given chain can be found as the maximum value of the index r satisfying the inequality

$$\delta \ll \delta_r = \left(\frac{n}{f} + \frac{(r-1)(2n-r)}{2\mu} \right)^{-1}. \tag{17.21}$$

It follows from (17.20), (17.21) that, although the Klein-Gordon chain includes n identical oscillators, the loss of energy in each oscillator increases with an increasing number of oscillators n as well as with an increasing distance r of the rth oscillator from the source of energy. This means that the criteria of resonance, which are valid for a non-dissipative chain, cannot be directly transferred to a similar weakly damped chain. Then, it follows from (17.19), (17.20) that the phase shift between two neighboring oscillators diminishes but the absolute value $\left|\sin \bar{\Delta}_r\right|$ grows with the change of the index r from $r = 1$ to $r = n$. Therefore, resonance may arise either in a short-length chain with a small number of particles or in an initial segment of a long-length chain consisting of $p < n$ particles. The distant "tail" of the chain with the oscillator numbers from $r = p + 1$ to $r = n$ executes small oscillations. In this case, the index p defines the so-called *localization length* for resonant oscillations.

Figure 17.4 illustrates resonant dynamics of the 8-particle chain with parameters $f = 0.25$, $\mu = 0.25$ and dissipation $\delta = 0.01$. It is seen from Fig. 17.4 that, although the amplitudes a_r tend to their stationary values (17.13) at large times, the respective phases Δ_r remain far from zero, thus making approximations (17.20) inaccurate.

Formulas (17.19) give the following values of the stationary phases: $\cos \bar{\Delta}_1 = 0947$; $\cos \bar{\Delta}_2 = 0.847$; $\cos \bar{\Delta}_3 = 0.777$; $\cos \bar{\Delta}_4 = 0.533$; $\cos \bar{\Delta}_5 = 0.445$; $\cos \bar{\Delta}_6 = 0.371$; $\cos \bar{\Delta}_7 = 0.32$; $\cos \bar{\Delta}_8 = 0.28$. These theoretical results are close to the numerical results presented in Fig. 17.4.

Figure 17.5 illustrates the dynamics of the 4-particle chain with parameters $f = 0.4$, $\mu = 0.25$, $\delta = 0.01$. Note that critical dissipation $\delta_4 = 0.03 > \delta$ for this chain. From Fig. 17.5, it is clearly seen that the chain with dissipation $\delta < \delta_4$ is completely captured into resonance.

Figure 17.6 demonstrates exit from resonance of the last oscillator in the 4-particle chain with parameters $f = 0.4$, $\mu = 0.25$ and dissipation $\delta = 0.05 > \delta_4$. From Fig. 17.6, it is seen that the first three oscillators ($r = 1, 2, 3$) are resonant but the 4th oscillator is non-resonant.

Finally, we consider the appearance of resonance and escape from it in the 8- and 12-particle arrays with parameters $f = 0.25$, $\mu = 0.12$, $\delta = 0.005$. It follows from definition (17.21) that $\delta_1 = 0.0312 > \delta$, $\delta_8 = 0.003 < \delta$ for the 8-particle chain but $\delta_1 = 0.021 > \delta$, $\delta_{12} = 0.002 < \delta$ for the 12-particle chain. Also, we note that the parameters $(f, \mu) \in D$. This implies resonant oscillations of the exited oscillator but the behavior of the attachment should be studied separately.

The results presented in Fig. 17.7 indicate that the oscillators close to the source of energy are resonant but the distant oscillators are non-resonant in both cases. Since the resonant amplitudes fluctuate near the value $\bar{a}_r = 1$, Fig. 17.7a demonstrates only the amplitudes a_1, a_2, a_7 and the non-resonant amplitude a_8 in the 8-particle chain.

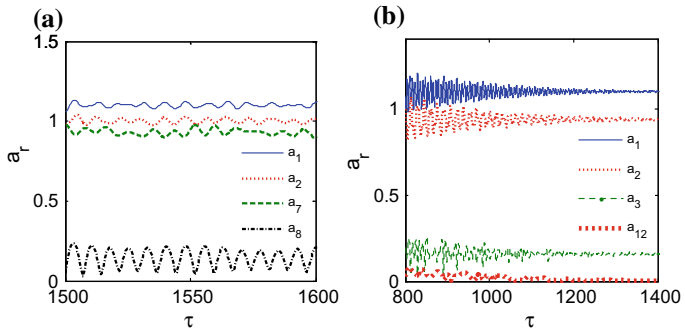

Fig. 17.7 Dynamics of the 8-particle (**a**) and 12-particle (**b**) chains with parameters $f = 0.25$, $\mu = 0.12$, $\delta = 0.005$

Similarly, Fig. 17.7b demonstrates resonance in the first and second oscillators ($r = 1, 2$) and exit from resonance of the distant oscillators in the 12-particle chain.

Acknowledgements Support for this work from the Russian Foundation for Basic Research (grants 16-02-00400, 17-01-00582) is gratefully acknowledged.

References

1. Vazquez, L., MacKay, R., Zorzano, M.P.: Localization and Energy Transfer in Nonlinear Systems. World Scientific, Singapore (2003)
2. Dauxois, T., Litvak-Hinenzon, A., MacKay, R., Spanoudaki, A.: Energy Localization and Transfer. World Scientific, Singapore (2004)
3. Vakakis, A.F., Gendelman, O., Bergman, L.A., McFarland, D.M., Kerschen, G., Lee, Y.S.: Passive Nonlinear Targeted Energy Transfer in Mechanical and Structural Systems. Springer, Berlin New (2008)
4. May, V., Kühn, O.: Charge and Energy Transfer Dynamics in Molecular Systems. Wiley, Weinheim, Germany (2011)
5. Sato, M., Hubbard, B.E., Sievers, A.J.: Nonlinear energy localization and its manipulation in micromechanical oscillator arrays. Rev. Mod. Phys. **78**, 137–157 (2006)
6. Flach, S., Gorbach, A.V.: Discrete breathers with dissipation. Lect. Notes Phys. **751**, 289–320 (2008)
7. Egorov, O., Peschel, U., Lederer, F.: Mobility of discrete cavity solitons. Phys. Rev. E **72**, 066603 (2005)
8. Sato, M., Hubbard, B.E., Sievers, A.J., Ilic, B., Czaplewski, D.A., Craighead, H.G.: Observation of locked intrinsic localized vibrational modes in a micromechanical oscillator array. Phys. Rev. Lett. **90**, 044102 (2003)
9. Kimura, M., Hikihara, T.: Coupled cantilever array with tunable on-site nonlinearity and observation of localized oscillations. Phys. Lett. A **373**, 1257 (2009)
10. Dick, A., Balachandran, B., Mote Jr., C.D.: Localization in micro-resonator arrays: influence of natural frequency tuning. J. Comput. Nonlinear Dyn. **5**(1), 011002 (2009)
11. Balachandran, B., Perkins, E., Fitzgerald, T.: Response localization in micro-scale oscillator arrays: influence of cubic coupling nonlinearities. Int. J. Dyn. Control **3**, 183 (2015)

12. Sanders, J.A., Verhulst, F., Murdock, J.: Averaging Methods in Nonlinear Dynamical Systems. Springer, Berlin (2007)
13. Kovaleva, A.: Capture into resonance of coupled Duffing oscillators. Phys. Rev. E **92**, 022909 (2015)
14. Manevitch, L.I., Kovaleva, A., Shepelev, D.: Non-smooth approximations of the limiting phase trajectories for the Duffing oscillator near 1:1 resonance. Phys. D **240**, 1–12 (2011)
15. Kovaleva, A., Manevitch, L.I.: Limiting phase trajectories and emergence of autoresonance in nonlinear oscillators. Phys. Rev. E **88**, 024901 (2013)
16. Korn, G.A., Korn, T.M.: Mathematical Handbook for Scientists and Engineers, 2nd edn. Dover, New York (2000)

Chapter 18
Asynchronous Modes of Beams on Elastic Media Subjected to Varying Normal Force: Continuous and Discrete Models

Carlos E. N. Mazzilli and Eduardo A. R. Ribeiro

Abstract The asynchronous vibration modes of a prismatic beam on elastic media under varying normal force are addressed for both continuous and discrete models. For the latter ones, with three DOF (degrees of freedom), the classical linear analysis was used to discuss the vibration modes, whereas for the continuous model quasi-Bessel modes are proposed. In the 3-DOF model, pre-stressing is force-imposed, while in the continuous one it is applied through a displacement imposition. Even if both models are calibrated in order to lead to the "same" asynchronous vibration mode in linearised formulations, it is seen that the differently assumed boundary conditions lead to distinct non-linear behaviour: softening for the 3-DOF and hardening for the continuous model. Classic linear modal analysis for associated finite-element models is addressed for the sake of comparison and to bring about the issue of modal accumulation, which seems to be an accompanying phenomenon to that of modal asynchronicity.

Keywords Asynchronicity · Asynchronous modes · Quasi-Bessel modes · Modal accumulation

18.1 Introduction

The classical linear normal modes of non-gyroscopic conservative systems are characterised by stationary waves, in the sense that the system's physical coordinates oscillate with the same frequency and phase, attaining their maxima/minima simultaneously. Such classical modes are, therefore, periodic synchronous motions. Rosenberg's extension to non-linear systems led to the so-called "similar modes",

C. E. N. Mazzilli (✉) · E. A. R. Ribeiro
Escola Politécnica da Universidade de São Paulo, Prédio da Engenharia Civil, Avenida Professor Luciano Gualberto, Butantã, São Paulo, SP 05508-010, Brazil
e-mail: cenmazzi@usp.br

E. A. R. Ribeiro
e-mail: asceduardo@usp.br

I. Kovacic and S. Lenci (eds.), *IUTAM Symposium on Exploiting Nonlinear Dynamics for Engineering Systems*, IUTAM Bookseries 37,
https://doi.org/10.1007/978-3-030-23692-2_18

which basically share the same synchronicity properties with the classic linear modes [10–12]. Later, Shaw and Pierre proposed the invariant manifold definition for the non-linear realm [14–16], according to which non-linear normal modes are free-vibration motions that take place in a 2D invariant manifold in the phase space, tangent to the respective linearised-system eigenplane in the equilibrium point. For conservative systems, such non-linear modes still yield periodic motions. However, when non-conservative ones are regarded, the motions might not be characterised by stationary waves anymore, due to phase differences among the generalised displacement-velocity fields. In such scenario, the motions are referred to "non-similar" modes.

With regard to asynchronicity in modal analysis, there are basically two lines of investigation. In the first approach, it is assumed that different parts of the physical system (with non-null measure, if it is continuous) display different frequency contents. Yet, since the frequency contents of an oscillation are obtained through Fourier's transform, which is an intrinsically linear operator, this approach seems to lead to a "linear definition" of asynchronicity, posing restrictions to its application to the non-linear modal analysis. A second approach can alternatively be envisaged: asynchronous modes would simply be localised ones, in which parts of the system (with non-null measure, if it is a continuous one) are at rest (with zero frequency), while other parts oscillate with a non-null frequency ω. Hence, different frequency spectra would already co-exist. Obviously, the (even linear) combination of a number of synchronous and asynchronous modes, each one with its own frequency, may give origin to a generic asynchronous response, which, as in the first approach, will be characterised by different frequency spectra in different parts of the physical system. Furthermore, asynchronous modes can also be understood as classical modes of a modified system, so that virtual constraints have been "added" to the original one in order to prevent parts of it to move. Of course, the reactions associated to these virtual constraints should be null, so that the modified and the original systems would be mechanically equivalent. This point of view allows to determine asynchronous modes as those that cause the vanishing of the virtual reactions.

In what follows, the concept of asynchronous modes of vibration adopted is that one associated to the localisation phenomenon, as already been recently explored in the literature [3–6, 8, 9]. The asynchronous modes of a pre-stressed prismatic beam on elastic media of constant stiffness, subjected to varying normal force, are addressed in this paper, in addition to a simplified 3-DOF model. Possible application of the reported results is expected to be found in the dynamics of guyed masts, guyed vertical offshore risers and pre-stressed cylindrical shells subjected to dead weight (resorting to the classical analogy with beams on elastic foundation [17]).

The 3-DOF model depicted in Fig. 18.1a, with lumped masses and rigid rods interconnected by displacement and rotational linear elastic springs, has been thoroughly studied in [9], both in the linear and non-linear analysis, and the system parameters were adjusted to comply with the admissibility conditions for the occurrence of asynchronous modes. Some of the results reported in [9] will be recast in what follows.

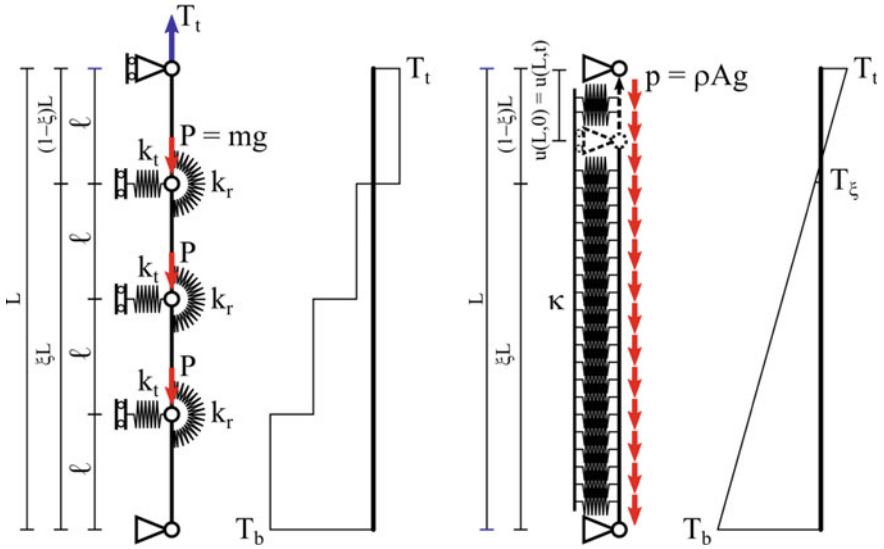

(a) 3-DOF model **(b)** Infinite-DOF model

Fig. 18.1 Discrete and continuous models

Also, a model with infinite DOF is further considered (Fig. 18.1b), for which the so-called Bessel-like modes (according to [7]) are imposed in part of the beam length (for $0 \leq x \leq \xi L$ and $0 < \xi < 1$), the complementary part being at rest (for $\xi L \leq x \leq L$ and $0 < \xi < 1$). Parameters of the continuous system are correlated with those of the corresponding 3-DOF model and carefully chosen for the sake of satisfying the condition for a nearly "equivalent" (localised) asynchronous free-vibration motion. The corresponding static normal force diagrams are also illustrated in Fig. 18.1.

18.2 Asynchronous Modes of Vibration of the Continuous Model

Figure 18.2 illustrates Bernoulli–Euler kinematics for the beam theory, from which the following coupled non-linear equations of motion, for a linearly elastic beam with Young's modulus E, can be written [7]:

$$\rho A\ddot{u} - \left[EA\left(u' + \frac{1}{2}w'^2\right)\right]' + p = 0 \tag{18.1}$$

$$\rho A\ddot{w} + EIw'''' - \left[EA\left(u' + \frac{1}{2}w'^2\right)w'\right]' + \kappa w = 0 \tag{18.2}$$

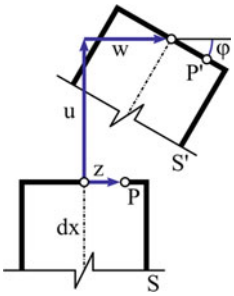

Fig. 18.2 Bernoulli–Euler kinematics for beam theory

in which ρ is the beam material density, A and I are respectively the cross-section area and moment of inertia, p is the uniformly distributed axial load, κ is the Winkler medium stiffness coefficient, and u and w are respectively the longitudinal and the transversal displacements. Over dots mean differentiation with respect to time t and primes mean differentiation with respect to the axial coordinate x.

Using the classical approximation of negligible inertial axial forces ($\rho A\ddot{u} = 0$), the normal forces $T(x,t)$ are readily evaluated:

$$T(x,t) = \left[EA\left(u' + \frac{1}{2}w'^2\right)\right] = T_b(t) + px = T_t(t) - pL + px \tag{18.3}$$

where $T_b(t) = T(0,t)$ and $T_t(t) = T(L,t)$ are respectively the normal forces at the bottom and top sections. Integration of (18.3) from $x = 0$ to $x = L$ when $\rho A\ddot{u} = 0$ leads to:

$$T(x,t) = \frac{EA}{L}u(L,t) - \frac{pL}{2} + px + \frac{EA}{2L}\int_0^L \left[w'(x,t)\right]^2 dx \tag{18.4}$$

Imposing the boundary condition $u(L,t) = u(L,0)$, *i.e.* constant pre-stressing applied via displacement imposition at time $t = 0$, it comes out:

$$T(x,t) = \overbrace{\frac{EA}{L}u(L,0) - \frac{pL}{2} + px}^{T(x,0)} + \frac{EA}{2L}\int_0^L \left[w'(x,t)\right]^2 dx = T(x,0) + \frac{EA}{2L}\int_0^L \left[w'(x,t)\right]^2 dx \tag{18.5}$$

Finally, from (18.2) and (18.5), the de-coupled equation of motion in the transversal direction is obtained, in which the notation $T(x) = T(x,0)$ has been used for short:

$$EIw'''' - T(x)w'' - pw' + \kappa w - \frac{EA}{2L}w''\int_0^L \left[w'(x,t)\right]^2 dx + \rho A\ddot{w} = 0 \tag{18.6}$$

Single-mode dynamics is next pursued, assuming variable separation in the form:

$$w(x,t) = W(x)\sin(\omega t) \tag{18.7}$$

where $W(x)$ is the modal shape and ω is the modal frequency. Of course, full variable separation is not achieved using (18.7) in the non-linear Eq. (18.6), because of the non-linearity. Yet, an approximate solution is searched making use of a temporal Galerkin projection over a cycle, leading to:

$$EIW'''' - T(x)W'' - pW' + \kappa W - \frac{3EA}{8L}W''\int_0^L W'^2 dx - \rho A\omega^2 W = 0 \tag{18.8}$$

Following [13], yet within the non-linear realm here, the so-called fictitious normal force $N(x)$ is introduced through:

$$EIW'''' - \frac{3EA}{8L}W''\int_0^L W'^2 dx = -N(x)W'' \tag{18.9}$$

For the sake of grasping the meaning of this fictitious normal force, it is interesting to evaluate it from its "definition" in (18.9), when the classical linear modes are used:

$$W_n(x) = W_{0n}\sin(\frac{n\pi x}{L}) \tag{18.10}$$

(with $n \in \mathbb{Z}^+$ designating the mode number) leading to:

$$N(x) \cong N_{0n} = \left(\frac{n\pi}{L}\right)^2 EI_{eq} \tag{18.11}$$

$$EI_{eq} = EI\left(1 + \frac{3\eta_n^2}{16}\right) \tag{18.12}$$

$$\eta_n = \frac{W_{0n}}{r} \tag{18.13}$$

$$r = \sqrt{\frac{I}{A}} \tag{18.14}$$

Taking (18.9) into (18.8), an "equivalent" cable equation is obtained, in which the true normal force $T(x)$ is replaced by $T(x) + N(x)$:

$$[T(x) + N(x)]\,W'' + pW' + \left(\rho A\omega^2 - \kappa\right)W = 0 \tag{18.15}$$

The solution of (18.15) can be written in terms of the Bessel functions of first and second kind and zero order. Yet, in this paper it is resorted to a quasi-Bessel solution, which can be accomplished from a perturbation procedure explained in [7], according to which the natural frequency and the mode n are given by:

$$\omega_n = \frac{1}{\sqrt{\rho A}}\sqrt{\kappa + \left[\frac{n\pi}{2L}\left(\sqrt{T_{tn}} + \sqrt{T_{bn}}\right)\right]^2} \tag{18.16}$$

$$W_n(x) = \sqrt[4]{\frac{T_{bn}}{T_{bn} + px}}\,\sin(z - z_b) \tag{18.17}$$

$$z(x) = \frac{\sqrt{T_{bn} + px}}{\sqrt{T_{tn}} - \sqrt{T_{bn}}}n\pi \tag{18.18}$$

$$z_b = z(0) = \frac{\sqrt{T_{bn}}}{\sqrt{T_{tn}} - \sqrt{T_{bn}}}n\pi \tag{18.19}$$

If it is assumed that a localised mode exists along the bottom part of length ξL, where $0 < \xi < 1$, the aforementioned quasi-Bessel solution can be adapted in the following way:

$$\omega_n = \frac{1}{\sqrt{\rho A}}\sqrt{\kappa + \left[\frac{n\pi}{2\xi L}\left(\sqrt{T_{\xi n}} + \sqrt{T_{bn}}\right)\right]^2} \tag{18.20}$$

$$W_n(x) = \begin{cases} \sqrt[4]{\dfrac{T_{bn}}{T_{bn} + px}}\,\sin(z - z_b) & \text{for } 0 \le x \le \xi L \\ 0 & \text{for } \xi L \le x \le L \end{cases} \tag{18.21}$$

$$z(x) = \frac{\sqrt{T_{bn} + px}}{\sqrt{T_{\xi n}} - \sqrt{T_{bn}}}n\pi \tag{18.22}$$

$$z_b = z(0) = \frac{\sqrt{T_{bn}}}{\sqrt{T_{\xi n}} - \sqrt{T_{bn}}}n\pi \tag{18.23}$$

18.3 Example

For the sake of an example, Fig. 18.3 depicts the asynchronous modes (with $n = 2$) for the models with infinite and three DOF, respectively, with the following system parameters:

$$k_t = 1.2 \times 10^7\ \mathrm{Nm^{-1}};\ k_r = 4.8 \times 10^7\ \mathrm{Nm};\ EI = 10^9\ \mathrm{Nm^2};\ \kappa = 45\,000\ \mathrm{Nm^{-2}}$$
$$m = 184\,245\,\mathrm{kg};\quad \rho A = 691\,\mathrm{kg\,m^{-1}};\quad T_t = 370\,030\,\mathrm{N};\quad g = 10\,\mathrm{ms^{-2}}$$
$$L = 800\,\mathrm{m};\qquad \ell = 200\,\mathrm{m};\qquad \xi = 0.75$$

Establishing the "equivalence" between discrete and continuous models is by no means a trivial task. It is expected that, for an effective comparison, the resulting values of the systems' parameters in both models be the same. In fact, correlating the mass and the transversal stiffness in both systems is straightforward, since the distributed mass ρA and the Winkler-medium stiffness κ are uniformly spread throughout the structure, so that:

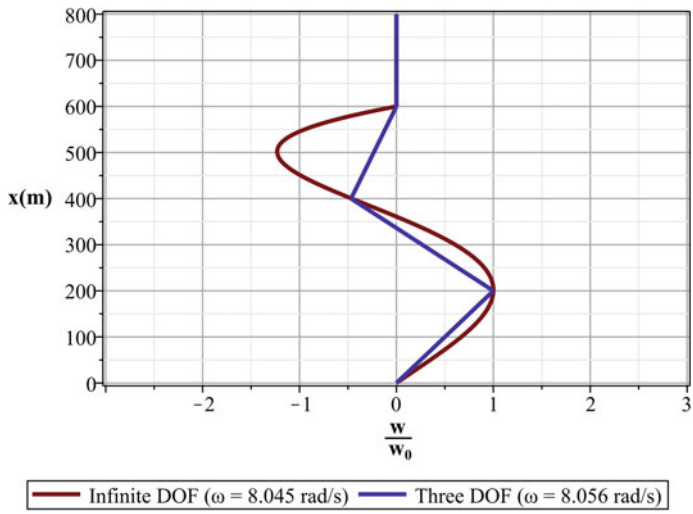

Fig. 18.3 Asynchronous mode for the continuous and 3-DOF models

$$\rho AL = \sum_{i=1}^{3} m_i = 3\,\mathrm{m} \tag{18.24}$$

$$\kappa L = \sum_{i=1}^{3} k_{t,i} = 3k_t \tag{18.25}$$

On the other hand, equating the bending stiffness product EI and the concentrated stiffness of rotational springs k_r is not trivial, because such parameters have different natures: EI is related to the proportionality between the bending moment M and the cross-section angle variation rate φ', while k_r stands for the proportionality between such a moment and the rotational spring deformation φ at a given point. Therefore, the bending stiffness product requires smooth deflections, while the discrete rotational stiffness accepts discontinuities. However, as a first approximation, the elastic curve equation (for beams with negligible axial force) and the moment for one rotational spring are regarded:

$$|M| = EI|w''| \approx EI|\varphi'| \tag{18.26}$$

$$|M| = k_r|\varphi| \tag{18.27}$$

Equating (18.26) and (18.27) and considering that $\ell \approx dx$ for a discrete model with a considerably large number of DOF, the following expression is obtained:

$$EI = \mu k_r \ell \tag{18.28}$$

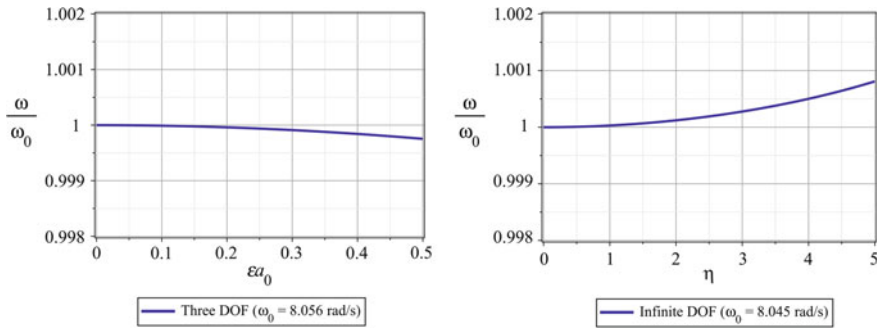

(a) 3-DOF model **(b)** Infinite-DOF model

Fig. 18.4 Non-linear frequency-amplitude relationship

where $\mu = 0.1042$ stands for a correcting dimensionless factor, calibrated according to the second mode frequency, so that $EI = 10^9\,\mathrm{Nm}^2$. Such a factor must be defined so that the natural frequency of the second quasi-Bessel mode, for the continuous model of a beam with a span of $0.75L$ ($\omega = 8.045\,\mathrm{rad\,s}^{-1}$), be approximately the same as the natural frequency for the 3-DOF model ($\omega = 8.056\,\mathrm{rad\,s}^{-1}$), recalling that $0.75L$ is precisely the part of this model set into vibration in the localised mode. Figure 18.3 indicates that the normalization of both modes with respect to the maximum amplitude displays a non-negligible difference in the modal shapes, both in terms of the functional values in each abscissa and of the localisation of their crests. Of course, one should not expect more from the 3-DOF model than a qualitative identification of the asynchronicity phenomenon. This discussion will be recast shortly, when finite-element models with many more degrees of freedom will also be discussed.

Before this is pursued, it is interesting to see the effect that different forms of pre-stressing application have in the post-critical behaviour of the non-linear asynchronous modes. It is recalled that in the 3-DOF model such a pre-stressing was imposed through a constant axial force in one of the beam ends, whereas in the continuous model it was imposed through a fixed displacement at the same beam end. These distinctly assumed boundary conditions lead to different behaviour: softening for the former (as discussed in [8, 9]), Fig. 18.4a, or hardening for the latter (as discussed in [7]), Fig. 18.4b.

Now, a finite-element model with 97 beam elements and properties consistent with those of the continuous model is discussed and a classical modal analysis is carried out with ADINA [1]. It is remarkable that its first modes are asynchronous, localisation being more intense in the lower modes, as seen in Fig. 18.5. Moreover, the associated modal frequencies are squeezed in a very small range (from 7.60 to $7.95\,\mathrm{rad\,s}^{-1}$, therefore very close to the second-mode estimations of both the 3-DOF and the continuous models).

These results suggest that a combination of these modes of the finite-element model would be able to reproduce the single second mode of the continuous model.

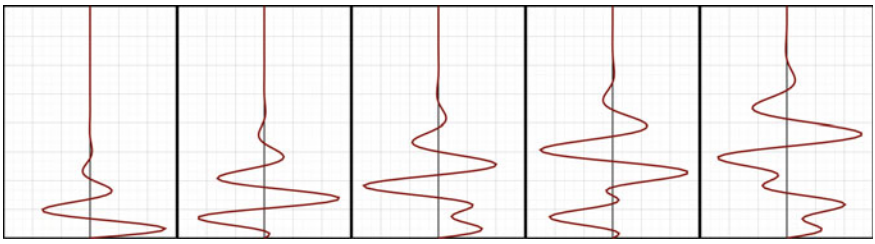

(a) Mode 1 **(b)** Mode 2 **(c)** Mode 3 **(d)** Mode 4 **(e)** Mode 5
($\omega = 7.60\,\mathrm{rad\,s^{-1}}$)($\omega = 7.75\,\mathrm{rad\,s^{-1}}$)($\omega = 7.83\,\mathrm{rad\,s^{-1}}$)($\omega = 7.90\,\mathrm{rad\,s^{-1}}$)($\omega = 7.95\,\mathrm{rad\,s^{-1}}$)

Fig. 18.5 Finite-element modes from ADINA

Furthermore, the asynchronicity phenomenon is accompanied here by another phenomenon, namely that of the modal accumulation. The question is: are the two phenomena (asynchronicity and modal accumulation) somehow related? In other words, is it to be expected that asynchronicity would be accompanied by modal accumulation and would modal accumulation be an indicative of asynchronicity? Answers to these questions go beyond the limits of this initial peering into this sort of problems. Nevertheless, it is to be recalled that modal accumulation has been reported in cylindrical shells [2] and that beams on elastic media, such as those addressed in this paper, are lower hierarchy models for these structures, as far as axi-symmetric behaviour is concerned, resorting to the already mentioned analogy [17].

18.4 Concluding Remarks

The 3-DOF model should be regarded as a low-hierarchy one, with respect to the infinite-dimensional continuous model and the finite-element models. Nevertheless, the former was able to qualitatively capture asynchronous modes of vibration that are also seen to exist in the higher-hierarchy ones. A reasonable quantitative matching can also be said to happen with regard to the linear natural frequencies of the modes studied, provided a careful calibration of system parameters is carried out, although the modes have different maxima at different positions. This discrepancy may be explained here by the combination of several localised modes, as seen in the finite-element model. More remarkably, it is the occurrence of modal accumulation, arising a questioning of a possible link between the phenomena of modal asynchronicity and modal accumulation.

Acknowledgements The first author acknowledges the support of the Brazilian National Research Council (CNPq) through the grant 32757/2013-9 and the second author acknowledges the support of the State of São Paulo Research Foundation (FAPESP) through the grant 2017/12779-3.

References

1. Bathe, J.K.: Automatic dynamic incremental nonlinear analysis (ADINA). http://www.adina.com/ (1986)
2. Biedermann, J., Winter, R., Wandel, M., Böswald, M.: Energy based correlation criteria in the mid-frequency range. J. Sound Vib. **400**, 457–480 (2017). https://doi.org/10.1016/j.jsv.2017.04.024
3. Lenci, S., Mazzilli, C.E.N.: Asynchronous free oscillations of linear mechanical systems: a general appraisal and a digression on a column with a follower force. Int. J. Non-Linear Mech. **94**, 223–234 (2017). https://doi.org/10.1016/j.ijnonlinmec.2017.02.017
4. Lenci, S., Mazzilli, C.E.N.: Asynchronous modes of vibrations in linear conservative systems: an illustrative discussion of plane framed structures. Meccanica **52**(13), 3131–3147 (2017). https://doi.org/10.1007/s11012-017-0670-9
5. Mazzilli, C.E.N., Lenci, S.: Asynchronous modes of vibration in a heavy-chain model. In: 17th International Symposium on Dynamics Problems of Mechanics. https://eventos.abcm.org.br/diname2017/ (2017)
6. Mazzilli, C.E.N., Lenci, S.: Asynchronous modes of vibration in a heavy-chain model with linear and rotational springs. In: 9th European Nonlinear Dynamics Conference, Budapest, Hungary. https://congressline.hu/enoc2017/ (2017)
7. Mazzilli, C.E.N., Ribeiro, E.A.R., Lenci, S., Demeio, L.: Non-linear vibration modes of beams and cables on elastic media subjected to linearly varying normal forces. In: ESMC 2018 Conference Proceedings. European Mechanics Society. http://www.esmc2018.org/drupal8/node/1 (2018)
8. Ribeiro, E.A.R., Mazzilli, C.E.N., Lenci, S.: Influence of geometric non-linearities in the asynchronous modes of a heavy-chain model. In: 2017 EMI International Conference, Rio de Janeiro, Brazil (2017)
9. Ribeiro, E.A.R., Mazzilli, C.E.N., Lenci, S.: Influence of geometric nonlinearities on the asynchronous modes of an articulated prestressed slender structure. J. Vib. Acoust. **141**(2), 021,007 (2018). https://doi.org/10.1115/1.4041305
10. Rosenberg, R.M.: Normal modes of nonlinear dual-mode systems. J. Appl. Mech. **27**, 263–268 (1960)
11. Rosenberg, R.M.: The normal modes of non-linear n-degree-of freedom systems. J. Appl. Mech. **29**, 7–14 (1962)
12. Rosenberg, R.M.: On nonlinear vibrations of systems with many degrees of freedom. Adv. Appl. Mech. **9**, 155–242 (1966)
13. Senjanović, I., Ljuština, A.M., Parunov, J.: Natural vibration analysis of tensioned risers by segmentation method. Oil Gas Sci. Technol.- Revue de l'IFP **61**(5), 647–659 (2006). https://doi.org/10.2516/ogst:2006004
14. Shaw, S.W., Pierre, C.: Non-linear normal modes and invariant manifolds. J. Sound Vib. **150**, 170–173 (1991)
15. Shaw, S.W., Pierre, C.: Normal modes for non-linear vibratory systems. J. Sound Vib. **164**, 85–124 (1993)
16. Shaw, S.W., Pierre, C.: Normal modes of vibration for non-linear continuous systems. J. Sound Vib. **169**, 319–347 (1994)
17. Timoshenko, S.: Strength of Materials, vol. 1 and 2. Krieger Pub. Co., New York (1940)

Chapter 19
Modelling and Analysis of Bifurcation Dynamics of Two Coupled Pendulums with a Magnetic Forcing

Krystian Polczyński, Adam Wijata, Grzegorz Wasilewski, Grzegorz Kudra and Jan Awrejcewicz

Abstract The paper presents a novel mechatronic system comprised two flexibly coupled pendulums forced by a repulsive magnetic field. The dynamics of the system is investigated theoretically and experimentally. General equations of motion including magnetic interaction are derived as well as the potential energy of the system is presented. Bifurcation analysis proves presence of periodic, quasi-periodic and chaotic types of the system motion. Chaotic attractors and their neighboring regular responses are shown, coexisting of the regular attractors is detected too and basins of attraction for these regular solutions are calculated numerically in terms of initial conditions.

Keywords Pendulum · Modelling · Bifurcation · Chaos · Magnetic forcing

19.1 Introduction

In engineering and physics there are three fundamental fields which are useful. The first one is gravitational field and it occurs between particles endowed with a mass. The second and the third ones are electric and magnetic fields, respectively. These two last fields have a very similar character of interaction, moreover they induct and

K. Polczyński · A. Wijata · G. Wasilewski · G. Kudra (✉) · J. Awrejcewicz
Department of Automation, Biomechanics and Mechatronics, Lodz University of Technology, 1/15 Stefanowskiego St, 90-924 Łódź, Poland
e-mail: grzegorz.kudra@p.lodz.pl

K. Polczyński
e-mail: kryst.polczynski@gmail.com

A. Wijata
e-mail: adam.wijata@edu.p.lodz.pl

G. Wasilewski
e-mail: grzegorz.wasilewski@p.lodz.pl

J. Awrejcewicz
e-mail: jan.awrejcewicz@p.lodz.pl

I. Kovacic and S. Lenci (eds.), *IUTAM Symposium on Exploiting Nonlinear Dynamics for Engineering Systems*, IUTAM Bookseries 37,
https://doi.org/10.1007/978-3-030-23692-2_19

coexist mutually. Mechatronic systems often use advantages of electric and magnetic fields.

Fradkov et al. [1] have studied problems of excitation and synchronization of oscillations in system of two coupled double pendulums with interacting magnets. The algorithms for typical analysis, design problems and synchronization have been described. Speed-gradient approach has been used to obtain pulse-width modulate algorithm and excitability index of the system. Therefore they have justified that the behavior of a system of controlled single pendulum may not exhibit chaos regarding behavior of one double pendulum [2].

In works [3, 4] the coupled pendulum systems forced by magnetic field have been investigated numerically and experimentally. Bifurcation diagrams, phase plots and Poincaré sections have revealed periodic, quasi-periodic and chaotic behaviors in the systems. A novel experimental model of a magnetic torque has been also presented and confronted with experimental data.

Studies on the single pendulum embedded in a repulsive magnetic field and sinusoidally excited are presented in papers [5, 6]. In the first reference, the characteristic features of non-linear dynamics such as bistable states, hysteresis and amplitude jumps are displayed. The features have been justified theoretically and experimentally. In the second reference we can read that parametric damping without periodic fluctuation may amplify or mitigate chaos whereas parametric damping with periodic fluctuation can extend a region of regular motion.

Khomeriki [7] has considered a damped driven pendulum with magnetic driven force. Lyapunov exponents for the system have been calculated by using numerical simulations and compared with a theoretical growth rate. Conclusion is that chaotic motion of the system has occurred only when the conditions for parametric resonance are fulfilled.

Tran et al. [8] have developed system of pendulum driven by DC motor and subjected to steady magnetic field. The coefficients of the system have been validated for a one drive frequency and can be used to predict the behavior of the system at a different drive frequency. The chosen frequency has not corresponded to the case of regular motion of the system. Both quantitatively and qualitatively the ability to predict the structure of chaotic attractors (outside of the regions in which the models were fit) has been demonstrated.

Mann [9] has examined the non-linear dynamics of a bistable experiment comprised a pendulum and two magnets. The shape of the potential energy curve has been determined experimentally. Studies of parametric excitation yield that a potential well escape has interrupted a series of period-doubling cascades Sensitivity to initial conditions has been observed and investigated by computing basins of attraction.

19.2 Experimental Apparatus

Our experimental stand (see Fig. 19.1) consists of two coupled pendulums (1) and (2), where pendulum shafts (3) are clutched by an elastic cuboidal rubber element (4). The pendulum marked as 1 possesses a brass element (5a), whereas the pendulum marked as 2 has a neodymium magnet (5b). Coils (6) generate alternating magnetic field, during our investigation only the coil that lies below pendulum 2 was active. Disk (7) is an element used for measurement of magnetic torques. The stand is made of non-magnetic materials to eliminate a distortion of the magnetic field between the coil and the magnet.

A control current signal which occurs inside the coil is shown in Fig. 19.2 and it is characterized by square shape with a variable frequency f and a duty cycle w.

The tests of the system dynamics have been conducted for a coil current amplitude equal to $I_{2a} = 1.5$ A.

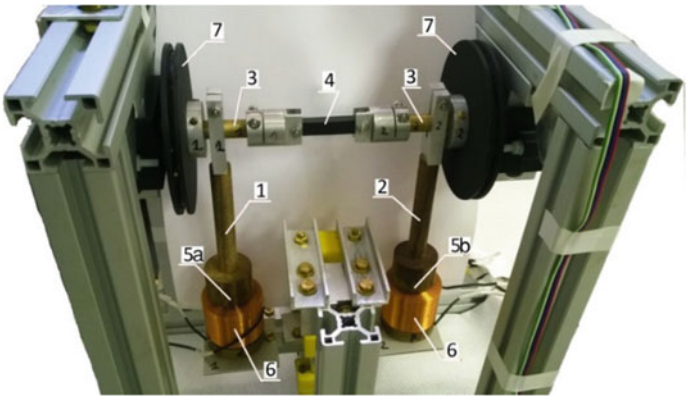

Fig. 19.1 A stand of coupled pendulums: 1, 2-pendulums; 3-shafts; 4-elastic element; 5-magnet/brass element; 6-coils, 7-disk

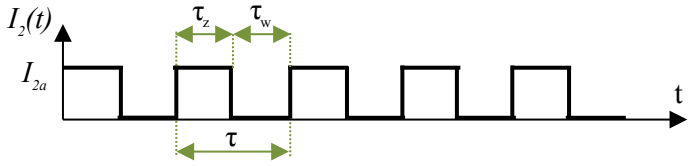

Fig. 19.2 A current signal which flows in a coil; τ_z—high state; τ_w—low state; $f = 1/\tau$—frequency; $w = (\tau_z/\tau) \cdot 100\%$—duty cycle

19.3 System Description and Equations of Motion

In this section, there is presented a physical and a mathematical model of the experimental rig described in Sect. 19.2. The physical model of the investigated system is shown in Fig. 19.3. Terms T_{D1} and T_{D2} describe damping torques for each pendulum and they are a sum of viscous damping and dry friction. The coefficients of viscous damping, which originates from bearings and air resistance, are denoted as c_1 and c_2, respectively to the pendulum 1 and 2, whereas the elastic element is characterized by a viscous damping coefficient c_e and stiffness k_e. The coefficients c_{B1} and c_{B2} represent a dry friction inside the bearings. The torque T_{mag2} introduces a magnetic excitation. Gravitational forces mg are put in the center of mass of each pendulum. The distances of these centers from the axes of rotation are denoted by s. Parameters J_1 and J_2 are the moments of inertia of the pendulums.

The governing equations of the investigated system are

$$\boldsymbol{J}\ddot{\boldsymbol{q}} + \boldsymbol{C}(\dot{\boldsymbol{q}}) + \boldsymbol{K}(\boldsymbol{q}) = \boldsymbol{P}(\boldsymbol{q}, t), \tag{19.1}$$

where

$$\begin{gathered}
\boldsymbol{q} = \begin{Bmatrix} \varphi_1 \\ \varphi_2 \end{Bmatrix}, \dot{\boldsymbol{q}} = \begin{Bmatrix} \dot{\varphi}_1 \\ \dot{\varphi}_2 \end{Bmatrix}, \ddot{\boldsymbol{q}} = \begin{Bmatrix} \ddot{\varphi}_1 \\ \ddot{\varphi}_2 \end{Bmatrix}, \boldsymbol{J} = \begin{bmatrix} J_1 & 0 \\ 0 & J_2 \end{bmatrix}, \\
\boldsymbol{C}(\dot{\boldsymbol{q}}) = \begin{Bmatrix} c_1\dot{\varphi}_1 + c_{B1}\frac{2}{\pi}\arctan(\epsilon \cdot \dot{\varphi}_1) + c_e(\dot{\varphi}_1 - \dot{\varphi}_2) \\ c_2\dot{\varphi}_2 + c_{B2}\frac{2}{\pi}\arctan(\epsilon \cdot \dot{\varphi}_2) + c_e(\dot{\varphi}_2 - \dot{\varphi}_1) \end{Bmatrix}, \\
\boldsymbol{K}(\boldsymbol{q}) = \begin{Bmatrix} mgs\ \sin\varphi_1 + k_e(\varphi_1 - \varphi_2) \\ mgs\ \sin\varphi_2 + k_e(\varphi_2 - \varphi_1) \end{Bmatrix}, \boldsymbol{P}(\boldsymbol{q}, t) = \begin{Bmatrix} 0 \\ T_{mag\,2}(\varphi_2, t) \end{Bmatrix}.
\end{gathered} \tag{19.2}$$

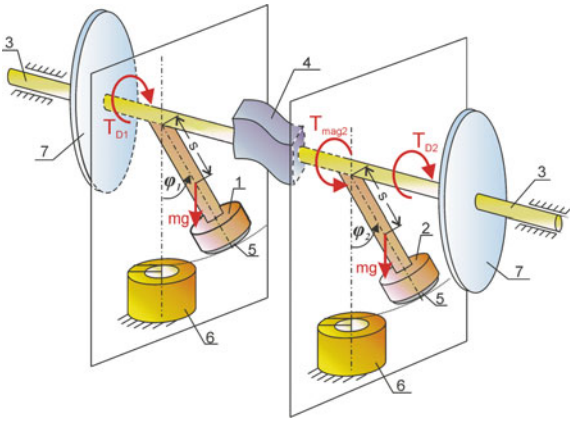

Fig. 19.3 Scheme of coupled pendulums system with the forces and torques acting on it, where: 1, 2-pendulums; 3-shafts; 4-elastic element; 5-magnet/brass element; 6-coils, 7-disk

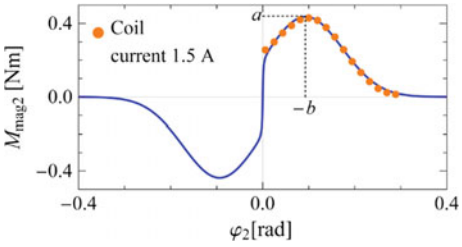

Fig. 19.4 Comparison of theoretical function $M_{mag2}(\varphi_2)$ (blue line) and experimentally obtained data point (orange dots)

The parameter ϵ is a large number used in mathematical model regularization. Vector $\boldsymbol{P}(\boldsymbol{q}, t)$ comprises excitation torque $T_{mag}(\varphi_2, t)$ which is function of time and angular position of pendulum 2. We assumed that the form of this excitation is

$$T_{mag\,2}(\varphi_2, t) = M_{mag\,2}(\varphi_2) \cdot \frac{2}{\pi} \arctan(\epsilon \cdot I(t)), \tag{19.3}$$

where M_{mag2} is a torque of magnetic forces, which depends on an angular position of the pendulum 2. We have experimentally evaluated M_{mag2} values for a constant coil current $I(t) = I_{2a} = 1.5$ A. In work [3] we have developed a special formula to approximate obtained data points, the formula is as follows:

$$M_{mag\,2}(\varphi_2) = \mathrm{a} \cdot \frac{2}{\pi} \arctan(\epsilon \cdot \varphi_2) \cdot \exp\left[-\left(\frac{\frac{2}{\pi} \arctan(\epsilon \cdot \varphi_2) \cdot \varphi_2 + b}{c} \right)^2 \right], \tag{19.4}$$

where the maximum value of the function is a point with coordinates $(a, -b)$ and parameter c controls a shape of function. Figure 19.4 shows the obtained data points of M_{mag2} and the fitted function (19.4).

19.4 Potential

Switching on and off an electrical coil underneath the pendulum with a magnet creates a non-stationary potential. The potential switches between two states: simple gravitational potential (one well) and the one with added magnetic interaction (two-well), which is shown in the Fig. 19.5. Magnetic interaction divides gravitational potential well into two (for $\varphi \in (-\pi, \pi)$), which is the reason for rich dynamical behaviour of the magnetic pendulum system [8].

In our system the pendulum with magnet is coupled with the second pendulum via a rubber element. This elastic coupling also modifies the summary potential of the system. Its influence increases according to the difference between the pendulums' angles, since the elastic potential is equal to $\frac{1}{2}k(\varphi_1 - \varphi_2)^2$. The way elastic element

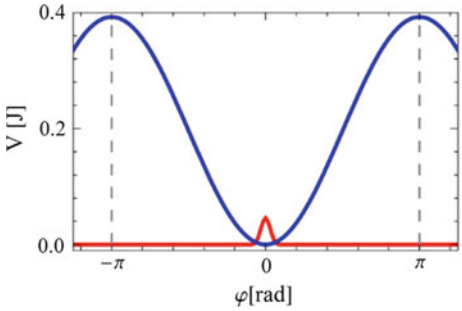

Fig. 19.5 Gravitational (blue) and magnetic (red) potential for a single magnetic pendulum system

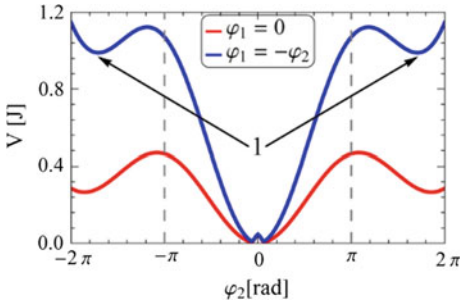

Fig. 19.6 Cross sections of the overall systems potential

influences the overall potential is illustrated in the Fig. 19.6, where cross section for $\varphi_1 = 0$ and $\varphi_1 = -\varphi_2$ are shown. In order to prevent the system from getting stuck in the well 1 (as marked in the Fig. 19.6) we have limited the coil current to 1 A. For higher values of the current round angle revolutions of the pendulums have been observed.

The system which is stuck in the potential well 1 is shown in the Fig. 19.7. Plot of the summarized gravitational, magnetic and elastic potentials is presented in the Fig. 19.8.

19.5 Bifurcation Dynamics

In order to examine the system by means of numerical simulations, following parameters have been identified for the mechanical system: $J_1 = 6.8025 \cdot 10^{-4}\,\mathrm{kg\,m^2}$, $J_2 = 6.7101 \cdot 10^{-4}\,\mathrm{kg\,m^2}$, $mgs = 0.0578\,\mathrm{N\,m}$, $k_e = 145.073 \cdot 10^{-4}\,\mathrm{N}\,m^{-1}$, $c_1 = 3.1 \cdot 10^{-5}\,\mathrm{N\,m}$, $c_2 = 7.2 \cdot 10^{-5}\,\mathrm{N\,m}$, $c_e = 13.736 \cdot 10^{-5}\,\mathrm{N\,m}$, $c_{B1} = 27.523 \cdot 10^{-5}\,\mathrm{N\,m}$, $c_{B2} = 27.888 \cdot 10^{-5}\,\mathrm{N\,m}$; and for the magnetic model (for $I_{a2} = 1$ A): $a = 0.287684$, $b = -0.107082$, $c = -0.095541$.

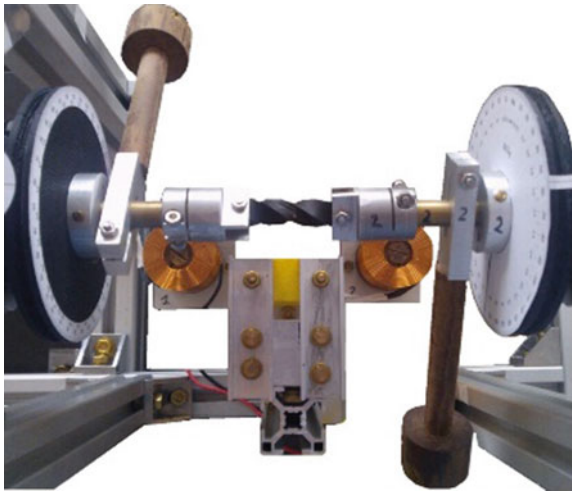

Fig. 19.7 Pendulums stuck in the potential well

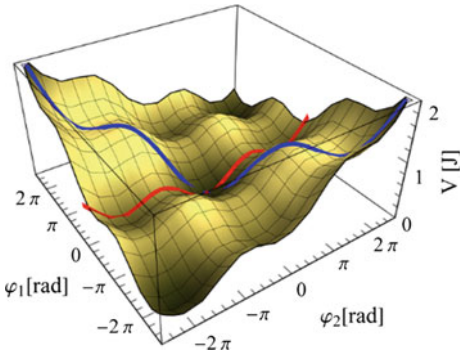

Fig. 19.8 Overall systems potential $V = f(\varphi_1, \varphi_2)$

Dynamics of the system has been investigated in terms of bifurcation produced by the increasing and decreasing excitation frequency. The amplitude of the electrical current signal has been set to 1 A and the signal duty cycle has been set to 30%. Results of the carried out numerical and experimental investigation in a wide frequency range ($1.5 \div 6$ Hz) are illustrated and compared in the Fig. 19.9.

The algorithm used for a numerical computation of the bifurcation diagram follows a stable solution, i.e. initial conditions for consecutive simulations are taken from the results of the previous ones. On the other hand, experimental diagrams have been obtained by feeding the system with an excitation signal with a fixed amplitude, duty cycle and a frequency that has been linearly growing (or decreasing) with a relatively small slope (around $2 \times 10^{-3}\,\mathrm{Hz\,s^{-1}}$). There are several points of similarity between numerically and experimentally generated diagrams. Both show potentially chaotic and periodical solutions. One can observe the coincidence of the frequency zones of chaotic, period-1 and period-2 orbits. However, the zones are slightly shifted. A possible reason for that are long transitional processes, which have

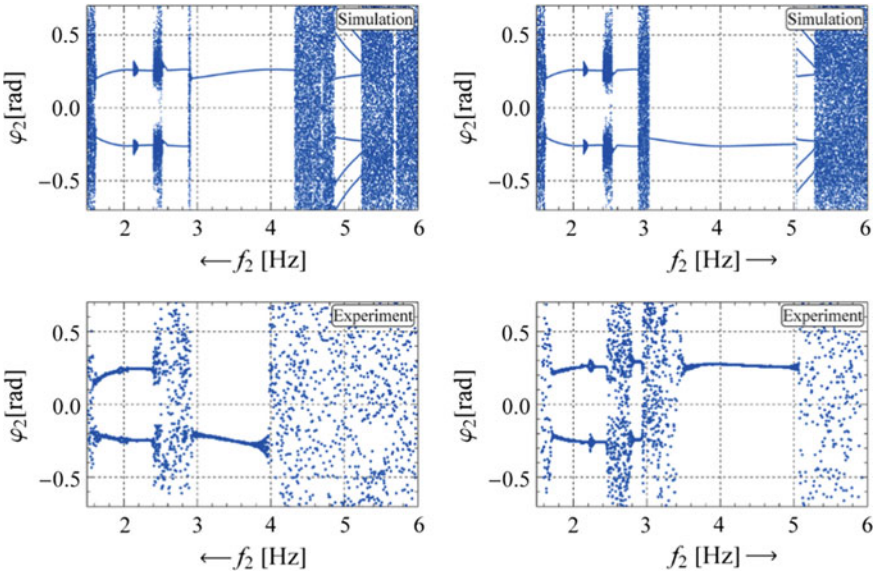

Fig. 19.9 Comparison between experimental and numerical bifurcation diagrams for the forced pendulum with a magnet

not been omitted in our experimental study. The same explanation can be applied to the lack of the period-6 solution around 5.1 Hz frequency in the experimental results. However, this solution has been verified, by an experiment with constant-frequency excitation signal, what is shown in the Fig. 19.10.

One can see in the Fig. 19.9, that bifurcation dynamic of the studied system is characterized by alternating regions of chaotic and regular motion. Cross sections of the bifurcation diagram have been prepared and analysed for the consecutive chaotic and regular zones (see Figs. 19.11 and 19.12). One can observe how chaotic attractors reflect a near stable solution. It is visible, that Poincare sections of the system in the chaotic regime orbits the points from nearby (frequency-wise) periodic solutions.

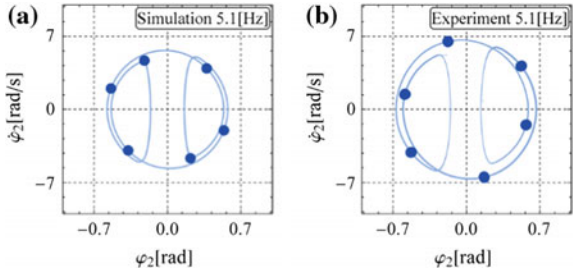

Fig. 19.10 Phase plots and Poincaré sections for period-6 motion obtained numerically (**a**) and experimentally (**b**) for 5.1 Hz

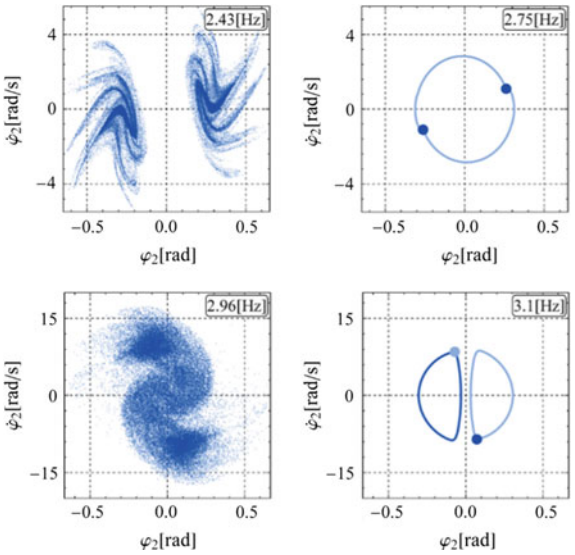

Fig. 19.11 Chaotic attractors (2.43 Hz, 2.96 Hz) and nearby periodic solutions (2.75 Hz, 3.1 Hz)

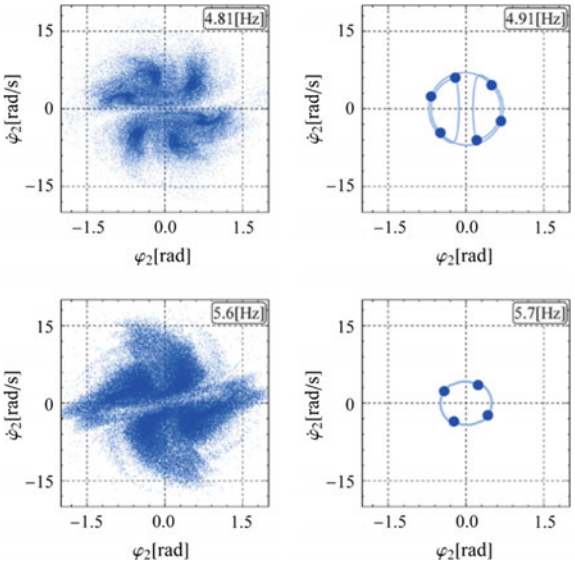

Fig. 19.12 Chaotic attractors (4.81 Hz, 5.6 Hz) and nearby periodic solutions (4.91 Hz, 5.7 Hz)

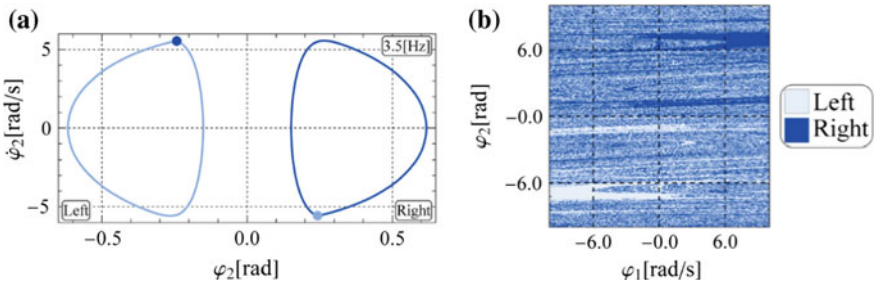

Fig. 19.13 **a** Symmetrical periodic solutions and **b** basins of attraction of them for excitation frequency equal to 3.5 Hz

The bifurcation diagrams from the Fig. 19.9 shows, that there are some regions where different solutions coexists. For example, between 3 and 4 Hz there are two types of a periodic solution. Figure 19.13a shows that Poincare section and phase plots of them have symmetrical structures, what was expected, since two symmetrical solutions are typical for pendulum systems.

We have tried to found regions of existence of these two solutions in terms of initial conditions. Therefore basins of attraction of the solutions, which are shown in the Fig. 19.13a, were numerically computed. Initial conditions have been changed in $\varphi_1 - \varphi_2$ plane, while $\dot{\varphi}_1$ and $\dot{\varphi}_2$ have been set to zero. Corresponding plot is reported in the Fig. 19.13b. Obtained results show that it is not easy to predict the solution variant basing on applied initial conditions. Indeed the system seems to be very sensitive in this frequency regime as far as initial conditions are concerned, although some patterns and relatively large individual basins can be distinguished.

19.6 Conclusions

The novel magneto-mechanical system with two coupled pendulums has been studied. The system is non-autonomous due to time-dependent and angular-position-dependent excitation, which originates from repulsive magnetic interaction between an electrical coil and a permanent magnet, which is mounted at the end of one pendulum. The combination of a magnetic interaction and elastic coupling results in a multi-well systems potential, which is likely the reason for rich non-linear dynamics of the system. Magnetic interaction modelling has been based on experimentally obtained data. The proposed system's model has proved its validity in terms of bifurcation diagrams, phase plots and Poincaré section comparison between experimentally and numerically obtained results. Proposed system may be the starting point in modelling and analysis of more elaborate magneto-mechanical systems like electric stepper motors with an elastic rotor or electric motors joined with a flexible element i.e. an Oldham clutch. Our so far carried out analysis of the system does not

account phenomena like synchronization and the transfer of energy, nevertheless it seems interesting for the future investigation topics.

Acknowledgements This work has been supported by the Polish National Science Centre under the grant OPUS 14 No. 2017/27/B/ST8/01330.

References

1. Fradkov, A., Andrievsky, B., Boykov, K.: Control of the coupled double pendulums system. Mechatronics **15**, 1289–1303 (2005)
2. Fradkov, A., Andrievsky, B.: Singular perturbations of systems controlled by energy-speed-gradient method. In: 43rd IEEE Conference on Decision and Control (CDC 2004), vol. 4, pp. 3441–3446. IEEE, Bahamas (2004)
3. Polczyński, K., Wasilewski, G., Awrejcewicz, J., Wijata, A.: Modeling and experimental investigation of dynamics of two pendulums elastically coupled and driven by magnetic field. In: Awrejcewicz, J., Kaźmierczak, M., Mrozowski, J., Olejnik, P. (eds.) Engineering Dynamics and Life Sciences, pp. 451–462. DAB&M of TUL Press, Lodz (2017)
4. Wojna, M., Wijata, A., Wasilewski, G., Awrejcewicz, J.: Numerical and experimental study of a double physical pendulum with magnetic interaction. J. Sound Vib. **430**, 214–230 (2018). https://doi.org/10.1016/J.JSV.2018.05.032
5. Siahmakoun, A., French, V., Patterson, J.: Nonlinear dynamics of a sinusoidally driven pendulum in a repulsive magnetic field. Am. J. Phys. **65**, 393–400 (1997). https://doi.org/10.1119/1.18546
6. Kitio Kwuimy, C.A., Nataraj, C., Belhaq, M.: Chaos in a magnetic pendulum subjected to tilted excitation and parametric damping. Math. Probl. Eng. **2012**, 1–18 (2012). https://doi.org/10.1155/2012/546364
7. Khomeriki, G.: Parametric resonance induced chaos in magnetic damped driven pendulum. Phys. Lett. A **380**, 2382–2385 (2016). https://doi.org/10.1016/J.PHYSLETA.2016.05.049
8. Tran, V., Brost, E., Johnston, M., Jalkio, J.: Predicting the behavior of a chaotic pendulum with a variable interaction potential. Chaos Interdiscip. J. Nonlinear Sci. **23**, 033103 (2013). https://doi.org/10.1063/1.4812721
9. Mann, B.: Energy criterion for potential well escapes in a bistable magnetic pendulum. J. Sound Vib. **323**, 864–876 (2009)

Chapter 20
Dynamics of a System of Two Coupled MEMS Oscillators

Richard H. Rand, Alan T. Zehnder, B. Shayak and Aditya Bhaskar

Abstract We investigate the dynamics of two limit cycle MEMS oscillators connected via spring coupling. Each individual oscillator is based on a MEMS structure which moves within a laser-driven interference pattern. As the structure vibrates, it changes the interference gap, causing the quantity of absorbed light to change, producing a feedback loop between the motion and the absorbed light and resulting in a limit cycle oscillation. A simplified model of this MEMS oscillator, omitting parametric feedback and structural damping, has been previously presented (Rand et al in Proceedings of 9th European Nonlinear Dynamics Conference (ENOC 2017), 2017, [3]). For the coupled system, a perturbation method is used to obtain a slow flow which is investigated using AUTO and numerical integration. Various bifurcations which occur as a result of changing the coupling strength are identified.

Keywords Coupled oscillators · MEMS · Bifurcations · Perturbations

20.1 Introduction

This work is motivated by a type of MEMS device in which a laser is used to determine the motion of the device by interference. The MEMS device is typically a clamped-clamped beam fabricated from a thin layer of Si and suspended above a Si substrate. Laser light is focused onto the beam surface and is partially reflected, absorbed and

R. H. Rand (✉) · A. T. Zehnder · B. Shayak · A. Bhaskar
Theoretical and Applied Mechanics, Sibley School of Mechanical and Aerospace Engineering, and Department of Mathematics, Cornell University, Ithaca, NY 14853, USA
e-mail: rhr2@cornell.edu

A. T. Zehnder
e-mail: atz2@cornell.edu

B. Shayak
e-mail: sb2344@cornell.edu

A. Bhaskar
e-mail: ab2823@cornell.edu

I. Kovacic and S. Lenci (eds.), *IUTAM Symposium on Exploiting Nonlinear Dynamics for Engineering Systems*, IUTAM Bookseries 37,
https://doi.org/10.1007/978-3-030-23692-2_20

transmitted. The transmitted portion is further reflected from the substrate and will interfere with the reflected light to form a cavity interferometer. The net effect is that both the reflected and absorbed light are periodic functions of the gap between the beam and the substrate. Thus, vibration of the beam will modulate both the reflected and absorbed light. The reflected light, directed to an AC coupled photo diode is used to transduce the motion of the MEMS device.

The absorbed portion of the laser light causes heating of the MEMS device by the laser beam, resulting in the deflection of the device, which then changes the amount of heat absorbed, with the net effect of feedback between the motion and the thermal heating, which can produce limit cycle (LC) oscillations.

We are interested in studying the dynamics of a system of such coupled LC oscillators. Each one consists of an elastic system, modeled as a second order ODE, coupled to a first order ODE representing the heat transfer due to the laser heating effects.

A system of this kind was studied by Aubin et al. in [1], and may be written in the following form:

$$\ddot{z} + \frac{\dot{z}}{Q} + (1 + CT)z + \beta z^3 = DT, \tag{20.1}$$

$$\dot{T} + BT = HP[a + \gamma \sin^2 2\pi(z - z_0)] \tag{20.2}$$

Here z is the displacement of a mechanical oscillator and T is its temperature due to laser illumination. In the mechanical equation Q is the quality factor, C is the stiffness change due to temperature, D is the displacement due to temperature and β is the coefficient of the cubic nonlinearity. In the thermal equation the quantities a and γ represent the average and contrast of the absorption of laser power, P is the laser power, H and B represent the thermal mass and heat loss rate. The offset, z_0, models the equilibrium position of the oscillator with respect to the interference field created by the oscillator/gap/substrate stack. This complicated model, which includes effects of damping, stiffness change due to heating, periodic dependence of light absorption on interferometric gap, and nonlinearity, was shown to support LC oscillations.

In a recent paper, Zehnder et al. [2] considered a coupled system of two such LC oscillators:

$$\ddot{z}_1 + \frac{\dot{z}_1}{Q} + (1 + CT_1)z_1 + \beta z_1^3 + \frac{V^2(z_1 - z_2)}{1 + |z_1 - z_2|^p} = DT_1\ , \tag{20.3}$$

$$\dot{T}_1 + BT_1 = HP[a + \gamma \sin^2(2\pi(z_1 - z_0))]\ , \tag{20.4}$$

$$\ddot{z}_2 + \frac{\dot{z}_2}{Q} + \kappa(1 + CT_2)z_2 + \beta z_2^3 + \frac{V^2(z_2 - z_1)}{1 + |z_2 - z_1|^p} = DT_2\ , \tag{20.5}$$

$$\dot{T}_2 + BT_2 = HP[a + \gamma \sin^2(2\pi(z_2 - z_0))]\ . \tag{20.6}$$

Here the V^2 terms represent electrostatic fringing field coupling, see Fig. 20.1.

Numerous interesting effects were observed in this numerical study of the governing differential equations, including regions of 1:1 locking, and more generally of m:n locking. However, these differential equations are very complicated and it

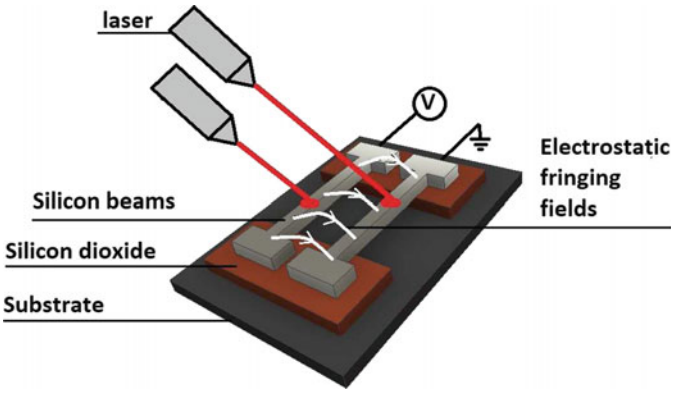

Fig. 20.1 A system of two coupled MEMS oscillators

is hard to tell which terms are responsible for the changes in qualitative dynamical behavior. Thus, in order to better understand the dynamics, we posited a simpler system which omitted effects such as damping, nonlinearity and stiffness changes due to heating [3]:

$$\ddot{z} + z = T \qquad \text{and} \qquad \dot{T} + T = z^2 - pz \tag{20.7}$$

To produce the simplest possible model, all constants have been taken equal to unity. The parameter z_0 in Eqs. (20.3)–(20.6) is referred to as p and takes on a representative value of 0.1. Numerical integration shows that this system supports a limit cycle [3].

In the present study, two oscillators of the form of Eq. (20.7) are considered, connected via spring coupling. The equations of motion are:

$$\ddot{z_1} + z_1 = T_1 + \alpha(z_2 - z_1) \qquad \text{and} \qquad \dot{T_1} + T_1 = z_1^2 - pz_1 \tag{20.8}$$
$$\ddot{z_2} + z_2 = T_2 + \alpha(z_1 - z_2) \qquad \text{and} \qquad \dot{T_2} + T_2 = z_2^2 - pz_2 \tag{20.9}$$

where α is a positive parameter, the coupling strength. The spring coupling is analogous to the electrostatic fringing field of Eqs. (20.3), (20.5), see Fig. 20.1.

20.2 Perturbations

In order to prepare Eqs. (20.8), (20.9) for treatment by perturbations, a parameter ε is introduced as follows:

$$\ddot{z_1} + z_1 = \varepsilon T_1 + \varepsilon^2\alpha(z_2 - z_1) \qquad \text{and} \qquad \dot{T_1} + T_1 = z_1^2 - \varepsilon pz_1 \tag{20.10}$$
$$\ddot{z_2} + z_2 = \varepsilon T_2 + \varepsilon^2\alpha(z_1 - z_2) \qquad \text{and} \qquad \dot{T_2} + T_2 = z_2^2 - \varepsilon pz_2 \tag{20.11}$$

We use a three variable perturbation method (also known as multiple scales) [4], which involves replacing the independent variable t with three new variables, $\xi = t$, $\eta = \varepsilon t$ (slow time) and $\zeta = \varepsilon^2 t$ (very slow time). The chain rule gives:

$$\frac{dz}{dt} = \frac{\partial z}{\partial \xi}\frac{d\xi}{dt} + \frac{\partial z}{\partial \eta}\frac{d\eta}{dt} + \frac{\partial z}{\partial \zeta}\frac{d\zeta}{dt} = \frac{\partial z}{\partial \xi} + \varepsilon\frac{\partial z}{\partial \eta} + \varepsilon^2\frac{\partial z}{\partial \zeta} \tag{20.12}$$

$$\frac{d^2z}{dt^2} = \frac{\partial^2 z}{\partial \xi^2} + +2\varepsilon\frac{\partial^2 z}{\partial \eta \partial \xi} + \varepsilon^2\left(\frac{\partial^2 z}{\partial \zeta \partial \xi} + \frac{\partial^2 z}{\partial \eta^2}\right) \tag{20.13}$$

Next all 4 variables z_1, T_1, z_2, T_2 are expanded in power series in ε and are substituted into Eqs. (20.10), (20.11). After collecting like powers of ε, we obtain:

$$z_1 = A(\zeta)\cos\xi + B(\zeta)\sin\xi + O(\varepsilon) \quad \text{and} \quad z_2 = C(\zeta)\cos\xi + D(\zeta)\sin\xi + O(\varepsilon) \tag{20.14}$$

where the slowly varying parameters A, B, C, D are determined by the following slow flow, which is obtained by eliminating secular terms from the $O(\varepsilon^2)$ equations:

$$\frac{d\,A}{d\,\zeta} = -\frac{60\,\alpha\,D + 31\,B^3 + 27\,A\,B^2 + \left(31\,A^2 - 30\,p - 60\,\alpha\right)\,B + 27\,A^3 - 30\,p\,A}{120} \tag{20.15}$$

$$\frac{d\,B}{d\,\zeta} = \frac{60\,\alpha\,C - 27\,B^3 + 31\,A\,B^2 + \left(30\,p - 27\,A^2\right)\,B + 31\,A^3 + (-30\,p - 60\,\alpha)\,A}{120} \tag{20.16}$$

$$\frac{d\,C}{d\,\zeta} = -\frac{31\,D^3 + 27\,C\,D^2 + \left(31\,C^2 - 30\,p - 60\,\alpha\right)\,D + 27\,C^3 - 30\,p\,C + 60\,\alpha\,B}{120} \tag{20.17}$$

$$\frac{d\,D}{d\,\zeta} = -\frac{27\,D^3 - 31\,C\,D^2 + \left(27\,C^2 - 30\,p\right)\,D - 31\,C^3 + (30\,p + 60\,\alpha)\,C - 60\,\alpha\,A}{120} \tag{20.18}$$

These equations can be simplified by transforming to polar coordinates:

$$A = r_1\cos\theta_1, \quad B = r_1\sin\theta_1, \quad C = r_2\cos\theta_2, \quad D = r_2\sin\theta_2, \tag{20.19}$$

with the following result, where $\varphi = \theta_2 - \theta_1$:

$$\frac{\mathrm{d}r_1}{\mathrm{d}\zeta} = \frac{pr_1}{4} - \frac{9r_1^3}{40} - \frac{\alpha}{2}r_2\sin\varphi \tag{20.20}$$

$$\frac{\mathrm{d}r_2}{\mathrm{d}\zeta} = \frac{pr_2}{4} - \frac{9r_2^3}{40} + \frac{\alpha}{2}r_1\sin\varphi \tag{20.21}$$

$$\frac{\mathrm{d}\varphi}{\mathrm{d}\zeta} = \frac{31}{120}\left(r_2^2 - r_1^2\right) + \frac{\alpha}{2}\cos\varphi\left(\frac{r_1}{r_2} - \frac{r_2}{r_1}\right) \tag{20.22}$$

The rest of this paper is based on an analysis of these last three equations.

20.3 Bifurcations

The first thing to notice about Eqs. (20.20)–(20.22) is that they exhibit a symmetry: they are invariant under the transformation

$$r_1 \longrightarrow r_2, \quad r_2 \longrightarrow r_1, \quad \varphi \longrightarrow -\varphi \tag{20.23}$$

As we will see, this symmetry will have a profound effect on the bifurcations associated with Eqs. (20.20)–(20.22).

Let us begin by looking for equilibria in the slow flow (20.20)–(20.22). These turn out to satisfy

$$r_1 = r_2 = \frac{\sqrt{10p}}{3} \quad \text{and} \quad \sin\varphi = 0 \Longrightarrow \varphi = 0 \ \text{ or } \ \pi \tag{20.24}$$

Here $\varphi = 0$ corresponds to the in phase (IP) mode and $\varphi = \pi$ corresponds to the out of phase (OP) mode.

As a first step in understanding the bifurcations occurring in Eqs. (20.20)–(20.22), we use the bifurcation software AUTO [5]. See Fig. 20.2 where equilibrium points in the slow flow are displayed using the convention that a solid (dashed) line represents a stable (unstable) equilibrium. Limit cycles in the slow flow (born in a Hopf bifurcation) are not shown. The OP mode at $\varphi = \pi$ is not shown, and is stable.

Note that for $\alpha > 0.0574$ AUTO predicts that both the IP and OP modes are stable. These slow flow equilibria are separated by an unstable slow flow limit cycle which we shall refer to as a separatrix. Moving from the 3 dimensional slow flow space to the 6 dimensional space of Eqs. (20.8), (20.9), the separatrix appears as a quasiperiodic motion. Although it is unstable we may nevertheless see what the separatrix looks like by numerically integrating Eqs. (20.8), (20.9) for initial conditions of the form $(z_1(0), \dot{z}_1(0), T_1(0), z_2(0), \dot{z}_2(0), T_2(0)) = (0.1, 0, 0, \mu, 0, 0)$, and iteratively varying μ so that the large time behavior (approximately) lies on the basin boundary between the two equilibria. See Fig. 20.3 where we find that $\mu \approx 0.0021$ for $\alpha = 0.07$.

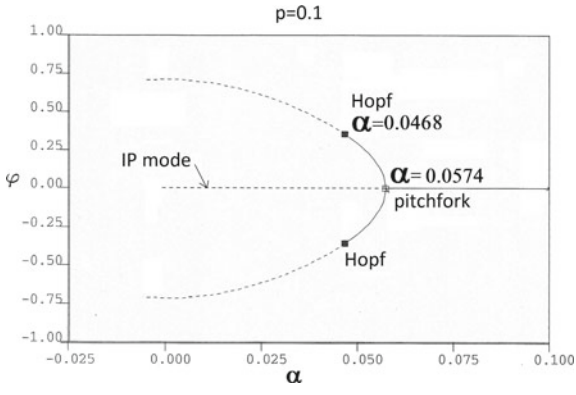

Fig. 20.2 AUTO bifurcation diagram for Eqs. (20.20)–(20.22). A solid (dashed) line represents a stable (unstable) equilibrium point in the slow flow. Limit cycles in the slow flow born in the Hopf bifurcations are not shown. The OP mode at $\varphi = \pi$ is not shown, and is stable

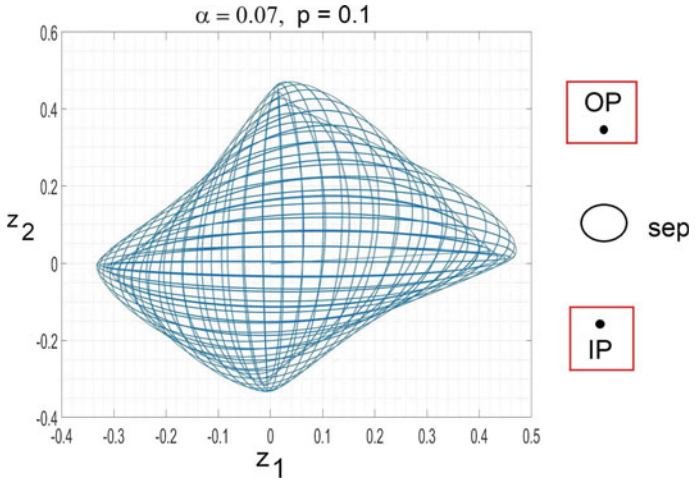

Fig. 20.3 LEFT: Separatrix motion, unstable, separates stable IP and OP modes. RIGHT: Schematic view showing IP, OP and separatrix. Stable motions are boxed in Red

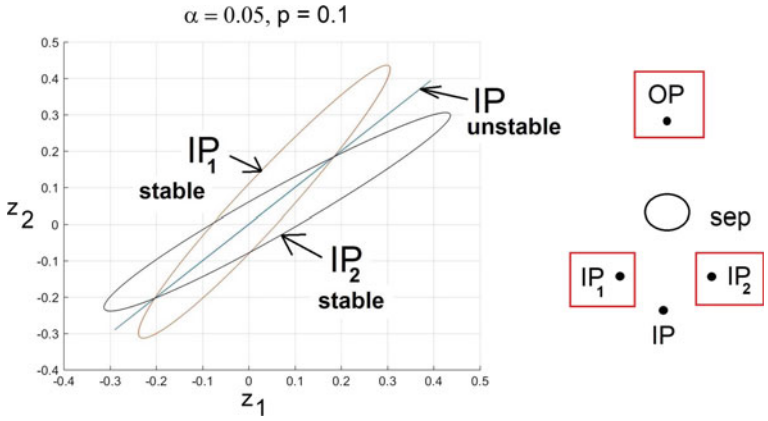

Fig. 20.4 LEFT: Two new slow flow equilibria are born in a pitchfork, denoted by IP_1 and IP_2. In the 6 dimensional space these are seen to be periodic motions, symmetrically located about the IP mode. RIGHT: Schematic view showing IP_1, IP_2, IP, OP and separatrix. Stable motions are boxed in Red

From Fig. 20.2 we see that when α is decreased through 0.0574, the IP mode loses stability in a pitchfork bifurcation. Two new slow flow equilibria are born in this pitchfork, denoted by IP_1 and IP_2. In the 6 dimensional space these are seen to be periodic motions, see Fig. 20.4.

From Fig. 20.2 we see that when α is further decreased through 0.0468, the slow flow equilibria IP_1 and IP_2 lose stability in Hopf bifurcations, resulting in stable slow flow limit cycles LC_1 and LC_2. In the 6 dimensional space these are seen to be quasiperiodic motions, see Fig. 20.5.

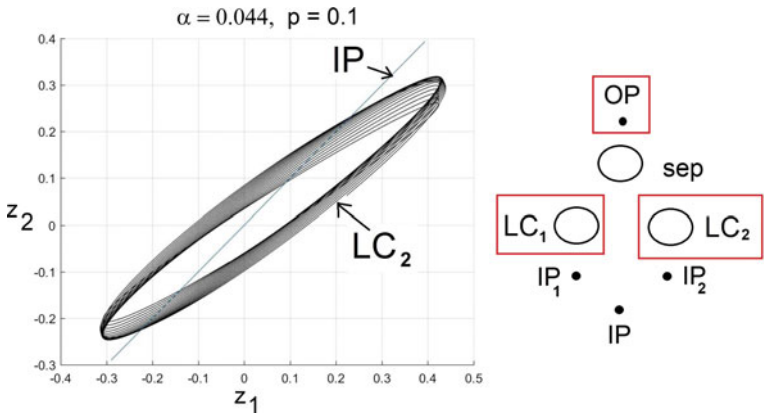

Fig. 20.5 LEFT: Two new slow flow limit cycles are born in Hopf bifurcations, denoted by LC_1 and LC_2. In the 6 dimensional space these are seen to be quasiperiodic motions, symmetrically located about the IP mode, cf. Fig. 20.4. Note: For clarity of presentation, LC_1 is not shown. RIGHT: Schematic view showing LC_1, LC_2, IP_1, IP_2, IP, OP and separatrix. Stable motions are boxed in Red

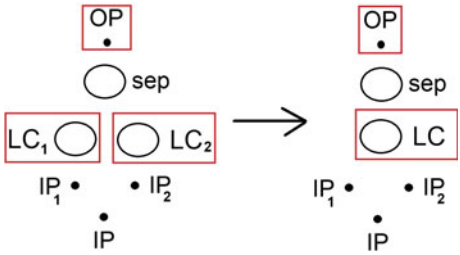

Fig. 20.6 A schematic representation of the double homoclinic bifurcation in which the asymmetric slow flow limit cycles LC_1 and LC_2 join to become a single slow flow limit cycle LC which exhibits the symmetry of Eq. (20.23). Stable motions are boxed in Red

A further bifurcation occurs when α decreases through approximately 0.0436, though this is not shown in Fig. 20.2. In this case there is a homoclinic bifurcation in which the asymmetric slow flow limit cycles LC_1 and LC_2 join to become a single slow flow limit cycle LC which exhibits the symmetry of Eq. (20.23). See Fig. 20.6.

Another bifurcation occurs when α decreases through approximately 0.0415, in which two slow flow limit cycles merge together in a limit cycle fold and disappear. Specifically, the unstable separatrix limit cycle "sep" merges simultaneously and symmetrically with the symmetric slow flow stable limit cycle "LC". See Fig. 20.7. For values of α less than approximately 0.0415, the OP mode is the only stable motion.

The last two bifurcations (shown in Figs. 20.5 and 20.6) involve the merging of two limit cycles into a single limit cycle (a double homoclinic bifurcation), which is then followed by a limit cycle fold in which a stable and an unstable limit cycle come together and disappear. This sequence of bifurcations has been seen in other, unrelated dynamical systems. See [6] p. 376, Fig. 7.3.9, and [7] p. 69, Fig. 7.

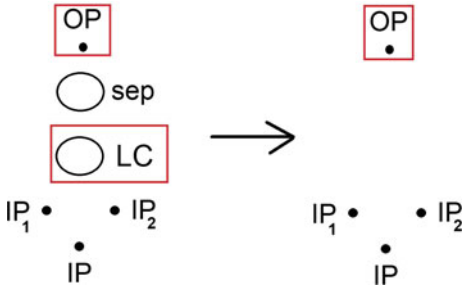

Fig. 20.7 A schematic representation of the limit cycle fold in which two slow flow limit cycles merge together and disappear, leaving the OP mode as the only stable motion. Stable motions are boxed in Red

20.4 Conclusions

In this work we have investigated the dynamics of a system inspired by a pair of coupled identical MEMS oscillators, Eqs. (20.8), (20.9). Our method involved introducing a small parameter ε which permitted us to use a perturbation method, resulting in a slow flow, Eqs. (20.20)–(20.22). We then used AUTO and numerical integration to determine the various bifurcations which occurred when the coupling constant α was varied (for fixed parameter $p = 0.1$). Since the perturbation method is by its very nature approximate, we should not be surprised to find that the derived results are in some cases incorrect. In particular analysis of the slow flow predicts that both the IP and OP modes are stable for α sufficiently large. While this is true of the IP mode, linear stability analysis of the OP mode shows that it becomes unstable for $\alpha > 0.82$. Proof of this statement will be the subject of another paper by the same authors.

We noted that the derived slow flow (20.20)–(20.22) possessed a symmetry which led to nongeneric bifurcations such as a pitchfork and a homoclinic bifurcation with symmetry. A useful extension of this work will involve a comparable study of the dynamics of a pair of coupled nonidentical third order oscillators, which is not expected to display these kinds of nongeneric bifurcations.

Perhaps the most important lesson learned from this study is that the IP mode can be made stable by increasing the coupling between the oscillators. This result is reminiscent of a comparable property of similarly coupled van der Pol oscillators [4].

Acknowledgements The authors wish to thank Professor J. Guckenheimer for advising them on the bifurcations involved in this paper. This material is based upon work supported by the National Science Foundation under grant number CMMI-1634664.

References

1. Aubin, K., Zalalutdinov, M., Alan, T., Reichenbach, R.B., Rand, R., Zehnder, A., Parpia, J., Craighead, H.: Limit cycle oscillations in CW laser-driven NEMS. J. Microelectromechanical Syst. **13**, 1018–1026 (2004)
2. Zehnder, A.T., Rand, R.H., Krylov, S.: Phase locking of electrostatically coupled thermo-optically driven MEMS limit cycle oscillators. Int. J. Non-Linear Mech. **102**, 92–100 (2018)

3. Rand, R.H., Zehnder, A.T., Shayak B.: Analysis of a simplified MEMS oscillator. In: Proceedings of 9th European Nonlinear Dynamics Conference (ENOC 2017), 25–30 June 2017, Budapest, Hungary. https://congressline.hu/enoc2017/abstracts/77.pdf (2017)
4. Rand, R.H.: Lecture Notes in Nonlinear Vibrations. The Internet-First University Press. http://ecommons.library.cornell.edu/handle/1813/28989 (2012)
5. Doedel, E.: see AUTO homepage. http://indy.cs.concordia.ca/auto/ (1996)
6. Guckenheimer, J., Holmes, P.: Nonlinear Oscillations, Dynamical Systems, and Bifurcation of Vector Fields. Springer, Berlin (1983)
7. Lazarus, L., Davidow, M., Rand, R.: Dynamics of an oscillator with delay parametric excitation. Int. J. Non-Linear Mech. **78**, 66–71 (2016)

Chapter 21
A Multimodal Nonlinear Tuned Vibration Absorber

Ghislain Raze and Gaetan Kerschen

Abstract This paper presents a tuning methodology to design a vibration absorber able to mitigate the vibratory amplitude of multiple resonances of a nonlinear structure. The linear characteristics of the absorber are first tuned to obtain the equal-peak design on every mode to be controlled when the structure is behaving linearly. Nonlinearities are then introduced intentionally in the absorber to counteract the effect of the nonlinearities inside the host structure. Their functional form is chosen according to a principle of similarity, and their coefficients are determined to enforce equal peaks in the nonlinear regime.

Keywords Nonlinear vibrations · Tuned vibration absorber · Multimodal vibration absorber · Principle of similarity · Equal peak method

21.1 Introduction

Engineering structures are becoming lighter and more complex to suit the needs of an ever-increasing demand for performance and to comply with stringent regulations. This trend comes with several challenges, one of which being the increased susceptibility to high-amplitude vibrations. These vibrations can be detrimental to the device performance and lifetime, or even be threatening safety. Passive vibration reduction techniques can provide a solution to this issue. The linear tuned vibration absorber (LTVA, also often referred to as "tuned mass damper" or "dynamic vibration absorber") enters this category and is a widely-used device of proven efficiency [4].

The LTVA was first proposed by Frahm [5]. By attaching a one-degree-of-freedom undamped oscillator to a host structure, one particular vibration mode can be completely suppressed. Ormondroyd and den Hartog [11] proposed to add a damping

G. Raze (✉) · G. Kerschen
Space Structures and Systems Laboratory, Allée de la Découverte 9, 4000 Liege, Belgium
e-mail: g.raze@uliege.be

G. Kerschen
e-mail: g.kerschen@uliege.be

I. Kovacic and S. Lenci (eds.), *IUTAM Symposium on Exploiting Nonlinear Dynamics for Engineering Systems*, IUTAM Bookseries 37,
https://doi.org/10.1007/978-3-030-23692-2_21

element to broaden the bandwidth in which the absorber is efficient. They based the tuning methodology on invariant points in the frequency response function. These points are insensitive to the absorber damping. The stiffness of the absorber is tuned to make the amplitude of the frequency response function at these points equal and the absorber damping may be chosen so that one of this two points is a local maximum of the frequency response function, yielding two possible values. Brock [1] later proposed to take the average of these damping values to yield a nearly optimal design. Almost sixty years later, Nishihara and Asami [10] found the exact closed-form solution to this problem, based on the minimization of the maximal vibratory amplitude of the host structure. With this design, the frequency response function of the controlled structure exhibits two peaks of equal amplitude near the original resonance of the host structure. Hence, this design was termed equal-peak design.

Many structures might have multiple resonances inside a frequency band of interest. Considering a structure with multiple modes brings new challenge to the design of tuned vibration absorbers. The influence of non-resonant modes might detune the absorber, which is detrimental for its performance. Krenk and Høgsberg [9] proposed to introduce quasi-dynamic background corrections to take into account the influence of non-resonant modes. Ozer and Royston [12] proposed a numerical optimization algorithm based on the invariant points of the frequency response function to tune the absorbers. If the excitation frequency is uncertain or varying, or the structure is subjected to a multiharmonic or broadband forcing, multiple resonances might be excited. A simultaneous control of these resonances may be desirable.

Lighter and more flexible structures are more prone to high-amplitude vibrations. These vibrations can trigger the nonlinearities present in the structure. One peculiarity of nonlinear structures is their frequency-energy dependence: the resonance frequencies of a nonlinear structure may change with the forcing amplitude. This can be particularly detrimental to tuned vibration absorbers, as the nonlinear resonance frequencies shift away from their initial position, detuning the absorber. This detuning is often the cause for a loss of performance. Habib and Kerschen [8] purposely used a nonlinear stiffness in a nonlinear tuned vibration absorber (NLTVA) to counteract this undesirable phenomenon. They proposed to use a principle of similarity for the design of nonlinear vibration absorbers. This principle states that the functional form of the nonlinearity in the absorber should be identical to that of the host structure. They designed a nonlinear vibration absorber able to maintain equal peaks over a broader range of forcing amplitude than when using a linear vibration absorber. This same principle of similarity was recently used by Habib and Kerschen [7] to modify the characteristics of multiple nonlinear resonances. By introducing and properly tuning nonlinearities in a structure, they were able to linearise its dynamics.

The purpose of this work is to associate the multimodal and nonlinear aspects of a tuned vibration absorber. More specifically, this paper describes how to design a vibration absorber able to mitigate the vibratory amplitude of multiple nonlinear resonances. To this end, the absorber is first designed considering the underlying linear dynamics of the host structure. A design approach based on a modal expansion of the frequency response function of the host structure is proposed. If more precision is required in the tuning, an objective function for an optimisation algorithm

is proposed. The nonlinear behaviour of the structure is then taken into account. Nonlinearities are intentionally introduced in the absorber. Their functional form is chosen according to a principle of similarity. The same formalism as [7] is used to impose equal peaks in the nonlinear frequency response function. With this new design, the working range of vibration absorbers can be extended to higher forcing amplitudes.

21.2 Multimodal Linear Tuned Vibration Absorber

This section introduces a tuning methodology for multiple LTVAs placed on an undamped structure. The structure is modelled as a one-degree-of-freedom oscillator from the point of view of the absorber, similarly to [9]. With this model, it is possible to tune the parameters of the absorber. If a further precision is required, a cost function for an optimisation algorithm is proposed.

The undamped equations of motion of the host structure are given by

$$\mathbf{M}_0\ddot{\mathbf{x}}_0 + \mathbf{K}_0\mathbf{x}_0 = \mathbf{f}_0(t), \tag{21.1}$$

where $\mathbf{M}_0$ is the structural mass matrix, $\mathbf{K}_0$ is the structural stiffness matrix, $\mathbf{x}_0$ is the vector of generalized coordinates and $\mathbf{f}_0(t)$ is the generalized loading vector. The subscript 0 indicates quantities exclusively related to the host structure. Under the assumption of a periodic forcing, i.e. $\mathbf{f}_0(t) = \mathbf{f}_0 \cos \omega t$, the equations of motion can be solved by expanding the response in the basis of the structural normal modes and by projecting them onto this basis [6]. Eventually, by reconstructing the physical response from the modal response,

$$\mathbf{x}_0 = \mathbf{\Phi}_0 \left(\mathbf{\Omega}_0^2 - \omega^2\mathbf{I}\right)^{-1} \mathbf{\Phi}_0^T \mathbf{f}_0, \tag{21.2}$$

where $\mathbf{\Phi}_0$ is the matrix of mass-normalized mode shapes, $\mathbf{\Omega}_0$ is a diagonal matrix containing the associated mode frequencies, $\mathbf{I}$ is the identity matrix and the superscript T denotes a transposition. This harmonic response can be used in the design of the absorbers. Assuming that the absorber is placed at a location given by the localisation vector $\mathbf{w}$, its base displacement can be found as $u = \mathbf{w}^T\mathbf{x}_0$. Introducing

$$\mathbf{w}^T\mathbf{\Phi}_0 = \left[\phi_{u,1}, \ldots, \phi_{u,N_0}\right], \tag{21.3}$$

$$\mathbf{\Phi}_0^T\mathbf{f}_0 = \left[\phi_{f,1}, \ldots, \phi_{f,N_0}\right]^T f_0, \tag{21.4}$$

with the number of modes N_0 and the forcing amplitude f_0, the forced harmonic response can be expressed as a sum of contributions from the different modes

$$u = \sum_{i=1}^{N_0} \frac{\phi_{u,i}\phi_{f,i}}{\omega_i^2 - \omega^2} f_0. \tag{21.5}$$

Around the resonance frequency of mode i, the harmonic response may be approximated by that of a single-degree-of-freedom spring-mass system. Neglecting all the terms different than those related to mode i in the sum of Eq. (21.5), the modal mass m_i and the modal stiffness k_i are identified as

$$m_i = \frac{1}{\phi_{u,i}\phi_{f,i}}, \qquad k_i = \frac{\omega_i^2}{\phi_{u,i}\phi_{f,i}}, \tag{21.6}$$

respectively. Using this one-degree-of-freedom approximation, the stiffness $k_{a,i}$ and damping $c_{a,i}$ of an LTVA of mass $m_{a,i}$ designed to mitigate the vibrations of mode i can be determined using the classical one-degree-of-freedom absorber design ([1, 11] or [10]) from the modal characteristics in Eq. (21.6) and the modal mass ratio

$$\mu_i = \frac{m_{a,i}}{m_i}. \tag{21.7}$$

Moreover, Eqs. (21.6) and (21.7) give guidelines on where to place the absorber. Since the vibration reduction increases with the modal mass ratio, it is desirable to maximize this ratio. For a given absorber mass and a given forcing, the best placement is the one that maximizes the modal amplitude $\phi_{u,i}$ in the position at which the absorber is placed.

To mitigate multiple resonances, multiple LTVAs can be placed on the structure. The above procedure can be repeated N times to tune the characteristics of N vibration absorbers. This would result in a reduced amplitude around the N targeted resonances, with ideally N pairs of equal peaks.

Because the truncation of the harmonic response in Eq. (21.5) involves neglecting several terms due to the non-resonant modes and because the interactions between the LTVAs are not properly taken into account by the aforementioned method, the frequency response function (FRF) will generally not exhibit perfectly equal peaks, as in the single-degree-of-freedom case. Numerical optimisation may be used to enforce equal peaks up to the desired accuracy. If two peaks related to mode i are located at the frequencies $\omega_{i,1}$ and $\omega_{i,2}$ and if H denotes the square modulus of the FRF for which equal peaks should be enforced, the following cost function can be used

$$f(m_{a,1}, c_{a,1}, k_{a,1}, \ldots, m_{a,N}, c_{a,N}, k_{a,N}) = \sum_{i=1}^{N} \left(H(\omega_{i,1}) - H(\omega_{i,2})\right)^2 \tag{21.8}$$

Minimizing this cost function will result in a design with N pairs of equal peaks. The peaks may be found by sampling the FRF, by using suitably initialised gradient ascent algorithms or by using H_∞ norm computation algorithms [2] in a limited range of frequencies to properly locate all the peaks. The sensitivity of the cost function may be computed numerically through finite differences, or analytically.

21.3 Multimodal Nonlinear Tuned Vibration Absorber

In this section, nonlinear elements are added to each absorbers to improve the vibration reduction in the nonlinear regime. It is assumed that the linear characteristics of the absorbers have been properly tuned so that the frequency response function of the controlled structure exhibits equal (or nearly equal) peaks in the linear regime. The functional form of the introduced nonlinear elements is chosen according to a principle of similarity, and their coefficients are computed by requiring that the nonlinear frequency response function exhibit equal peaks in the nonlinear regime.

The same formalism as Habib and Kerschen [7] is used in the following. The nonlinear equations of motion of the structure and of the nonlinear absorbers attached to it are given by

$$\mathbf{M}\ddot{\mathbf{x}} + \mathbf{C}\dot{\mathbf{x}} + \mathbf{K}\mathbf{x} + k_{nl}\left(\mathbf{b}_{nl}(\mathbf{x}) + \sum_{i=1}^{N} b_{nl,i}\mathbf{b}_{nl,i}(\mathbf{x})\right) = \mathbf{f}(t), \tag{21.9}$$

where $\mathbf{b}_{nl}$ represents the nonlinearities in the primary structure, and $\mathbf{b}_{nl,i}$ are the nonlinearities in the absorbers. According to the principle of similarity [8], the latter are chosen to have the same mathematical form as the former. The remaining unknowns are the nonlinear coefficients of the absorbers, $b_{nl,i}$.

The equations of motion are normalised considering $\mathbf{y} = \mathbf{x}/f$, with f being a forcing amplitude

$$\mathbf{M}\ddot{\mathbf{y}} + \mathbf{C}\dot{\mathbf{y}} + \mathbf{K}\mathbf{y} + \alpha\left(\mathbf{b}_{nl}(\mathbf{y}) + \sum_{i=1}^{N} b_{nl,i}\mathbf{b}_{nl,i}(\mathbf{y})\right) = \frac{\mathbf{f}(t)}{f}. \tag{21.10}$$

α is a nonlinearity parameter that depends on both the nonlinearity and the forcing. For a polynomial nonlinear force of type $f_{nl}(x) = k_{nl}x^p$, it is given by

$$\alpha = f^{p-1}k_{nl} \tag{21.11}$$

This parameter can be seen as a measure of how the structural behaviour is affected by the nonlinearities. The solution of Eq. (21.10) under a harmonic forcing can be approximated with a first-order harmonic balance (HB) method. Using

$$\mathbf{y} = \mathbf{q}_c\cos(\omega t) + \mathbf{q}_s\sin(\omega t), \tag{21.12}$$

and introducing $\mathbf{q}^T = [\mathbf{q}_c^T, \mathbf{q}_s^T]$, Eq. (21.10) becomes

$$\mathbf{W}\mathbf{q} + \alpha\left(\mathbf{d}_{1,nl}(\mathbf{q}) + \sum_{i=1}^{N} b_{nl,i}\mathbf{d}_{1,nl,i}(\mathbf{q})\right) = \mathbf{c}. \tag{21.13}$$

In Eq. (21.13), the matrix $\mathbf{W}$ represents the linear dynamics, $\mathbf{c}$ is the forcing term, and the terms $\mathbf{d}_{1,nl}$ and $\mathbf{d}_{1,nl,i}$ represent the nonlinearities in the primary structure and in the ith absorber, respectively. These vectors can be computed from $\mathbf{q}$ either analytically, or numerically with the alternating frequency/time-domain technique [3]. Thanks to the HB method, the set of nonlinear ordinary differential equations given in Eq. (21.10) has been transformed into a set of nonlinear algebraic equations. To find an approximate solution, it is further assumed that the nonlinearity parameter α is small. Hence, the nonlinear response of the system may be expressed as a series expansion in terms of α as

$$\mathbf{q} = \sum_{i=0}^{\infty} \alpha^i \mathbf{q}^{(i)}. \tag{21.14}$$

Inserting Eq. (21.14) into (21.13) and equating coefficients of like powers of α up to first order leads to the following explicit relations:

$$\mathbf{q}^{(0)} = \mathbf{W}^{-1}\mathbf{c}, \tag{21.15}$$

$$\mathbf{q}^{(1)} = -\mathbf{W}^{-1}\left(\mathbf{d}_{1,nl}(\mathbf{q}^{(0)}) + \sum_{i=1}^{N} b_{nl,i}\mathbf{d}_{1,nl,i}(\mathbf{q}^{(0)})\right) = \mathbf{q}_{nl}^{(1)} + \sum_{i=1}^{N} b_{nl,i}\mathbf{q}_{nl,i}^{(1)}. \tag{21.16}$$

Equation (21.15) indicates that $\mathbf{q}^{(0)}$ represents the response of the system when no nonlinearity is present. Equation (21.16) shows that first-order terms $\mathbf{q}^{(1)}$ are generated by the nonlinear forces triggered by the zeroth-order motion. These terms can be separated into terms due to the nonlinearities inside the primary structure $\mathbf{q}_{nl}^{(1)}$ and terms due to the nonlinearities inside the ith absorber $\mathbf{q}_{nl,i}^{(1)}$. The square of the frequency response function at a given degree of freedom is given by

$$H = (\mathbf{q}_c)_j^2 + (\mathbf{q}_s)_j^2. \tag{21.17}$$

Inserting the solution of (21.15) and (21.16) into (21.17) and keeping only the first-order terms leads to

$$\begin{aligned} H = \left(\mathbf{q}_c^{(0)}\right)_j^2 + \left(\mathbf{q}_s^{(0)}\right)_j^2 + & \quad \alpha\left[2\left(\mathbf{q}_c^{(0)}\right)_j\left(\mathbf{q}_{c,nl}^{(1)}\right)_j + 2\left(\mathbf{q}_s^{(0)}\right)_j\left(\mathbf{q}_{s,nl}^{(1)}\right)_j\right] \\ & + \alpha\left[\sum_{i=1}^{N} b_{nl,i}\left[2\left(\mathbf{q}_c^{(0)}\right)_j\left(\mathbf{q}_{c,nl,i}^{(1)}\right)_j + 2\left(\mathbf{q}_s^{(0)}\right)_j\left(\mathbf{q}_{s,nl,i}^{(1)}\right)_j\right]\right]. \\ = \quad H^{(0)} \quad + & \quad \alpha H_{nl}^{(1)} \\ + & \quad \alpha\sum_{i=1}^{N} b_{nl,i}H_{nl,i}^{(1)} \end{aligned} \tag{21.18}$$

In Eq. (21.18), three types of term can be identified. The term $H^{(0)}$ stands for the frequency response function of the underlying linear structure. The term $\alpha H_{nl}^{(1)}$ is the

modification brought by the (supposedly small) nonlinear forces generated by the linear motion in the nonlinearities of the primary structure. The term $\alpha b_{nl,i} H^{(1)}_{nl,i}$ is the modification brought by the (supposedly small) nonlinear forces generated by the linear motion in the nonlinearitiy i of the absorbers. Thanks to the straightforward expansion, all these effects can be separated to first order in α.

With Eq. (21.18), it is now possible to impose N conditions on the first-order nonlinear FRF. This yields a system of size $N \times N$, where the nonlinear coefficients $b_{nl,i}$ are the unknowns. Depending on the imposed conditions, this system can be linear and the nonlinear coefficients may or may not depend on the parameter α.

21.3.1 Equal Peaks in the Nonlinear Regime

A condition enforcing equal peaks in the nonlinear regime will now be derived. The linear absorbers are assumed to result in the equal-peak design, i.e. the peaks are equal in magnitude and located at frequencies $\omega_{i,1}$ and $\omega_{i,2}$ in the linear regime. The nonlinear effects cause a shift in these nonlinear peak frequencies, which are noted $\tilde{\omega}_{i,1}$ and $\tilde{\omega}_{i,2}$. Using a series development in α of the nonlinear frequency response, these nonlinear resonance frequencies are defined as

$$\left.\frac{\partial H}{\partial \omega}\right|_{\tilde{\omega}_{i,j}} = \sum_{n=0}^{\infty} \alpha^n \left.\frac{\partial H^{(n)}}{\partial \omega}\right|_{\tilde{\omega}_{i,j}} = 0 \tag{21.19}$$

They can be found by using a second series development in terms of the difference between the linear and nonlinear resonance frequencies $\Delta\omega_{i,j} = \tilde{\omega}_{i,j} - \omega_{i,j}$.

$$\left.\frac{\partial H}{\partial \omega}\right|_{\tilde{\omega}_{i,j}} = \sum_{n=0}^{\infty} \alpha^n \sum_{m=1}^{\infty} \frac{\left(\Delta\omega_{i,j}\right)^{m-1}}{(m-1)!} \left.\frac{\partial^m H^{(n)}}{\partial \omega^m}\right|_{\omega_{i,j}} = 0 \tag{21.20}$$

Keeping terms up to first order in $\Delta\omega_{i,j}$ and in α in the previous sum leads to

$$\left.\frac{\partial H^{(0)}}{\partial \omega}\right|_{\omega_{i,j}} + \Delta\omega_{i,j} \left.\frac{\partial^2 H^{(0)}}{\partial \omega^2}\right|_{\omega_{i,j}} + O\left(\Delta\omega_{i,j}\right)^2 + \alpha \left.\frac{\partial H^{(1)}}{\partial \omega}\right|_{\omega_{i,j}} + O\left(\Delta\omega_{i,j}\alpha\right) = 0 \tag{21.21}$$

Because $H^{(0)}$ is the linear frequency response function, the first term in Eq. (21.21) vanishes. Hence, the nonlinear resonance frequency shift is of the order of α. Now, the nonlinear frequency response at the nonlinear resonance frequency can be expressed as

$$H|_{\tilde{\omega}_{i,j}} = \sum_{n=0}^{\infty} \alpha^n \sum_{m=0}^{\infty} \frac{\left(\Delta\omega_{i,j}\right)^m}{m!} \left.\frac{\partial^m H^{(n)}}{\partial \omega^m}\right|_{\omega_{i,j}}. \tag{21.22}$$

Evaluating Eq. (21.22) at both nonlinear resonance frequencies, equating the two obtained nonlinear frequency response functions and keeping terms up to first order in α leads to

$$H^{(0)}\big|_{\omega_{i,1}} + \Delta\omega_{i,1} \left.\frac{\partial H^{(0)}}{\partial \omega}\right|_{\omega_{i,1}} + \alpha\ H^{(1)}\big|_{\omega_{i,1}} + O(\alpha^2) = H^{(0)}\big|_{\omega_{i,2}} + \Delta\omega_{i,2} \left.\frac{\partial H^{(0)}}{\partial \omega}\right|_{\omega_{i,2}} + \alpha\ H^{(1)}\big|_{\omega_{i,2}} + O(\alpha^2). \tag{21.23}$$

Since equal peaks were assumed in the linear regime, the first terms in the left and right hand side of Equation (21.23) cancel out. Moreover, the second terms also vanish by definition of the linear resonance frequencies. Then, Eq. (21.23) becomes independent of α and, using the contributions from the different nonlinearities highlighted by Eq. (21.18), it can be written as

$$\sum_{n=1}^{N} b_{nl,n} \left(H^{(1)}_{nl,n}(\omega_{i,1}) - H^{(1)}_{nl,n}(\omega_{i,2}) \right) = H^{(1)}_{nl}(\omega_{i,2}) - H^{(1)}_{nl}(\omega_{i,1}). \tag{21.24}$$

Interestingly, the nonlinear resonance frequency shift is not taken into account in the first-order frequency response function. Thus, the knowledge of the nonlinear resonance frequencies is not needed to design absorbers, at least to first order in α. Enforcing Eq. (21.24) for $i = 1, \ldots, N$ yields the following linear system of size $N \times N$:

$$\begin{bmatrix} \Delta_{\omega_1} H^{(1)}_{nl,1} & \Delta_{\omega_1} H^{(1)}_{nl,2} & \cdots & \Delta_{\omega_1} H^{(1)}_{nl,N} \\ \Delta_{\omega_2} H^{(1)}_{nl,1} & \Delta_{\omega_2} H^{(1)}_{nl,2} & \cdots & \vdots \\ \vdots & \vdots & \ddots & \vdots \\ \Delta_{\omega_N} H^{(1)}_{nl,1} & \cdots & \cdots & \Delta_{\omega_N} H^{(1)}_{nl,N} \end{bmatrix} \begin{bmatrix} b_{nl,1} \\ b_{nl,2} \\ \vdots \\ b_{nl,N} \end{bmatrix} = - \begin{bmatrix} \Delta_{\omega_1} H^{(1)}_{nl} \\ \Delta_{\omega_2} H^{(1)}_{nl} \\ \vdots \\ \Delta_{\omega_N} H^{(1)}_{nl} \end{bmatrix}, \tag{21.25}$$

in which

$$\Delta_{\omega_i} H = H(\omega_{i,1}) - H(\omega_{i,2}). \tag{21.26}$$

Equation (21.24) expresses that the (first-order) effects of all the nonlinearities is the same at $\omega_{i,1}$ and $\omega_{i,2}$. Therefore, the perfect equality between the amplitudes of the resonance peaks is not mandatory in practice. Peaks of approximately equal amplitude in the linear regime will remain approximately equal in the nonlinear regime.

Due to the series expansions limited to first order, this approach is a local approach, in the sense that the obtained results will gradually lose their validity with increasing α, that is, as the forcing amplitude or the nonlinear coefficients become large.

Nevertheless, it is expected that the nonlinear absorbers yield better result than their linear counterparts for small values of α.

21.4 Numerical Example

To demonstrate the efficiency of the proposed approach, a five-degree-of-freedom structure depicted in Fig. 21.1 is studied, with numerical parameters given in Table 21.1. A cubic spring is attached to the first mass. A harmonic forcing is applied to this mass and the structural response is measured at this same point.

Modes 1, 2 and 4 of the structure are targeted for vibration mitigation. The linear absorbers are placed at the maximum amplitude of the mode they are supposed to damp. Their parameters are optimised to obtain three pairs of equal peaks. The numerical values of the parameters are given in Table 21.2.

Figure 21.2 shows the nonlinear frequency response functions (NFRFs) of the structure with linear and nonlinear absorbers for two values of the nonlinearity parameter α. The NFRFs were computed with a continuation procedure coupled with a harmonic balance formalism [3] with five harmonics. For $\alpha = 0.01$, the nonlinear effects are strong enough to detune the linear absorber of mode 2, whereas adding a nonlinear spring to that absorbers helps enforcing equal peaks. Mode 1 and 4 are less affected, namely due to their lower vibratory amplitude. When α is increased,

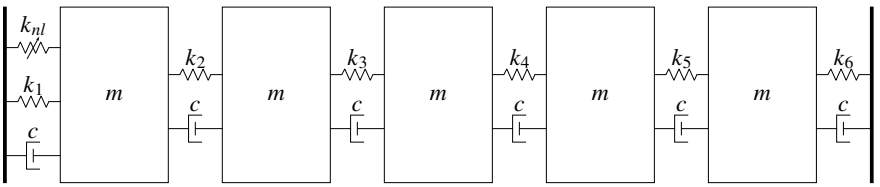

Fig. 21.1 Five-degree-of-freedom structure

Table 21.1 Numerical parameters of the five-degree-of-freedom structure

k_1 (N/m)	k_2 (N/m)	k_3 (N/m)	k_4 (N/m)	k_5 (N/m)	k_6 (N/m)	k_{nl} (N/m^3)	c (Ns/m)	m (kg)
1	1	0.1	1	1	1	1	0.03	1

Table 21.2 Parameters of the absorbers

Absorber	Location	m_a (kg)	c_a (Ns/m)	k_a (N/m)	$k_{nl,a}$ (N/m^3)
Mode 1	dof 3	0.05	3.88×10^{-3}	1.16×10^{-2}	1.38×10^{-5}
Mode 2	dof 2	0.05	6.03×10^{-3}	2.19×10^{-2}	3.02×10^{-4}
Mode 4	dof 1	0.05	1.66×10^{-2}	1.27×10^{-1}	1.95×10^{-3}

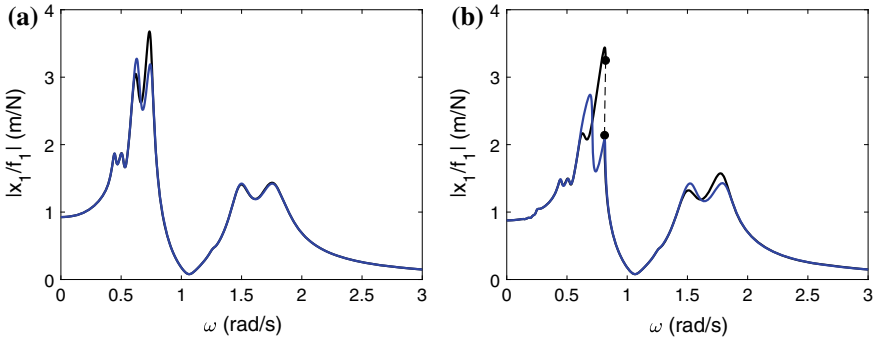

Fig. 21.2 NFRFs of the five-degree-of-freedom structure with linear (—: stable solution, - -: unstable solution, •: fold bifurcation) and nonlinear (—) absorbers: $\alpha = 0.01$ N^3/m^3 (**a**) and $\alpha = 0.09$ N^3/m^3 (**b**)

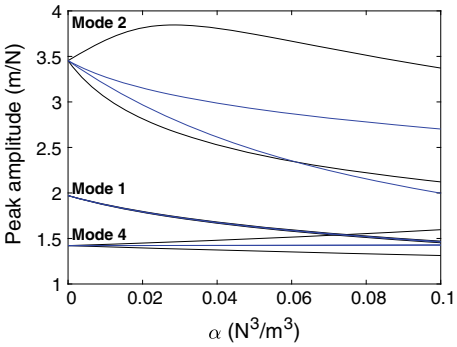

Fig. 21.3 Evolution of the peaks amplitudes with the nonlinearity parameter α: linear (—) and nonlinear (—) absorbers

mode 4 becomes affected. Equal peaks can be obtained thanks to the nonlinearities in the absorber for mode 4. As for mode 2, the peaks can no longer be considered as equal, but the situation is still improved compared to that of the linear absorbers. Indeed, the maximum vibratory amplitude is lower when nonlinear absorbers are used.

Figure 21.3 shows how the amplitudes of the six peaks evolve with α. When no nonlinear effect is present ($\alpha = 0$), the linear and nonlinear absorbers are equivalent. As α increases, the two lines representing the pair of peaks associated to a particular mode diverges more quickly when no nonlinearity is used in the absorbers. Thanks to Eq. (21.24), these lines are tangent at $\alpha = 0$ when the nonlinearities are properly tuned, which slows down their divergence for small α. This means that equal peaks are enforced over a broader amplitude range when using nonlinear absorbers. It is also clear that using nonlinear absorbers in this case leads to a lower maximum vibratory amplitude.

Going beyond that nonlinear regime can reveal more on the behaviour and the limitations of the proposed multimodal nonlinear tuned vibration absorber. The NFRFs of the structure in the strongly ($\alpha = 0.36$) and in the extremely ($\alpha = 0.81$) nonlinear

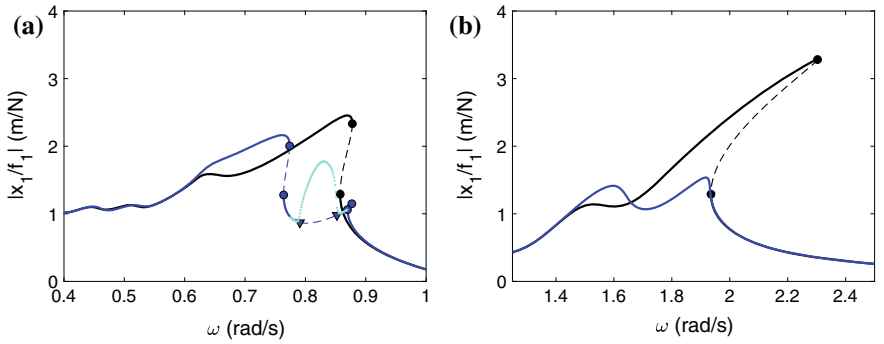

Fig. 21.4 NFRFs of the five-degree-of-freedom structure with linear (—: stable solution, - -: unstable solution, •: fold bifurcation) and nonlinear (—: stable solution, - -: unstable solution, •: fold bifurcation, ▼: Neimark–Sacker bifurcation, • : time-integrated solution) absorbers at $\alpha = 0.36$ N^3/m^3: close-up on modes 1 and 2 (**a**) and close-up on mode 4 (**b**)

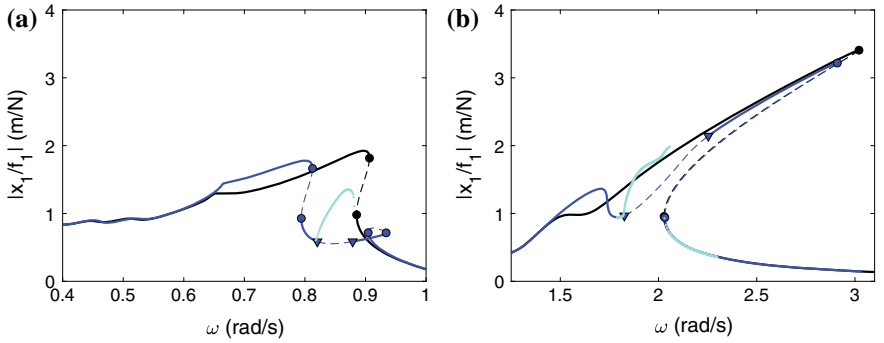

Fig. 21.5 NFRFs of the five-degree-of-freedom structure with linear (—: stable solution, - -: unstable solution, •: fold bifurcation) and nonlinear (—: stable solution, - -: unstable solution, •: fold bifurcation, ▼: Neimark–Sacker bifurcation, • : time-integrated solution) absorbers at $\alpha = 0.81$ N^3/m^3: close-up on modes 1 and 2 (**a**) and close-up on mode 4 (**b**)

regimes are shown in Figs. 21.4 and 21.5, respectively. With nonlinear absorbers, the onset of quasiperiodic oscillations can be observed on mode two, with the appearance of a pair of Neimark–Sacker bifurcations. The amplitude of those vibrations can be computed through direct time integration of the equations of motion. The linear absorbers are progressively detuned, which results in higher vibratory amplitudes as α increases. With the nonlinear absorbers, a detached resonance curve (DRC) merges with the rightmost peak of mode 4 at $\alpha = 0.518$, leading to the possibility of much higher vibration amplitudes. At this point, there is little difference of performance (in terms of maximal vibratory amplitude) between the linear and the nonlinear absorbers. Interestingly, the DRC of the nonlinear absorbers is connected to the NFRF through a branch of quasiperiodic solutions, which seems to lose its

stability when the lower-amplitude periodic solutions become stable again, as the behaviour of the amplitude obtained with time integration seems to indicate.

21.5 Conclusion

This paper proposed a tuning methodology for a multimodal nonlinear tuned vibration absorber. The linear characteristics of this absorber are first tuned. Based on a modal expansion of the frequency response function of the structure at the degree of freedom at which the absorbers are placed, an equivalent one-degree-of-freedom model is derived. The tuning rules of the absorber for a single-degree-of-freedom system can thus be used with multiple vibration absorbers to mitigate multiple resonances. A better equality between the peaks amplitudes can be obtained with the help of numerical optimisation. Nonlinearities are then added to the absorbers. Thanks to a principle of similarity, the functional form of these nonlinearities are chosen to be identical to those of the host structure. Their coefficients are determined by enforcing equal peaks in the nonlinear regime.

The example showed that the nonlinear absorbers placed on a nonlinear structure are more efficient than their linear counterpart. Not only are they able to enforce equal peaks over a broader amplitude range, but they also allow to obtain frequency response functions with lower maximal amplitudes than when using linear absorbers. The nonlinear absorbers trigger nonlinear phenomena, such as quasiperiodic oscillations and detached resonance curves. But even when these phenomena arise, the situation is at worse equivalent to that of the linear absorbers.

Future work may involve the use of a modal approach to simplify the computation of the nonlinear coefficients, therefore not requiring the full structural matrices.

Acknowledgements The authors would like to acknowledge the financial support of the SPW (WALInnov grant 1610122).

References

1. Brock, J.E.: A note on the damped vibration absorber. Trans. ASME J. Appl. Mech. **13**(4), A–284 (1946)
2. Bruinsma, N., Steinbuch, M.: A fast algorithm to compute the h_∞-norm of a transfer function matrix. Syst. Control. Lett. **14**(4), 287–293 (1990)
3. Detroux, T., Renson, L., Masset, L., Kerschen, G.: The harmonic balance method for bifurcation analysis of large-scale nonlinear mechanical systems. Comput. Methods Appl. Mech. Eng. **296**, 18–38 (2015)
4. Elias, S., Matsagar, V.: Research developments in vibration control of structures using passive tuned mass dampers. Annu. Rev. Control. **44**, 129–156 (2017). https://doi.org/10.1016/j.arcontrol.2017.09.015
5. Frahm, H.: Device for damping vibrations of bodies. US Patent 989,958 (1911)

6. Géradin, M., Rixen, D.J.: Mechanical Vibrations: Theory and Application to Structural Dynamics. Wiley, New York (2014)
7. Habib, G., Grappasonni, C., Kerschen, G.: Passive linearization of nonlinear resonances. J. Appl. Phys. **120**(4), 4–9 (2016). https://doi.org/10.1063/1.4959814
8. Habib, G., Kerschen, G.: A principle of similarity for nonlinear vibration absorbers. Phys. D Nonlinear Phenom. **332**, 1–8 (2016)
9. Krenk, S., Høgsberg, J.: Tuned resonant mass or inerter-based absorbers: unified calibration with quasi-dynamic flexibility and inertia correction. Proc. R. Soc. A Math. Phys. Eng. Sci. **472**(2185) (2016). https://doi.org/10.1098/rspa.2015.0718
10. Nishihara, O., Asami, T.: Closed-form solutions to the exact optimizations of dynamic vibration absorbers (minimizations of the maximum amplitude magnification factors). J. Vib. Acoust. **124**(4), 576–582 (2002)
11. Ormondroyd, J.: The theory of the dynamic vibration absorber. Trans. ASME Appl. Mech. **50**, 9–22 (1928)
12. Ozer, M.B., Royston, T.J.: Extending den hartog's vibration absorber technique to multi-degree-of-freedom systems. J. Vib. Acoust. **127**(4), 341–350 (2005)

Chapter 22
Unveiling Transient to Steady Effects in Reduced Order Models of Thermomechanical Plates via Global Dynamics

Valeria Settimi, Giuseppe Rega and Eduardo Saetta

Abstract A reduced model of third-order shear deformable plate with cubic temperature is used to investigate the system nonlinear dynamic response in a full thermomechanical coupling framework. Numerical investigations of local and global dynamics allow to highlight distinct response features as occurring under different (constant or dome-shaped) prescribed spatial temperatures on the plate surfaces. In both cases, the important role played by global analysis for unveiling meaningful transient to steady effects in the system dynamics clearly comes out.

Keywords Laminated plate · Reduced order model · Thermomechanical coupling · Thermal boundary conditions · Local and global analysis

22.1 Introduction

Reduced order modeling and nonlinear dynamics of composite plates under different excitation conditions in a thermomechanical environment have been the subject of recent papers aimed at highlighting the role of multiphysics coupling and the main local and global features of the nonlinear response [1–5].

In the framework of a unified formulation of the thermomechanical problem based on the Tonti approach to physical theories [6], two different 2D models of laminated plates with von Kármán nonlinearities have been proposed, by either neglecting [1] or considering [2] shear deformability and by consistently assuming a corresponding linear or cubic variation of the unknown thermal field along the plate thickness. For symmetric cross-ply laminates, proper and controllable dimension reduction

V. Settimi (✉) · G. Rega · E. Saetta
Department of Structural and Geotechnical Engineering, Sapienza University of Rome, Via A. Gramsci 53, 00197 Rome, Italy
e-mail: valeria.settimi@uniroma1.it

G. Rega
e-mail: giuseppe.rega@uniroma1.it

E. Saetta
e-mail: e.saetta@virgilio.it

I. Kovacic and S. Lenci (eds.), *IUTAM Symposium on Exploiting Nonlinear Dynamics for Engineering Systems*, IUTAM Bookseries 37,
https://doi.org/10.1007/978-3-030-23692-2_22

accomplished via Galerkin approximations has allowed in both cases to attain a minimal model (with one mechanical and two thermal equations/unknowns) still exhibiting the fundamental features of geometrical nonlinearity and thermomechanical coupling embedded in the underlying, yet more complicated, continuum models.

The simpler (shear indeformable with linear temperature) reduced model—labelled CTC for being based on the Classical theory with Thermomechanical Coupling—has been employed for extended investigations of the plate nonlinear dynamic response under both passive [5] and active [3, 4] thermal conditions. The former refer to a situation in which thermal phenomena are dragged into the system overall response by the distributed transverse mechanical excitation, as a result of the full coupling; the latter account also for the presence of a thermal source (of variable nature) entailing direct activation of the plate temperature field, in addition to mechanical excitation. Compressive in-plane forces distributed along the plate edges have been considered, too (see Fig. 22.1a).

Local and global nonlinear dynamics have been investigated, highlighting the transition to mechanically- or thermally-induced buckled responses and also focusing on the different role played by coupling effects in different excitation conditions, with the ensuing possibility to consider simplified or partially coupled models [3]. Global dynamics has shown to be of major importance mostly in active thermal conditions [3, 4], where it turns out to be decisive for reliably catching the non-trivial influence of the slow transient thermal dynamics on the steady outcome of the faster mechanical response.

In contrast, no parallel nonlinear dynamic analyses have been conducted yet with the richer (shear deformable with cubic temperature) reduced model, labelled TTC for being based on the Third-order theory with Thermomechanical Coupling. Yet, its major richness, inherently embedded in the description of the thermal field [2], allows us to consider a remarkably larger set of thermal boundary conditions with respect to the CTC model.

The present paper is a first step in this direction, and aims at further highlighting how proper consideration of system global dynamics turns out to be essential to reliably unveil the transient to steady effects due to thermomechanical coupling. Parametric investigation of the response under two different conditions of prescribed temperature on the external surfaces (of interest in a variety of multiphysics structural applications) is accomplished by means of local bifurcation diagrams, phase portraits and planar cross sections of the four-dimensional basins of attraction. This allows us to highlight some ensuing meaningful qualitative changes and to get an overall confirmation of the role played by global analysis for attaining a comprehensive understanding of system dynamics.

22.2 Thermomechanically Coupled Models

The mathematical model describing the motion of the thermomechanical plate under analysis is derived in the framework of a unified 2D formulation presented in [2], to refer to for all details, in which von Kármán nonlinearities, third-order shear

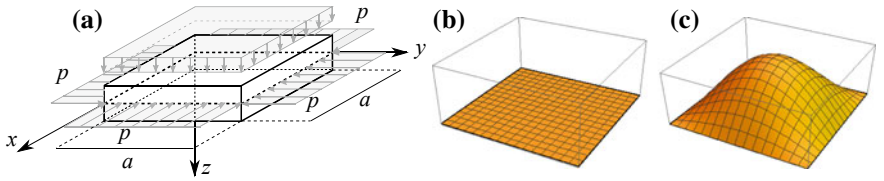

Fig. 22.1 Composite plate subjected to mechanical loads (**a**); Spatially constant (**b**) and dome-shaped (**c**) temperature distributions on the external surfaces

deformability and a cubic temperature distribution along the thickness are considered (TTC model). Moving from seven (five mechanical and two thermal) generalized 2D variables, and under the assumption of symmetric cross-ply laminates, kinematic condensation of the in-plane displacements and shear angles is performed at the continuum and discretized level, respectively; then, a minimal dimension reduction via a Galerkin procedure with dome-shape functions assumed for the remaining (two) thermal and (one) mechanical variables is developed. Thanks to the richness and flexibility of the underlying continuum formulation, the model allows us to account for a variety of thermomechanical assumptions, excitations and boundary conditions. Thus, it represents a substantial improvement of the CTC thermomechanical model with shear indeformability and linear temperature variation along the thickness, previously investigated by the authors in the nonlinear dynamics regime [3–5], in which the sole thermal boundary condition of free heat exchange between plate and environment can be taken into account. Under this condition, anyway, the governing thermomechanical equations of the TTC and CTC models are formally equal, of course with different expressions of the coefficients. Moreover, results not reported here have shown that for the thin (i.e. ratio 1/100 between length and thickness) orthotropic single-layered epoxy/carbon fibre composite plate with simply supported, movable and isothermal edges [4], herein considered (Fig. 22.1a), the outcomes furnished by the two models are practically coincident in terms of both local and global dynamics analysis, as somewhat expected at least from the mechanical viewpoint. For this reason, the following sections are devoted to the description of the TTC model response under two different thermal boundary conditions while, when needing to bring up the results relevant to the free heat exchange case, in a comparison perspective, reference will be made to the corresponding outcomes presented for the CTC model in [4].

22.2.1 TTC Model with Constant Prescribed Temperature on the External Surfaces

The first thermal boundary condition considered is associated with the condition of prescribed temperature on the external, upper and lower, surfaces of the plate, with

the temperature distribution which is assumed to be constant on each of the surfaces (TTC_C model, Fig. 22.1b). Referring to Eqs. 72 of [2], nondimensionalization with respect to time and plate thickness allows us to obtain the following set of governing equations

$$\ddot{W} + a_{12}\dot{W} + a_{13}W + a_{14}W^3 + a_{15}T_{R1} + a_{16}W \cdot T_{R0} + a_{17}\cos(t) = 0, \quad (22.1)$$

$$\dot{T}_{R0} + a_{22}T_{R0} + a_{23}\alpha_1(T_{up} + T_{down}) + a_{24}\dot{W} \cdot W + a_{25}e_0(t) = 0, \quad (22.2)$$

$$\dot{T}_{R1} + a_{32}T_{R1} + a_{33}\dot{W} + a_{34}e_1(t) + a_{35}\alpha_1(T_{up} - T_{down}) = 0, \quad (22.3)$$

in terms of the unknown 0D configuration nondimensional reduced variables W (deflection of the center of the plate), T_{R0} (membrane temperature), T_{R1} (bending temperature). Note that, for the sake of generality, besides the non-vanishing harmonic transversal mechanical excitation in Eq. (22.1), body thermal membrane (e_0) and bending (e_1) excitations also appear in Eqs. (22.2)–(22.3); however, they are given here zero values for the interest being in evaluating the effects of the sole boundary conditions. The parameters representing the thermal boundary conditions are T_{up} and T_{down}, corresponding to the dimensional (in Kelvin) prescribed constant variations of the temperature on the upper and lower external surface, respectively, with respect to the reference value T_{ref}. The expressions of the a_{ij} coefficients are not reported here for the sake of brevity. However, the comparison with those obtained in Eq. 2.1 of [4], for the case of plate with free heat exchange, points out the general increase of the coefficients values in case of the TTC_C model, due to the different physical process activated by the two types of thermal boundary conditions. The choice of a different boundary condition causes the replacement of the T_∞ term (expressing the difference between plate and environment temperatures) in the membrane equation (22.2) by a substantially equivalent thermal term and, more important, the addition, into the bending temperature Eq. (22.3), of a new term related to the difference between the upper and lower temperatures on the plate surfaces. As a consequence, when the two faces have different temperatures, both the membrane and the bending thermal variables are activated. This differs from the free heat exchange condition which, considering a unique temperature for the external environment, determines the triggering of the sole membrane thermal variable.

The different effect of the thermal boundary condition on the system equations of motion reflects also in the dynamical response of the system, as highlighted by the bifurcation diagram of Fig. 22.2 as a function of the temperature on the lower surface T_{down}. In fact, the symmetry characterizing the dynamics of the buckled responses in the system with free heat exchange (see Fig. 3a of [4]) is here broken, due to the contemporary activation of the (along the thickness) symmetric membrane and anti-symmetric bending thermal variables. In particular, the results of Fig. 22.2 are obtained for a pre-buckling in-plane mechanical precompression value $p = 2.51$ and fixed temperature on the upper surface $T_{up} = 100$ able to bring up the two high-amplitude buckled responses $P1^{III}$ and $P1^{IV}$. Starting from this scenario, the varying temperature on the lower plate surface drastically modifies the mechanical system response. For $T_{down} > 0$ the buckled scenario is strengthened by the arise of the

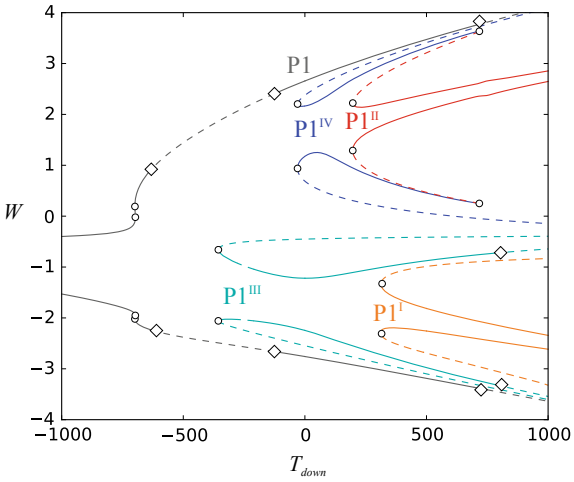

Fig. 22.2 Bifurcation diagram of the transversal displacement W of the $\mathrm{TTC_C}$ model as a function of the temperature on the lower surface T_{down}, for $p = 2.51$ and $T_{up} = 100$. Circle: saddle-node bifurcation; diamond: period-doubling bifurcation

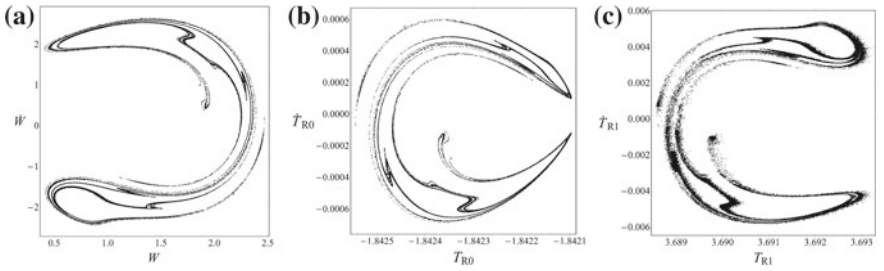

Fig. 22.3 For $p = 2.51$, $T_{up} = 100$ and $T_{down} = -400$, phase portraits of the chaotic solution for the $\mathrm{TTC_C}$ model in the mechanical (**a**), membrane temperature (**b**) and bending temperature (**c**) planes

two low-amplitude $\mathrm{P1^I}$ and $\mathrm{P1^{II}}$ solutions which, as the other ones, differ from each other by amplitude as well as by region of occurrence. When the lower surface is cooled (i.e. for $T_{down} < 0$), conversely, buckling is reduced up to the disappearance of multistability. However, for $-633 < T_{down} < -356$, the $\mathrm{TTC_C}$ system displays a peculiar behavior, not present in the model with free heat exchange, marked out by the presence of chaotic responses representing the sole stable solutions for the system. Their characterization in terms of phase portraits is reported in Fig. 22.3, with the first Lyapunov exponent being $+0.05$. Finally, for lower T_{down} values, the cross-well pre-buckling P1 solution regains stability.

To complete the description of the dynamical response for the $\mathrm{TTC_C}$ model, the global dynamics is investigated by realizing planar cross sections, with fixed thermal initial conditions (i.c.), of the four-dimensional basins of attractions. As a sample

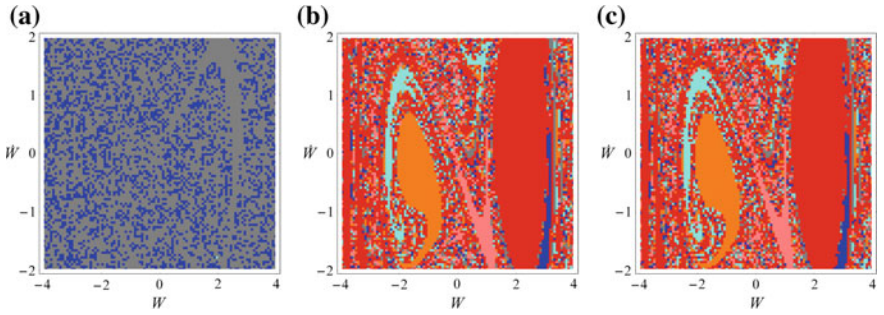

Fig. 22.4 For $p = 2.51$, $T_{up} = 100$ and $T_{down} = 400$, cross sections of the basins of attraction of the TTC_C model in the $(W, \dot{W})$ plane and thermal initial conditions $T_{R0} = 0.0$, $T_{R1} = 0.0$ (**a**), $T_{R0} = 2.30275$, $T_{R1} = 2.77037$ (**b**), basins of attraction of the purely mechanical model (**c**). Red basin: $P1^{II}$ solution; Blue basin: $P1^{IV}$ solution; Cyan basin: $P1^{III}$ solution; Gray basin: P1 solution; Orange basin: $P1^{I}$ solution; Pink basin: P2 solution

case, the general situation of different prescribed temperatures on the external surfaces (i.e. $T_{up} = 100$, $T_{down} = 400$) is reported in Fig. 22.4. When considering trivial thermal initial conditions, representing the most natural configuration from a physical viewpoint, the outcomes furnished by the global dynamics analysis, reported in Fig. 22.4a, are evidently different from those obtained by the bifurcation diagram of Fig. 22.2. In fact, despite the contemporary presence of the five main 1-period solutions detected by the bifurcation diagram, only two basins are identified by the global analysis, corresponding to the P1 and $P1^{IV}$ solutions. This apparent discrepancy of results between local and global dynamics analyses has to be attributed to the effect of the thermal transient dynamics, as already pointed out in [4] for the free heat exchange case. As confirmation, basins of Fig. 22.4a are compared with those obtained by the relevant uncoupled system and reported in Fig. 22.4c. The latter model is described by the sole mechanical Eq. (22.1) in which the thermal boundary condition is taken into account by substituting the thermal variables T_{R0} and T_{R1} with the relevant steady mean values achieved at the end of their temporal evolution, thus neglecting the thermal transient. The outcomes display a strongly different scenario, with the evident presence of the buckled, positive and negative, wells and the identification of all five 1-period basins. This is coherent with what detected with the local dynamics analysis, with also the addition of a basin related to a 2-period response, in pink, not reported in the bifurcation diagram for the sake of readability of that figure. The crucial role played by the thermal transient emphasizes the importance of the choice of the thermal i.c. when analyzing the TTC_C model, since their selection is fundamental in determining the lasting of the thermal evolution. In fact, if the thermal transient is neglected also in the coupled model, i.e. the thermal i.c. are assumed equal to the relevant steady state values as in Fig. 22.4b, the obtained response turns out to be coincident with that of the uncoupled system (Fig. 22.4c); this underlines how the latter is able to describe a specific dynamical scenario of the system achievable only under selected, and physically barely realizable, thermal conditions. As

a final remark, the non-symmetric behavior of the TTC_C model highlighted by the bifurcation diagram is confirmed also by the basins analysis, which organize inside the two wells in a clearly different way.

22.2.2 TTC Model with Dome-Shape Prescribed Temperature on the External Surfaces

In order to ensure consistency between modeling of internal and boundary temperatures, the thermal condition of prescribed temperature on the external surfaces of the plate is here considered by referring to a dome-shape profile in both the upper and lower faces (TTC_DS model, Fig. 22.1c). The relevant governing equations read

$$\ddot{W} + a_{12}\dot{W} + a_{13}W + a_{14}W^3 + a_{15}T_{R1} + a_{16}W \cdot T_{R0} + a_{17}\cos(t) + a_{18}(T_{up} + T_{down})W + a_{19}(T_{up} - T_{down}) = 0, \quad (22.4)$$

$$\dot{T}_{R0} + a_{22}T_{R0} + a_{23}\alpha_1(T_{up} + T_{down}) + a_{24}\dot{W} \cdot W + a_{25}e_0(t) = 0, \quad (22.5)$$

$$\dot{T}_{R1} + a_{32}T_{R1} + a_{33}\dot{W} + a_{34}e_1(t) + a_{35}\alpha_1(T_{up} - T_{down}) = 0. \quad (22.6)$$

Comparing Eq. (22.4) with Eq. (22.1), the presence of two new terms related to the T_{up} and T_{down} parameters into the mechanical equation is pointed out, modifying the linear mechanical stiffness and adding a constant external excitation. However, looking at the numerical values of the relevant coefficients it can be observed that a_{18} and a_{19} parameters are two orders of magnitude lower that the others, so that their effect on the transversal displacement can be grasped only if temperatures on the surfaces have great sum or difference. As a general observation, it can be noted that the numerical coefficients of the TTC_DS model are equal to those of the TTC_C model, with exception of those related to T_{up} and T_{down} which are higher in the latter case.

The local dynamics analysis is here performed by realizing again bifurcation diagrams as a function of the T_{down} parameter, with $p = 2.51$ and $T_{up} = 100$, and comparing in Fig. 22.5 the results (in red) with those already presented in Fig. 22.2 (here reported in black). Looking at positive values of T_{down}, the main differences between the responses of the two models can be detected inside the negative buckled well, corresponding to the plate bending towards the upper surface, which for $T_{down} > 100$ (representing most of the range here considered) is the colder side of the plate. The differences pertain to amplitude as well as existence region of the main periodic solutions. Conversely, responses around the positive buckled configuration are almost coincident in the two models. Diverse behavior between TTC_C and TTC_DS model can be observed also for $T_{down} < 0$, where the chaotic region is substituted, in the TTC_DS model, by the low-amplitude buckled P1^{III} response represented in terms of phase portraits in Fig. 22.6, which remains stable in the whole negative range analyzed.

Moving to the analysis of the basins of attraction of the TTC_DS model, the results presented in Fig. 22.7 allow us to confirm the importance of properly describing the

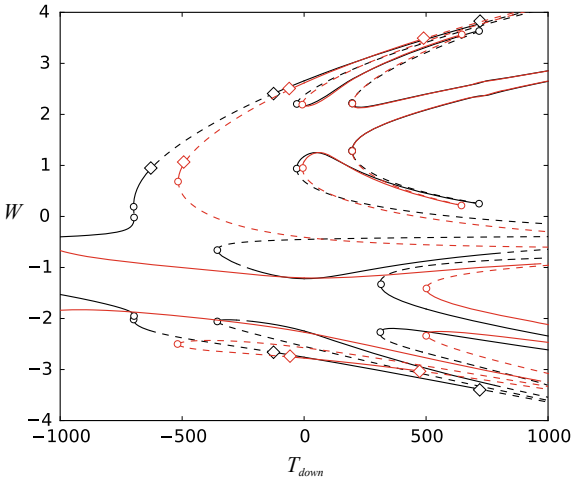

Fig. 22.5 Bifurcation diagrams of the transversal displacement W as a function of the temperature on the lower surface T_{down}, for $p = 2.51$ and $T_{up} = 100$: comparison between TTC_C (black) and TTC_{DS} (red) models. Circle: saddle-node bifurcation; diamond: period-doubling bifurcation

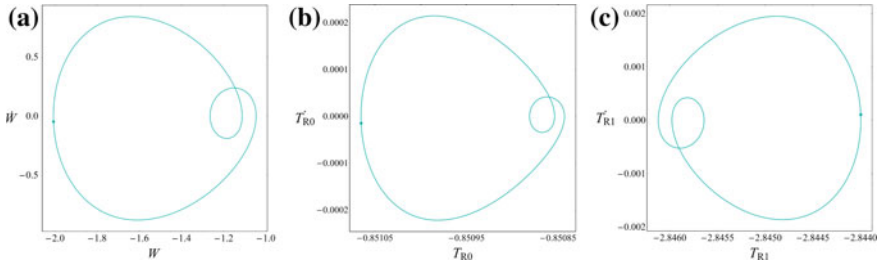

Fig. 22.6 For $p = 2.51$, $T_{up} = 100$ and $T_{down} = -400$, phase portraits of the $P1^{III}$ solution for the TTC_{DS} model in the mechanical (**a**), membrane temperature (**b**) and bending temperature (**c**) planes

thermal transient via the coupled model in order to determine the steady state response of the system. This proves to be a general characteristic of the thermomechanical model under analysis, irrespective of the thermal boundary condition considered. In fact, the behavior of the coupled TTC_{DS} model with trivial thermal i.c. reported in Fig. 22.7a is clearly different from the outcomes obtained by the relevant uncoupled mechanical system with prescribed thermal steady values (Fig. 22.7c), which however can be perfectly reproduced setting the i.c. to the relevant steady values (Fig. 22.7b). Moreover, comparing Figs. 22.4a and 22.7a, it can be observed that the shape chosen for modeling the prescribed temperature on the external surfaces is able to influence the steady dynamics of the system, by modifying the role of the P1 (gray) and $P1^{IV}$ (blue) basins, the former dominating the response of the TTC_C model, the latter becoming the main basin for the TTC_{DS} system, as shown also in

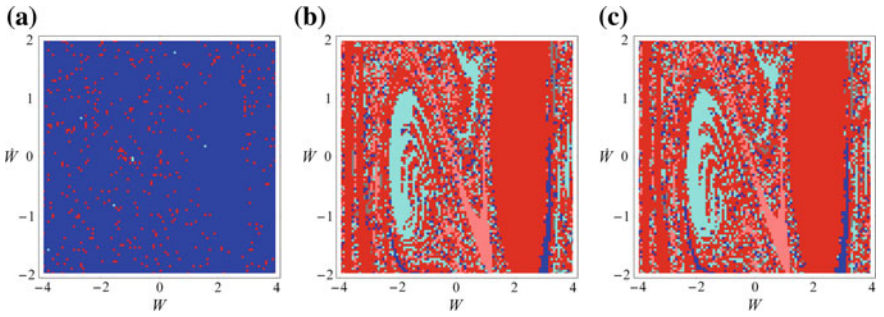

Fig. 22.7 For $p = 2.51$, $T_{up} = 100$ and $T_{down} = 400$, cross sections of the basins of attraction of the TTC_{DS} model in the $(W, \dot{W})$ plane and thermal initial conditions $T_{R0} = 0.0$, $T_{R1} = 0.0$ (**a**), $T_{R0} = 1.41818$, $T_{R1} = 1.70726$ (**b**), basins of attraction of the purely mechanical model (**c**). Red basin: P1^{II} solution; Blue basin: P1^{IV} solution; Cyan basin: P1^{III} solution; Gray basin: P1 solution; Pink basin: P2 solution

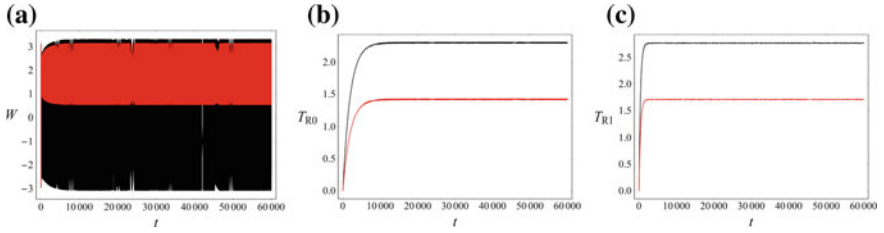

Fig. 22.8 For $p = 2.51$, $T_{up} = 100$, $T_{down} = 400$ and i.c. (0, 0, 0, 0), time histories of the P1 solution of the TTC_{C} model (black) and of the P1^{IV} solution of the TTC_{DS} model (red)

Fig. 22.8a. Here, apart from highlighting the different mechanical response achieved by the two models, the effect of the boundary conditions on the thermal variable evolution can be observed. As a general comment, the time histories of Fig. 22.8 clearly stress the length of the thermal transients with respect to the mechanical one, even if they are shorter than those relevant to the case of plate with free heat exchange (see, e.g., Fig. 7(ii) of [4]). Furthermore, the steady values reached by the thermal variables of the TTC_{DS} model are lower than those of the TTC_{C} model, a behavior which is confirmed by the bifurcation diagrams with respect to the thermal variables, not reported here, thus showing to be robust with respect to possible variations of the thermal boundary parameters. Finally, also when neglecting the thermal transient, e.g., in Figs. 22.7b and 22.4b, TTC_{DS} and TTC_{C} models display differences in the basins organization, mostly localized in the negative well, as already deduced by the bifurcation diagram of Fig. 22.5.

22.3 Conclusions

A reduced model of third-order shear deformable laminated plate with spatially assumed cubic variation of the unknown thermal field along the thickness has been used for the first time to investigate the nonlinear dynamic response of an orthotropic single-layered epoxy/carbon fibre composite plate with simply supported, movable and isothermal edges. The analysis has been conducted in a full (i.e., two-way) thermomechanical coupling framework. Besides mechanical (transverse harmonically varying and in-plane constant) excitations and body thermal excitations, the third-order model allows us to consider a remarkable variety of thermal boundary conditions to be possibly prescribed on the plate upper and lower surfaces. A condition of prescribed temperature entailing direct activation of the plate temperature field has been considered in the numerical investigation; yet, two relevant spatial shapes, either constant or dome-shaped, have been considered, the latter being more consistent with the modeling assumption about the spatial distribution of the unknown thermal field made in the Galerkin modal reduction. Local and global nonlinear dynamics have been investigated, highlighting the transition to thermally-induced buckled responses, however with meaningfully distinct response features occurring when considering either one of the two different prescribed shapes. Nonetheless, the remarkable influence of the slow transient thermal dynamics on the steady outcome of the faster mechanical response clearly emerges in both cases. It can be suitably caught only through the construction and comparison of proper planar cross sections of the system actual four-dimensional basins of attraction, getting an overall confirmation of the role played by global analysis for attaining a comprehensive understanding of system dynamics. Owing to its considerable richness and flexibility, the third-order model is currently being used to perform systematic investigations of the effects of a variety of physically meaningful thermal boundary conditions on the nonlinear dynamic response, by also looking at the results reliability in terms of consistency of assumptions made in both the modeling and the analysis stage.

Acknowledgements The financial support of PRIN 2015 (No. 2015JW9NJT) is gratefully acknowledged.

References

1. Saetta, E., Rega, G.: Unified 2D continuous and reduced order modeling of thermomechanically coupled laminated plate for nonlinear vibrations. Meccanica **49**, 1723–1749 (2014)
2. Saetta, E., Rega, G.: Third-order thermomechanically coupled laminated plates: 2D nonlinear modeling, minimal reduction and transient/post-buckled dynamics under different thermal excitations. Compos. Struct. **174**, 420–441 (2017)
3. Settimi, V., Rega, G.: Thermomechanical coupling and transient to steady global dynamics of orthotropic plates. In: Andrianov, I., et al. (eds.) Problems of Nonlinear Mechanics and Physics of Materials. Advanced Structured Materials, vol. 94, pp. 483–499. Springer International Publishing AG, Part of Springer Nature, Cham (2018)

4. Settimi, V., Rega, G., Saetta, E.: Avoiding/inducing dynamic buckling in a thermomechanically coupled plate: a local and global analysis of slow/fast response. Proc. R. Soc. A **474**(2213), 20180206 (2018)
5. Settimi, V., Saetta, E., Rega, G.: Local and global nonlinear dynamics of thermomechanically coupled laminated plates in passive thermal regime. Nonlinear Dyn. **93**(1), 167–187 (2018)
6. Tonti, E.: The Mathematical Structure of Classical and Relativistic Physics. A General Classification Diagram. Birkhäuser-Springer, Basel (2013)

Chapter 23
Non-linear Free Vibrations of a Hanging Cable with Small Sag

Guilherme Jorge Vernizzi, Guilherme Rosa Franzini and Celso Pupo Pesce

Abstract This paper presents a method for evaluating non-linear modes and the corresponding natural frequencies of hanging cables with small sag. The use of a Galerkin temporal scheme on the governing equations of motion associated with a fictitious normal force accounting for the effects of the resulting non-linear terms leads to a closed-form solution for the non-linear free vibration problem. The influence of amplitude on the modal shapes and frequencies are presented.

Keywords Non-linear normal modes · Extensible cable · Small sag · Closed form solution · Galerkin projection

23.1 Introduction

Structural solutions based on tensioned cables with varying traction along the length are commonly found in engineering applications. The study of the dynamic response of those structures is of great importance in fatigue design and stability analysis. Particularly, the study of the free-vibration problem is of interest, since it provides intrinsic characteristics such as its natural frequencies and modes. Considering a linear problem in free vibrations, the system oscillates with the form of a particular normal mode if the initial conditions match this mode. This concept can be expanded for non-linear systems by using the concept of the non-linear normal modes; see [1].

Reference [2] analytically investigates the linear free oscillations of a catenary riser with negligible bending stiffness, providing a Wentzel–Kramers–Brillouin

G. Jorge Vernizzi (✉) · G. Rosa Franzini · C. Pupo Pesce
Offshore Mechanics Laboratory - LMO, Escola Politécnica, University of São Paulo, São Paulo, Brazil
e-mail: guilherme.jorge.lopes@usp.br

G. Rosa Franzini
e-mail: gfranzini@usp.br

C. Pupo Pesce
e-mail: ceppesce@usp.br

I. Kovacic and S. Lenci (eds.), *IUTAM Symposium on Exploiting Nonlinear Dynamics for Engineering Systems*, IUTAM Bookseries 37,
https://doi.org/10.1007/978-3-030-23692-2_23

(WKB) (see for example [3]) closed-form solution for the problem. Following, the non-linear modes for a vertical beam with varying tension were addressed in [4], which presents a closed-form expression for the modal shape and the natural frequencies. In the latter paper, the authors employed a temporal Galerkin projection and a fictitious normal force similar to that previously proposed in [5].

The present paper aims at contributing with the planar non-linear dynamics of cables in free vibrations. Particularly, the major interest lies on determining the non-linear modes and frequencies of a cable hanging between two points at different heights, with a sag to span relation of order of 1:20 or smaller. The formulation herein presented extends the results of [4], allowing for use in cables that are in a configuration different from the vertical one. Furthermore, the formulation herein presented includes some non-linear effects neglected in [2].

23.2 Mathematical Model

Consider a cable made of an elastic-linear material, with axial stiffness EA, mass per unit length μ and unstretched length l, as sketched in Fig. 23.1. Let u and v be, respectively, the displacements in the tangential and in the normal directions defined with respect to the static configuration. In addition to these quantities, we define T as the traction and θ as the angle with the horizontal in the static configuration, τ as the dynamic traction variation, γ as the dynamic variation of θ and ε as the engineering strain component related to τ. The definition $\mathbb{T} = T + \tau$ is used in some mathematical steps. Throughout this paper, primes denote differentiation with respect to the arclength coordinate s in the static configuration and dots represent differentiation with respect to time. Since the sag is small and the tangential displacements are considered small compared to the transversal ones, the approximation $\gamma \cong v'$ is used. This is possible due to the fact that the term $u\theta'$, although linear in the dynamical perturbations, becomes of second order when compared to v'. A detailed analysis on order of magnitude of terms arising from a dynamic perturbation approach around the equilibrium configuration may be found in [6].

The equations of motion herein analysed are based on the Clebsch–Love equations (see for example [7]). For the sake of a future generalization of this mathematical model, the static terms are not approximated using a parabolic static configuration as in [8]. Let b_u and b_v be the external forces per unit length in the tangential and transversal directions, respectively. Defining f_u and f_v as the corresponding elastic forces and neglecting rotatory inertial forces, the equations of motion are written as:

$$f_u + b_u = \mu \ddot{u} \ . \tag{23.1}$$

$$f_v + b_v = \mu \ddot{v} \ . \tag{23.2}$$

Considering a cable segment δs, the resulting elastic forces in the tangential and transversal directions are given by:

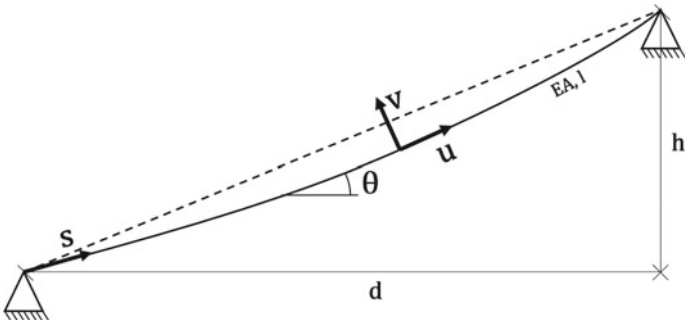

Fig. 23.1 Basic sketch and principal parameters

$$\delta F_u = \mathbb{T}(s+\delta s)\cos(\delta\theta + \gamma(s+\delta s)) - \mathbb{T}(s)\cos(\gamma(s)) \ . \tag{23.3}$$

$$\delta F_v = \mathbb{T}(s+\delta s)\sin(\delta\theta + \gamma(s+\delta s)) - \mathbb{T}(s)\sin(\gamma(s)) \ . \tag{23.4}$$

Taking the limit $\delta s \to 0$ in Eqs. (23.3) and (23.4), considering that γ is small, the resulting terms are:

$$f_u = \lim_{\delta s \to 0} \delta F_u = \mathbb{T}' - \mathbb{T}\left(\theta' + \gamma'\right)\gamma \ . \tag{23.5}$$

$$f_v = \lim_{\delta s \to 0} \delta F_v = (\mathbb{T}\gamma)' + \mathbb{T}\theta' \ . \tag{23.6}$$

The resulting equations of motion are then:

$$[T + b_u] + \tau' - T\gamma\theta' - T\gamma\gamma' - \tau\gamma\theta' - \tau\gamma\gamma' = \mu\ddot{u} \ . \tag{23.7}$$

$$\left[T\theta' + b_v\right] + \tau\theta' + (T\gamma)' + (\tau\gamma)' = \mu\ddot{v} \ . \tag{23.8}$$

Note that the expressions between brackets in Eqs. (23.7) and (23.8) are the equations of static equilibrium when the dynamical changes in the external forces can be disregarded or are, in fact, null. Now a static condensation procedure is applied. Following [2, 9], the inertial term in the tangential direction is disregarded. A price to be paid is missing the mutual inertial effect between tangent and transverse dynamics. The well known frequency cross-over phenomenon analysed in [8] is missing as well. However, the tangential component of the mode function may still be written as a function of the transversal one (see [2, 9]).

Also, a scaling analysis is used to simplify Eq. (23.7). The scaling is made considering v of unity order, which implies that v' is of order η, the latter being a small parameter. The additional curvature v'' is of order η^2, and the same order is considered for the small static curvature. This is in fact a strong hypothesis, limiting the dynamic amplitude to a fraction of the wave length of the modes that will be sought. Also, considering valid the scaling between tangential and transversal displacements obtained in [8], τ is considered of order η. Keeping only terms of the smallest power of η, the condensed equation for the tangential displacements becomes:

$$EA\varepsilon' - Tv'\theta' - Tv'v'' = 0\,. \tag{23.9}$$

To ensure mathematical clearness, a dummy variable ξ is used when indefinite integrals of functions of s are required. Integration of Eq. (23.9) leads to:

$$EA\varepsilon = C_1 + \int_0^s Tv'\theta'\,\mathrm{d}\xi + \int_0^s Tv'v''\,\mathrm{d}\xi\,. \tag{23.10}$$

Now, as made in [9], the constant C_1 is obtained considering a spatial averaging of Eq. (23.10). Also, the strain measure is defined as $\varepsilon = u' - v\theta' + \left(v'\right)^2/2$. The retained terms follow the smallest power of η that appears in the geometrically complete expression of ε. The constant C_1 is given by:

$$C_1 = \frac{EA}{2l}\int_0^l \left(v'\right)^2\,\mathrm{d}s - \frac{EA}{l}\int_0^l v\theta'\,\mathrm{d}s - \frac{1}{l}\int_0^l\int_0^s Tv'\theta'\,\mathrm{d}\xi\,\mathrm{d}s - \frac{1}{l}\int_0^l\int_0^s Tv'v''\,\mathrm{d}\xi\,\mathrm{d}s\,. \tag{23.11}$$

Equation (23.11) allows writing the equation of transversal motion in an isolated manner, i.e., decoupled from that associated with the tangential one. The resulting equation is given by Eq. (23.12).

$$\theta'\left(C_1 + \int_0^s Tv'\theta'\,\mathrm{d}\xi + \int_0^s Tv'v''\,\mathrm{d}\xi\right) + \left(Tv'\right)' + Tv'^2\left(\theta' + v''\right) + v''\left(C_1 + \int_0^s Tv'\theta'\,\mathrm{d}\xi + \int_0^s Tv'v''\,\mathrm{d}\xi\right) = \mu\ddot{v}\,. \tag{23.12}$$

Supposing that the dynamics is governed by a single mode, the solution is sought in the form $v = \psi\,(s)\sin(\omega t)$. After a series of algebraic manipulations and the use of a Galerkin's temporal scheme (see [4]), the equation of the modal shape for the modes associated with the transversal direction becomes:

$$-\frac{EA\theta'}{l}\int_0^l \psi\theta'\,\mathrm{d}s - \frac{\theta'}{l}\int_0^l\left(\int_0^s T\psi'\theta'\,\mathrm{d}\xi\right)\mathrm{d}s + \theta'\int_0^s T\psi'\theta'\,\mathrm{d}\xi + T'\psi' + T\psi'' + \frac{3}{4}T\psi'^2\psi'' + \frac{3EA}{8l}\psi''\int_0^l\left(\psi'\right)^2\,\mathrm{d}s - \frac{3}{4l}\psi''\int_0^l\int_0^s T\psi'\psi''\,\mathrm{d}\xi\,\mathrm{d}s + \frac{3}{4}\psi''\int_0^s T\psi'\psi''\,\mathrm{d}\xi + \mu\omega^2\psi = 0\,. \tag{23.13}$$

Following [4, 5], a fictitious or equivalent "normal force" N is proposed as:

$$
\begin{aligned}
&-\frac{EA\theta'}{l}\int_0^l \psi\theta'\,\mathrm{d}s - \frac{\theta'}{l}\int_0^l\left(\int_0^s T\psi'\theta'\,\mathrm{d}\xi\right)\mathrm{d}s \\
&+\theta'\int_0^s T\psi'\theta'\,\mathrm{d}\xi + \frac{3}{4}T\psi'^2\psi'' + \frac{3EA}{8l}\psi''\int_0^l\left(\psi'\right)^2\,\mathrm{d}s \\
&-\frac{3}{4l}\psi''\int_0^l\int_0^s T\psi'\psi''\,\mathrm{d}\xi\,\mathrm{d}s + \frac{3}{4}\psi''\int_0^s T\psi'\psi''\,\mathrm{d}\xi = N\psi'' \,. \qquad (23.14)
\end{aligned}
$$

The numerical evaluation of this term is made using a spatial Galerkin projection considering a set of sinusoidal functions[1] $\sin(n\pi s/l)$, where n is the number of half-waves existing in the mode considered. The consideration of the number of half-waves is needed since, for inclined cables, the mode number is not necessarily the number of half-waves since mode hybridization can occur; see [10]. Using the wrong consideration regarding n leads to higher values of the fictitious normal force, specially for the lower modes.

For a catenary configuration, the approximation $T \cong \overline{T} = \alpha + \beta s$ can be used as a simplification for the static traction with small errors (see [2]). The fictitious normal force is then associated with the number of half-waves n used in the Galerkin projection, and is indicated by N_n. The vibration modes will then be non-linear because some terms in Eq. (23.14) maintain a quadratic relation with the amplitude used in the projection functions when computing the fictitious normal force. Applying the approximation for the static traction and the evaluated fictitious normal force in Eq. (23.13), the modal shapes ψ_n must satisfy Eq. (23.15).

$$
\left(\overline{T} + N_n\right)\psi_n'' + \overline{T}'\psi_n' + \mu\omega_n^2\psi_n = 0 \,. \qquad (23.15)
$$

Notice that the averaging procedure represented by Eq. (23.14) transformed the nonlinear Eq. (23.13) into a linear one. Following [4], some new quantities are defined, being $a = \beta/\mu\omega_n^2$, $T_{bn} = \alpha + N_n$ and $T_{tn} = \alpha + l\beta + N_n$. Note that T_{bn} and T_{tn} are the modal tractions at the lower and upper ends of the cable respectively, while ω_n is the natural frequency associated with the mode containing n half-waves. Defining now, as in [2, 4], a variable transformation, and the corresponding inverse transformation:

$$
z = \frac{2\omega_n}{\beta}\sqrt{\mu\left(T_{bn} + \beta s\right)} \,, \qquad (23.16)
$$

$$
s = \frac{az^2}{4} - \frac{T_{bn}}{\beta} \,. \qquad (23.17)
$$

[1] Sinusoidal functions are used for simplicity. Linear modes, given by the Bessel approximation or by the WKB closed form solution in [2] might be used instead.

Equation (23.15) turns out to a familiar Bessel form:

$$\frac{\mathrm{d}^2\psi_n}{\mathrm{d}z^2} + \frac{1}{z}\frac{\mathrm{d}\psi_n}{\mathrm{d}z} + \psi_n = 0\ . \tag{23.18}$$

The solution of Eq. (23.18) can be written as a combination of zero-order Bessel functions of first and second kinds ($J_0(z)$ and $Y_0(z)$, respectively). The relations in the combination and the natural frequencies are obtained by applying the essential boundary conditions of the cable and using the solvability condition for non-trivial solutions. Although the use of Bessel functions is already a solution, the high values of z for a catenary cable with small sag allows the use of an asymptotic solution. Following [4, 5], consider the following transformation:

$$\psi_n = \frac{1}{\sqrt{z}}\Psi_n\ . \tag{23.19}$$

Equation (23.18) becomes then:

$$\frac{\mathrm{d}^2\Psi_n}{\mathrm{d}z^2} + \left(1 + \frac{1}{4z^2}\right)\Psi_n = 0\ . \tag{23.20}$$

In the case of a catenary with small sag, $1/4z^2 \ll 1$. Such result allows substituting this term in Eq. (23.20) by a small perturbation parameter, evaluated as the mean value of $1/4z^2$ along the cable. As shown in [4], the solution of Eq.(23.20) can then be well approximated by:

$$\Psi_n = A_n \sin(z) + B_n \cos(z)\ . \tag{23.21}$$

This leads finally to:

$$\psi_n = \frac{1}{\sqrt{z}}\left(A_n \sin(z) + B_n \cos(z)\right)\ . \tag{23.22}$$

Notice that Eq. (23.22) resembles the WKB solution previously obtained in [2]. Now, since the transversal displacements must be zero at both ends of the cable, the system of the boundary conditions reads:

$$\begin{bmatrix} \dfrac{\sin z_0}{\sqrt{z_0}} & \dfrac{\cos z_0}{\sqrt{z_0}} \\ \dfrac{\sin z_l}{\sqrt{z_l}} & \dfrac{\cos z_l}{\sqrt{z_l}} \end{bmatrix} \begin{bmatrix} A_n \\ B_n \end{bmatrix} = \begin{bmatrix} 0 \\ 0 \end{bmatrix}\ . \tag{23.23}$$

Being z_0 and z_l the values of z at $s = 0$ and $s = l$, respectively. Since is desired to obtain non-trivial solutions of Eq. (23.23), the solvability condition leads to:

$$\frac{\sin(z_l - z_0)}{\sqrt{z_l z_0}} = 0 \ . \tag{23.24}$$

The solution of Eq. (23.24) is $z_l - z_0 = n\pi$, which, using Eq. (23.16) leads to:

$$\omega_n = \frac{n\pi}{2l\sqrt{\mu}} \left(\sqrt{T_{tn}} + \sqrt{T_{bn}} \right) \ . \tag{23.25}$$

The modal shapes can then be written as:

$$\psi_n = \sqrt[4]{\frac{T_{bn}}{T_{bn} + \beta s}} \sin(z - z_0) \ . \tag{23.26}$$

Using Eq. (23.25) in Eq. (23.16), the coordinate z can be written in terms of the modal tensions and the number of half-waves as:

$$z = \frac{\sqrt{T_{bn} + \beta s}}{\sqrt{T_{tn}} - \sqrt{T_{bn}}} n\pi \ . \tag{23.27}$$

23.3 Numerical Example

To illustrate the effects of the non-linearities, preserved in the presented formulation, consider a cable with axial stiffness $EA = 22970\,\text{kN}$, diameter $D = 1.57\,\text{cm}$ and $\mu = 1.29\,\text{kg/m}$. This cable is hanged such as $h = 200\,\text{m}$ and $d = 100\,\text{m}$, and $l = 223.73\,\text{m}$. The length refers to the static equilibrium configuration length. In Fig. 23.2, the superposition of linear and non-linear modes is presented for the mode with $n = 20$, for a modal amplitude $A_n = 3D$. The modal shape functions are presented in dimensionless form, normalized by the maximum value of itself. As can be seen, there is no appreciable change in modal shape, since the modal amplitude is small.

Now, in Figs. 23.3 and 23.4, the superposition of linear and non-linear modes is presented for modes with $n = 10$ and $n = 20$ respectively, considering for the non-linear mode a modal amplitude of $A_n = 20D$. The change in modal shape now is visible, altering the position of nodal points and rate of change of the vibration amplitude along the cable. Those figures also show that higher modes are more affected by non-linearities compared to lower ones.

The effects of the non-linearities over the natural frequencies are shown in Table 23.1. The natural frequencies for some modal amplitude values and modes are shown. The modes are listed by the number of half-waves n in the modal shape. It is possible to conclude that the non-linearities have a hardening effect over the cable vibrations, and cause an increase in the natural frequencies. Such an increase is more significant for higher modes and for larger modal amplitude. Table 23.1 is graphically summarized in the backbone curves presented in Fig. 23.5. Those curves

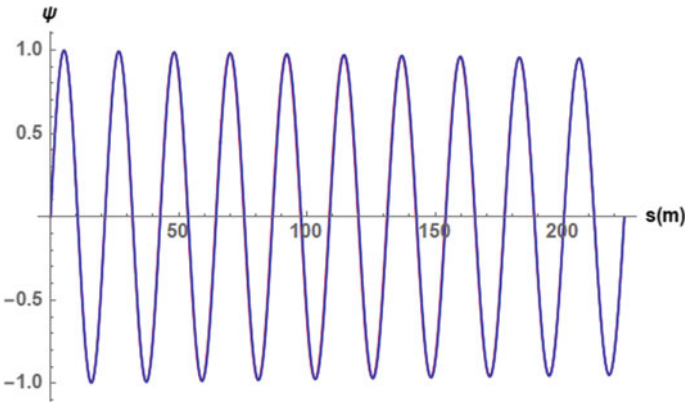

Fig. 23.2 Mode $n = 20$, linear solution in red and non-linear in blue with $A_n = 3D$

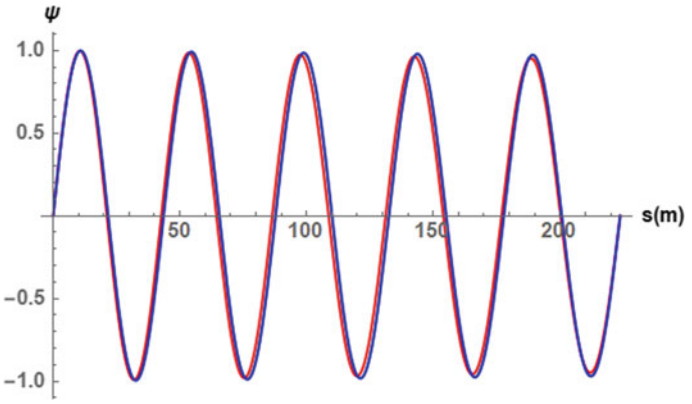

Fig. 23.3 Mode $n = 10$, linear solution in red and non-linear in blue with $A_n = 20D$

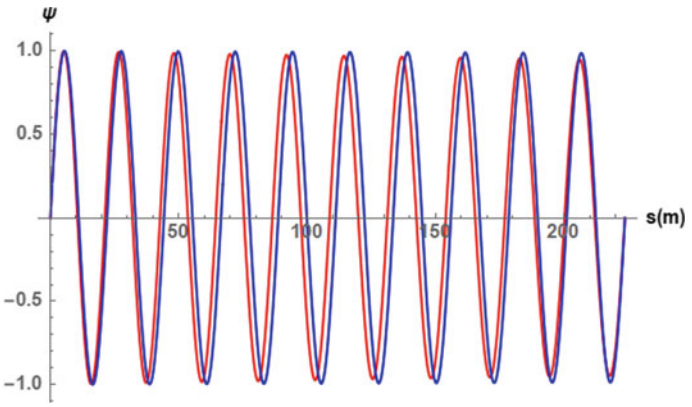

Fig. 23.4 Mode $n = 20$, linear solution in red and non-linear in blue with $A_n = 20D$

Table 23.1 Frequencies comparison (rad/s)

n	Linear	$A_n = 1D$	$A_n = 3D$	$A_n = 5D$	$A_n = 10D$	$A_n = 20D$
2	2.617	2.626	2.627	2.628	2.635	2.665
3	3.926	3.980	3.983	3.988	4.013	4.109
5	6.543	6.556	6.568	6.593	6.706	7.141
10	13.086	13.098	13.196	13.389	14.260	17.310
15	19.629	19.670	19.998	20.639	23.406	32.169
20	26.171	26.269	27.041	28.521	34.619	52.317
30	39.257	39.587	42.135	46.812	64.338	109.205

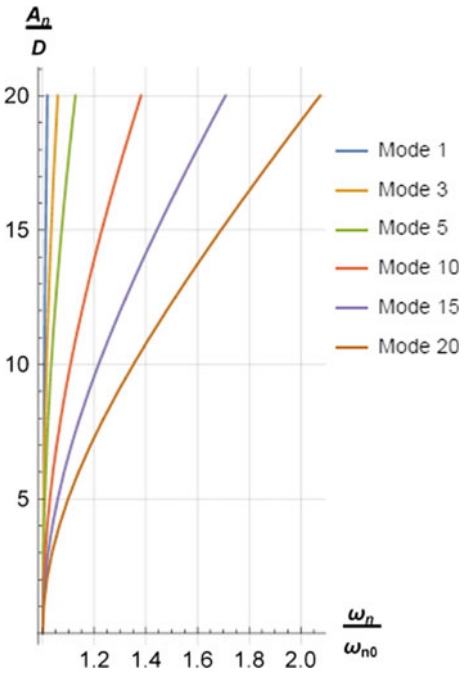

Fig. 23.5 Backbone curves for the cable in study, being ω_{n0} the natural frequency of the linear problem

were numerically obtained by applying the proposed model to some values of modal amplitude in the range presented in the figure.

23.4 Conclusions

A closed-form solution for the non-linear modes and natural frequencies of a hanging cable with small sag was obtained. The results showed the dependence of the frequencies on the amplitude of motion and the change in the modal shape, resulting

in a shift of nodal points, changing the amplitude variation along the length. It is important to highlight the increasing in natural frequencies due to the preserved non-linearities, which may be significant for fatigue analysis for example. Finally, besides giving intrinsic characteristics of the system, closed-form solutions for modal shapes also allow for further direct implementations of projection methods in dynamic analysis, such as the Galerkin projection. Further work includes the search for non-linear modes of hanging cables with arbitrary sag, and the application of non-linear modes in Galerkin schemes to obtain reduced order models for problems of interest such as cables subjected to vortex-induced vibrations or under the action of parametric excitation.

Acknowledgements The first author acknowledges São Paulo Research Foundation (FAPESP) for his PhD scholarship, grant 2016/25457-1. The second and the third author are grateful to the Brazilian National Research Council (CNPq) for the research grants n. 310595/2015-0 and 308990/2014-5.

References

1. Shaw, S.W., Pierre, C.: Normal modes for non-linear vibratory systems. J. Sound Vib. **164**, 85–124 (1993)
2. Pesce, C.P., Fujarra, A.L.C., Simos, A.N., Tannuri, E.A.: Analytical and closed form solutions for deep water riser-like eigenvalue problem. In: Chung, J.S., Matsui, T., Koterayama W. (eds). Proceedings of the Ninth (9th) International Offshore and Polar Engineering Conference, Brest, France, pp. 255–264 (1999)
3. Bender, C.M., Orszag, S.A.: Advanced Mathematical Methods for Scientists and Engineers. McGraw-Hill, New York (1978)
4. Mazzilli, C.E.N., Lenci, S., Demeio, L.: Non-linear free vibrations of tensioned vertical risers. In: Ecker, H., Steindl, A., Jakubek S. (eds.) ENOC Proceedings of the 8th European Nonlinear Dynamics Conference, Vienna, Austria (2014)
5. Senjanović, I., Ljustina, A.M., Parunov, J.: Natural vibration analysis of tensioned risers by segmentation method. Oil Gas Sci. Technol. **61**, 647–659 (2006)
6. Pesce, C.P.: Mechanics of cables and tubes in catenary configuration: an analytical and experimental approach. 'Livre-Docência' Thesis, (in Portuguese). University of São Paulo (1997)
7. O'Reilly, O.M.: Modeling Nonlinear Problems in the Mechanics of Strings and Rods, The Role of the Balance Laws. Springer International Publishing, Berlin (2017)
8. Irvine, H.M., Caughey, T.K.: The linear theory of Free vibrations of a suspended cable. Proc. R. Soc. A **341**, 299–317 (1974)
9. Mazzilli, C.E.N., Sanches, C.T., Baracho Neto, O.G.P., Wiercigroch, M., Keber, M.: Non-linear modal analysis for beams subjected to axial loads: analytical and finite-element solutions. Int. J. Non Linear Mech. **43**, 551–561 (2008)
10. Triantafyllou, M.S.: The dynamics of taut inclined cables. Q. J. Mech. Appl. Math. **37**, 421–440 (1984)

Chapter 24
Analytical and FEM Modelling of the Behaviour of Pile in Dynamic Load Test

Vladimir Zivaljevic, Dusan Kovacevic and Zvonko Rakaric

Abstract Pile load testing may be of static and dynamic character. Dynamic load tests are carried out by applying an axial impulse load by the use of falling mass. In this paper a dynamic load testing of a single pile foundation and its analytical and numerical modelling by the use of finite element method (FEM) are described. The vertical deflection due to the determined maximum allowed static force was calculated in FEM model and was used to control the value of the deflection in nonlinear dynamic FEM analysis. The correlation between the force value, soil properties and deflection is analysed. Hence, a proper FEM model for the purposes of pile dynamic load testing procedures could be recommended.

Keywords Pile foundation · Dynamic test by load · FEM analysis · Clay soil

24.1 Introduction

Foundation piles are often used to transfer loads to the ground in order to increase the soil bearing capacity or to reduce the settlement of the structure. Due to the nature of their construction, quality control is limited. Therefore, calculation of the bearing capacity of piles is one of the key steps in pile foundation design. Aside from theoretical methods based on the physical-mechanical properties of the soil and methods based on the dynamic data obtained during pile driving, another way of the bearing capacity assessment of the piles is by the pile dynamic load tests using a drop-weight system. This testing method implies assessment of the pile bearing

V. Zivaljevic (✉) · D. Kovacevic
Department of Civil Engineering and Geodesy, Faculty of Technical Sciences, University of Novi Sad, Novi Sad, Serbia
e-mail: zivaljevic.vladimir@uns.ac.rs

Z. Rakaric
Department of Technical Mechanics, Faculty of Technical Sciences, University of Novi Sad, Novi Sad, Serbia

I. Kovacic and S. Lenci (eds.), *IUTAM Symposium on Exploiting Nonlinear Dynamics for Engineering Systems*, IUTAM Bookseries 37,
https://doi.org/10.1007/978-3-030-23692-2_24

capacity based on the measurement of the force and velocity near the top of the pile due to the axial impact force [1].

The problem here is analysed on a 32 m long concrete pile. Foundation depth is 30.0 m and the extension of 2.0 m above the ground was formed to give a more realistic representation of the actual in situ conditions, where piles often extend over the terrain surface in order to make connections of measuring instruments accessible. The soil type that had been analysed is a clay soil of medium density.

In this paper, the dynamic load testing is analysed in two ways: analytical and numerical.

24.2 Dynamic Test by Load of the Pile

A dynamic test by load can be applied to any type of pile regardless of the construction method. It implies assessment of the pile bearing capacity based on the measurement of force and velocity near the top of the pile due to the axial impact force. The axial impact force can be applied by the use of conventional pile driving hammers and by the use of a drop weight system designed especially for testing purposes. These tests are of great significance for high-capacity piles (over 2.5 MN [2]), for which static test by load is very expensive or physically difficult to perform (e.g. over water). In this paper the emphasis will be put on a dynamic test with the use of drop weight system, which is increasingly being used for dynamic testing of drilled piles and caissons.

A typical system of drop weight consists of four components: a frame and/or a guide for drop weight (ram), ram, mechanism for the release of ram and impact plates with or without cushion.

The appliance of dynamic testing is performed by letting the mass fall from a certain height to the top of the pile. The impact of the ram creates a dynamic stress wave that proceeds to move towards the base of the pile. The impact force of the ram should be large enough to induce the sufficient settlement of the pile, which will fully mobilize its bearing capacity. Therefore, the requirement of great importance for pile dynamic test by load is the utilization of a ram of suitable weight. This is above all essential in cases of testing of high-capacity piles, and in cases where the pile is located in the soft soil (in order to achieve proper settlement with the purpose of activating the maximum resistance of the soil). Some authors [2] suggest that the mass of the falling ram (in tons) is at least 0.1–0.2% of the required bearing capacity of the pile (in kN) divided by the acceleration of 9.81 m/s^2. By combining the results of this test method with the results of pile static test by load, the accuracy of determining the actual pile bearing capacity can be increased.

Some of difficulties that may compromise dynamic measurements are usually related to construction, impact of the ram, pile resistance and measuring point. Irregular geometric shape, poor concrete quality, an inhomogeneous cross-section, an uneven concrete surface can cause irregular reflection of stress waves generated during the impact, uneven results in terms of stress distribution, which lead to an

unacceptable calculation of generated forces. Uneven impacts, in particular impacts over one contact point (rotated ram), cause unequal stresses along the pile at a great distance from the impact point. High friction resistance that develops near the surface of the soil, which is more common in drilled rather than in driven piles, creates large signal reflections at an early stage and may lead to difficulties in signal analysis.

24.3 Definition of Analytical Model

Analytical model that was considered consists of n masses connected with spring elements. The nth mass is connected to the non-movable ground support via nonlinear spring element as well (Fig. 24.1).

Spring elements from i = 1 to i = n − 1 are assumed to be linear and the nth nonlinear. The nonlinear change of force of the nth spring is described with the Eq. (24.1):

$$F_{nl} = k_{nl} \cdot \Delta l^{\alpha} \tag{24.1}$$

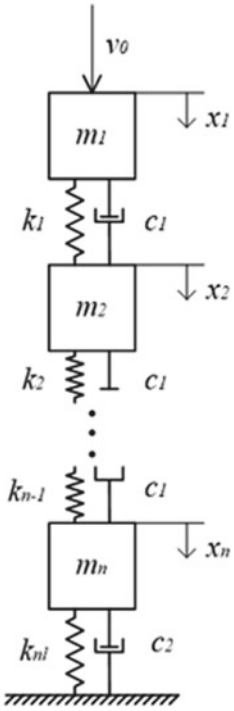

Fig. 24.1 Analytical model of the dynamic pile load testing

In Eq. (24.1) $\alpha \in R^+$ and $\alpha < 1$, k_{nl} is spring stiffness and Δl is spring elongation. Furthermore, damping is considered as linear viscous and is taken into account as Rayleigh damping. Damping between the masses of the pile is labelled as c_1 and damping between the nth mass and the ground is labelled as c_2.

24.4 Definition of FEM Model

Numerical modelling of pile dynamic load testing was done using the FEM software Midas GTS NX©, which is aimed for analysis of structure-soil interaction.

The geometry of the model can be very comfortably discretized using various geometry tools, which enable the definition of points, lines, surfaces and various 3D shapes over which a mesh of FE is generated. The FE are further attributed the characteristics of the material and/or some other characteristics that adequately describe the behaviour of the model. The FEM model considered in this paper is spatial (3D). The rendered view of cross section of numerical model is given in Fig. 24.2.

The considered pile element is modelled using concrete material with the Young's modulus of elasticity of 30.0 GPa, Poisson's ratio of 0.2 and damping ratio of 0.05

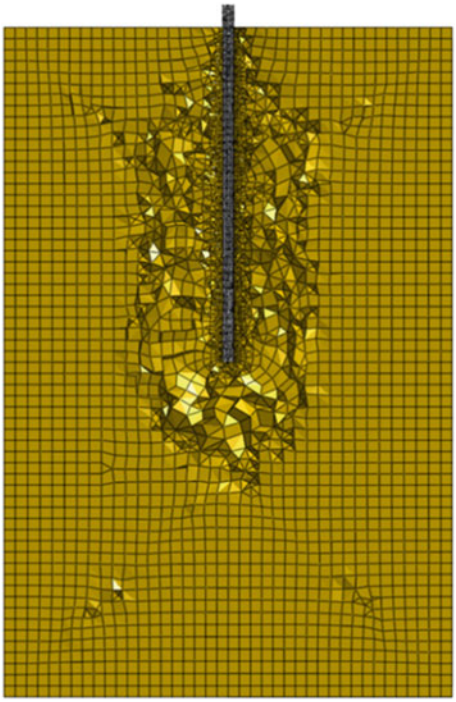

Fig. 24.2 Rendered view of cross section of numerical model

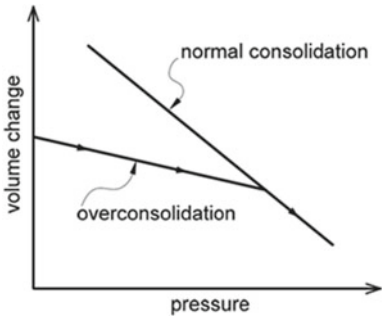

Fig. 24.3 Modified cam-clay model: the volume change and pressure ratio in soil

(which is value commonly used for concrete structures). The length of the pile is 32.0 m. Since the modulus of elasticity of pile element is 1.1×10^3 times greater than the soil modulus of elasticity, material behaviour of pile is assumed to be linear-elastic, while behaviour of soil is considered as nonlinear-elastic.

The model covers the soil "half-space" prism, with dimensions $40 \times 40 \times 60$ m. These dimensions provide enough distance from the pile to the edge of the soil half-space in order make influences of the impact force far enough from the pile negligible. Translational displacement of half-space prism is constrained in all three global directions. The soil type that had been analysed is a clay soil of medium density, homogeneous along the depth, with the Young's modulus of elasticity of 27.5 MPa and Poisson's ratio of 0.45. For the modelling of concrete pile and soil 3D hexahedral FEs are used. Nonlinear parameters are included through the so-called modified cam-clay model of the soil, which is embedded in the software as one of the many possible nonlinear soil models [3]. This type of material model is used to simulate the behaviour of clay materials. In general, the relationship between the volume change and pressure in clay ground can be expressed using the concept of normal consolidation line and overconsolidation line. The increase in load (i.e. stress in ground) follows the overconsolidation line to the normal consolidation line (Fig. 24.3). After the stress increase reaches the point of intersection of overconsolidation line and line of normal consolidation, the stress state is further described by the normal consolidation line.

This type of soil behaviour can be interpreted in another way - through the elasto-hardening plastic ratio of stress and strain (Fig. 24.4).

The dynamic calculation includes a nonlinear dynamic (time-history) analysis for a time interval of 100 ms. The dynamic force acting on the pile is of a pulse character and is given by the Eq. (24.2):

$$F_{dyn} = F_{stat} \cdot f(t) \tag{24.2}$$

In Eq. (24.2) F_{stat} is a static value of force and f(t) is a function that describes a change in the force intensity depending on the time (Fig. 24.5). The change of force with time is defined so that the function linearly changes the value from 0 to

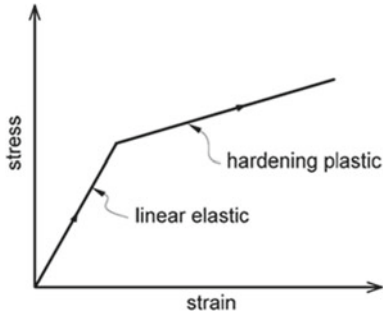

Fig. 24.4 Modified cam-clay model: the stress-strain ratio in soil

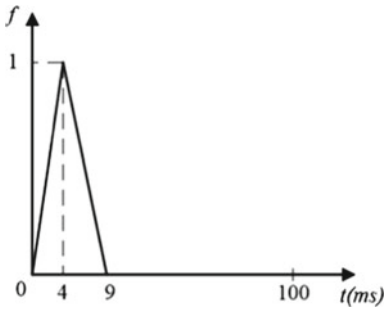

Fig. 24.5 Time function of force intensity

1 in the interval from 0 to 4 ms, and in the interval from 4 to 9 ms the function value is also linearly back to zero value. After this period, the function has a zero value, which represents the interval in which the dropping mass is in the air after bouncing off of pile surface after the impact. The peak intensity of the dynamic force is determined using analytical methods. As a reference value, the values of the nominal pile bearing capacity determined by theoretical methods based on the physical-mechanical properties of the soil given in [4] were used to obtain the same settlement as that due to the impulse force.

24.5 Analysis of the Results

Results of dynamic analyses are shown in the form of figures and diagrams. Diagrams show the values of calculated velocity (m/s) and the settlement of the top and base of the pile (m) at the four nodes along the pile's cross-section radius (central, 0.1, 0.3 and 0.5 from the pile's axis—Fig. 24.6) in function of time. Distribution of the principal stresses due to the impulse force is given at time increments of 1.0, 9.0, 10.0, 12.0, 14.0 and 16.0 ms.

Figures 24.7 and 24.8 show a large difference between the value of the results in the same time increments at different curves in the initial phase of the analysis. Since these figures show the results on the top surface of the pile, the reason for this

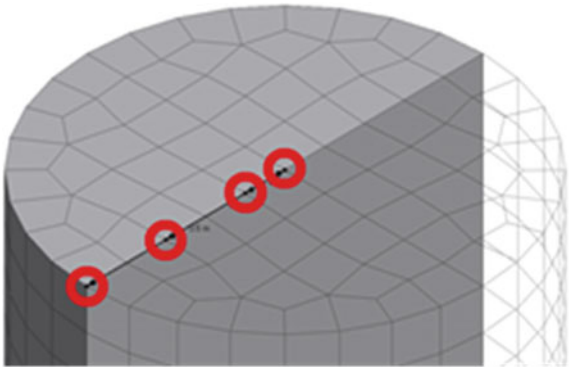

Fig. 24.6 Display of nodes along the radius of a pile's cross-section for a more detailed view of results

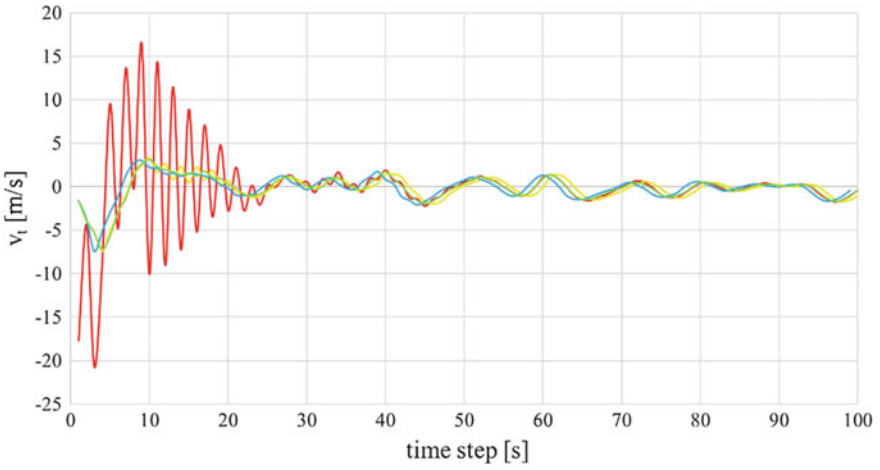

Fig. 24.7 Velocities (m/s) for time interval 0–100 ms (central node (red curve), 0.1 m (yellow curve), 0.3 m (blue curve) and 0.5 m (green curve) from the pile's axis)

phenomenon lies in the fact that the impulse force is modelled as a nodal load and as such is applied in the central node of the upper surface of the pile. Therefore, the high velocity and settlement peaks in the loaded node should be taken with the reserve and in the analysis of the results the priority should be given to the results referring to the points located at a certain distance from the loaded node (in this case at 0.1, 0.3 and 0.5 m from the central node) since the values of the results in the same time increments on these curves are almost identical.

In Fig. 24.9, which represents the pile base settlement, settlement values in all increments, on all curves (i.e. at all points along the radius of the lower surface of the pile) are roughly equal. Therefore, it can be concluded that the stress concentration at a sufficient distance from the loaded node does not affect the results of the analysis. By comparing Figs. 24.8 and 24.9, it can be noticed that the peaks of settlement curves of the base and the top of the pile are "translated" for 10 ms. This phenomenon

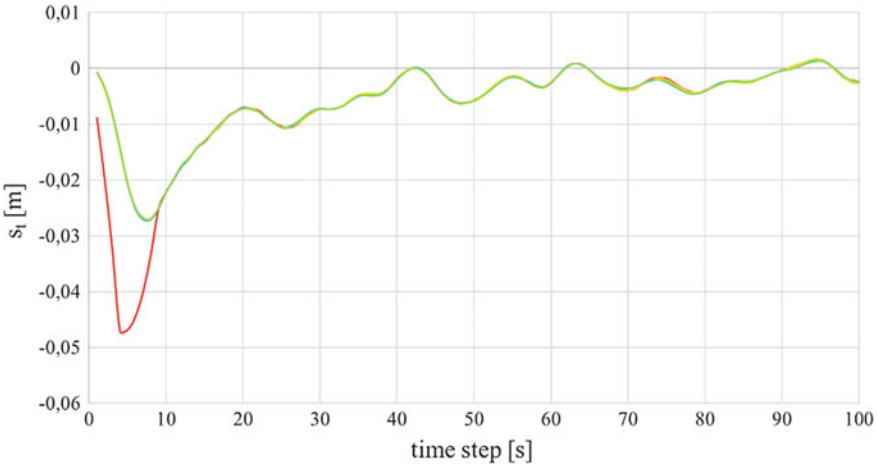

Fig. 24.8 Settlement of the top of the pile (m) for time interval 0–100 ms (central node (red curve), 0.1 m (blue curve), 0.3 m (yellow curve) and 0.5 m (green curve) from the pile's axis)

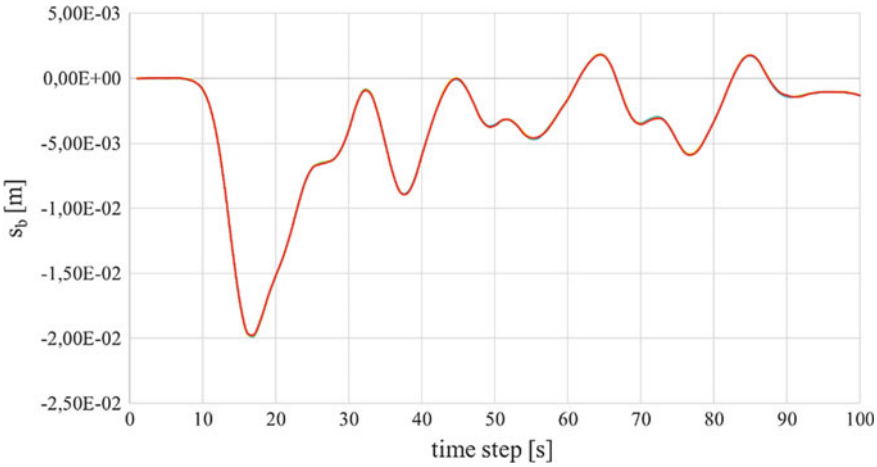

Fig. 24.9 Settlement of the base of the pile (m) for time interval 0–100 ms (central node (yellow curve), 0.1 m (blue curve), 0.3 m (green curve) and 0.5 m (red curve) from the pile's axis)

indicates the time necessary for the stress wave from the moment of impact to cover the distance from the top to the base of the pile. Additional thing to notice is the aperiodic mitigation of settlement after the impact.

The maximum settlement of the top of the pile is $s_{t,max} = 27.0$ mm and occurs at the time increment $t = 7$ ms (the central node is exempted). The maximum settlement of the base of the pile is $s_{b,max} = 20.0$ mm and occurs at the time increment $t = 17$ ms. The maximum calculated peak velocity is $v_{t,max} = 7.5$ m/s (the central node is exempted).

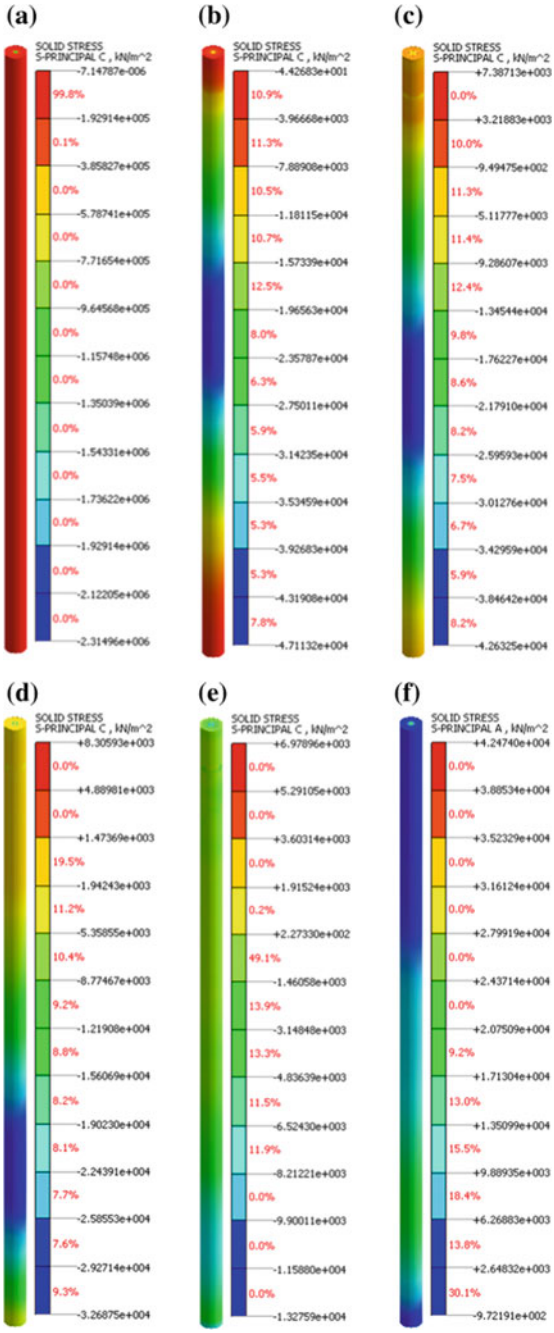

Fig. 24.10 Normal stresses (kN/m^2) in pile in time increments: **a** 1 ms, **b** 9 ms, **c** 10 ms, **d** 12 ms, **e** 14 ms, **f** 16 ms

Figure 24.10 indicate that the migration of the stress wave through the pile is uniform. Stress wave in its early stage is shown.

24.6 Conclusions

In this paper recommendations considering the use of FEM analysis for the purposes of pile dynamic load testing are given. After analysing the results of the dynamic calculation, the following conclusions were made:

The large difference between the value of the results in the loaded node and nodes along the radius of the pile in the same increments of time should be taken with reserve because the impulse force was modelled as a nodal and as such was applied in the central node of the upper surface of the pile. Hence, during the analysis of the results the priority should be given to the results referring to the points located at a certain distance across the cross-section radius from the loaded node.

Values of settlement in all increments are at all points along the radius of the lower surface of the pile equal. Therefore, it can be concluded that the stress concentration does not affect the results of the analysis at a sufficient distance from the point of load. The maximum settlement of the base and the top of the pile values are "translated" for 10 ms, indicating the time necessary for the stress wave from the moment of impact to reach from the top to the base of the pile.

Definite determination of the pile bearing capacity would be derived as a result of calibration of analytical and numerical methods by the experimental load testing.

Acknowledgements The presented paper has been done within the scientific research project TR 36043 "Development and application of a comprehensive approach to the design of new and safety assessment of existing structures for seismic risk reduction in Serbia", which is funded by the Ministry of Science of Serbia.

References

1. https://www.uml.edu/docs/SW%202004_Paikowsky_color_tcm18-106946.pdf, Accessed 27 Nov 2017
2. http://www.gsp-mannheim.de/pdfs/downloads/FMGM2011_Schallert-Klingm%C3%BCller.pdf, Accessed 30 Nov 2017
3. Roscoe, K.H., Burland, J.B.: On the generalized behaviour of "wet" clay. Eng. Plast. **48**, 535–609 (1968)
4. Stevanovic, S.: Foundation I (in Serbian). Scientific Book, Belgrade (1989)

Chapter 25
Harnessing Geometric Nonlinearity to Design Tunable Twist-Coupled Locally Resonant Metastructure

Yitian Wang, Rui Zhu, Xiaoning Liu and Gengkai Hu

Abstract In this paper, a lightweight metastructure is designed based on the prismatic tensegrity structure (PTS) which enables unique twist-coupled effect. Dynamically, the coupling between axial and torsional waves can also be observed in a PTS chain. A theoretical model with the coupling stiffness matrix is developed to study wave behavior of the proposed metastructures with local resonance-induced low-frequency bandgaps. Tunable static stiffness as well as wave behaviors can be achieved by harnessing the geometrically nonlinear deformation of the periodical tensegrity prisms under global torsional or/and axial loads. The proposed tensegrity metastructure could be useful for various engineering applications in the fields of space and civil engineering where high strength-to-weight ratio as well as low-frequency vibration suspension are in a high demand.

Keywords Metastructure · Nonlinearity · Vibration suspension

25.1 Introduction

A conventional way to attenuate structure-borne waves is attaching dampers to the vibrating components, however, it becomes less efficient for the low frequency wave due to the dissipation difficulty induced by the large wavelength. Metastructure, as a metamaterial inspired concept, has recently emerged to refer to a lightweight periodic material system with excellent low frequency wave attenuation abilities as well as high stiffness-to-weight ratio [1, 2]. Like any passive structures, once the functional units of the metastructures are manufactured, changing the position or size of metastructures' bandgap would be very difficult if not impossible in practice.

Y. Wang · R. Zhu (✉) · X. Liu · G. Hu (✉)
Department of Mechanics, School of Aerospace Engineering, Beijing Institute of Technology, Beijing, China
e-mail: rzhu83ac@gmail.com

G. Hu
e-mail: hugeng@bit.edu.cn

I. Kovacic and S. Lenci (eds.), *IUTAM Symposium on Exploiting Nonlinear Dynamics for Engineering Systems*, IUTAM Bookseries 37,
https://doi.org/10.1007/978-3-030-23692-2_25

One solution for actively controlling the wave behavior of the metastructure is to introduce electromechanical coupling which provides an externally controlled degree of freedom in each unit cell [3–5]. However, in this way, the metastructure's unit cell is difficult to manufacture and the complicated stability condition in the control circuits could also become a problem to the robustness of the active system. On the other hand, harnessing geometric nonlinearity provides an alternative solution to tune the dynamic behavior of the metastructure without introducing the complicated multi-physics coupling and therefore, becomes an excellent choice for the active control of the small-amplitude linear elastic waves [6, 7]. This tunable design significantly promotes manufacturing feasibility of the metastructure as well as decreases the complexity of the entire system.

In this paper, a theoretical model is first developed to investigate the unique twist coupling in a PTS through a coupling stiffness matrix. A lightweight metastructure is then designed based on local resonance mechanism to suspend the low frequency vibration. Tunable static stiffness and wave behaviors of metastructure with the periodically-ranged PTSs are observed under an axil static force which introduces the needed nonlinear deformation for tuning the elastic waves.

25.2 Theoretical Modelling of PTS Inspired Metastructure Unit Cell

A schematic of the studied PTS unit cell is shown in Fig. 25.1a, which is modified from the well-studied T3 module [8]. The PTS consists of two Aluminum (Al) disks at the top and bottom ends. The mass and moment of inertia of the disks are 9.7 g and 175 g cm^2, respectively. The two disks are then connected with three gray colored cross-strings and three yellow colored bars, which are made of Nylon and polylactic acid (PLA), respectively. The bars and strings constitute the PTS in a right-handed chiral fashion. The stiffness of strings/bars are 4.8×10^4 and 4.6×10^4 N/m. Due to the large differences in the material properties and mass between the disks and the string/bars, the mass of the strings/bars can be ignored and the disks can be considered rigid in the following study. The gray spheres in Fig. 25.1a represent the spherical joints that permit rotational degrees of freedom (DOFs) of unit cell. A reference configuration of the PTS is shown in Fig. 25.1b, where the radius of the end-disks, the height of the PTS and the relative angle of the two end-disks are R = 6 cm, h and ϕ, respectively. In this study, we assume that the PTS is only loaded by the axial force and torsion, so that the two end-disks are maintained to be parallel and the central axis of the PTS, $OO^{'}$, is always along the z direction. As a result, only two DOFs of the PTS are permitted, which are the relative axial displacement u and the relative rotational angle ϕ between the two end-disks.

Considering the symmetry of the PTS and using a local coordinate system n-t-z, the equilibrium equation at joint $E^{'}$ can then be expressed as:

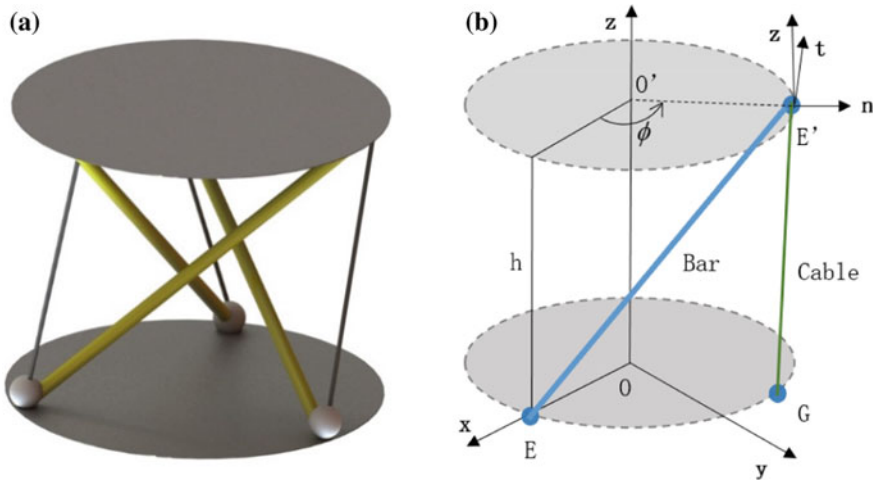

Fig. 25.1 **a** Schematic of the right-handed chiral PTS unit cell; **b** reference configuration of the PTS unit cell

$$q_{\mathrm{b}}\frac{(\mathbf{OE}'-\mathbf{OE})}{|\mathbf{OE}'-\mathbf{OE}|}+q_{\mathrm{s}}\frac{(\mathbf{OE}'-\mathbf{OG})}{|\mathbf{OE}'-\mathbf{OG}|}+q_{\mathrm{d}}\frac{(\mathbf{OE}'-\mathbf{OO}')}{|\mathbf{OE}'-\mathbf{OO}'|}=\mathbf{f} \tag{25.1}$$

where, $\mathbf{f}=(f_n,\ f_t,\ f_z)$ is the force applied at E', q_{b}, q_{s} and q_{d} are the forces density along the bar, the string and the radius of the disk plane, respectively. Then, Eq. (25.1) can be written in a matrix form as

$$\mathbf{CQ}=\mathbf{f} \tag{25.2}$$

where $\mathbf{C}$ is a 3 by 3 matrix with each component as a function of ϕ and h. The PTS must be in a stable equilibrium configuration under null nodal force. In such a configuration, the homogeneous equation $\mathbf{CQ}=\mathbf{0}$ should have a nontrivial solution. As a result, the determinant of the matrix $\mathbf{C}$ should be zero as

$$\det(\mathbf{C})=0 \tag{25.3}$$

which results in two possible initial angles with $\phi_0=-\pi/6$ or $5\pi/6$. However, the position $\phi_0=-\pi/6$ always yields a maximum of potential energy, so it's an unstable equilibrium configuration [8]. Therefore, $\phi_0=5\pi/6$ is the only stable tensegrity configuration of the PTS, and h_0 defines as the height h when the PTS under null nodal force, which is equal to 9.5 cm. Then, the two DOFs of the PTS can be rewritten as the torsional angle $\theta=\phi-\phi_0$ and the relative axial displacement between the two end-disks is $u=h-h_0$. The potential energy of the PTS under large displacement u and torsional angle θ can be given as

$$E = \frac{3}{2}k_b\left[\sqrt{(\mathrm{R}\cos(\phi_0+\theta)-\mathrm{R})^2+(\mathrm{R}\sin(\phi_0+\theta))^2+(\mathrm{h}_0+u)^2}-L_b^n\right]^2 + \frac{3}{2}k_s\left[\sqrt{(\mathrm{R}\cos(\phi_0+\theta)-\mathrm{R}\cos(2/3\pi))^2+(\mathrm{R}\sin(\phi_0+\theta)-\mathrm{R}\sin(2/3\pi))^2+(\mathrm{h}_0+u)^2}-L_s^n\right]^2 \tag{25.4}$$

where L_s^n and L_b^n are the nature length of the strings and bars, respectively.

The externally applied axial force and torque can be given as

$$F=\frac{\partial E}{\partial u},\ T=\frac{\partial E}{\partial \theta} \tag{25.5}$$

where F and T are nonlinear functions of u and θ. To demonstrate the tunability of the PTS, the effective tangent stiffness is first calculated by taking the partial derivatives of T and F, which can be given as the nonlinear functions of the equilibrium state θ_0 and u_0

$$k_m=\frac{\partial T}{\partial \theta}(u_0,\theta_0),\ k_h=\frac{\partial F}{\partial u}(u_0,\theta_0),\ k_c=\frac{\partial F}{\partial \theta}(u_0,\theta_0), \tag{25.6}$$

where k_m, k_h, and k_c are effective rotation stiffness, the effective axial stiffness and effective coupling stiffness, respectively. Since geometrical nonlinear behavior can be found intrinsically in the PTS [8, 9], large modifications in the structural configuration induced by the external loadings could consequently vary the effective stiffness and therefore, change the static as well as dynamic responses of the PTS. Figure 25.2a shows that effective stiffness k_h, k_c and k_m as a nonlinear function of the axial and rotational displacements state (u_0, θ_0) of the PTS. It can be found that both the rotational angle and axial displacement can be utilized to control the effective stiffness. Here, the applied axial force is chosen to adjust the effective stiffness as well as the dynamic behavior due to the easy realization. Figure 25.2b shows the applied static force F adjustments on the k_h, k_c and k_m. In the figure, k_h and k_c increase monotonically when F increases while k_m decreases monotonically when F increases, which suggests positive applied force (such as case 1) and negative applied force (such as case 2) are different control strategies for the elastic wave propagations in the tensegrity metastructure, which will be explained in the following part.

Although nonlinear wave behavior can be found in the tensegrity system, we here only study the small-amplitude linear elastic wave propagations, which are defined as $\Delta u(\mathrm{t})$, $\Delta\theta(\mathrm{t})$, superimposed upon an equilibrium state in the 1D infinite tensegrity metastructure, which is constructed by periodically arranging PTSs with same elastic, inertial and geometrical properties. The governing equation of the nth PTS cell can then be obtained with effective stiffness as

$$\begin{bmatrix} \mathrm{m} & 0 \\ 0 & J \end{bmatrix}\begin{Bmatrix} \ddot{\Delta u}_\mathrm{n} \\ \ddot{\Delta\theta}_\mathrm{n} \end{Bmatrix} = \begin{bmatrix} k_\mathrm{h}(u_0,\theta_0) & k_\mathrm{c}(u_0,\theta_0) \\ k_\mathrm{c}(u_0,\theta_0) & k_\mathrm{m}(u_0,\theta_0) \end{bmatrix}\begin{Bmatrix} \Delta u_{\mathrm{n}+1}+\Delta u_{\mathrm{n}-1}-2\Delta u_\mathrm{n} \\ \Delta\theta_{\mathrm{n}+1}+\Delta\theta_{\mathrm{n}-1}-2\Delta\theta_\mathrm{n} \end{Bmatrix} \tag{25.7}$$

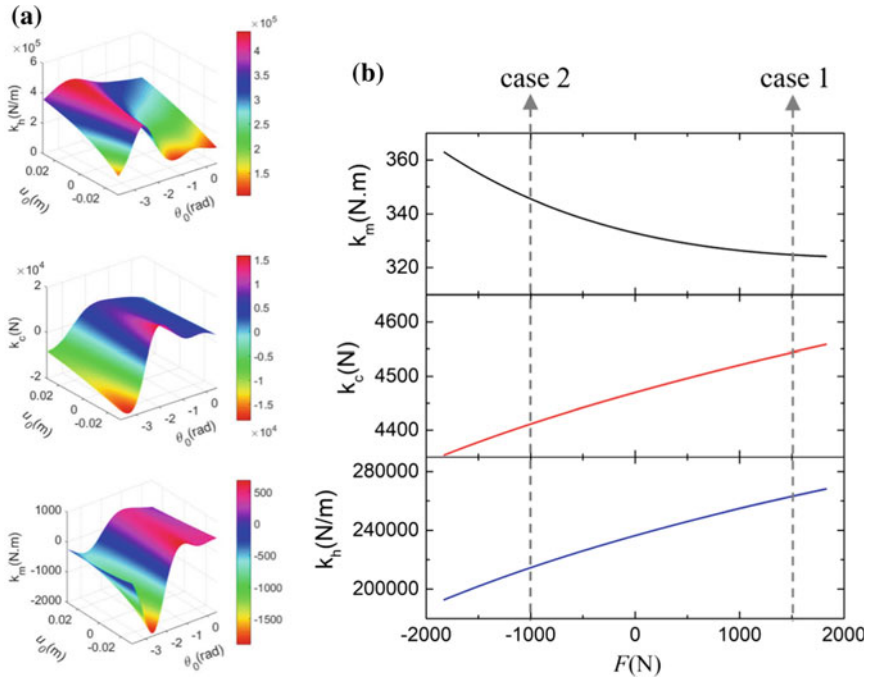

Fig. 25.2 **a** k_h, k_c and k_m as functions of u_0 and θ_0; **b** k_h, k_c and k_m change with applied static axial force F

where J and m are the moment of inertia and mass of the PTS's disk, respectively. Considering harmonic wave excitations with angular frequency ω and periodic boundary condition on the unit cell's boundaries, an eigenvalue problem can be formed and the dispersion results for two wave modes can be calculated. Figure 25.3 shows the dispersion curve of the system. The blue dot dash line is dispersion relationship of the quasi torsional wave, which has lower cut-off frequency and wave velocity. While the red solid line is dispersion relationship of the quasi axial wave, which has higher cut-off frequency and wave velocity.

25.3 Tunable Tensegrity Metastructure for Vibration Suspension

Figure 25.4a shows the schematic of a local resonance-based tensegrity metastructure. The introduced resonator in each unit cell consists of a cylindrical resonator ($m_R = 10.17$ g) and two strings ($k_R = 4.6417 \times 10^4$ N/m) that connects the resonator to the PTS's end disks. The diameter of the resonator is designed to fit inside the central space of the chiral bars and strings without blocking their motions. In order

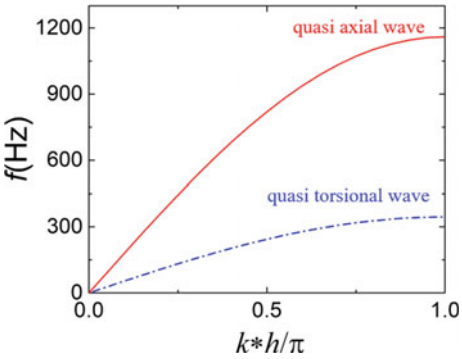

Fig. 25.3 The dispersion curves of the 1D infinite tensegrity metastructure constructed by periodically arranging PTSs, where k is the wave vector

to reduce the overall weight of the metastructure, cross-patterned end disks (m_C, J_C) with $m_C = 4.63$ g and $J_C = 83.36$ g cm^2 are used in each PTS. Figure 25.4b shows the dispersion curves of the LR-type metastructure. First, no full-wave bandgap can be found in the low frequency region. Second, an axial wave bandgap can be found in the light blue shaded region. The local resonance origin of the axial wave bandgap is evidenced by the lower edge-maximum profile of the k^*(Im) curve in the corresponding frequency range [10]. Therefore, the LR-based tensegrity metastructure can block axial wave in the frequency range from 447 to 696 Hz, while keeping the light weight property of the entire structure unchanged.

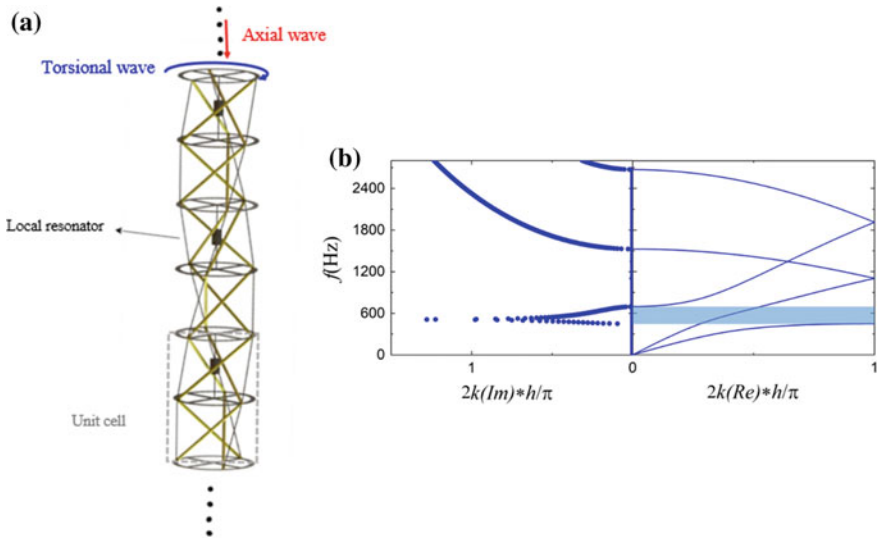

Fig. 25.4 **a** Schematic of the LR-type tensegrity metastructure; **b** dispersion curves with real and imaginary wavenumbers. Light blue-shaded region indicates axial wave bandgap

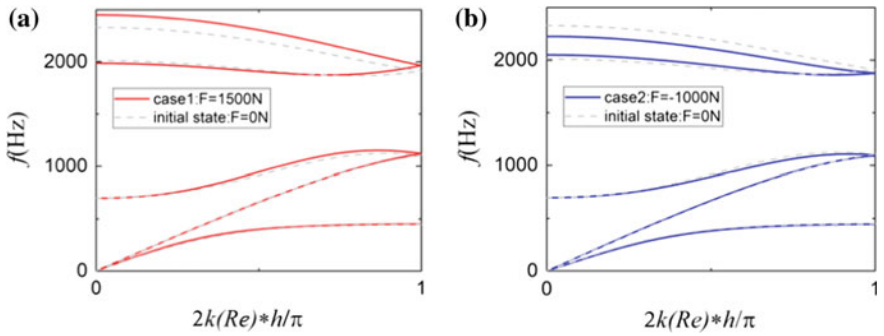

Fig. 25.5 **a** Dispersion curves of the tensegrity metastructure under positive control axial force and **b** negative control axial force

In the previous section, quantitative analysis on the PTS's effective stiffness controlled by an external axial force loading has been conducted statically (Fig. 25.2b). In order to controlled the band structure of the tensegrity metastructure, the 'small-on-large' tunability [6, 7] is considered in this section. The 'large' means giving a large global static external loading on the metastructure, therefore, causing the geometrically nonlinear deformation and the effective stiffness changing of the PTS, which is the fundamental formation of the tensegrity metastructure. The 'small' means the small amplitude linear wave propagating in the metastructure, which is affected by the 'large' nonlinear deformation. A kind of metastructure with a right-handed chiral PTS, a left-handed chiral PTS and a local resonator in the unit cell, is design to exhibit the 'small-on-large' tunability of the tensegrity metastructure. Both positive (case1 $F = 1500$ N) and negative (case2 $F = -1000$ N) control axial force are applied to tune the band structure of the tensegrity metastructure. The tuned dispersion curves are shown in Fig. 25.5a, b, respectively. First, in the dispersion curve of this kind of metastructure which is shown as gray dash line, a bandgap for both two kinds of wave can be found in the frequency region 1124–1867 Hz. Second the axial wave bandgap is unchanged in both case1 and case2. Third, by imposing the positive control force (case1), the full wave bandgap and cutoff frequency rises to a higher frequency region, as shown in Fig. 25.5a. By imposing a negative control force (case2), the full wave bandgap and cutoff frequency drops to a lower frequency region.

In the previous sections, wave propagations in the infinite tensegrity metastructures based on local resonance mechanism have been systematically investigated. However, the infinite structure can't be realized in the engineering field. Therefore, we conduct the vibration tests in a finite tensegrity metastructure with defined boundary conditions, which can validate the predicted wave properties of the tensegrity metastructure in the previous part. Figure 25.6a shows the schematic of the finite tensegrity metastructure with LR-type unit cells. The schematic only shows the side views of the metastructure with the green thin lines, black thick lines and blue thin lines being the thin strings connecting local resonators, the elastic bars and the strings

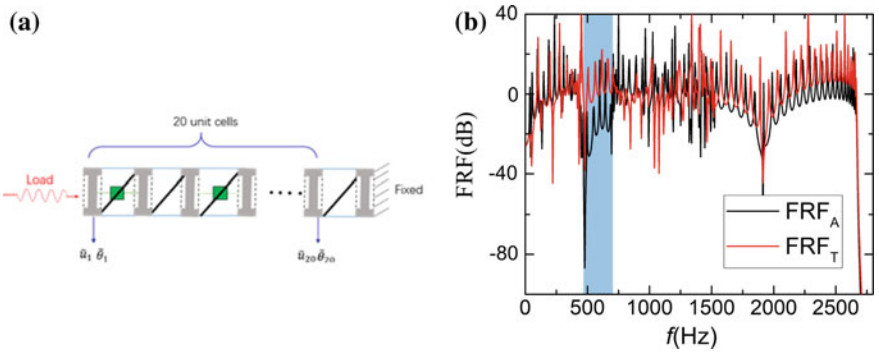

Fig. 25.6 **a** Schematic of the 20 unit cells finite tensegrity metastructure; **b** corresponding FRF results of the metastructure

connecting PTSs, respectively. The cross-linked disks are presented by the gray I-pattern rectangles. The tensegrity metastructures are constituted of 20 unit cells. The right side of the metastructure is fixed. The harmonic torsional and axial force excite on the left side. A frequency sweep is conducted in the frequency range $f = (0,$ 2800 Hz). Frequency-response functions (FRFs) then are defined for the torsional and axial waves as $\mathrm{FRF_T}$ and $\mathrm{FRF_A}$, respectively. For steady-state vibrations, the FRFs for the two wave modes can be defined as follows:

$$\begin{aligned} \mathrm{FRF_T} &= 20\log\left(\frac{\theta_{20}}{\theta_1}\right) \\ \mathrm{FRF_A} &= 20\log\left(\frac{u_{20}}{u_1}\right) \end{aligned} \tag{25.8}$$

where

$$\theta_j = \tilde{\theta}_j e^{-i\omega t}, \quad j = 1 \text{ or } 20$$

$$u_j = \tilde{u}_j e^{-i\omega t}, \quad j = 1 \text{ or } 20$$

are the torsional and axial displacements measured at the sensor points located at first end disks of the 1st and 20th metastructure unit cells. Significantly decreased $\mathrm{FRF_A}$ curve can be found in the frequency range $f = (450,$ 690 Hz) in Fig. 25.6b, which is in good agreement with the local resonance-induced axial wave bandgap (light blue-shaded zone) found in the corresponding infinite LR-type metastructure. In this frequency range, the $\mathrm{FRF_A}$ amplitudes at most frequency points are below -20 dB except for those at the four peaks which are generated by the global resonant motions of the entire finite tensegrity metastructure.

25.4 Conclusions

A theoretical model is developed to study the nonlinear axial-torsional coupling effect of the prismatic tensegrity structure. Then, the band structures are calculated to describe the axial-torsional coupling wave propagation in the metastructures consisting of PTS cells. The unit cells are design on local resonance mechanism, which can realize the low frequency vibration suspension. Moreover, the 'small-on-large' tunability is introduce to control of the wave propagation and vibration suspension in the tensegrity metastructure by harnessing the geometrically nonlinear deformation of the PTS. Finally, the vibration tests in finite tensegrity metastructure is conducted to validate the axial wave blocking ability of the proposed tensegrity metastructures.

References

1. Hussein, M.I., Leamy, M.J., Ruzzene, M.: Dynamics of phononic materials and structures: historical origins, recent progress, and future outlook. Appl. Mech. Rev. **66**, 040802 (2014)
2. Reichl, K.K., Inman, D.J.: Lumped mass model of a 1d metastructure for vibration suppression with no additional mass. J. Sound Vib. **403**, 75–89 (2017)
3. Zhu, R., et al.: Experimental study of an adaptive elastic metamaterial controlled by electric circuits. Appl. Phys. Lett. **108**, 0119051 (2016)
4. Airoldi, L., Ruzzene, M.: Design of tunable acoustic metamaterials through periodic arrays of resonant shunted piezos. New J. Phys. **13**, 113010 (2011)
5. Wang, Z., Zhang, Q., Zhang, K., Hu, G.: Tunable digital metamaterial for broadband vibration isolation at low frequency. Adv. Mater. **28**, 9857 (2016)
6. Wang, P., Shim, J., Bertoldi, K.: Effects of geometric and material nonlinearities on tunable band gaps and low-frequency directionality of phononic crystals. Phys. Rev. B **88**, 0143041 (2013)
7. Wang, P., Casadei, F., Shan, S., Weaver, J.C., Bertoldi, K.: Harnessing buckling to design tunable locally resonant acoustic metamaterials. Phys. Rev. Lett. **113**, 0143011 (2014)
8. Oppenheim, I.J., Williams, W.O.: Geometric effects in an elastic tensegrity structure. J. Elast. **59**, 51–65 (2000)
9. Zhang, L., Li, Y., Cao, Y., Feng, X., Gao, H.: A numerical method for simulating nonlinear mechanical responses of tensegrity structures under large deformations. J. Appl. Mech. Trans. ASME **80**, 0610186 (2013)
10. Xiao, Y., Mace, B.R., Wen, J., Wen, X.: Formation and coupling of band gaps in a locally resonant elastic system comprising a string with attached resonators. Phys. Lett. A **375**, 1485–1491 (2011)

Chapter 26
Vibrations of Rotating Thin-Walled Composite Beams with Nonlinear Piezoelectric Layers

Jerzy Warminski and Jaroslaw Latalski

Abstract A nonlinear model of a structure consisting of a rigid hub and three thin-walled flexible laminated beams is analysed in this paper. It is assumed the considered blades have additional piezoceramic layers embedded into master laminate, so due to elastic specimen deformation an electric field is induced. In the mathematical model of the multi-material blades a full two-way piezoelectric coupling effect involving mutual mechanical and electrical interactions is adopted. Moreover, a nonlinear constitutive relation for piezoceramic material with respect to electrical field is considered to properly model the active structure behaviour when operated in near resonance conditions. The governing equations of the system have been sourced from the previous authors' research. Next, resonance curve plots of the coupled electromechanical system considering both the blades and the hub dynamics have been prepared. Within the performed studies cases of a fully symmetric and next a slightly mistuned rotor configuration have been discussed.

Keywords Rotating structures · Active blades · Nonlinear vibrations · Composites

26.1 Introduction

Rotating structures play a very important role in many branches of mechanical and aerospace engineering. Representative examples of actual designs might be steam and gas turbines, generators, fans, compressors, aircraft propellers, helicopter rotor blades etc. [1, 2]. Recent trends in rotating structures development are aimed at enhancing their functionality so that they can react to the changing external conditions and

J. Warminski (✉) · J. Latalski
Department of Applied Mechanics, Faculty of Mechanical Engineering, Lublin University of Technology, Nadbystrzycka 36, 20618 Lublin, Poland
e-mail: j.warminski@pollub.pl

J. Latalski
DICEAA, University of L'Aquila, Via Giovanni Gronchi 18, 67100 L'Aquila, AQ, Italy
e-mail: j.latalski@pollub.pl

I. Kovacic and S. Lenci (eds.), *IUTAM Symposium on Exploiting Nonlinear Dynamics for Engineering Systems*, IUTAM Bookseries 37,
https://doi.org/10.1007/978-3-030-23692-2_26

behave as smart devices. This goal may be achieved by combining active materials, like piezoceramics, shape memory alloys or magnetostrictive ferrofluids with tailored hosting structures usually made of lightweight composites [3].

In the above context, a multi-disciplinary effort in materials, mechanics, electricity and structural analysis is needed to address these challenges. It involves more accurate mathematical and computational models to properly capture the complex multi-domain structural behaviour. For instance, while considering piezoceramic layers embedded into fibre reinforced composites an accurate and reliable mathematical model has to take into account anisotropic properties of the master composite material as well as mutual coupling of electro-mechanical properties of the active material [4, 5]. In the classical approach, when dealing with mechanical structural domain, a nonlinear model is often adopted for small strains but large amplitude oscillations. However, if a coupled piezo-composite structure is considered a set of additional nonlinear constitutive equations for piezoelectric layers must be taken into account [4, 6].

When looking at the mathematical models of transducers and active devices made of piezoceramics there are two ways in which one may deal with the problem. The most popular formulations are based on the converse effect only, where the impact of the known electrical field on the mechanical one is considered, but the direct piezoelectric effect is neglected. Unfortunately, this one-way coupling approach is not sufficiently accurate since it tends to underestimate the material stiffness and natural frequencies of the structure [7].

Another group of mathematical models are the two-way coupling ones that incorporate both converse and direct piezoelectric effects. These models are more accurate when comparing to the one-way coupling ones. Moreover, they provide an additional electrical degree of freedom apart from regular mechanical ones.

The analytical two-way coupling model of a rotating composite thin-walled beam with embedded nonlinear piezo-layers has been proposed recently in [8]. In the mathematical formulation of the problem both direct and converse piezoelectric effects are considered by adopting the assumption of a spanwise electric field variation. In this research a special laminate stacking configuration—so called circumferentially asymmetric stiffness (CAS)—exhibiting strong coupling of bending and torsional deformations of the beam has been considered. Free vibration tests and analysis of individual components of mode shapes has shown some significant diversities in the electric field distribution regarding the angular speed of the system and the type of master structure deformation. The most prominent effects have been observed for first modes. Moreover, the forced vibration analysis has revealed the presence of the softening effect in systems with nonlinear piezoceramic material.

In the current paper the previous authors studies [8, 9] on rotor structures are continued. In particular, a three bladed design with piezoelectric layers embedded on two opposite outer surfaces of each beam is examined. Similar to the previous studies it is assumed the piezoceramic material exhibits nonlinear constitutive properties with respect to electric field. The dynamics of a fully symmetric and next a slightly mistuned rotor configuration are examined in detail.

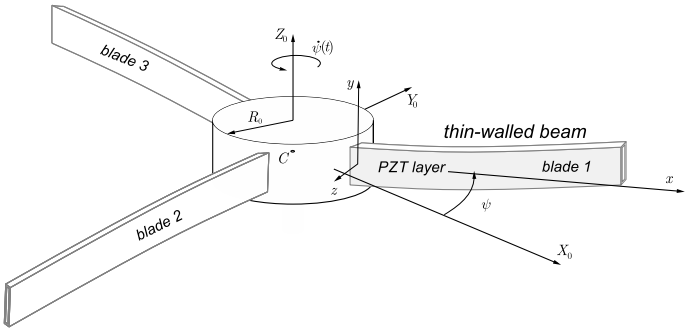

Fig. 26.1 Model of the rotor composed of a rigid hub and three flexible blades with active piezo-layers

26.2 Mathematical Model of a Rotating Structure

The investigated rotating structure is composed of a rigid hub and three flexible thin-walled symmetric composite blades in the spatial setting presented in Fig. 26.1. The blades are laminated according to the circumferentially asymmetric stiffness CAS scheme. This configuration demonstrates the mutual coupling of beam flapwise bending occurring in the plane of rotation and torsional deformations. The magnitude of this coupling depends on the reinforcing fibres orientation [10].

According to the previous authors' papers [8, 10] and presented therein detailed derivation procedure by means of the Hamilton principle and Galerkin discretisation method the ordinary differential equations of motion of the system are

$$\begin{aligned}\left(J_{\mathrm{h}}+\sum_{j=1}^{3}J_{\mathrm{b}j}+\sum_{j=1}^{3}\alpha_{\mathrm{h}j2}q_j^2\right)\ddot{\psi}+\zeta_{\mathrm{h}}\dot{\psi}+\sum_{j=1}^{3}\left(\alpha_{\mathrm{h}j1}\ddot{q}_j+\alpha_{\mathrm{h}j3}q_j\dot{q}_j\dot{\psi}\right)=\mu,\\ \ddot{q}_j+\zeta_j\dot{q}_j+\alpha_{j2}\ddot{\psi}+\left(\alpha_{j1}+\alpha_{j3}\dot{\psi}^2\right)q_j+\alpha_{j4}q_j\dot{q}_j\dot{\psi}\\ +\alpha_{j5}\mathrm{sgn}(q_j)q_j^2+\alpha_{j6}q_j^3=0\end{aligned} \tag{26.1}$$

where index $j = 1, 2$ or 3 represents the individual beam of the rotor. Moreover, q_j is a generalised beam coordinate, J_{h}, $J_{\mathrm{b}j}$ denote dimensionless mass moment of inertia of the hub and each beam, respectively. Coefficients ζ_{h}, ζ_j are viscous damping factors of the hub and each individual beam; $\alpha_{\mathrm{h}j1}, \alpha_{\mathrm{h}j2}, \alpha_{\mathrm{h}j3}, \alpha_{j1}, \alpha_{j2}, \alpha_{j3}$, $\alpha_{j4}, \alpha_{j5}, \alpha_{j6}$ are coefficients obtained from the modal reduction procedure for each j beam. The variable μ present on the right-hand side of the first formula represents the dimensionless driving torque applied to the hub that in general case might be a dimensionless time τ dependent function $\mu = \mu(\tau)$.

Provided the given above system of relations, the mathematical model of the considered structure is represented by a set of four equations. The first one Eq. $(26.1)_1$

Table 26.1 Dimensionless coefficients of the rotating structure model

Hub equation Eq. $(26.1)_1$			
	$J_{\mathrm{h}} = 5$	$J_{\mathrm{b}1} = J_{\mathrm{b}2} = J_{\mathrm{b}3} = 1$	$\zeta_{\mathrm{h}} = 0.1$
	$\alpha_{\mathrm{h}j1} = 0.5323$	$\alpha_{\mathrm{h}j2} = -0.4042$	$\alpha_{\mathrm{h}j3} = -0.8085$
	$\rho = 0.2$	ω – varied	
Beams equations Eq. $(26.1)_2$			
	$\alpha_{j1} = 10.8636$	$\alpha_{j2} = -1.7723$	$\alpha_{j3} = 0.3484$
	$\alpha_{j4} = 1.5498$	$\alpha_{j5} = -2.3268$	$\alpha_{j6} = 0$
	$\zeta_j = 0.02 \times \sqrt{\alpha_{j1}}$		

represents the dynamics of the hub and it is coupled to the three equations of every individual beam Eq. $(26.1)_2$ ($j = 1, 2, 3$) by appropriate inertia terms $J_{\mathrm{b}j}$. Further studies of this relations reveal there are no elastic couplings in the system.

Moreover, it is to be noted the presented formulation includes the Coriolis, centrifugal and inertia terms due to rotation of the structure, variable angular velocity of the hub $\dot{\psi}$, as well as higher order geometric terms resulting from the nonlinear piezoelectric effect.

26.3 Numerical Results

Numerical simulations are prepared for the graphite-epoxy laminate beams with embedded layers of PZT-3203HD piezoceramic. Engineering constants for these materials as well as geometric dimensions of the structure are given in [8]. The final values of the coefficients α_{ij} present in Eqs. (26.1) and resulting from the assumed mode discretisation method are collected in Table 26.1.

26.3.1 Analysis of the Symmetric Rotor

To start the analysis, let us estimate the first natural frequency of the non-rotating structure—i.e. the hub and three piezo-blades system at rest. This can be done based on the linearised form of governing Eqs. (26.1). For the sake of brevity details of these calculations are not presented here. However, the interested reader may refer for more details to [10] where the mathematical procedure for a single bladed system is presented. If all the blades are exactly the same the first natural frequency of the whole rotor is $\omega_{01} = 2.833$. As one may notice, this is different from the first natural frequency of a cantilever beam $\omega_{1(\mathrm{beam})} = \sqrt{\alpha_{11}} = 3.296$. This is due to the fact that, as opposed to the separated beam case, the natural frequencies of the full rotor (hub

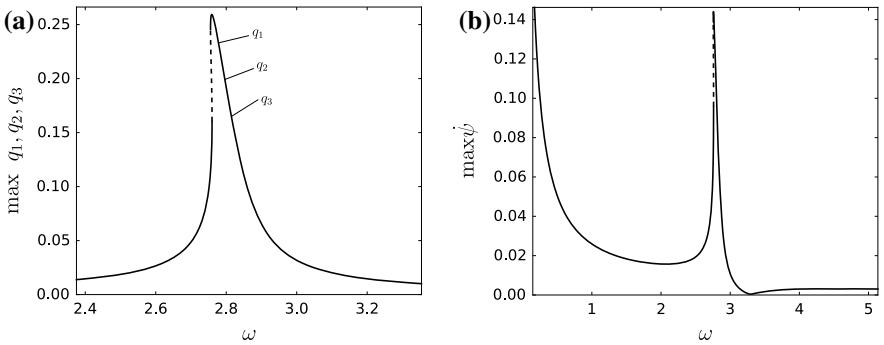

Fig. 26.2 Resonance curves for a symmetric rotor with piezo-blades: blades (**a**) and hub (**b**) response; oscillations of the structure about its rest position ($\mu_0 = 0$)

and beam system) depend on the relative hub to beam inertia. The detailed discussion on this observation can be found in [10].

Now consider the system response if the structure is excited by external torque $\mu(\tau)$ imposed to the hub. To capture the possibly general excitation case it is assumed the provided forcing might be composed of two terms, namely the constant and the harmonic one $\mu(\tau) = \mu_0 + \rho \sin \omega\tau$.

First consider the case with $\mu_0 = 0$ that corresponds to the oscillations of the structure about its rest position. The torque amplitude is set to $\rho = 0.2$ and excitation frequency ω is varied in the neighbourhood of the first resonance. For this analysis and the following ones the system of governing Eqs. (26.1) is solved numerically by the direct integration method. Outcomes of the simulations for the fully symmetric rotor are presented in Fig. 26.2.

The provided plots reveal a clear softening behaviour exhibited by the resonance peaks leaning to the left. This effect results from the nonlinear properties of the piezoelectric active layers and is typical for the nonlinear models which include the quadratic terms accompanied by the small structural displacements constraint [11]. It should be noted the discussed softening phenomenon is present for the beams Fig. 26.2a and for the hub Fig. 26.2b as well. Short segments of both characteristics reveal the existence of unstable solutions. Moreover, one observes the responses of all three beams are exactly the same due to the perfect symmetry of the system. Another effect to be noticed on the presented plots is the hub vibration absorption phenomenon. For the excitation frequency $\omega \approx 3.3$ energy from the excitation is accommodated solely by the blades while the hub stays at rest ($\dot{\psi} = 0$).

In the further analysis the impact of the system rotation on the response of the perfectly symmetric rotor is studied. It can be done by setting any nonzero value to the μ_0 torque summand. This assignment results in mean angular speed $\dot{\psi}(\tau)$ different from zero. Outcomes of the performed simulations for $\mu_0 = 0$, $\mu_0 = 0.02$ and $\mu_0 = 0.05$ are presented in Fig. 26.3.

Similar to the former case a softening effect is visible on the beams and the hub resonance curves, note subplots (a) and (b) respectively. Besides, the responses of

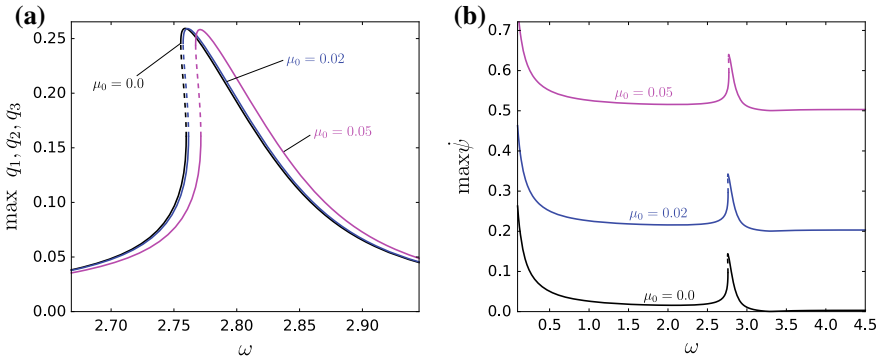

Fig. 26.3 Resonance curves of the blades (**a**) and the hub (**b**) obtained for various external torques μ_0. Colours: $\mu_0 = 0$—black, $\mu_0 = 0.02$—blue, $\mu_0 = 0.05$—magenta; rotor in symmetric configuration with nonlinear blades

the beams are slightly shifted towards higher frequencies but without any significant change in their overall shape. This shift is known as the centrifugal stiffening effect and it comes from the additional linear stiffness term present in the governing equations that is proportional to $\dot{\psi}^2$—see Eq. (26.1)$_2$. The same stiffening effect is observed on the resonance curves of the hub—Fig. 26.3b. However, a simultaneous upward shift is present that corresponds to the nonzero mean angular velocity of the rotor.

26.3.2 Analysis of the Mistuned System

Next we consider the case of a mistuned design. To this aim the blades No. 2 and 3 are replaced by the new ones of the same geometry and mechanical properties but without nonlinearities in the piezoelectric effect ($\alpha_{j5} = \alpha_{j6} = 0$ for $j = 2, 3$). The beam No. 1 stays the same as in the preceding reference case.

Similar to the former research stage the first simulation is performed for the rotor just oscillating about its rest position keeping the same torque excitation amplitude $\rho = 0.2$, the system response is demonstrated in Fig. 26.4. The previously spotted softening effect is still present, however it is less apparent now. In particular, within the tested range of excitation frequencies all the solutions are stable. This applies both to the blades (Fig. 26.4a) and to the hub (Fig. 26.4b). The interesting further insight to these results is that the softening effect is observed for all the beams i.e. also for the beams No. 2 and No. 3 despite their linear properties (green curve). But no matter of this disparity the peaks on both response curves correspond to the same resonance frequency. However, the difference in the response amplitude between linear and nonlinear blades is observed. Since the beams No. 2 and No. 3 exhibit linear characteristics they are stiffer, therefore their response amplitude is smaller

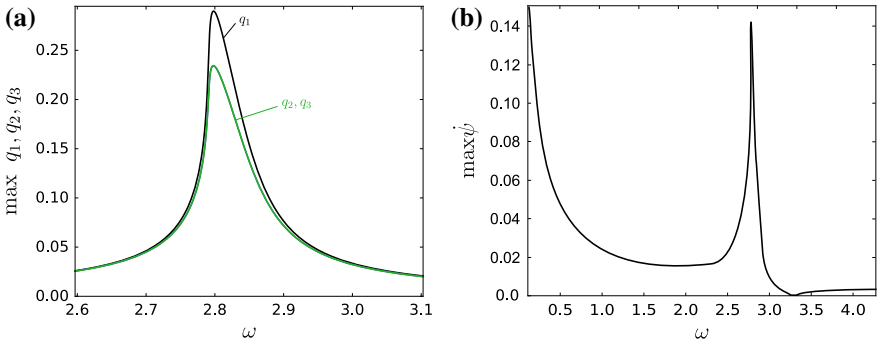

Fig. 26.4 Resonance curves for a rotor: blades (**a**) and hub (**b**) response; oscillations of the structure about its rest position ($\mu_0 = 0$, $\rho = 0.2$); rotor in mistuned configuration

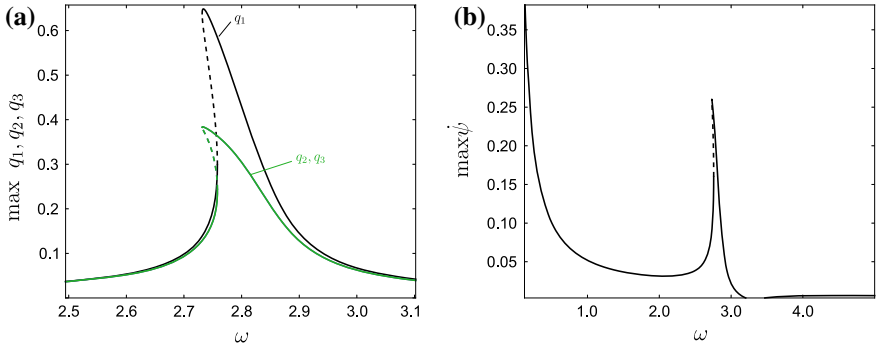

Fig. 26.5 Resonance curves for a rotor: blades (**a**) and hub (**b**) response; oscillations of the structure about its rest position ($\mu_0 = 0$, $\rho = 0.4$); rotor in mistuned configuration

when comparing to the nonlinear blade No. 1. Simultaneously, the peak value of the response q_1 is now slightly higher if compared to the symmetric design case (0.29 vs. 0.26—see Fig. 26.2 for reference). The final comment regards the hub vibration absorption phenomenon to occur at the same excitation frequency $\omega \approx 3.3$ as in the case of perfectly symmetric rotor design.

To study the separated impact of the torque excitation amplitude the last simulation is repeated for the ρ parameter set to 0.4 value. Results of this numerical experiment are presented in Fig. 26.5.

Studying the beams and the hub response plots (subfigures (a) and (b), respectively) one notice the already discussed softening effect to be much more emphasized when compared to the previous analysis. Some parts of all three response curves are unstable again and the response amplitudes are much higher as for the $\rho = 0.2$ case. However, it should be commented the observed magnitudes are beyond the scope of small displacements assumptions adopted to the mathematical model of the structure. Nevertheless, one may conclude the response of the structure is sensi-

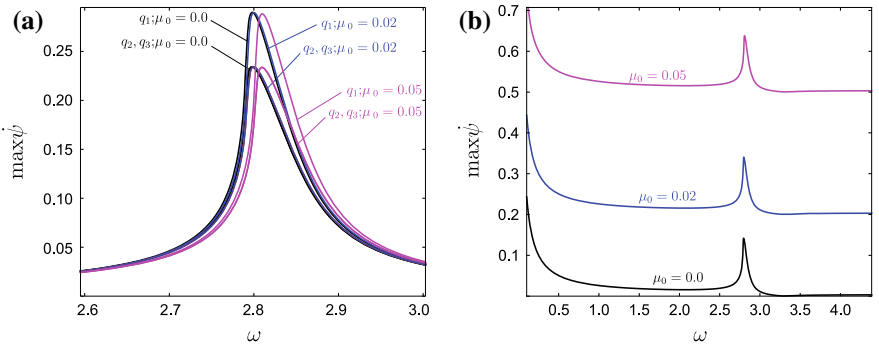

Fig. 26.6 Resonance curves of the blades (**a**) and the hub (**b**) obtained for various external torques μ_0. Colours: $\mu_0 = 0$—black, $\mu_0 = 0.02$—blue, $\mu_0 = 0.05$—magenta; rotor in mistuned configuration

tive both quantitatively and qualitatively to the amplitude ρ of the torque periodic component.

At the next research stage the dynamics of the mistuned rotor performing full rotation is investigated. Similar to the analysis of the perfectly symmetric design given in Sect. 26.3.1 the cases of $\mu_0 = 0.02$ and $\mu_0 = 0.05$ are studied and referenced to the $\mu_0 = 0.0$ outcome. Results of these simulations are presented in Fig. 26.6.

Similar to the perfectly symmetric design case the centrifugal stiffening effect can be observed due to the increased mean rotating speed ($\mu_0 > 0$). The direct consequences of this stiffening are the right shift of response curves towards higher frequencies and a slight reduction of amplitudes magnitude. However, this second effect can be noticed only under very high magnification. By virtue of the space limitation this plot is not presented here. The previously reported difference in the response amplitude between linear and nonlinear blades for the μ_0 case (see Fig. 26.4 for reference) is observed also for rotating structure. This is featured on the response plot by two separated curves for every driving torque case—Fig. 26.6a.

At the final stage the impact of rotating speed on system dynamics is investigated more thoroughly. This analysis is carried out by varying the mean torque μ_0 parameter over a wide range of values. To highlight some interesting effects the amplitude of the periodic excitation term $\rho \sin \omega\tau$ is increased to $\rho = 0.4$. At this magnitude the unstable solutions on system response characteristics are present—see results in Fig. 26.5 for reference.

Studies are carried out for two different torque frequencies ω starting from $\omega = 2.75$. This value corresponds to the range of system response where, due to the beam No. 1 nonlinearity, exactly three solutions are present. Outcomes of this simulation are presented in Fig. 26.7.

It should be noted the system has multiple solutions but only within the range of μ_0 close to zero. These solutions correspond to the low or high vibration amplitudes and are observed for the nonlinear and linear blades as well (Fig. 26.7a black and green curves, respectively). However, the high amplitude solutions, namely the stable

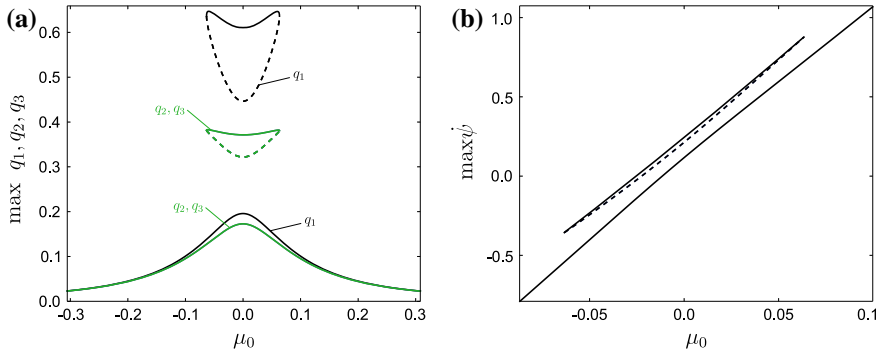

Fig. 26.7 Dynamics of the rotor at the excitation loading $\rho = 0.4$ and $\omega = 2.75$—beams (**a**) and hub (**b**) responses; rotor in mistuned configuration

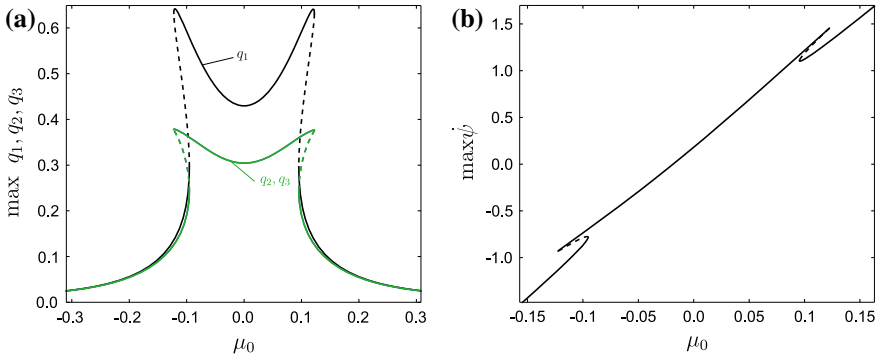

Fig. 26.8 Dynamics of the rotor at the excitation loading $\rho = 0.4$ and $\omega = 2.8$—beams (**a**) and hub (**b**) responses; rotor in mistuned configuration

and unstable ones, coalesce in a saddle-node bifurcation as the magnitude of the μ_0 parameter reaches the threshold value of 0.063. Above this limit only low amplitude vibrations are observed. This phenomenon is explained by the stabilising action of the centrifugal forces and blades stiffening as the rotor angular speed increases. Exactly the same effect is observed for the hub—Fig. 26.7b. The final comment on these two plots regards their symmetry with respect to vertical axis. This can be easily explained since there is no difference in blades/hub behaviour while the rotor rotates clockwise or counterclockwise.

The next simulation is carried out when setting the excitation frequency ω to 2.8. This value corresponds to the range of system response where just single solutions for the blades and the hub are present (providing $\mu_0 = 0$)—see Fig. 26.5 for reference. Outcomes of this simulation are presented in Fig. 26.8.

Studying these plots one observes the qualitatively different behaviour with respect to μ_0 parameter when compared to the previous case $\omega = 2.75$ (Fig. 26.7). Now the single solutions are present for both low and high values. However, there is

a narrow range $|\mu_0| \in < 0.096, 0.122 >$ where unstable solutions occur apart from the two stable ones.

Nevertheless, when collating both Figs. 26.7 and 26.8 plots one may spot some pattern. Namely, by expanding down the high response curves seen in Fig. 26.7 at certain moment they merge with low response ones and contribute to just one continuous line including both stable and unstable solutions as seen in Fig. 26.8. It should be noted this comment refers both to the blades and to hub response curves.

26.4 Conclusions

The analysed model of the rotor with piezo-beams has demonstrated the resonance softening effect due to nonlinearity in constitutive relation of the piezoceramic material. This phenomenon has been observed either for the beams or the hub response. Due to the perfect symmetry of the structure motion of all the beam has been identical and fully synchronised. In the following analysis the rotor has been mistuned by replacing two blades by the similar ones but featuring linear properties. Interestingly, the nonlinear softening phenomenon has been observed too, but not only for the nonlinear bean but for linear ones as well. This behaviour has been caused by internal coupling in the system through the hub substructure oscillations. Another spotted phenomenon is the hub vibration absorption. For the excitation frequency equal to the natural frequency of an isolated cantilever beam the oscillations have been localised in beams motion with close to zero vibrations of the hub.

Acknowledgements The work is financially supported by grant 2016/23/B/ST8/01865 from the National Science Centre, Poland.

References

1. Friswell, M.O., Penny, J.E.T., Garvey, S.D., Lees, A.W.: Dynamics of Rotating Machines. Cambridge University Press, Cambridge (2010)
2. Subbiah, R., Littleton, J.E.: Rotor and Structural Dynamics of Turbomachinery. Springer, Berlin (2018)
3. Chopra, I., Sirohi, J.: Smart Structures Theory. Cambridge University Press, New York (2013)
4. Joshi, S.P.: Non-linear constitutive relations for piezoceramic materials. Smart Mater. Struct. **1**, 80–83 (1992)
5. Guyomar, D., Aurelle, N., Eyraud, L.: Piezoelectric ceramics nonlinear behavior. Application to Langevin transducer. J. Phys. **III**(7), 1197–1208 (1997)
6. Tan, D., Yavarow, P., Erturk, A.: Nonlinear elastodynamics of piezoelectric macro-fiber composites with interdigitated electrodes for resonant actuation. Compos. Struct. **187**, 137–143 (2018)
7. Thornburgh, R., Chattopadhyay, A., Ghoshal, A.: Transient vibration of smart structures using a coupled piezoelectricmechanical theory. J. Sound Vib. **274**(1–2), 53–72 (2004)
8. Latalski, J.: A coupled-field model of a rotating composite beam with an integrated nonlinear piezoelectric active element. Nonlinear Dynam. **90**(3), 2145–2162 (2017)

9. Warminski, J., Latalski, J., Szmit, Z.: Vibration of a mistuned three-bladed rotor under regular and chaotic excitations. J. Theor. App. Mech-Pol. **56**(2), 549–566 (2018)
10. Latalski, J., Warminski, J., Rega, G.: Bending-twisting vibrations of a rotating hub-thin-walled composite beam system. Math. Mech. Solids **22**(6), 1303–1325 (2017)
11. Londoño, J.M., Cooper, J.E., Neild, S.A.: Identification of systems containing nonlinear stiffnesses using backbone curves. Mech. Syst. Signal Pr. **84**, 116–135 (2017)

Chapter 27
Nonlinear Analysis of Hunting Motion by Focusing on Non-selfadjointness

Weiyan Wei and Hiroshi Yabuno

Abstract When the running speed of railway vehicles exceeds critical limits, they begin to suffer from hunting motion that can affect ride comfort and threaten their safety. Even below such critical speeds, which can be obtained by linear analysis, such vehicles can experience hunting motions because their wheel systems have nonlinear characteristics. In this study, by taking into consideration the non-selfadjointness of such systems, we derive the normal form of the equation of motion for a single wheel set under the relevant cubic and quintic nonlinearities. Equations for the different orders that arise due to those nonlinearities are then derived from an original equation using a method of multiple scales, and an adjoint linear operator is used to obtain the equation governing the dynamics with a slower timescale. Additionally, a normal form with two unknown coefficients was obtained, after which we identify the nonlinear coefficients of the normal form using the experimental method proposed in our previous research. We also obtain a subcritical Hopf bifurcation diagram from the normal form, the theoretical results of which agree well with our experimental results.

Keywords Hunting motion · Quintic nonlinearity · Non-selfadjointness · Single wheel set

27.1 Introduction

For more than a century, the stability of railway vehicles has been studied as part of efforts to improve ride comfort, minimize damage to vehicle wheels, and reduce derailment risks [1]. It is well known that railway vehicles become unstable and

W. Wei (✉) · H. Yabuno
University of Tsukuba, Tsukuba, Ibaraki, Japan
e-mail: 455066951wwy@gmail.com

H. Yabuno
e-mail: yabuno@esys.tsukuba.ac.jp

I. Kovacic and S. Lenci (eds.), *IUTAM Symposium on Exploiting Nonlinear Dynamics for Engineering Systems*, IUTAM Bookseries 37,
https://doi.org/10.1007/978-3-030-23692-2_27

undergo hunting motions when their running speeds exceed critical limits [2]. These hunting motions are a kind of flutter-type self-excited oscillation that results from the development of creep force between the wheels and the track [3].

Recently, nonlinear analysis has revealed that Hopf bifurcations are produced at those critical speeds. However, even below such speeds, railway vehicles can produce hunting motion depending on the magnitude of disturbance they experience [4–6]. This phenomenon is due to the subcritical Hopf bifurcation caused by the softening cubic nonlinearity. In the subcritical Hopf bifurcation, the critical speed of the hunting motion is called the linear critical speed. The other critical speed in the subcritical Hopf bifurcation, which is slower than the linear critical speed, is called the nonlinear critical speed.

Within the range that exists between these two critical speed types, there are stable and unstable nontrivial steady states that coexist with the stable trivial steady state [7]. This means that a disturbance whose magnitude is larger than the unstable steady-state amplitude can cause the hunting motion, even if the running speed is less than the linear critical speed. If only the cubic nonlinear terms are considered in a theoretical analysis, we will be unable to discern a stable nontrivial steady state within the range between the above-mentioned two critical speed types. Thus, in order to investigate the steady-state amplitude of hunting motion when the running speed is less than the linear critical speed, it is important to consider quintic nonlinearity.

There have been a number of previous numerical studies that considered the nonlinear characteristics of hunting motion under cubic and quintic terms [8–10]. However, there are very few analytical methods for qualitatively investigating the nonlinear phenomena of hunting motions. Therefore, in this study, by focusing on non-selfadjointness and obtaining the normal form of steady-state amplitude, we devise an analytical method that will allow us to investigate the essential characteristics of bifurcation phenomena.

This method works as follows. First, by introducing the method of multiple scales [11], we derive the equations of different orders from the original equations of motion. Next, we define an adjoint linear operator to obtain the equation governing the dynamics with a slow timescale. Then, we obtain the normal form [12] of the steady-state amplitude. As a result, by considering the cubic and quintic terms in the original equations, the nonlinear characteristics of the subcritical elements can be obtained. Furthermore, by using the experimental identification method proposed in our previous research, the nonlinear coefficients of the normal form can be identified. A comparison of the theoretically and experimentally obtained bifurcation diagrams verifies the validity of the analytical method proposed in this study.

27.2 Theoretical Analysis of Nonlinear Characteristics of Hunting Motion

27.2.1 Equations of Motion of a Single Wheel Set

In this study, we consider a suspended single wheel set that can freely move in the lateral and yaw directions, y and ψ, while traveling on a track. The mathematical model of this single wheel set is shown in Fig. 27.1, where r_0, k_x, γ_0, d_0, d_1, and v are the centered wheel rolling radius, the x direction stiffness, the wheel tread angle, the half-track gauge, the half-gap of stiffness, and the running speed, respectively. The dimensionless equations governing the lateral and yaw motions are expressed as follows [13].

$$\begin{aligned} \ddot{y}^* + \frac{d'_{11}}{v^*}\dot{y}^* + k_{11}y^* + k_{12}\psi + \beta_3 y^{*3} + \beta_5 y^{*5} &= 0, \\ \ddot{\psi} + \frac{d'_{22}}{v^*}\dot{\psi} + k_{21}y^* + k_{22}\psi &= 0, \end{aligned} \tag{27.1}$$

where the half-track gauge d_0 is used as the representative length and the inverse value of the linear natural frequency of the yaw motion ω_ψ is used as the representative time. In these original equations of motion, most of the nonlinearity is caused by the stiffness and structure of the wheels. However, the values of the nonlinear terms and their coefficients are not clear. Accordingly, we use the cubic and quintic nonlinear terms with two unknown coefficients, β_3 and β_5, to express the nonlinearity and show that they are sufficient for obtaining the nonlinear characteristics of hunting motion. According to the results shown in this paper, the coefficients of the nonlinear terms in the theoretically obtained normal form can be expressed by the linear parameters r_0, k_x, …, d_1, and the nonlinear coefficients in the original equations. We assume that the value of the coefficients in the normal form, from which the cubic and quintic nonlinear terms are chosen in the original equations, are constant and independent. Therefore, β_3 and β_5 in Eq. (27.1) are the unknown coefficients of the cubic and quintic nonlinear terms chosen to express the nonlinearity of the wheel system.

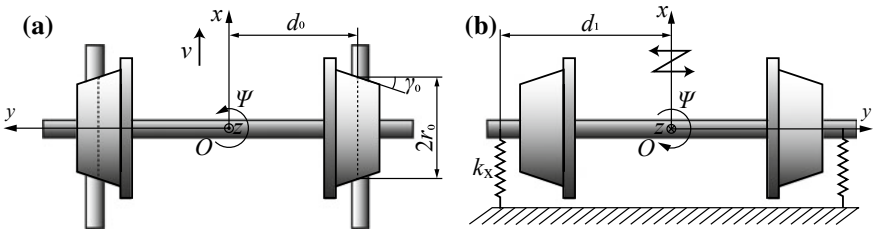

Fig. 27.1 Configuration of the single wheel set and the rails: **a** top view, **b** bottom view (the suspensions from the truck)

The other dimensionless coefficients of the above equations are expressed by the dimensional parameters as

$$d'_{11} = \frac{2\kappa_{yy}}{md_0\omega_\psi^2}, d'_{22} = \frac{\kappa_{xx}d_0}{k_x d_1^2}, k_{11} = \frac{\omega_y^2}{\omega_\psi^2}, k_{12} = \frac{-2\kappa_{yy}}{md_0\omega_\psi^2},$$
$$k_{21} = \frac{d_0^2\kappa_{xx}\gamma_0}{k_x d_1^2 r_0}, k_{22} = 1, \beta_3 = \varepsilon\hat{\beta}_3, \beta_5 = \varepsilon^2\hat{\beta}_5, \tag{27.2}$$

where κ_{xx} and κ_{yy} are the creep coefficients in the x and y directions, respectively [14], and ε is a small dimensionless parameter ($|\varepsilon| << 1$). We transform Eq. (27.1) into a matrix equation as

$$\ddot{\boldsymbol{x}} + \boldsymbol{C}\dot{\boldsymbol{x}} + \boldsymbol{K}\boldsymbol{x} + \boldsymbol{N}(\boldsymbol{x}) = 0, \tag{27.3}$$

where

$$\boldsymbol{x} = \begin{bmatrix} y^* \\ \psi \end{bmatrix}, \boldsymbol{C} = \begin{bmatrix} \dfrac{d'_{11}}{v^*} & 0 \\ 0 & \dfrac{d'_{22}}{v^*} \end{bmatrix}, \boldsymbol{K} = \begin{bmatrix} k_{11} & k_{12} \\ k_{21} & k_{22} \end{bmatrix}. \tag{27.4}$$

In the next section, we study the nonlinear characteristics of hunting motion by theoretically analyzing the vicinity of the linear critical speed.

27.2.2 Orders Analysis with Method of Multiple Scales

In order to investigate the nonlinear characteristics of hunting motion near the linear critical speed, we set

$$v^* = v_c^*(1 + \Delta v) = v_c^*(1 + \varepsilon\Delta\hat{v}), \tag{27.5}$$

where v_c^* is the dimensionless linear critical speed. Then, matrix $\boldsymbol{C}$ can be expressed as

$$\boldsymbol{C} = \frac{\boldsymbol{C}_c}{(1 + \varepsilon\Delta\hat{v})} \approx \boldsymbol{C}_c(1 - \varepsilon\Delta\hat{v} + \varepsilon^2\Delta\hat{v}^2), \tag{27.6}$$

where

$$\boldsymbol{C}_c = \begin{bmatrix} d_{11} & 0 \\ 0 & d_{22} \end{bmatrix}, d_{11} = \frac{d'_{11}}{v_c^*}, d_{22} = \frac{d'_{22}}{v_c^*}. \tag{27.7}$$

The amplitude of $\boldsymbol{x}$ is changed near the linear critical speed. However, this amplitude change is slower than the phase change of $\boldsymbol{x}$. Therefore, the amplitude and phase changes cannot be expressed by a single time scale. Accordingly, we introduce multiple time scales in order to express the amplitude changes that result due to the cubic

and quintic nonlinearities. These multiple time scales are expressed as

$$t_0 = t, t_1 = \varepsilon t, t_2 = \varepsilon^2 t. \tag{27.8}$$

Then, the time derivatives are expressed as follows:

$$\frac{d}{dt} = D_0 + \varepsilon D_1 + \varepsilon^2 D_2, \tag{27.9}$$

$$\frac{d^2}{dt^2} = D_0^2 + 2\varepsilon D_1 D_0 + 2\varepsilon^2 D_2 D_0 + \varepsilon^2 D_1^2, \tag{27.10}$$

where

$$D_0 = \frac{\partial}{\partial t_0}, D_1 = \frac{\partial}{\partial t_1}, D_2 = \frac{\partial}{\partial t_2}. \tag{27.11}$$

We use the small dimensionless parameter ε to express the uniform asymptotic expansion of $\boldsymbol{x}$ as

$$\boldsymbol{x} = \boldsymbol{x}_0 + \varepsilon \boldsymbol{x}_1 + \varepsilon^2 \boldsymbol{x}_2. \tag{27.12}$$

In addition, $\boldsymbol{x}_0$ is assumed as

$$\boldsymbol{x}_0 = a(t_1, t_2) e^{\lambda_0 t_0} \begin{bmatrix} y_0 \\ \psi_0 \end{bmatrix} = a e^{\lambda_0 t_0} \boldsymbol{\Phi_0}, \tag{27.13}$$

where λ_0 is the eigenvalue of the linear part in Eq. (27.3), $\boldsymbol{\Phi}_0$ is the eigenvector of λ_0, $a(t_1, t_2)$ is the amplitude of mode $\boldsymbol{\Phi}_0$ and with respect to the slow time scales t_1 and t_2. We find that substituting Eq. (27.12) into Eq. (27.3), and equating the coefficients of the like powers of ε yields the following equations for linear part $O(\varepsilon^0)$, cubic nonlinear part $O(\varepsilon^1)$ and quintic nonlinear part $O(\varepsilon^2)$

$$O(\varepsilon^0) : D_0^2 \boldsymbol{x}_0 + \boldsymbol{C}_c D_0 \boldsymbol{x}_0 + \boldsymbol{K} \boldsymbol{x}_0 = 0, \tag{27.14}$$

$$O(\varepsilon^1) : D_0^2 \boldsymbol{x}_1 + \boldsymbol{C}_c D_0 \boldsymbol{x}_1 + \boldsymbol{K} \boldsymbol{x}_1 = -2 D_1 D_0 \boldsymbol{x}_0 - \boldsymbol{C}_c D_1 \boldsymbol{x}_0 + \boldsymbol{C}_c \Delta \hat{v} D_0 \boldsymbol{x}_0 - \hat{\beta}_3 (a e^{\lambda_0 t_0} + \bar{a} e^{\bar{\lambda}_0 t_0})^3 \begin{bmatrix} 1 \\ 0 \end{bmatrix}, \tag{27.15}$$

$$O(\varepsilon^2) : D_0^2 \boldsymbol{x}_2 + \boldsymbol{C}_c D_0 \boldsymbol{x}_2 + \boldsymbol{K} \boldsymbol{x}_2 = -2 D_2 D_0 \boldsymbol{x}_0 - \boldsymbol{C}_c D_2 \boldsymbol{x}_0 + \boldsymbol{C}_c \Delta \hat{v} D_1 \boldsymbol{x}_0 - D_1^2 \boldsymbol{x}_0 - \boldsymbol{C}_c \Delta \hat{v}^2 D_0 \boldsymbol{x}_0 - 10 \hat{\beta}_5 |a|^4 a |y_0|^4 y_0 e^{i\omega t_0} \begin{bmatrix} 1 \\ 0 \end{bmatrix} + \cdots, \tag{27.16}$$

and the linear part can be rewritten as

$$O(\varepsilon^0) : \boldsymbol{L} \boldsymbol{\Phi}_0 a = 0, \tag{27.17}$$

where

$$\boldsymbol{L} = \lambda_0^2 \boldsymbol{I} + \lambda_0 \boldsymbol{C}_c + \boldsymbol{K} = \begin{bmatrix} \lambda_0^2 + d_{11}\lambda_0 + k_{11} & k_{12} \\ k_{21} & \lambda_0^2 + d_{22}\lambda_0 + k_{22} \end{bmatrix}. \tag{27.18}$$

We obtain λ_0 by considering $|\boldsymbol{L}| = 0$ as

$$\lambda_0^4 + (d_{11} + d_{22})\lambda_0^3 + (d_{11}d_{22} + k_{11} + k_{22})\lambda_0^2 + (d_{11}k_{22} + d_{22}k_{11})\lambda_0 + k_{11}k_{22} - k_{12}k_{21} = 0. \tag{27.19}$$

When the running speed reaches the linear critical speed of the hunting motion, the matrix $\boldsymbol{L}$ has four eigenvalues: a pair of pure imaginary eigenvalues $\pm i\omega$ and one complex conjugate pair of eigenvalues $\lambda_r \pm i\lambda_i$. Substituting $\lambda_0 = \pm i\omega$ into Eq. (27.19) and separating the result into real and imaginary parts

$$Re : \omega^4 - (d_{11}d_{22} + k_{11} + k_{22})\omega^2 + k_{11}k_{22} - k_{12}k_{21} = 0, \tag{27.20}$$

$$Im : -(d_{11} + d_{22})\omega^3 + (d_{11}k_{22} + d_{22}k_{11})\omega = 0, \tag{27.21}$$

yields the dimensionless linear critical speed and eigenvalue ω as follows:

$$v_c^* = \sqrt{\frac{d'_{11}d'_{22}\omega^2}{\omega^4 + k_{11}k_{22} - k_{12}k_{21} - (k_{11} + k_{22})\omega^2}}, \tag{27.22}$$

$$\omega = \sqrt{\frac{d_{11}k_{22} + d_{22}k_{11}}{d_{11} + d_{22}}}. \tag{27.23}$$

In addition, the equation of the four eigenvalues can be expressed as

$$(\lambda_0^2 + \omega^2)(\lambda_0 - \lambda_r - i\lambda_i)(\lambda_0 - \lambda_r + i\lambda_i) = 0. \tag{27.24}$$

Equating with Eq. (27.19) to obtain the real part of the complex conjugate pair of eigenvalues as follows:

$$\lambda_r = -\frac{1}{2}(d_{11} + d_{22}) < 0. \tag{27.25}$$

Therefore, we can only focus on the mode with the eigenvalues $\pm i\omega$ because the other mode has the complex conjugate pair of eigenvalues with a negative real part. The eigenvector for $i\omega$ can be obtained as

$$\boldsymbol{\Phi}_0 = \begin{bmatrix} k_{12} \\ \omega^2 - k_{11} - id_{11}\omega \end{bmatrix}. \tag{27.26}$$

Substituting $\lambda_0 = i\omega$ into Eq. (27.15) yields the equation for cubic nonlinear part $O(\varepsilon^1)$ as

$$D_0^2\boldsymbol{x}_1 + \boldsymbol{C}_c D_0\boldsymbol{x}_1 + \boldsymbol{K}\boldsymbol{x}_1 = [(-2i\omega\boldsymbol{I} - \boldsymbol{C}_c)D_1 a + i\omega\Delta\hat{v}a\boldsymbol{C}_c]\begin{bmatrix} y_0 \\ \psi_0 \end{bmatrix} e^{i\omega t_0}$$
$$- 3\hat{\beta}_3|a|^2 a|y_0|^2 y_0 \begin{bmatrix} 1 \\ 0 \end{bmatrix} e^{i\omega t_0} - \hat{\beta}_3 a^3 y_0^3 e^{3i\omega t_0}\begin{bmatrix} 1 \\ 0 \end{bmatrix} + c.c. \tag{27.27}$$

In the next section, we derive the equation governing the dynamics with t_1 from the solvability condition of $\boldsymbol{\Phi}_1$, which is the mode of $\boldsymbol{x}_1$.

27.2.3 Nonlinear Analysis Using an Adjoint Linear Operator

We consider an adjoint linear operator $\bar{\boldsymbol{L}}^T$ of the non-selfadjointness matrix $\boldsymbol{L}$, and define a vector $\tilde{\boldsymbol{\Phi}}_0$ associated with ω_0 to satisfy

$$\bar{\boldsymbol{L}}^T\tilde{\boldsymbol{\Phi}}_0 = \bar{\tilde{\boldsymbol{\Phi}}}_0^T\boldsymbol{L} = 0, \tag{27.28}$$

yields the vector $\tilde{\boldsymbol{\Phi}}_0$ as

$$\tilde{\boldsymbol{\Phi}}_0 = \begin{bmatrix} \omega^2 - k_{22} + id_{22}\omega \\ k_{12} \end{bmatrix}. \tag{27.29}$$

Multiplying both sides of Eq. (27.27) by $\tilde{\boldsymbol{\Phi}}_0$ from the left side and picking up the terms including $e^{i\omega t_0}$ yields the equation that is, with respect to the timescale t_1, written as

$$\bar{\tilde{\boldsymbol{\Phi}}}_0^T\left\{[(-2i\omega\boldsymbol{I} - \boldsymbol{C}_c)D_1 a + i\omega\Delta\hat{v}a\boldsymbol{C}_c]\begin{bmatrix} y_0 \\ \psi_0 \end{bmatrix} - 3\hat{\beta}_3|a|^2 a|y_0|^2 y_0\begin{bmatrix} 1 \\ 0 \end{bmatrix}\right\} e^{i\omega t_0} = 0, \tag{27.30}$$

or

$$D_1 a = -\frac{Q}{P}\Delta\hat{v}a - \frac{R}{P}\hat{\beta}_3|a|^2 a, \tag{27.31}$$

where

$$P = a_r + a_i i,\ a_r = -2k_{12}(d_{11}k_{22} + d_{22}k_{11}),\ a_i = -2\omega k_{12}(2\omega^2 - k_{11} - k_{22} - d_{11}d_{22}),$$
$$Q = b_r + b_i i,\ b_r = 2k_{12}\omega^2 d_{11}d_{22},\ b_i = 0,$$
$$R = c_r + c_i i,\ c_r = |y_0|^2 y_0(k_{22} - \omega^2),\ c_i = |y_0|^2 y_0 d_{22}\omega. \tag{27.32}$$

The partial derivative of amplitude a with respect to t_1 effected by the cubic nonlinearities is obtained.

Next, we obtain the particular solution $\boldsymbol{x}_1$ by setting

$$\boldsymbol{x}_1 = \begin{bmatrix} y_1 \\ \psi_1 \end{bmatrix} e^{3i\omega t_0}. \tag{27.33}$$

Substituting Eq. (27.33) into Eq. (27.27) to pick up the terms including $e^{3i\omega t_0}$ as

$$D_0^2\boldsymbol{x}_1 + \boldsymbol{C}_c D_0\boldsymbol{x}_1 + \boldsymbol{K}\boldsymbol{x}_1 = -\hat{\beta}_3 a^3 y_0^3 e^{3i\omega t_0}\begin{bmatrix}1\\0\end{bmatrix} + c.c. \tag{27.34}$$

The particular solution $\boldsymbol{x}_1$ is

$$\boldsymbol{x}_1 = \frac{\hat{\alpha}_3 a^3 y_0^3 k_{12}}{64\omega^4 k_{12} - 4\omega a_i + 12i\omega a_r}\begin{bmatrix}9\omega^2 - k_{22} - 3i\omega d_{22}\\ k_{21}\end{bmatrix} e^{3i\omega t_0}. \tag{27.35}$$

Then, substituting Eq. (27.35) into Eq. (27.16) yields the following equation for the quintic nonlinear part $O(\varepsilon^2)$ as

$$\begin{aligned} D_0^2\boldsymbol{x}_2 + \boldsymbol{C}_c D_0\boldsymbol{x}_2 + \boldsymbol{K}\boldsymbol{x}_2 =& -2D_2 D_0\boldsymbol{x}_0 - \boldsymbol{C}_c D_2\boldsymbol{x}_0 + \boldsymbol{C}_c\Delta\hat{v} D_1\boldsymbol{x}_0 - D_1^2\boldsymbol{x}_0 - \boldsymbol{C}_c\Delta\hat{v}^2 D_0\boldsymbol{x}_0 \\ &+ (-10\hat{\beta}_5|a|^4 a|y_0|^4 y_0 - 3\hat{\beta}_3\bar{a}^2\bar{y}_0^2 y_1)e^{i\omega t_0}\begin{bmatrix}1\\0\end{bmatrix} \\ &- 2D_1 D_0\boldsymbol{x}_1 - \boldsymbol{C}_c D_1\boldsymbol{x}_1 + \boldsymbol{C}_c\Delta\hat{v} D_0\boldsymbol{x}_1 + \{\cdots\}e^{3i\omega t_0} \\ &+ \{\cdots\}e^{5i\omega t_0} + c.c. \end{aligned} \tag{27.36}$$

Multiplying both sides of Eq. (27.36) by $\tilde{\bar{\boldsymbol{\Phi}}}_0$ from the left hand and picking up the terms including $e^{i\omega t_0}$ yields the equation that is, with respect to time scale t_2, written as

$$\begin{aligned} \tilde{\bar{\boldsymbol{\Phi}}}_0^T\{[(-2i\omega\boldsymbol{I} - \boldsymbol{C}_c)D_2 a + \Delta\hat{v} D_1 a\boldsymbol{C}_c - D_1^2 a - i\omega\Delta\hat{v}^2\boldsymbol{C}_c]\begin{bmatrix}y_0\\ \psi_0\end{bmatrix} \\ - (10\hat{\beta}_5|a|^4 a|y_0|^4 y_0 + 3\hat{\beta}_3\bar{a}^2\bar{y}_0^2 y_1)\begin{bmatrix}1\\0\end{bmatrix}\}e^{i\omega t_0} = 0, \end{aligned} \tag{27.37}$$

where $D_1^2 a$ is expressed from Eq. (27.31) as

$$\begin{aligned} D_1^2 a &= -\frac{Q}{P}\Delta\hat{v} D_1 a - \frac{R}{P}\hat{\beta}_3(2|a|^2 D_1 a + a^2 D_1\bar{a}) \\ &= \frac{Q^2}{P^2}\Delta\hat{v}^2 a + (\frac{3QR}{P^2} + \frac{R\bar{Q}}{|P|^2})\hat{\beta}_3\Delta\hat{v}|a|^2 a + (\frac{2R^2}{P^2} + \frac{|R|^2}{|P|^2})\hat{\beta}_3^2|a|^4 a. \end{aligned} \tag{27.38}$$

Substituting $D_1^2 a$ into Eq. (27.37) yields $D_2 a$ as

$$D_2 a = -\frac{H}{P}\Delta\hat{v}^2 a - \frac{G}{P}\hat{\beta}_3\Delta\hat{v}|a|^2 a - (\frac{M}{P}\hat{\beta}_3^2 + \frac{N}{P}\hat{\beta}_5)|a|^4 a, \tag{27.39}$$

where

$$H = -\frac{ib_r Q}{\omega P} + \frac{(\omega a_i - b_r)Q^2}{2\omega^2 P^2} - \frac{ia_r Q^2}{2\omega P^2} + b_r,$$

$$G = -\frac{ib_r R}{\omega P} + (\frac{\omega a_i - b_r}{2\omega^2} - \frac{ia_r}{2\omega})(\frac{3QR}{P^2} + \frac{R\bar{Q}}{|P|^2}),$$
$$M = (\frac{\omega a_i - b_r}{2\omega^2} - \frac{ia_r}{2\omega})(\frac{2R^2}{P^2} + \frac{|R|^2}{|P|^2}) + \frac{3(-8\omega^2 y_0^3 + c_r + 3ic_i)R}{64\omega^4 k_{12} - 4\omega a_i + 12i\omega a_r},$$
$$N = 10y_0^2 R. \tag{27.40}$$

As a result, the partial derivative of a with respect to t_1 and t_2 are obtained. In the next section, we derive the normal form of the amplitude $a(t_1, t_2)$.

27.2.4 Normal Form Governing Nonlinear Hunting Motion

The steady-state amplitude $a(t_1, t_2)$ can be expressed in a polar form as

$$a = \frac{1}{2}\alpha(t_1, t_2)e^{i\phi(t_1,t_2)}, \tag{27.41}$$

Therefore, we can express Da as

$$Da = \frac{1}{2}(D\alpha + i\alpha D\phi)e^{i\phi}. \tag{27.42}$$

Considering Eqs. (27.9) and (27.41), Da can be also expressed as

$$\begin{aligned} Da =& \varepsilon D_1 a + \varepsilon^2 D_2 a \\ =& \frac{1}{2}[-(\frac{H}{P}\Delta v + \frac{Q}{P})\Delta v - \frac{1}{4}(\frac{G}{P}\Delta v + \frac{R}{P})\beta_3\alpha^2 - \frac{1}{16}(\frac{M}{P}\beta_3^2 + \frac{N}{P}\beta_5)\alpha^4]\alpha e^{i\phi}. \end{aligned} \tag{27.43}$$

Equating the real part of Eqs. (27.42) and (27.43), we can obtain the normal form of the amplitude of $\boldsymbol{x}$ as

$$D\alpha = -(L_1\Delta v + L_2\Delta v^2 + N_1\alpha^2 + N_2\Delta v\alpha^2 + N_3\alpha^4)\alpha, \tag{27.44}$$

where

$$L_1 = Re[\frac{Q}{P}], L_2 = Re[\frac{H}{P}], N_1 = \frac{1}{4}Re[\frac{R}{P}]\beta_3,$$
$$N_2 = \frac{1}{4}Re[\frac{G}{P}]\beta_3, N_3 = \frac{1}{16}Re[\frac{M}{P}\beta_3^2 + \frac{N}{P}\beta_5]. \tag{27.45}$$

The trivial steady-state amplitude can be expressed as

$$\alpha_{st} = 0, \tag{27.46}$$

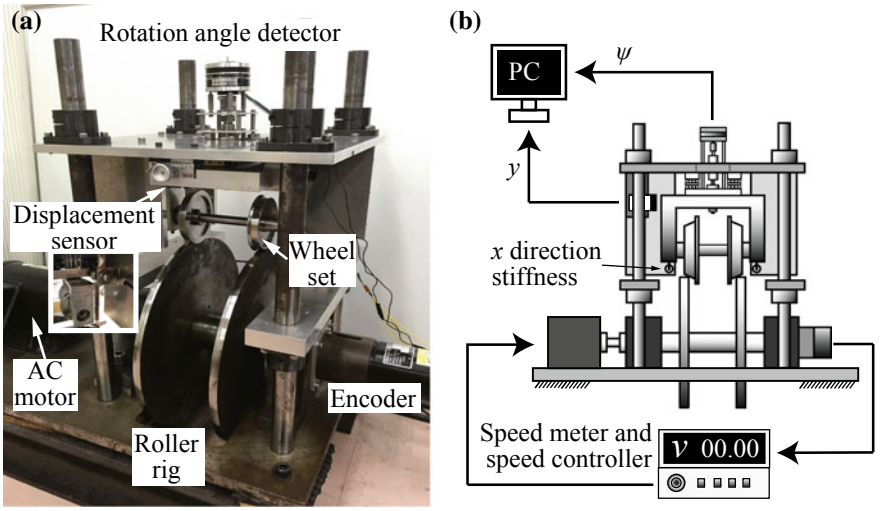

Fig. 27.2 Experimental setup: **a** photo of wheel set and roller rig, **b** mode diagram of total experimental devices

and the nontrivial steady-state amplitude can be obtained from the equation as follows:

$$L_1\Delta v + L_2\Delta v^2 + N_1\alpha_{st}^2 + N_2\Delta v\alpha_{st}^2 + N_3\alpha_{st}^4 = 0. \tag{27.47}$$

In the next section, we experimentally identify the coefficients of Eq. (27.47) for the experiment using a roller rig and a single wheel set.

27.3 Experimental Identification of Nonlinear Coefficients

27.3.1 Experimental Setup

We used a roller rig and a single wheel set to simulate the mathematical model that was considered in the previous theoretical analysis, as shown in Fig. 27.2. We placed the wheel set on the roller rig to simulate straight-line travel on a railway. The dimensional parameters of the experimental setup are: the mass of the wheel set m = 2.18 kg, the half-track gauge d_0 = 0.049 m, the half-gap of stiffness d_1 = 0.085 m, the centered wheel rolling radius r_0 = 0.036 m, the equilibrium state spring length l = 0.06 m, the natural spring length l_0 = 0.035 m, the wheel tread angle γ_0 = 0.04, the x direction stiffness k_x = 200 N/m, the moment of inertia I = 0.004 kg, the lateral natural frequency ω_y = 8.75 rad/s, and the yaw natural frequency ω_ψ = 25.9 rad/s.

27.3.2 Experimentally Observed Steady-State Amplitude

We observed the time histories of lateral and yaw directions of the wheel set at different running speeds in order to obtain the stable steady-state amplitude. In our experiments, fluctuation noise was produced from the surface roughness of the roller rig and wheels, and the running speed was controlled slowly to prevent artificial noise. In this situation, the linear critical speed of the hunting motion obtained from the experiment corresponds to that obtained from the linear theory.

Figure 27.3a is a subcritical Hopf bifurcation diagram obtained from a numerical simulation and shows the amplitude changes caused by running speed variations. The numbered arrows describe the progression of steps in our experiment. First, we increase the running speed at Point B to begin the hunting motion, which is called the Hopf bifurcation point and the speed of which is the linear critical speed. Once the running speed exceeds this speed, the amplitude increases abruptly as shown by Arrow (2). Next, the amplitude changes as the running speed decrease, as seen at Arrows (3) and (4). At Point A, which is called the saddle-node bifurcation point and is the nonlinear critical speed, the amplitude decreases abruptly as the running speed decreases.

In this experiment, we focus solely on the lateral motion because the yaw direction oscillation is similar to the lateral one. The experimentally observed steady-state amplitude at different running speeds is shown in Fig. 27.3b. Because the oscillation amplitude is not constant due to the experimental surface roughness of the roller rig, the component in the power spectrum diagram varies with time. Therefore, we regard the average value of the maximum oscillation amplitude as the steady-state amplitude. The reason why the amplitude corresponding to the lower branch in Fig. 27.3b is not zero is as follows. The time histories of the lateral displacement are translated into power spectrum diagrams. In the power spectrum diagrams, there is a small component with a frequency that changes with the wheel set running speed variations. This frequency is equal to the rotational speed frequency of the roller rig and the magnitude of the component is approximately equal to the magnitude of vibration seen before the linear critical speed in experiments. Therefore, the amplitude corresponding to the lower branch in Fig. 27.3b is due to the roller rig roughness. As a result, the linear critical speed is 7.5 m/s and the nonlinear critical speed is 6.5 m/s.

In the next section, we use the experimentally observed amplitudes at the linear and nonlinear critical speeds to identify the nonlinear coefficients of the theoretically obtained normal form.

27.3.3 Identification of Nonlinear Coefficients

First, we use the dimensional parameters of the experimental setup to obtain the dimensionless parameters as follows:

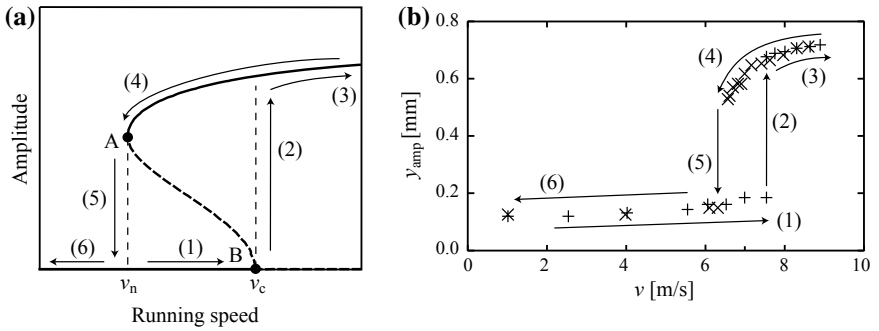

Fig. 27.3 Steady-state amplitude of the lateral displacement: **a** numerical simulation diagram, the solid and the dashed lines denote the stable and unstable steady states, respectively; **b** experimentally observed diagram, + and × denote the observed amplitude as increasing and decreasing running speed, respectively

$$v_c^* = 6, d_{11} = 0.3, d_{22} = 0.44, k_{11} = 0.11, k_{12} = -1.77, k_{21} = 0.14, k_{22} = 1,$$
$$P = 1.23 - 0.74i, Q = -0.22, R = -2.94 - 1.68i, H = -0.4 - 0.058i,$$
$$G = 1.7 - 1.0i, M = 14.4 + 1.88i, N = -92.1 - 52.63i. \tag{27.48}$$

The nontrivial steady state of α can be obtained as

$$\alpha_{st}^2 = \frac{-(0.34\Delta v - 0.29)\beta_3}{2(0.5\beta_3^2 - 2.26\beta_5)} \pm \frac{\sqrt{(0.34\Delta v - 0.29)^2\beta_3^2 + 4(-0.22\Delta v - 0.13)\Delta v(0.5\beta_3^2 - 2.26\beta_5)}}{2(0.5\beta_3^2 - 2.26\beta_5)}. \tag{27.49}$$

The relationship between the dimensional amplitude y_{st} and the dimensionless amplitude α_{st} can be expressed as

$$y_{st} = d_0 y_{st}^* = |d_0 k_{12} \alpha_{st}|. \tag{27.50}$$

We substitute the steady-state amplitudes $y_{st1} = 0.00067$ m and $y_{st2} = 0.00053$ m at linear and nonlinear critical speeds, i.e., $\Delta v_1 = 0$ and $\Delta v_2 = -0.13$, into Eq. (27.49) in order to obtain the nonlinear coefficients β_3 and β_5 as

$$\beta_3 = 2240, \beta_5 = -3.6 \times 10^6. \tag{27.51}$$

Therefore, Eq. (27.44) is rewritten as

$$D\alpha = (0.13 + 0.22\Delta v)\Delta v\alpha + (0.29 - 0.34\Delta v)\beta_3\alpha^3 + (-0.5\beta_3^2 + 2.26\beta_5)\alpha^5, \tag{27.52}$$

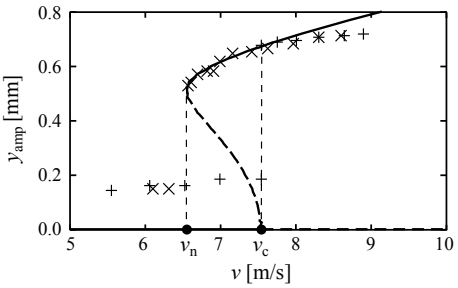

Fig. 27.4 Comparison of theoretical and experimental results for the steady-state amplitude of the lateral displacement for the single wheel set. The solid and dashed lines denote the theoretically obtained stable and unstable steady states, respectively. The plots show the stable steady-state amplitudes directly obtained from the experiment

where the first term $(0.13 + 0.22\Delta v)\Delta v\alpha$ is the linear term, the second term $(0.29 - 0.34\Delta v)\beta_3\alpha^3$ is cubic nonlinear term, and the third term $(-0.5\beta_3^2 + 2.26\beta_5)\alpha^5$ is the quintic nonlinear term. In addition, we checked the balance of each term in the normal form by substituting the value of Δv and the experimental amplitude at the nonlinear critical speed. The values of the linear, cubic, and quintic nonlinear terms are -0.013, 0.029, and -0.016, respectively. These values indicate that the terms are balanced.

The bifurcation diagram of the wheel set lateral displacement is obtained as Fig. 27.4. In our experimental results, surface roughness prevented us from obtaining zero amplitude below the nonlinear critical speed, but the Hopf and saddle-node bifurcations were experimentally and theoretically obtained in this study. In this study, only two experimental amplitudes are used for the identification of nonlinear coefficients in the normal form and the nontrivial steady state is very close to the experimental steady state. This confirms that the normal form with cubic and quintic normal nonlinearities can capture the nonlinear characteristics of hunting motion, not only qualitatively but also quantitatively.

27.4 Conclusions

In this study, using a single wheel set model, hunting motions were investigated by taking into account cubic and quintic nonlinearities. By considering the non-selfadjointness of the governing equations, the solvability conditions needed to express the variation of the response amplitude with a slow time scale were obtained. Furthermore, the normal form of the steady-state amplitude was derived using the solvability conditions. The nonlinear coefficients of the normal form were identified using two value of experimentally observed amplitudes. From the results obtained, the existence of the Hopf and saddle-node bifurcations could be theoretically

indicated. By comparing the theoretically and experimentally obtained bifurcation diagrams, it was shown that the normal form obtained from the experimental data at the linear and nonlinear critical speeds captures the nonlinear characteristics of steady state amplitude that depends on the running speed, i.e., the experimentally obtained bifurcation diagram.

References

1. Knothe, K., Bohm, F.: History of stability of railway and road vehicles. Veh. Syst. Dyn. **31**, 283–323 (1999)
2. Fujii, S., Yoshimoto, K., Kobayashi, F.: An analysis of the lateral hunting motion of a two-axle railway wagon by digital simulation. Bull. JSME **18**, 813–818 (1975)
3. Wickens, A.H.: The dynamic stability of railway vehicle wheelsets and bogies having profiled wheels. Int. J. Solids Struct. **1**, 319–341 (1965)
4. Yabuno, H., Okamoto, T., Aoshima, N.: Effect of lateral linear stiffness on nonlinear characteristics of hunting motion of a railway wheelset. Meccanica **37**, 555–568 (2002)
5. Iwnicki, S.: Handbook of Railway Vehicle Dynamics. Taylor and Francis, pp 385-395 (2006)
6. He, X.: Hopf bifurcation at infinity with discontinuous nonlinearities. ANZIAM J. **33**, 133–148 (1991)
7. Uyulan, G., Gokasan, M., Bogosyan, S.: Dynamic investigation of the hunting motion of a railway bogie in a curved track via bifurcation analysis. Math. Probl. Eng. **1**, 1–15 (2017)
8. Cheng, L., Wei, X., Cao, H.: Two-parameter bifurcation analysis of limit cycles of a simplified railway wheelset model. Nonlinear Dyn. **93**, 2415–2431 (2018)
9. Hamid, M.S., Kourosh, H.S.: Bifurcation analysis in hunting dynamical behavior in a railway bogie: using novel exact equivalent functions for discontinuous nonlinearities. Sci. Iranica **19**, 1493–1501 (2012)
10. Zhang, T., Dai, H.: Loss of stability of a railway wheel-set, subcritical or supercritical. Veh. Syst. Dyn. **55**, 1731–1747 (2017)
11. Kim, P., Seok, J.: Bifurcation analysis on the hunting behavior of a dual-bogie railway vehicle using the method of multiple scales. J. Sound Vib. **329**, 4017–4039 (2010)
12. Nayfeh, A.H.: The Method of Normal Forms. Wiley (2011)
13. Yabuno, H., Okamoto, T., Aoshima, N.: Stabilization control for the hunting motion of a railway wheelset. Veh. Syst. Dyn. **35**, 41–55 (2001)
14. Soomro, Z.A.: Parametric dynamics of railway vehicle-track interaction model: the influence of creep coefficients. JCSMD **5**, 33–37 (2017)